PhD Thesis

Star Formation and Nuclear Activity of Local Luminous Infrared Galaxies

Memoria de tesis doctoral presentada por

D. Miguel Pereira Santaella

para optar al grado de
Doctor en Ciencias Físicas

Universidad Autónoma de Madrid
Facultad de Ciencias
Departamento de Física Teórica

Consejo Superior de Investigaciones Científicas
Instituto de Estructura de la Materia
Centro de Astrobiología

Madrid, noviembre de 2011

Directora: Dra. Almudena Alonso Herrero — Instituto de Física de Cantabria
Tutora: Prof.ª Rosa Domínguez Tenreiro — Universidad Autónoma de Madrid

Agradecimientos

En primer lugar quería dar las gracias a mi directora de tesis, Almudena Alonso Herrero, por haber confiado en mi desde un principio para realizar este trabajo, así como por todo su interés y dedicación durante estos cuatro años. Además me gustaría agradecer la ayuda y consejos de Luis Colina.

En este tiempo he tenido la oportunidad de realizar estancias en centros de investigación extranjeros de los que guardo un grato recuerdo personal y científico. En particular me gustaría agradecer a George Rieke y a Martin Ward su hospitalidad y amabilidad durante mis visitas al Steward Observatory en la Universidad de Arizona y a la Universidad de Durham.

Y volviendo a Madrid, quisiera agradecer a Tanio y a Marce el apoyo y la ayuda que me ofrecieron en los inciertos comienzos de este proyecto. También quiero dar las gracias a todos (Arancha, Nuria, Álvaro, Alejandro, Julia, Jairo, Javier, Ruymán, Fabián, entre otros) por las interesantes conversaciones, a veces incluso sobre ciencia, en las sobremesas, cafés, etc. que han hecho que todo haya sido bastante más entretenido. Y también gracias a todas las personas que en algún momento pasaron por el Departamento de Astrofísica Molecular e Infrarroja. Una mención especial merecen Dani, Javi y Enrica. Con ellos he compartido, además de despachos, becarías y "naves", muchos de los mejores e inolvidables momentos del doctorado.

Por último, y más importante, quería dar las gracias a mi familia por su apoyo incondicional en todo momento. Sin ellos nada de este trabajo hubiera sido posible.

Durante la realización de esta tesis he disfrutado de una beca JAE-Predoc-2007 del Consejo Superior de Investigaciones Científicas. Asimismo, este trabajo ha recibido financiación procedente de los proyectos ESP2007-65475-C02-01 del Plan Nacional del Espacio y AYA2009-05705-E del Plan Nacional de Astronomía y Astrofísica.

Abstract

Luminous infrared galaxies (LIRGs) and ultraluminous infrared galaxies (ULIRGs) are galaxies with infrared (IR) luminosities ($L_{\rm IR}$) in the range between 10^{11} and $10^{12}\,L_{\odot}$, and $>10^{12}\,L_{\odot}$, respectively. Intense star-formation bursts and/or an active galactic nucleus (AGN) are the power sources of these galaxies. These galaxies are unusual in the local universe, they represent less than 6 % of the IR emission in the local universe. Nevertheless, at high-redshift, $z \sim 1$–2, (U)LIRGs have an important contribution to the star-formation rate (SFR) density of the Universe. Consequently, the study of local LIRGs is a fundamental piece to understanding their more distant counterparts.

This thesis is focused on the study of local LIRGs. For this purpose we defined a complete volume-limited sample of 53 local galaxies ($0.009 < z < 0.017$) with $\log(L_{\rm IR}/L_{\odot}) > 11.05$. We analyzed mid-IR imaging and spectroscopic data obtained with *Spitzer*, and X-ray data from *XMM-Newton* and *Chandra* of these local LIRGs. The *Spitzer* spectroscopic data include observations from two GTO programs. Likewise the *XMM-Newton* X-ray data were obtained through two guest observer programs. In addition we used *Spitzer*, *XMM-Newton*, and *Chandra* archival data.

As a first step in our study, we characterized the mid-IR high-ionization emission lines produced by AGN and star-formation for a large sample of local galaxies, including LIRGs, observed with *Spitzer* (Chapter 3). In Chapter 4 we studied the spatially resolved mid-IR properties of a sample of 15 local LIRGs using *Spitzer*/IRS spectral mapping observations. Finally, in Chapter 5, we present the analysis of the X-ray properties of a representative sample of 27 local LIRGs. The main results and conclusions of this thesis are:

- **Mid-IR High-ionization Lines from AGN and Star-forming Galaxies**
  We studied the *Spitzer* mid-IR spectra of a sample of 426 galaxies, including quasars, Seyferts, LINERs, and H II galaxies. According to their IR luminosities 15 % of them are LIRGs. We focused on the high-ionization emission lines ([Ne V], [O IV], and [Ne III]) originated principally in the AGN and commonly used as tracers of its luminosity. We confirmed the tight linear correlation between the [Ne V]14.3 and 24.3 μm and the [O IV] 25.89 μm emission lines for a large range

of AGN luminosities and types. The correlation between the [O IV] 25.89 μm and [Ne III] 15.56 μm emission lines holds only for active galaxies. Galaxies with strong star-formation have an excess of [Ne III] 15.56 μm emission with respect to that expected from the [O IV] 25.89 μm versus [Ne III] 15.56 μm correlation seen in AGN. That is, it is likely that the [Ne III] emission includes a noticeable contribution from star-formation. We also quantified the star-formation contribution to the [O IV] luminosity. Only when the AGN bolometric luminosity is below 5 % of the $L_{\rm IR}$, the [O IV] is dominated by star-formation.

- **Mid-IR Emission of Local LIRGs**
  The mid-IR spectral range contains a large number of features that can be used to disentangle the star-formation and AGN contributions to the total galaxy emission. Among these spectral features we analyzed the emission of the polycyclic aromatic hydrocarbon bands (PAHs), the ionized gas emission ([Ne II], [Ne III], [S III], and [S IV]), and the molecular gas emission (warm H_2). We found that, in general, the mid-IR spectra of these LIRGs are similar to those of local starbursts. The PAH ratios and equivalent widths are comparable to the values observed in starbursts. Moreover, their 9.7 μm silicate absorptions are moderate and intermediate between those of local starbursts and the extremely deep silicate features of local ULIRGs. However the nuclear [Ne III] 15.56 μm/[Ne II] 12.81 μm ratios are lower than that of H II regions and nearby star-forming galaxies. Photoionization models predictions suggest that the increased densities in the nuclei of LIRGs are responsible for the smaller nuclear ratios. This includes the possibility that a fraction of the most massive stars are hidden in ultra-compact H II regions or that the initial mass function (IMF) is truncated at 30 $M_\odot$ in the LIRG nuclei. The warm (300–1000 K) molecular hydrogen, traced by the H_2 S(1) and S(2) lines at 17.0 and 12.3 μm, is likely to be excited by the same mechanism as the PAHs, based on their similar morphologies and the small variation of the H_2 S(1)/PAH ratios (a factor of 2) in the sample. In some galaxies we found enhanced H_2 emission which can be attributed to large scale shocks associated to galaxy mergers. The derived warm molecular hydrogen gas masses are in the range 0.4–3$\times10^8$ $M_\odot$. This is similar to the values measured in ULIRGs and starbursts.

- **X-ray Emission of Local LIRGs**
  Galaxies with intense star-formation, such as LIRGs, are also strong X-ray emitters. The X-ray emission of starburst galaxies is mainly produced by high-mass X-ray binaries (HMXB), supernova remnants, and hot gas heated by the energy

released by supernova explosions. Both the soft (0.5–2 keV) and hard (2–10 keV) X-ray emissions are well correlated with the SFR in local starbursts. We found that most LIRGs follow these soft and hard X-ray luminosity versus SFR correlations. Only about 15 % of the non-Seyfert LIRGs have an excess hard X-ray emission relative to that expected from star-formation that might indicate the presence of an obscured AGN. The detection of the Fe Kα emission line at 6.4 keV with a large equivalent width is a signature of Compton-thick AGN. However we did not detect the Fe Kα emission line in the H II LIRGs. The line flux upper limits were used to put an upper limit to the bolometric luminosity for an obscured AGN in the star-forming LIRGs, $L_{\rm bol}$(AGN) $<10^{43}\,{\rm erg\,s^{-1}}$. That is, the AGN contribution to the total luminosity in these galaxies is < 10 %. Likewise the AGN contribution to the total energy output in our sample is between 7 % and 10 %.

Resumen

Las galaxias luminosas y ultraluminosas infrarrojas (LIRGs y ULIRGs) son galaxias cuya luminosidad infrarroja ($L_{\rm IR}$) está entre 10^{11} y $10^{12}\,L_{\odot}$ (LIRGs), o es mayor que $10^{12}L_{\odot}$ (ULIRGs). Las fuentes de energía de este tipo de galaxias son brotes intensos de formación estelar y/o un núcleo galáctico activo (AGN). No son comunes en el universo local, su luminosidad representa menos del 6 % de la emisión IR local. Sin embargo, a alto desplazamiento al rojo, $z \sim 1$–2, las (U)LIRGs contribuyen de forma importante a la densidad de tasa de formación estelar del Universo. Por lo tanto, el estudio de las LIRGs locales es fundamental para entender sus homólogas a alto z.

Esta tesis está enfocada al estudio de las LIRGs locales. Para esto definimos una muestra completa limitada en volumen de 53 galaxias locales ($0.009 < z < 0.017$) con $\log(L_{\rm IR}/L_{\odot}) > 11.05$. En este trabajo hemos analizado observaciones fotométricas y espectroscópicas en el infrarrojo medio obtenidas con el telescopio espacial *Spitzer*, y datos de rayos X obtenidos con los telescopios espaciales *XMM-Newton* y *Chandra*. Parte de los datos de *Spitzer* fueron obtenidos gracias a dos programas de tiempo garantizado. Asimismo, parte de los datos de *XMM-Newton* se obtuvieron a través de dos programas de observador invitado. El resto de datos usados estaban disponibles en los archivos de *Spitzer*, *XMM-Newton*, y *Chandra*.

Como primer paso de este estudio caracterizamos la emisión de las líneas atómicas de alta ionización en el infrarrojo medio producidas por formación estelar y AGNs en una muestra grande de galaxias locales (Capítulo 3). En el Capítulo 4 estudiamos las propiedades de la emisión infrarroja media espacialmente resuelta de una muestra de 15 LIRGs locales usando mapeados espectrales obtenidos con *Spitzer*. Por último, en el Capítulo 5, presentamos el análisis de las propiedades de la emisión de rayos X de una muestra representativa de 27 LIRGs locales. Los principales resultados y conclusiones de esta tesis son los siguientes:

- **Líneas de alta ionización en el infrarrojo medio producidas por formación estelar y AGNs**
  Hemos estudiado los espectros infrarrojos medios de una muestra de 426 galaxias que incluía: cuásares, Seyferts, LINERs, y galaxias H II. Según sus luminosidades

infrarrojas, un 15 % de ellas eran LIRGs. Nuestro estudio se centra en las líneas de alta ionización ([Ne V], [O IV], y [Ne III]) producidadas principalmente en el AGN y que son indicadores de su luminosidad. Confirmamos la buena correlación entre la emisión de las líneas de [Ne V]14.3 y 24.3 μm y [O IV] 25.89 μm para un amplio rango de tipos y luminosidades de AGNs. La correlación entre las líneas de [O IV] 25.89 μm y [Ne III] 15.56 μm se cumple sólo para galaxias activas. En las galaxias con altas tasas de formación estelar observamos un exceso de emisión de [Ne III] 15.56 μm respecto a la esperada de acuerdo a su luminosidad de [O IV] 25.89 μm. Es decir, es probable que en estos casos la emisión de [Ne III] incluya una contribución considerable debida a la formación estelar. También cuantificamos la contribución de la formación estelar a la luminosidad de [O IV]. Sólo cuando la luminosidad bolométrica del AGN es menor que el 5 % de la $L_{\rm IR}$, la formación estelar domina la emisión de [O IV].

- **La emisión infrarroja media de las LIRGs locales**
  El rango espectral infrarrojo medio contiene un gran número de características espectrales que pueden ser usadas para separar la contribución de la formación estelar y del AGN a la emisión total de las galaxias. En esta tesis hemos analizado aquellas debidas a la emisión de los hidrocarburos policíclicos aromáticos (PAH), del gas ionizado ([Ne II], [Ne III], [S III], y [S IV]), y del gas molecular (H_2 templado). En general, encontramos que los espectros infrarrojos medios de estas LIRGs son similares a los de las galaxias locales con brotes de formación estelar. Las anchuras equivalentes de las bandas de los PAHs también son comparables a las que se observan en galaxias con brotes de formación estelar. Además, encontramos que la absorción debida a los silicatos a 9.7 μm en las LIRGs es moderada, intermedia entre la de las de las galaxias locales con brotes de formación estelar y las extremas absorciones encontradas en las ULIRGs locales. El cociente nuclear entre la emisión de [Ne III] 15.56 μm y [Ne II] 12.81 μm es menor que el que se observa en regiones H II y galaxias con formación estelar cercanas. Los modelos de fotoionización sugieren que las altas densidades del gas en los núcleos de las LIRGs pueden ser responsables de esto. Otras posibilidades son que una fracción de las estrellas más masivas esté oculta en regiones H II ultracompactas o que la función inicial de masa esté truncada a 30 $M_\odot$ en los núcleos de las LIRGs. El gas molecular templado (300–1000 K), trazado por las líneas de emisión H_2 S(1) y S(2) a 17.0 y 12.3 μm, presenta una morfología parecida a la de los PAHs, además la variación del cociente entre la emisión de H_2 S(1) y los PAHs en nuestra muestra es pequeña (un factor 2). Esto indica que probablemente el gas molec-

ular templado sea excitado por el mismo mecanismo que los PAHs. En algunas galaxias encontramos un exceso de emisión de H_2 que puede ser asociado a ondas de choque a gran escala producidas en las fusiones de galaxias. Las masas de gas molecular templado calculadas para estas LIRGs están en el rango de 0.4 a $3{\times}10^8\,M_\odot$. Esto es similar a los valores medidos en ULIRGs y galaxias con formación estelar cercanas.

- **La emisión de rayos X de las LIRGs locales**
  Las galaxias que tienen altas tasas de formación estelar, como las LIRGs, son también fuentes brillantes de rayos X. La emisión de rayos X en este tipo de galaxias es producida principalmente por binarias de rayos X de alta masa, remanentes de supernova, y gas a altas temperaturas calentado por la energía liberada por las explosiones de supernovas. En las galaxias locales con brotes de formación estelar, tanto la emisión de rayos X blandos (0.5–2 keV) como la de rayos X duros (2–10 keV) están correlacionadas con la tasa de formación estelar. En nuestro estudio encontramos que las LIRGs locales también siguen estas correlaciones. Solamente un 15 % de las LIRGs no Seyfert tienen un exceso de emisión de rayos X duros respecto a la esperada por la formación estelar que puede indicar la presencia de un AGN oscurecido. La línea de emisión de Fe Kα a 6.4 keV con una gran anchura equivalente es una señal característica de los AGNs muy oscurecidos (*Compton-thick*). Sin embargo, no detectamos esta línea en las LIRGs de tipo H II. A partir del límite superior del flujo de esta línea estimamos que el límite superior de la luminosidad de un posible AGN oscurecido en estas galaxias es $L_{\rm bol}({\rm AGN}) < 10^{43}\,{\rm erg\,s^{-1}}$. Es decir, la contribución del AGN a la luminosidad total de estas galaxias es menor del 10 %. Asimismo, la contribución de los AGNs a la luminosidad total de nuestra muestra de LIRGs está entre un 7 y 10 %.

Contents

Acronyms

2MASS	*Two Microns All Sky Survey*
6dFGS	*Six-Degree Field Galaxy Survey*
A&A	*Astronomy and Astrophysics*
A&AS	*Astronomy and Astrophysics Supplement Series*
AGB	*Asymptotic Giant Branch*
AGN	*Active Galactic Nucleus*
AJ	*Astronomical Journal*
AOR	*Astronomical Observation Request*
ApJ	*Astrophysical Journal*
ApJS	*Astrophysical Journal Supplement*
ARA&A	*Annual Review of Astronomy and Astrophysics*
BCD	*Basic Calibrated Data*
BGS	*Bright Galaxy Sample*
BLR	*Broad Line Region*
CCD	*Charged Coupled Device*
CUBISM	*Cube Builder for IRS Spectra Maps*
EPIC	*European Photon Imaging Camera*
ESA	*European Space Agency*
FWHM	*Full Width Half Maximum*
GTO	*Guaranteed Time Observer*
HMXB	*High-Mass X-ray Binary*
HST	*Hubble Space Telescope*
HyLIRG	*Hyper Luminous Infrared Galaxy*
IMF	*Initial Mass Function*
IR	*Infrared*
IRAC	*Infrared Array Camera*
IRAS	*Infrared Astronomical Satellite*
IRS	*Infrared Spectrograph*
ISM	*Interstellar Medium*
ISO	*Infrared Space Observatory*
JWST	*James Webb Space Telescope*
LH	*Long-High*
LINER	*Low-Ionization Nuclear Emission-line Region*
LIRG	*Luminous Infrared Galaxy*
LMXB	*Low-Mass X-ray Binary*

LL	*Long-Low*
MIPS	*Multiband Imaging Photometer for Spitzer*
MNRAS	*Monthly Notices of the Royal Astronomical Society*
MOPEX	*Mosaicker and Point source Extractor*
MOS	*Metal Oxide Semiconductor*
NASA	*National Aeronautics and Space Administration*
NED	*NASA/IPAC Extragalactic Database*
NICMOS	*Near Infrared Camera and Multi-Object Spectrometer*
NLR	*Narrow Line Region*
ODF	*Observation Data File*
OM	*Optical Monitor*
PAH	*Polycyclic Aromatic Hydrocarbon*
PASP	*Publications of the Astronomical Society of the Pacific*
PN	*Planetary Nebulae*
PSF	*Point Spread Function*
QSO	*Quasi Stellar Object*
RBGS	*Revised Bright Galaxy Sample*
RGS	*Reflection Grating Spectrograph*
RRC	*Radiative Recombination Continua*
RSA	*Revised Shapley-Ames*
SAS	*Science Analysis Software*
SED	*Spectral Energy Distribution*
SF	*Star Formation*
SFR	*Star Formation Rate*
SH	*Short-High*
SL	*Short-Low*
SMBH	*Super-Massive Black Hole*
S/N	*Signal-to-Noise*
SNe	*Supernovae*
SNR	*Supernova Remnants*
SPICE	*Spitzer IRS Custom Extraction*
SSC	*Spitzer Science Center*
ULIRG	*Ultraluminous Infrared Galaxy*
UKST	*United Kingdom Schmidt Telescope*
UV	*Ultraviolet*
W-R	*Wolf-Rayet*
XMM-Newton	*X-ray Multi-Mirror Mission*

Chapter 1

Introduction

In this chapter we present a summary of the properties of local infrared bright galaxies. The morphology and nuclear activity of this class of galaxies are discussed. Next the properties of their high-redshift counterparts are outlined. In the second part of this chapter we discuss the general characteristics of the mid-infrared and X-ray emissions of infrared bright galaxies. Finally we present the thesis project.

1.1 Infrared Bright Galaxies

Infrared bright galaxies are the prevailing class of extragalactic objects at luminosities $> 10^{11}\,L_{\odot}$ in the local universe (see Sanders & Mirabel 1996 for a review). They are more common than optically selected starbursts, Seyfert galaxies and quasars (Soifer et al. 1987a). However, this class of objects remained unknown until the last decades of the 20th century as they are faint in the optical.

1.1.1 Discovery

The first ground-based infrared (IR[1]) observations at 1–25 μm of galaxies in the late 60's and the beginning 70's (e.g., Kleinmann & Low 1970; Rieke & Low 1972) revealed a population of bright IR galaxies. Some were even brighter in the IR than at optical wavelengths. Subsequent studies of nearby starbursts (e.g., Harper & Low 1973; Telesco & Harper 1980) and Seyfert galaxies (e.g., Rieke & Low 1975; Neugebauer et al. 1976) showed that an excess IR emission in these galaxies, which could not be explained by the photospheric emission of stars, was common.

The thermal origin of this tremendous IR emission was established soon after their discovery (Rieke & Lebofsky 1979). The optical and ultraviolet (UV) emission, from

[1]The IR wavelength range is usually divided into near-IR, from 0.7 to 5 μm, mid-IR, from 5 to 25 μm, and far-IR from 25 to 350 μm.

Table 1.1: Abbreviations and Definitions adopted for *IRAS* Galaxies

$F_{\rm FIR}$	$1.26 \times 10^{-14} \{2.58 f_{60} + f_{100}\}$ [W m^{-2}]
$L_{\rm FIR}$	$L(40 - 500\,\mu m) = 4\pi\, D_{\rm L}^2$ C $F_{\rm FIR}$ [$L_\odot$]
$F_{\rm IR}$	$1.8 \times 10^{-14} \{13.48 f_{12} + 5.16 f_{25} + 2.58 f_{60} + f_{100}\}$ [W m^{-2}]
$L_{\rm IR}$	$L(8 - 1000\,\mu m) = 4\pi\, D_{\rm L}^2\, F_{\rm IR}$ [$L_\odot$]
LIRG	Luminous Infrared Galaxy, $L_{\rm IR} > 10^{11}\, L_\odot$
ULIRG	Ultra-luminous Infrared Galaxy, $L_{\rm IR} > 10^{12}\, L_\odot$
HyLIRG	Hyper-luminous Infrared Galaxy, $L_{\rm IR} > 10^{13}\, L_\odot$

Notes. The quantities f_{12}, f_{25}, f_{60}, and f_{100} are the *IRAS* flux densities in Jy at 12, 25, 60, and 100 μm. C is a scaling factor in the range 1.4–1.8 to account for the extrapolated flux long-ward the 100 μm *IRAS* filter. $D_{\rm L}$ is the luminosity distance. $L_\odot = 3.84 \times 10^{26}$ W = 3.84×10^{33} erg s^{-1}. Table adapted from Sanders & Mirabel (1996).

star-formation and/or an active galactic nucleus (AGN), is absorbed by dust grains and then re-emitted at IR wavelengths approximately with the spectrum of a blackbody at the temperature of the dust (∼20–80 K).

A major step forward in the study of IR bright galaxies was the launch in 1983 of the *Infrared Astronomical Satellite* (*IRAS*; Neugebauer et al. 1984). It observed the whole sky in 4 IR bands centered at 12, 25, 60, and 100 μm detecting ∼250 000 sources (Helou & Walker 1988). About 25 000 of these sources are extragalactic objects and many of them had not been previously cataloged. Most of these galaxies emit the bulk of their luminosity in the IR (Houck et al. 1985; Soifer et al. 1987b), and are faint in the optical. Therefore they went unnoticed in preceding optical surveys. According to their IR luminosity in the range 8–1000 μm ($L_{\rm IR}$) they were classified as luminous ($L_{\rm IR} = 10^{11}$–$10^{12}\, L_\odot$), ultra-luminous ($L_{\rm IR} = 10^{12}$–$10^{13}\, L_\odot$), and hyper-luminous ($L_{\rm IR} > 10^{13}\, L_\odot$) infrared galaxies, LIRGs, ULIRGs and HyLIRGs, respectively. This classification is based on the definitions in Table 1.1.

1.1.2 Morphologies

Toomre & Toomre (1972) showed that the collision between two spiral galaxies can explain the morphological features (tidal tails, bridges, etc.) observed in close pairs of galaxies. These peculiar galaxies also have evidence of recent star-formation, thus Larson & Tinsley (1978) suggested that interactions may trigger the star-formation activity. During a merger the interstellar medium (ISM) of the colliding galaxies undergoes strong gravitational torques and tidal forces. As a result the gas flows toward the central region of the merger fueling intense star-formation bursts in small (< 1 kpc) regions (e.g., Barnes & Hernquist 1996).

The properties of the merger remnants mainly depends on the mass ratio of the interacting galaxies. For mass ratios 4:1 and 3:1 the remnants appear as disk galaxies. Whereas for mergers of equal mass systems, known as major mergers, the resulting product are massive elliptical galaxies (Toomre 1977; Naab & Burkert 2003).

Optical and near-IR studies showed that a large fraction of (U)LIRGs are interacting systems or have evidence of recent interactions (e.g., Melnick & Mirabel 1990; Clements et al. 1996; Veilleux et al. 2002). The fraction of interacting galaxies increases with increasing $L_{\rm IR}$ (see Figure 1.1). Actually, $> 90\,\%$ of the ULIRGs are interacting systems at different merger phases (Murphy et al. 1996; Veilleux et al. 2002). Local LIRGs, on the other hand, are mostly spiral galaxies. Often they are in an early stage of interaction, and their morphologies are much less disturbed than that ULIRGs (e.g., Wu et al. 1998).

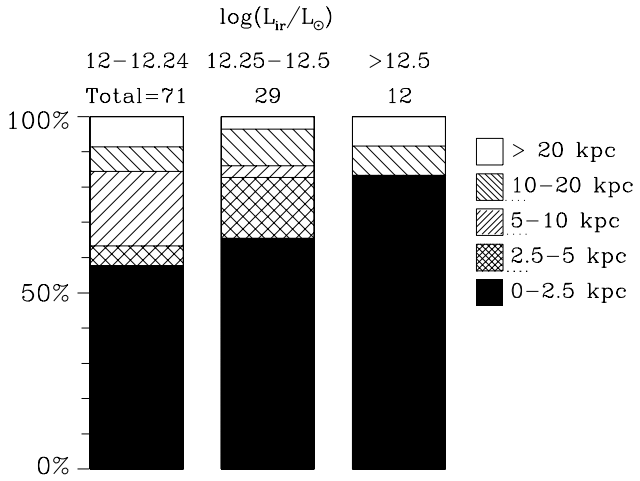

Figure 1.1: Apparent nuclear separation as function of the $L_{\rm IR}$. Most of the ULIRGs with $\log\,(L_{\rm IR}/L_{\odot})$,$>$ 12.5 are single-nucleus systems (separation $< 2.5\,$kpc). Figure from Veilleux et al. (2002).

1.1.3 Power Source of (U)LIRGs

Since their discovery there have been a large number of studies trying to determine what powers (U)LIRGs. Works based on optical spectroscopy showed that the lower luminosity LIRGs are principally powered by star-formation. Moreover, the fraction of AGN dominated galaxies increases with increasing $L_{\rm IR}$ (Figure 1.2). Optical spectroscopy studies of (U)LIRGs show that about $\sim$40 % of the local ULIRGs are classified as Seyfert galaxies (Veilleux et al. 1995; Kim et al. 1995; Kewley et al. 2001; Yuan et al.

2010). Yuan et al. (2010) studied a sample of ∼500 IR-selected galaxies. They classified the nuclear activity of (U)LIRGs as H II, composite, low-ionization emission line region (LINER), and Seyfert using their optical emission line ratios (e.g., [N II]λ6584/Hα vs. [O III]λ5007/Hβ). The fraction of LINER ULIRGs is below 5 % indicating that this class of galaxies usually does not have strong star-formation or AGN emission reprocessed by dust. Instead they found a large fraction, ∼30 %, of composite (U)LIRGs. Composite galaxies are likely to be a combination of AGN and star-formation activity. These galaxies would be the intermediate evolution state from starburst to AGN dominated (Seyfert) ULIRGs. In addition, it has been proposed that ULIRGs may be the initial dust-enshrouded stage of quasars (e.g., Sanders et al. 1988).

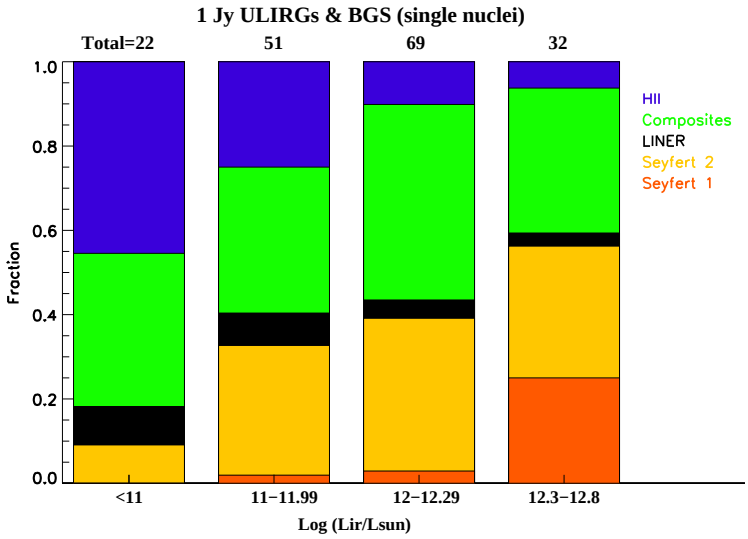

Figure 1.2: Nuclear activity from optical spectroscopy as function of $L_{\rm IR}$ for the 1 Jy ULIRG sample (Veilleux et al. 1999) and the LIRGs in the BGS sample (Veilleux et al. 1995). Figure from Yuan et al. (2010).

Optical studies are subject to extinction effects, especially in the case of (U)LIRGs. Due to the large amount of dust in these galaxies the extinction is high. In LIRGs $A_{\rm V}$ is 2–6 mag on average, although values larger than 10 mag are sometimes measured (e.g., Alonso-Herrero et al. 2006; Veilleux et al. 1995). In ULIRGs even higher extinctions are observed ($A_{\rm V} > 45$ mag; e.g., Genzel et al. 1998). Therefore, a large fraction of the young stars might be completely obscured at optical wavelengths. Rodríguez-Zaurín et al. (2011) found that the star-formation rate (SFR) derived from the extinction corrected $H\alpha$ emission represents less than 10 % of the SFR obtained using the $L_{\rm IR}$. For this reason (U)LIRGs have been widely studied by means of IR spectroscopy. Most of the IR spectral range is not accessible from ground-based telescopes due to the

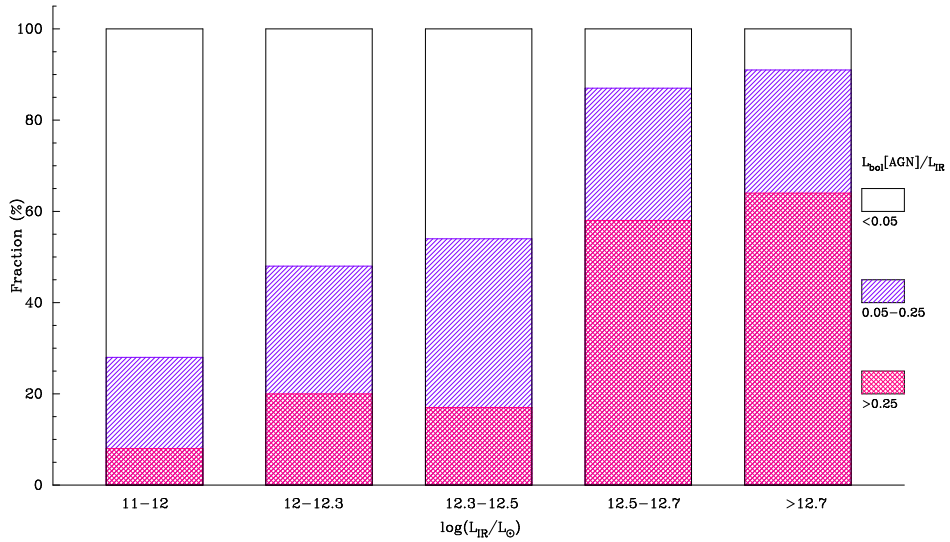

Figure 1.3: Fractional AGN bolometric contribution to the IR luminosity for a local sample of LIRGs and ULIRGs. The AGN bolometric contributions are from Nardini et al. (2010). Figure from Alonso-Herrero et al. (2011).

atmospheric absorption. But thanks to the space telescopes *Infrared Space Telescope* (*ISO*; Kessler et al. 1996), *Spitzer* (Werner et al. 2004), and, more recently, *Herschel* (Pilbratt et al. 2010), mid- and far-IR spectroscopy of (U)LIRGs was possible. Genzel et al. (1998) investigated a sample of 15 ULIRGs with *ISO* mid-IR spectroscopy. Using mid-IR diagnostic diagrams (e.g., [O IV]/Ne II ratio, see Section 1.2.4) they found that 70–80 % of the objects in their sample are mainly powered by star-formation. Although 50–60 % have simultaneously AGN and starburst activity.

With the advent of *Spitzer* larger samples of ULIRGs were observed (e.g., Farrah et al. 2007; Nardini et al. 2008, 2010; Veilleux et al. 2009). These studies confirmed that most of the luminosity of ULIRGs is produced by star-formation. Farrah et al. (2007) studied a sample of 53 local ULIRGs using *Spitzer* mid-IR high-resolution (R∼600) spectroscopy. They showed that the AGN dominates the IR emission only in 20 % of the ULIRGs. Indeed, the [Ne V]14.32 μm high-ionization emission line is detected in half of their sample, thus the AGN makes a significant contribution in just 50 % of their ULIRGs. The 5–8 μm mid-IR spectra of starbursts show small variations from one object to another (e.g., Brandl et al. 2006). Nardini et al. (2008, 2010) took advantage of this similarity in the spectra to decompose the spectrum of 71 local ULIRGs into starburst and AGN components. They detected AGN signatures in 70 % of the ULIRGs. However star-formation dominates the IR luminosity in their sample, although AGN emission accounts for 23 % of the global IR emission.

Similar studies for local LIRGs (e.g., Valiante et al. 2009; Petric et al. 2011; Alonso-Herrero et al. 2011) determined that they are also powered by star-formation, but with a lower AGN contribution than ULIRGs. Petric et al. (2011) analyzed the *Spitzer* spectra of 248 LIRGs. They employed diagnostic diagrams similar to those used with ULIRGs. They detected AGN signatures in 18 % of the LIRGs, although it dominates the IR emission only in 10 % of them. Using a similar approach to that of Nardini et al. (2008, 2010), Alonso-Herrero et al. (2011) decomposed the *Spitzer* mid-IR of a sample of 53 LIRGs into AGN and starburst components using star-forming galaxy templates and clumpy torus models. This method together with optical indicators reveals the presence of an AGN in 62 % of the individual nuclei of LIRGs. However, only 8 % of them have AGN with a significant bolometric contribution ($L_{\rm bol}/L_{\rm IR} > 0.25$), 70 % have AGN contributions below 5 % of their $L_{\rm IR}$, and for the remaining 20 % the AGN accounts for 5–25 % of their $L_{\rm IR}$ (Figure 1.3).

Young stellar populations emit most of their luminosity in the UV and optical spectral range, thus their emission is strongly affected by dust absorption. Assuming that the bolometric luminosity of the starbursts is re-emitted in the IR, Kennicutt (1998) used stellar population synthesis models to derive the relation between the $L_{\rm IR}$ and the SFR. Most of the IR emission of (U)LIRGs is produced by star-formation. Therefore, the $L_{\rm IR}$ is a good indicator of the SFR for these galaxies. The SFR of LIRGs is of the order of tens to hundreds of $M_{\odot}\,{\rm yr}^{-1}$ using the Kennicutt (1998) prescription.

1.1.4 High-redshift (U)LIRGs

Despite the fact that bright IR galaxies are the dominant object population at $L_{\rm bol} > 10^{11}\,L_{\odot}$, they are not common in the local universe. Indeed, only 1 ULIRG (Arp 220) is located within 120 Mpc. These galaxies only represent < 6 % of the IR emission in the local universe (Soifer & Neugebauer 1991; Goto et al. 2011). However, the space density of ULIRGs is higher than that of quasars (Figure 1.4).

The sensitivity of the *IRAS* survey limited the detection of ULIRGs up to redshift $z \sim 0.3$. Despite this limitation, an evolution in the space density of ULIRGs proportional to $(1+z)^{8\pm3}$ was found (Oliver et al. 1996; Kim & Sanders 1998). Surveys with *ISO* showed a strong evolution in the number of powerful starbursts (SFR $\sim$100 $M_{\odot}\,{\rm yr}^{-1}$) up to $z \sim 1$. Franceschini et al. (2001) explained this evolution in terms of an increasing number of galaxy interactions with z, which would trigger strong starbursts, in addition to an evolution in the IR luminosity, as the available gas to fuel the starbursts was more abundant in the past.

Spitzer provided new sensitive observations of (U)LIRGs up to $z \sim 3$ (Le Floc'h et al.

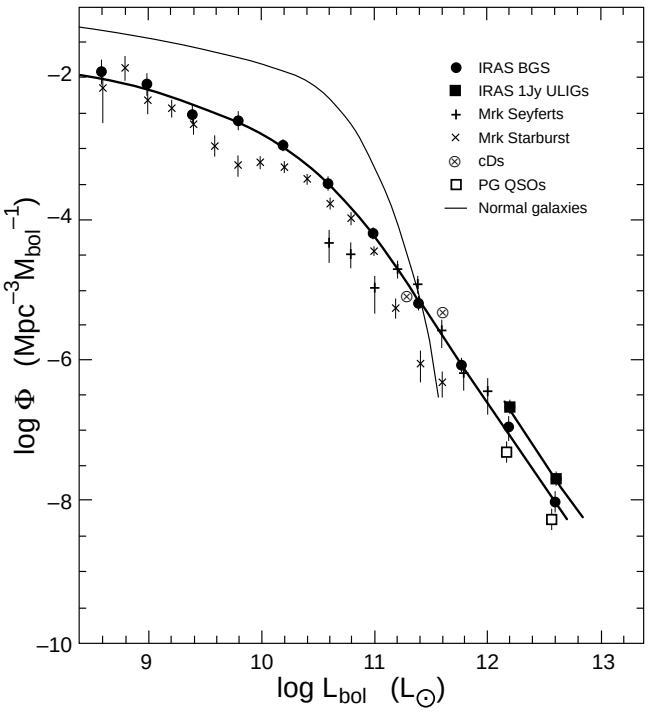

Figure 1.4: Comparison of the luminosity function of IR bright galaxies (*IRAS* BGS and *IRAS* 1 Jy ULIRGs) with other extragalactic objects (Seyfert galaxies, starbursts, giant ellipticals, quasars, and normal galaxies). Figure from Sanders & Mirabel (1996).

2005; Pérez-González et al. 2005; Lagache et al. 2005; Caputi et al. 2007). Samples of galaxies selected at 24 μm have been used to investigate the population of IR bright galaxies at high-redshift. These studies used spectral energy distribution (SED) fitting methods to estimate the $L_{\rm IR}$ of these galaxies. They showed that the typical infrared luminosity has decreased by an order of magnitude from $z \sim 2$ to the present (Pérez-González et al. 2005). In the same way, the SFR density, traced by the IR luminosity density, rises from $z = 0$ to 1.2 and then it remains almost constant up to $z \sim 3$. It is dominated by LIRGs from $z \sim 0.6$ to $z \sim 1.5$ (Figure 1.5; Lagache et al. 2005). At $z \gtrsim 1.5$ more than half of the new stars are formed in ULIRGs (Pérez-González et al. 2005).

Spitzer spectroscopic studies of IR bright galaxies at $z \sim 2$ reveal that most of them are powered by intense star-formation. Farrah et al. (2008) found that the spectra of these galaxies resemble those of local starbursts and LIRGs. They show strong polycyclic aromatic hydrocarbons (PAHs) emission bands similar to local starbursts/LIRGs, but several orders of magnitude more luminous (equivalent to SFR $> 1000\,M_\odot\,{\rm yr}^{-1}$). The shallow silicate absorption at 9.7 μm is also different from the deep absorption

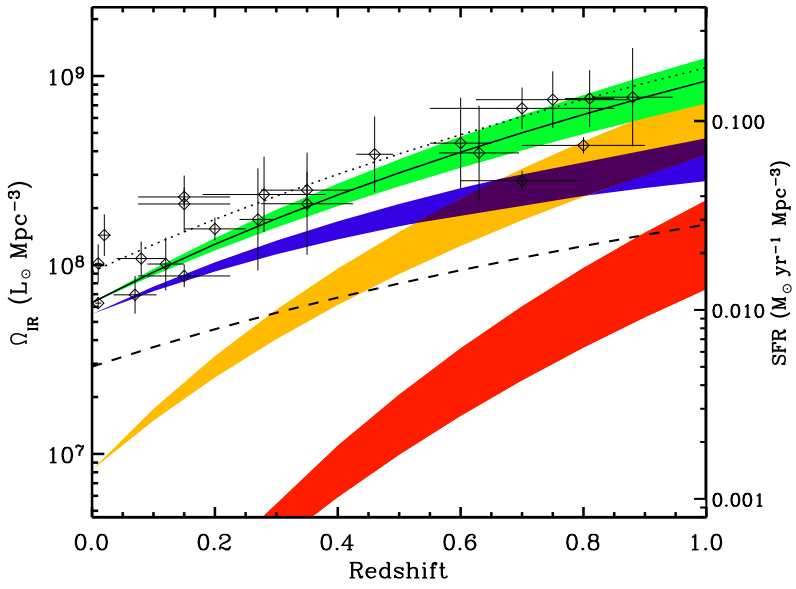

Figure 1.5: Evolution of the co-moving IR luminosity density with redshift (green filled region). The contribution from low-luminosity galaxies ($L_{\rm IR} < 10^{11}\,L_\odot$; blue filled region), LIRGs ($L_{\rm IR} > 10^{11}\,L_\odot$; orange filled region), and ULIRGs ($L_{\rm IR} > 10^{12}\,L_\odot$; red filled region) is shown. Figure from Le Floc'h et al. (2005).

features observed in local ULIRGs. This suggests a different geometry of the obscuring dust in distant ULIRGs. Star-formation in high-redshift ULIRGs might take place in few kpc scales instead of the < 1 kpc scales of local ULIRGs. AGN are likely present in these ULIRGs as well. 25 % (2 out of 8) of the $z \sim 2$ ULIRGs studied by Yan et al. (2005) have power-law continuum spectra typical of type 1 AGN. Half of the galaxies in their sample are likely composite systems with strong star-formation and a buried AGN.

1.2 The mid-IR Emission of (U)LIRGs

We discussed in the previous section that the origin of the IR emission of (U)LIRGs is mainly thermal. Dust grains absorb optical and UV light that then is re-emitted in the IR almost with the spectrum of a blackbody.

Besides this thermal continuum emission, there are a number of spectral features in the mid-IR spectra of galaxies. The most prominent features are the broad emission bands produced by PAHs. Several PAH bands are observed in the wavelength range from 3 to 20 μm. (U)LIRGs usually present a strong silicate absorption feature centered

at 9.7 μm. In some cases, mostly in type 1 AGNs, this feature is seen in emission (Shi et al. 2009). In addition, absorption bands from water ice, at 6 μm, and from aliphatic hydrocarbons, at 6.85 μm, are observed in some (U)LIRGs.

Forbidden emission lines from atoms with different ionization energies (from 8 to > 120 eV) are also present in this wavelength range, as well as the hydrogen Humphreys series emission lines. Finally, the pure rotational emission lines from warm molecular hydrogen ($300\,\mathrm{K} < T < 1000\,\mathrm{K}$) are usually detected in the mid-IR spectra of galaxies.

In the following we describe in detail these features of the IR spectra of (U)LIRGs, and starbursts galaxies and AGN in general.

1.2.1 Mid- and Far-IR Continuum

The interstellar dust absorbs a significant fraction of the UV and optical emission of galaxies and this energy is later radiated in the IR. The absorption at longer wavelengths is much lower than at the UV/optical range (e.g., Rieke & Lebofsky 1985), making the mid- and far-IR spectral ranges ideal for the study of obscured environments.

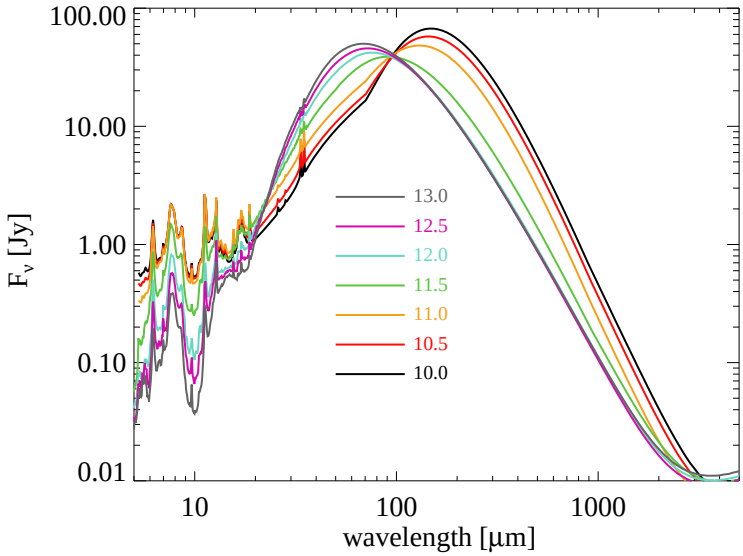

Figure 1.6: IR SED templates of star-forming (U)LIRGs for different L_{IR}. The PAH emission bands at $\lambda < 13$ μm and the silicate absorption feature centered at 9.7 μm are clearly visible in the templates. The key indicates the $\log(L_{\mathrm{IR}}/L_{\odot})$ of the templates. The templates are normalized to the same integrated flux. Figure adapted from Rieke et al. (2009).

The mid- and far-IR SED of galaxies can be modeled as the emission of a modified

blackbody at different temperatures: the emission from the IR cirrus ($T < 20\,\mathrm{K}$, $\lambda > 100\,\mu\mathrm{m}$) heated by old stellar populations; a warm ($T \sim 30$–$60\,\mathrm{K}$) component peaking at $60\,\mu\mathrm{m}$ associated to recent star-formation; and in Seyfert galaxies a warmer component ($T \sim 150$–$250\,\mathrm{K}$) produced by the dust directly illuminated by the AGN (Sanders & Mirabel 1996). Figure 1.6 shows a comparison of the IR SED of the templates of IR bright galaxies from Rieke et al. (2009). The peak at $60\,\mu\mathrm{m}$ from dust heated by star-formation is evident in the SED of (U)LIRGs. The peak at $\sim 140\,\mu\mathrm{m}$ observed in the lower L_{IR} SEDs is produced by colder dust heated by the interstellar radiation field. The warm dust component dominates the SED for high SFR, or equivalently, high L_{IR}.

IR bright galaxies are classified as warm (cold) if the ratio between the *IRAS* fluxes at 25 and $60\,\mu\mathrm{m}$ (f_{25}/f_{60}) is ≥ 0.3 (< 0.3). In general, galaxies with warm colors host an AGN (Sanders & Mirabel 1996). The small scatter in the f_{60}/f_{100} ratios (0.8 dex) in samples selected at $60\,\mu\mathrm{m}$, that is, galaxies with intense star-formation, can be explained by the dominance of the warm dust thermal emission (Sanders et al. 2003). To explain other observed *IRAS* flux ratios (e.g., f_{12}/f_{25}) a hot dust component is sometimes required, as we discussed above.

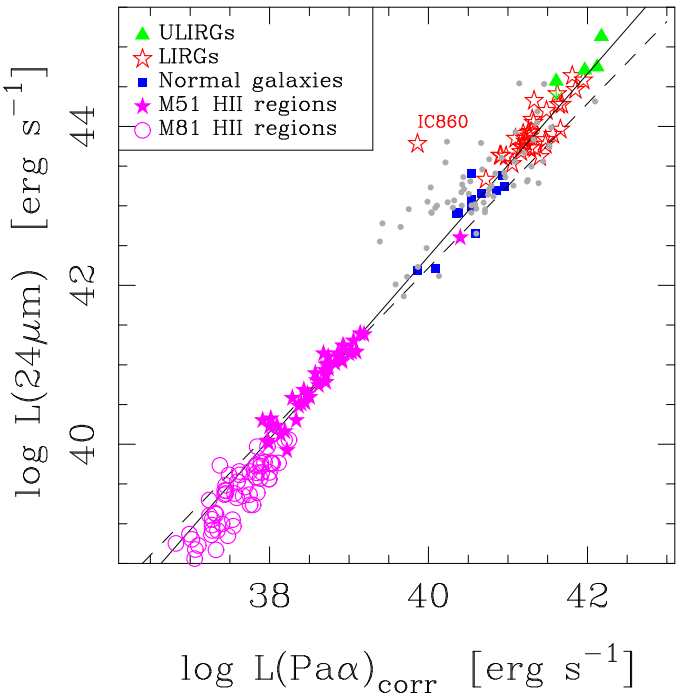

Figure 1.7: Comparison of the Paα and $24\,\mu\mathrm{m}$ luminosities for star-forming LIRGs and H II regions. Figure from Alonso-Herrero et al. (2006).

The mid- and far-IR monochromatic luminosities as well as the integrated IR lumi-

nosities can be used to estimate the SFR (e.g., Kennicutt 1998; Kennicutt et al. 2009). However, the far-IR luminosity may also include the emission of a cooler dust component (cirrus) heated by the interstellar radiation field and not be related with the current SFR. To minimize the contribution of the cooler dust it is possible to use the monochromatic IR luminosity at shorter wavelengths. A commonly used wavelength is 24 μm, which can be observed with the *Spitzer*/MIPS imager. The continuum at 24 μm is well correlated with the number of ionizing photons from young stars, traced by the Paα hydrogen recombination line (Figure 1.7). Several works (e.g., Alonso-Herrero et al. 2006; Calzetti et al. 2007; Rieke et al. 2009) have calibrated the SFR vs. $L_{24\mu m}$ for galaxies.

1.2.2 Polycyclic Aromatic Hydrocarbons

PAHs are molecules composed by a large number (∼10–1000) of carbon atoms. They are one the main components of the interstellar dust together with silicate and graphite grains. It is thought that a large number of PAH species are present in the interstellar medium, however the exact composition is not known (Draine 2003).

These molecules, that are mainly excited by UV photons, present several fluorescence emission bands in the mid-IR. The strongest bands are located at 3.3, 6.2, 7.7, 8.6, 11.3, 12.7, and 17 μm (Figure 1.8). Each band is produced by different types of molecular vibrations (e.g., C–H stretching, out-of-plane C–C modes, C–H bending modes, etc.; see Allamandola et al. 1989; Draine & Li 2001).

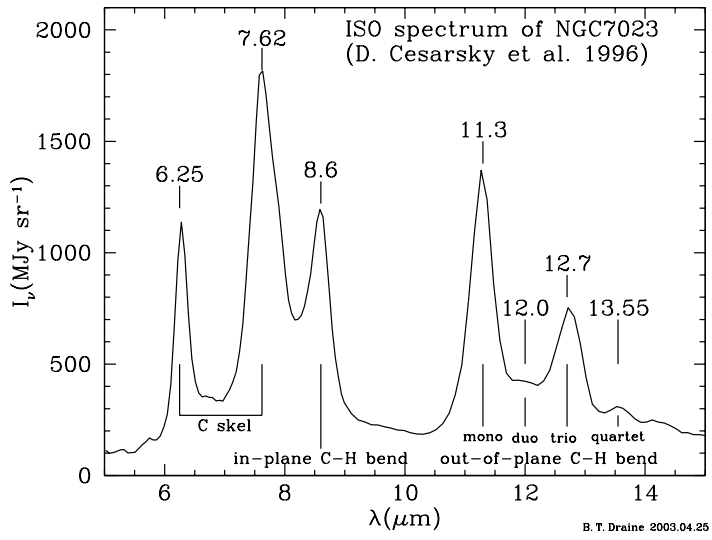

Figure 1.8: Mid-IR spectrum of the PAH emission features in the 5–15 μm range. Figure from Draine (2003).

The relative strength of the bands depends on the size and ionization state of the PAH. For ionized PAHs the emission of the 6.2, 7.7, and 8.6 μm features is favored whereas the 3.3 and 11.3 μm features are thought to be produced mainly by neutral PAHs. Similarly, small PAHs emit most of their power at the 6.2 and 7.7 μm features while larger molecules emit more strongly at 11.3 μm (Draine & Li 2001; Galliano et al. 2008b).

ISO spectroscopy revealed that PAHs are ubiquitous in the interstellar medium. The PAH emission bands have been observed in post-AGB stars, planetary nebulae, H II regions, etc. (Peeters et al. 2004a). Specifically, PAH bands are observed in the mid-IR spectra of galaxies with star-formation emitting up to 20–30 % of the total infrared emission (e.g., Genzel et al. 1998; Rigopoulou et al. 1999; Helou et al. 2000; Smith et al. 2007b). The PAH band ratios are remarkably uniform over the integrated spectra of different galaxy classes (Lu et al. 2003; Brandl et al. 2006; Smith et al. 2007b).

The formation and destruction processes of the PAH molecules are not well known. It is thought that they are formed in AGB stars together with carbon dust (Galliano et al. 2008a). The PAH bands are believed to be suppressed in harsh environments. For instance, they may not survive in intense UV radiation fields such those in young H II regions or in the vicinity of AGNs. This may explain the weak PAH emission in low metallicity galaxies, which have a much harder spectra than high-metallicity galaxies (e.g., Wu et al. 2006; Gordon et al. 2008).

Since the PAH molecules are excited by UV photons, the PAH emission is enhanced in regions with young stars (mainly B stars; see Peeters et al. 2004b). Thus the strength of the PAH bands can be used as a tracer of the SFR (e.g., Brandl et al. 2006; Houck et al. 2007; Farrah et al. 2007).

1.2.3 Silicate and Ice Features

Besides the PAH bands there are other broad spectral features in the mid-IR spectra of galaxies. Two features commonly detected in galaxies are the silicate absorption (or emission) feature and the absorption bands due to ices.

The water ice absorption features at 3.1 and 6.0 μm, associated to the stretching and bending modes, respectively, of the H_2O molecule (Draine 2003), have been observed in some ULIRGs and in deeply embedded sources. The obscuring dust attenuates the radiation field permitting the formation of ice (Spoon et al. 2002, 2007; Risaliti et al. 2006).

The strong feature at 9.7 μm in the spectra of local ULIRGs is produced by the

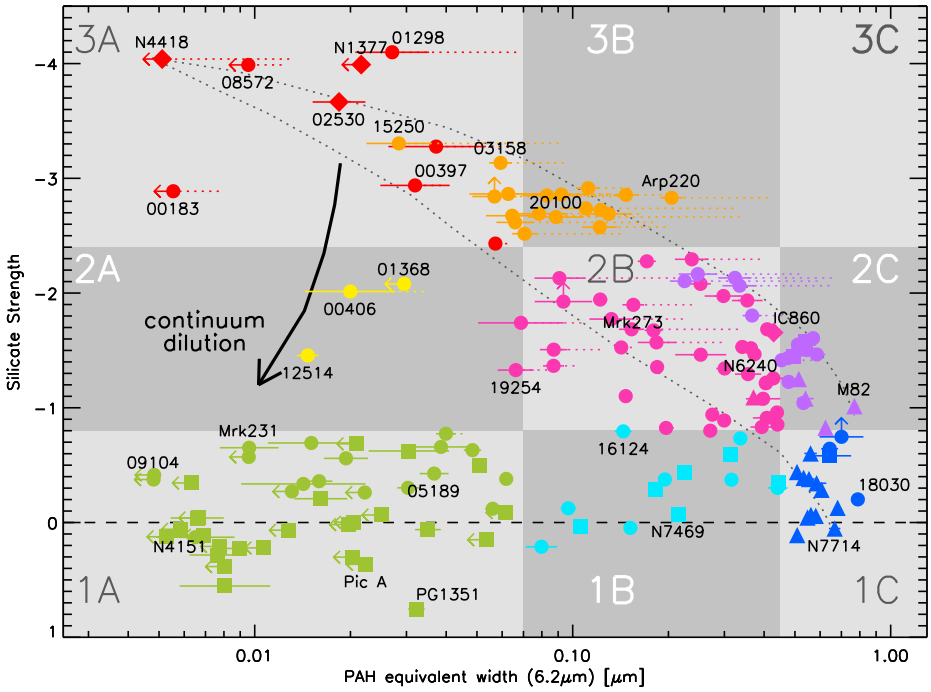

Figure 1.9: Diagnostic diagram of the EW of the 6.2 μm PAH vs. the strength of the 9.7 μm silicate feature. Colors indicate the galaxy classification from the diagram. Circles are ULIRGs and HyLIRGs, triangles are starburst galaxies, squares Seyferts and quasars, and diamonds other IR galaxies. Figure from Spoon et al. (2007).

Si–O stretching mode of amorphous silicate minerals. While this feature is also present in local LIRGs, it is not usually as deep as in local ULIRGs (Alonso-Herrero et al. 2011 and Chapter 4). A weaker feature at 18 μm is produced by the O–Si–O bending mode (Draine 2003).

Using ground mid-IR data Roche et al. (1991) found that the silicate features in (U)LIRGs and Type 2 Seyfert galaxies are usually observed in absorption. Indeed, the depth of the 9.7 μm feature is related to the optical extinction ($A_V/\tau_{Si} = 16.6 \pm 2.1$ for a simple dust screen model; Rieke & Lebofsky 1985). Silicate grains mixed with the emitting sources produce moderate silicate depths (e.g., Smith et al. 2007b). However for the deepest features (i.e., the most embedded sources) a foreground screen of cold dust is required (Levenson et al. 2007).

For some galaxies, mainly among those hosting a type 1 AGN, the silicate features are seen in emission (Sturm et al. 2005; Hao et al. 2007). The silicate feature in emission from the hot dust clouds surrounding the AGN is predicted by torus models as well as the silicate feature in absorption depending on the torus parameters (e.g., Nenkova et al. 2008).

In combination with the PAH emission, the depth of the silicate feature has been used to classify IR bright galaxies (Spoon et al. 2007). Figure 1.9 shows a commonly used diagram to determine the dominant power source of IR bright galaxies. Galaxies are distributed in two branches. The horizontal branch ranges from AGN dominated sources with low PAH equivalent width (EW) and shallow silicate absorption to starburst galaxies with large PAH EWs. The EW of the 6.2 μm PAH is lower in AGNs because the 6.2 μm continuum emission from hot dust is stronger in AGNs than in star-forming galaxies. Destruction of PAH molecules in AGNs may also contribute to reduce the EW of the PAH features. The diagonal branch in this diagram extends from starburst to absorption dominated sources (ULIRGs and HyLIRGs). Very few galaxies are found between the two branches. Local LIRGs in this diagram are mostly located in the horizontal branch and in the moderately absorbed regions. This is true for the nuclear and integrated measurements as well as for the spatially resolved measurements as we shall see in Chapter 4.

1.2.4 Atomic Emission Lines

In the mid-IR spectral range there are a number of fine structure emission lines that can be used to explore the physical conditions of the galaxies. The most common emission lines observed in galaxies are listed in Table 1.2. The ionization potential of the emitting species ranges from ∼8 to 125 eV, so it is possible to study a range of physical conditions from those of the neutral regions of the ISM to those of H II regions and AGNs. Next we describe the properties of the most prominent mid-IR emission lines.

The [Ne II] 12.81 μm emission line is one of the strongest mid-IR emission lines produced by star-formation. It has been observed in star-forming regions (e.g., Roche et al. 1991; Thornley et al. 2000; Verma et al. 2003; Brandl et al. 2006; Bernard-Salas et al. 2009) and it is correlated with the $L_{\rm IR}$ (Ho & Keto 2007). Therefore the [Ne II] 12.81 μm emission line can also be used as a tracer of the SFR.

Due to the intermediate ionization potential of Ne^{+2} (41.0 eV, Table 1.2), the [Ne III] 15.56 μm emission line may be produced by young massive stars or by AGNs. Like the [Ne II] 12.81 μm emission line the [Ne III] 15.56 μm is detected in starbursts (Verma et al. 2003; Brandl et al. 2006; Beirão et al. 2006; Bernard-Salas et al. 2009) and also in AGNs (Gorjian et al. 2007; Tommasin et al. 2008). Actually the [Ne III] 15.56 μm/[Ne II] 12.81 μm ratio can be used to measure the ionization parameter in star-forming regions, although it depends on the age and metallicity of the stellar populations (Brandl et al. 2006; Snijders et al. 2007; Alonso-Herrero et al. 2009b; Dale et al. 2009). The [Ne III]

Table 1.2: Mid-IR Fine Structure Emission Lines

Species	λ (μm)	$E_{\rm p}$ (eV)
[Ar II]	6.98	15.8
[Ne VI]	7.64	126.2
[Ar III]	8.99	27.6
[S IV]	10.51	34.8
[Ne II]	12.81	21.6
[Ne V]	14.32	97.1
[Cl II]	14.37	13.0
[Ne III]	15.56	41.0
[S III]	18.71	23.3
[Fe III]	22.93	16.2
[Ne V]	24.32	97.1
[O IV]	25.89	54.9
[Fe II]	25.99	7.9
[S III]	33.48	23.3
[Si II]	34.81	8.1
[Ne III]	36.01	41.0

Notes. Rest-frame wavelength and ionization potential of the most prominent emission lines observed in the mid-IR spectra of galaxies.

15.56 μm/[Ne II] 12.81 μm ratio combined with the [S IV] 10.51 μm/[S III] 18.71 μm ratio provides another estimate of the ionization parameter with smaller uncertainties (Gordon et al. 2008). Nonetheless, the [Ne III] 15.56 μm emission also seems to be a good proxy for AGN luminosity, at least for reasonably high luminosities (Gorjian et al. 2007; Dudik et al. 2009; Meléndez et al. 2008a; Tommasin et al. 2008).

The most important high-excitation lines accessible in the mid-IR include [Ne V] at 14.32 and 24.32 μm, and [O IV] at 25.89 μm. Because of their very high ionization potential, the [Ne V] lines are considered to be reliable signposts for an AGN (Genzel et al. 1998; Armus et al. 2007). These lines have been used to identify low-luminosity AGNs in local galaxies (Satyapal et al. 2008; Goulding & Alexander 2009). However, they are also produced in supernova remnants (SNR; Oliva et al. 1999; Smith et al. 2009), planetary nebulae (PN; Pottasch et al. 2009), and Wolf-Rayet stars (W-R; Schaerer & Stasińska 1999). Although the [Ne V] luminosities of these objects are low, $\sim 10^{34}$ erg s^{-1} (Smith et al. 2009; Pottasch et al. 2009), several thousands of them

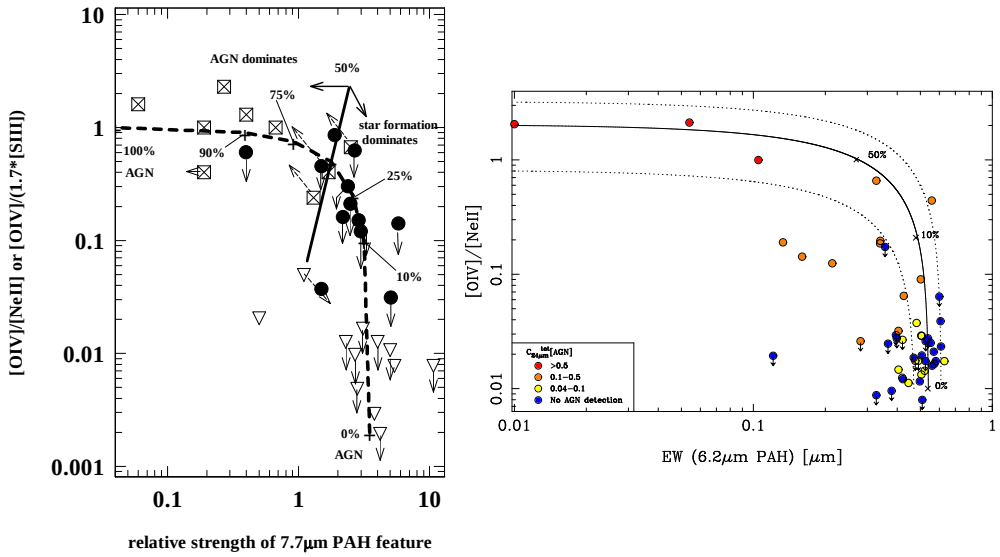

Figure 1.10: *Left panel*: Diagnostic diagram of the EW of the 7.7 μm PAH vs. [O IV]/[Ne II] ratio. Starbursts are open triangles, ULIRGs are marked as filled circles, and AGNs as crossed rectangles. The dashed line is the linear mixing curve between pure AGN and pure star-formation. *Right panel*: Same as the left panel but using the EW of the 6.2 μm PAH for a sample of local LIRGs. The galaxies are color coded according to the AGN contribution at 24 μm. The solid line is the mixing curve between AGN and starbursts and the dotted lines represent the 1σ dispersion of the curve. The left and right panels are from Genzel et al. (1998) and Alonso-Herrero et al. (2011), respectively.

might also produce detectable [Ne V] emission.

Despite the lower ionization potential of [O IV], the 25.89 μm emission line appears to be an accurate indicator of AGN power, since it correlates well with the very hard ($>$ 14 keV) X-ray luminosity (Meléndez et al. 2008a; Rigby et al. 2009; Diamond-Stanic et al. 2009) and the mid-IR [Ne V] emission lines (Dudik et al. 2009; Weaver et al. 2010). However, this line also appears in the spectra of starburst galaxies with no other evidence for AGN (Lutz et al. 1998a; Verma et al. 2003; Bernard-Salas et al. 2009), where it is attributed to W-R stars (Crowther et al. 1999; Schaerer & Stasińska 1999), and/or to shocks (Allen et al. 2008; Lutz et al. 1998a).

Combining low- and high-ionization emission lines it is possible to estimate the relative contribution of the AGN and star-formation to the emission of galaxies (see e.g., Genzel et al. 1998). A commonly used diagnostic diagram to separate starbursts from AGNs is shown in Figure 1.10. AGNs have larger [O IV]/[Ne II] ratios than galaxies with just star-formation. Likewise the relative strength of the PAH decreases for AGNs (see Section 1.2.3). This kind of diagrams have been used to successfully determine

Table 1.3: Mid-IR Molecular Hydrogen Emission Lines

Transition	λ (μm)	E_u/k (K)
0–0 S(7)	5.51	7196
0–0 S(6)	6.11	5828
0–0 S(5)	6.91	4585
0–0 S(4)	8.02	3473
0–0 S(3)	9.66	2503
0–0 S(2)	12.28	1681
0–0 S(1)	17.03	1051
0–0 S(0)	28.22	510

Notes. Rest-frame wavelength and rotational upper level energy of the strongest H_2 mid-IR emission lines in galaxies. Table adapted from Roussel et al. (2007).

the dominant power source for IR galaxies (e.g., Genzel et al. 1998; Dale et al. 2006; Veilleux et al. 2009; Petric et al. 2011). However when the AGN contribution is not dominant in the mid-IR (less than 50 % at 24 μm) this diagram may not provide an accurate estimate of the AGN contribution (Alonso-Herrero et al. 2011).

1.2.5 Molecular Hydrogen and Other Molecules

Molecular hydrogen (H_2) is the most abundant molecule in the universe. It represents about 20 % of the ISM mass (Ferrière 2001). However, the observation of H_2 is difficult since it does not possess an electric dipole moment and, therefore, the H_2 dipole transitions ($\Delta J = \pm 1$) are forbidden. The observable transitions are electric quadrupole transitions ($\Delta J = 0, \pm 2$). The low transition probability (Einstein's A coefficient) of the electric quadrupole transitions results in relatively low critical densities ($n_{\rm critical} = 10^3$–$10^5\,{\rm cm}^{-3}$) for the rotational transitions. In addition, this implies that H_2 has two independent states, one with odd J (ortho-H_2) and the other with even J (para-H_2). No radiative transitions are possible between ortho- and para-H_2, although collisions with atomic hydrogen can produce ortho–para conversions. In thermal equilibrium, for $T > 200\,{\rm K}$, the ortho-to-para ratio is 3 (see e.g., Burton et al. 1992).

Owing to the small moment of inertia of H_2, its rotational energy levels are widely spaced when compared to other diatomic molecules. As a consequence, the transitions between the lowest rotational levels lie in the mid-IR spectral range (see Table 1.3). Moreover, the high energy of the rotational levels means that these transitions probe warm molecular gas ($300\,{\rm K} < T < 1000\,{\rm K}$) that is only a small fraction, 1–10 %, of the

total H_2 in star-forming galaxies (Rigopoulou et al. 2002). The main processes that excite the H_2 molecule are UV fluorescence, shocks, and X-ray heating.

In star-forming galaxies the warm H_2 seems to be associated to photodissociation regions (Rigopoulou et al. 2002; Roussel et al. 2007). The same occurs in ULIRGs (Higdon et al. 2006). In these regions the UV photons from young stars and collisions between molecules excite the H_2 (e.g., Black & van Dishoeck 1987; Burton et al. 1992).

AGNs have an excess of warm H_2 emission with respect to normal galaxies (Rigopoulou et al. 2002; Roussel et al. 2007). X-ray and shock heating have been proposed to explain this. X-ray photons can reach the inner parts of the molecular clouds producing high-energy electrons that heat the molecular region (e.g., Maloney et al. 1996; Tine et al. 1997; Shaw et al. 2005). On the other hand, shocks dissociate most of the H_2 molecules that later are re-formed producing a spectrum similar to that of a UV illuminated molecular cloud (Hollenbach & McKee 1989; Burton et al. 1992). In some cases, galactic scale shocks in interacting galaxies provide an efficient mechanism to excite H_2 (Rieke et al. 1985; Appleton et al. 2006; Roussel et al. 2007).

Besides the rotational H_2 emission lines, there are molecular bands in the mid-IR produced by HCN (13.7 μm), C_2H_2 (14.0 μm), and CO_2 (15.0 μm). These bands have been observed in absorption in some (U)LIRGs, suggesting the presence of warm dense gas ($T \sim 200$–$700\,\mathrm{K}$, $n > 10^6\,\mathrm{cm}^{-3}$) which may be associated to the deeply embedded star formation in (U)LIRGs (Lahuis et al. 2007).

1.2.6 Summary

Figure 1.11 shows the observed mid-IR spectrum of a LIRG dominated by star-formation. The spectral features discussed above present in the spectrum are marked.

In this spectrum strong PAH bands with high EW are clearly seen. Indeed, the PAH emission dominates the mid-IR emission up to $\sim$12 μm. At longer wavelengths the continuum produced by warm dust heated by young stars is the dominant component.

This spectrum has an intermediate 9.7 μm silicate absorption feature. Local ULIRGs, in general, have deeper silicate absorption features than local LIRGs. The 18 μm silicate feature is weaker than that at 9.7 μm. In addition it is coincident with the 17 μm PAH complex and, therefore, it is only seen in highly obscured sources.

In general, the most intense atomic emission lines in the mid-IR spectra of star-forming LIRGs are the [Ne II] 12.81 μm and [Si II] 34.81 μm lines. Other intense emission lines are those produced by [S III].

Molecular hydrogen emission lines are also detected in the spectra of local LIRGs, although they are not especially strong. The brightest mid-IR H_2 emission line in

LIRGs is the S(1) at 17.03 μm. Molecular absorption features are only detected in those deeply embedded, as indicated by their large silicate depths, LIRGs.

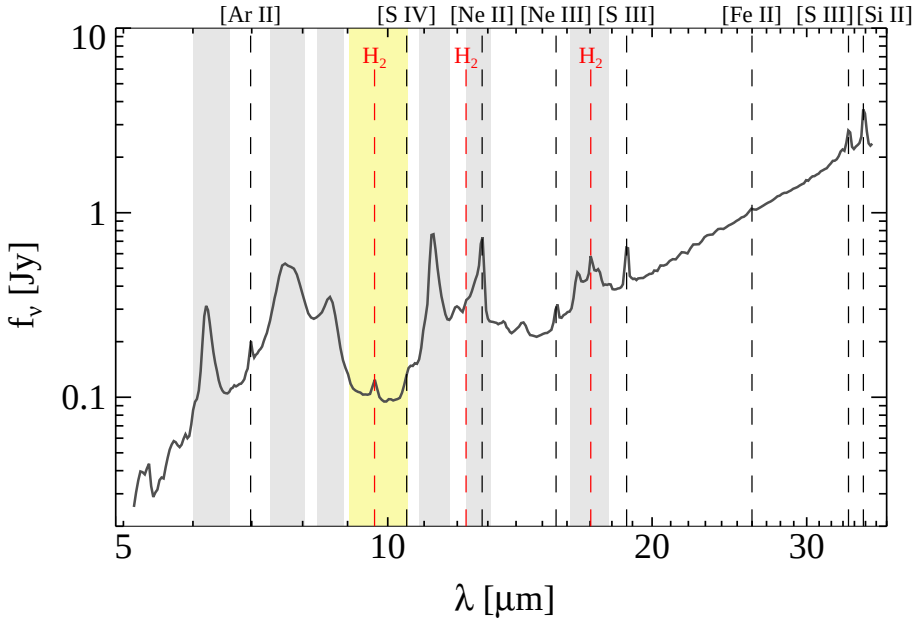

Figure 1.11: Example low-resolution mid-IR spectrum of a star-forming galaxy obtained with *Spitzer*. The most prominent spectral features are marked. Atomic emission lines are marked with black dashed lines and molecular hydrogen emission lines with dashed red lines. The shaded yellow background indicates the position of the 9.7 μm silicate absorption feature. PAH features are marked with gray background color.

1.3 The X-ray Emission of (U)LIRGs

Star-formation and AGN activity are the two main processes which give rise to the X-ray emission[2] in galaxies. As we discussed in Section 1.1, (U)LIRGs are galaxies with strong star-formation, and a large part of them also host an AGN. Therefore, this type of galaxies are also strong X-ray emitters.

Only few works have studied the X-ray emission of local (U)LIRGs (e.g., Rieke 1988; Risaliti et al. 2000; Ptak et al. 2003; Franceschini et al. 2003; Lehmer et al. 2010; Iwasawa et al. 2009, 2011; Nardini & Risaliti 2011). They show that the X-ray emission of some (U)LIRGs is dominated by an AGN, many are composite systems

[2]We consider the X-ray emission in the range from 0.5 to 10 keV. This energy range is usually divided into soft (0.5–2 keV) and hard (2–10 keV) X-ray emission.

with contributions from both star-formation and an AGN, and others do not have any AGN contribution.

Although star-formation and AGN emission is observed in the X-ray spectral range they have very different properties. In this Section we describe the physical origin and the characteristics of the X-ray emission produced by these processes.

1.3.1 Star-formation

In general the X-ray emission of starbursts is less luminous than that of galaxies hosting an AGN. However, sufficiently intense star-formation can produced intense X-ray emission. In particular, the X-ray luminosity of non-active LIRGs is about $10^{41}\,\mathrm{erg\,s^{-1}}$, which is comparable to the X-ray luminosity of low-luminosity Seyferts (Pereira-Santaella et al. 2011).

The X-ray emission in starbursts is mainly produced by X-ray binaries and hot gas heated by the energy originated in supernova explosions (Persic & Rephaeli 2002; Fabbiano 2006). Other minor contributors to the integrated X-ray emission are SNR, individual massive stars (types O and early-B) and Compton scattering of IR photons. The X-ray emission of star-forming galaxies is correlated with the SFR. However, this correspondence with other SFR indicators is not direct because, in general, the processes leading to the X-ray emission in starbursts are delayed with respect to the beginning of the burst (Mas-Hesse et al. 2008; Rosa González et al. 2009).

1.3.1.1 X-ray Binaries

X-ray binaries are binary systems consisting of a compact object, namely a black hole or a neutron star, accreting from a donor star. When the mass of the donor star is $> 8\,M_{\odot}$ they are classified as high-mass X-ray binaries (HMXBs). Otherwise, they are classified as low-mass X-ray binaries (LMXBs).

The X-ray emission of X-ray binaries is produced by the accretion of material from the donor star by the compact object. The companion star fills the Roche lobe and a flow of mass falls toward the compact object forming an accretion disk. In addition, the mass transfer through stellar winds might be also important in HMXBs. The mass of the donor star and the accretion rate determine the luminosity and variability of their X-ray emission.

Since the donors in HMXBs are massive stars, they are associated to recent star-formation. Actually, the hard X-ray emission of starbursts, which is dominated by the emission of HMXBs, is proportional to the SFR (Ranalli et al. 2003; Grimm et al. 2003; Persic et al. 2004). HMXBs have a universal luminosity function (Figure 1.12) that

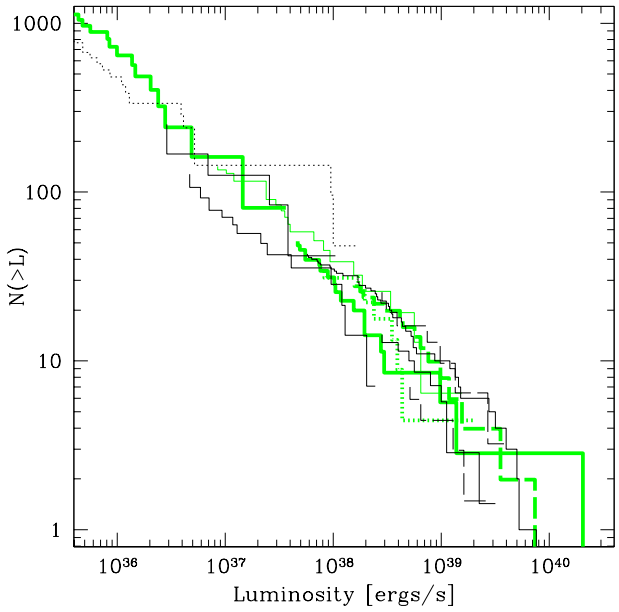

Figure 1.12: Hard X-ray luminosity function of compact X-ray sources in nearby galaxies scaled by their SFR. Figure from Grimm et al. (2003).

can be approximated with a power-law with a cut-off at $L_{2-10\,keV} \sim 2 \times 10^{40}\,\mathrm{erg\,s^{-1}}$. This luminosity function is scaled by the SFR of the host galaxy (Grimm et al. 2003). This luminosity function implies that for low SFR ($< 4\,M_\odot\,\mathrm{yr}^{-1}$) the integrated hard X-ray luminosity of a galaxy might be dominated by few bright sources. Therefore, the relation between the SFR and the integrated hard X-ray luminosity is not linear in the low SFR regime.

On the other hand, the number of LMXBs is proportional to the stellar mass of the galaxy (Gilfanov 2004). Thus, it is not related to the current SFR, but rather to the star-formation history of the host galaxy. Its contribution to the X-ray luminosity is not always negligible for galaxies with low SFR/$M_\star$, where $M_\star$ is the stellar mass (see Colbert et al. 2004; Lehmer et al. 2010). For (U)LIRGs the contributions of LMXB is small, about $\sim 10\,\%$ (Lehmer et al. 2010).

1.3.1.2 Hot Thermal Plasma

A component from hot gas ($kT = 0.3$–$0.7\,\mathrm{keV}$)[3] is observed in the spectra of starburst galaxies (Ptak et al. 1997, 1999; Ranalli et al. 2003). The ISM is heated by the

[3]In X-ray astronomy it is common to use kT in units of keV. The conversion factor between energy (keV) and temperature units (K) is: $1\,\mathrm{keV}/k = 1.16{\times}10^7\,\mathrm{K}$.

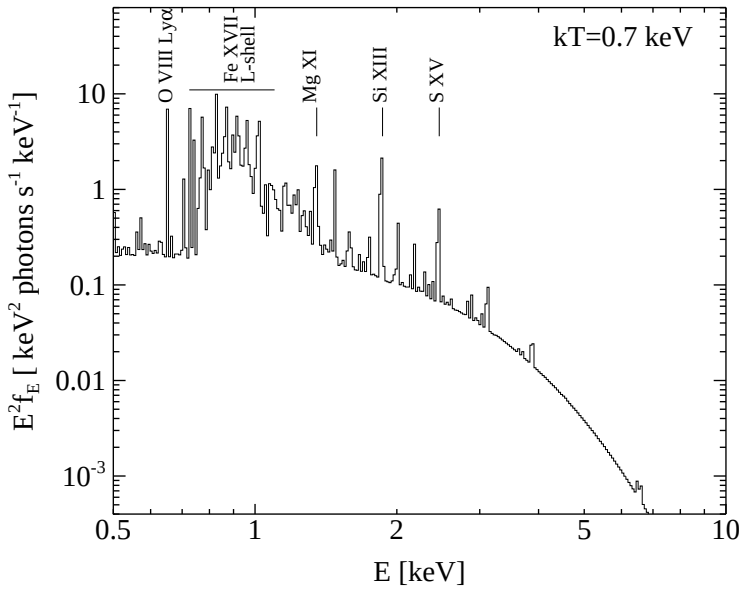

Figure 1.13: Synthetic spectrum of a soft ($kT = 0.7\,\mathrm{keV}$) thermal plasma calculated using the code `APEC` (Smith et al. 2001). The strongest emission lines are labeled.

mechanical energy from supernovae (SNe) and stellar winds with thermalization efficiency of ∼10 % (Mas-Hesse et al. 2008; Strickland & Heckman 2009). The soft X-ray emission of star-forming galaxies is dominated by this component, which is correlated with the SFR (Ranalli et al. 2003).

Another plasma component with higher temperature (kT = 2–5 keV) is detected is some galaxies (Cappi et al. 1999; Strickland et al. 2002; Iwasawa et al. 2009). This component is also produced by SNe and stellar winds, but in regions with higher thermalization efficiency (∼30–100 %). This hot plasma might dominate the hard X-ray emission in high-luminosity LIRGs and ULIRGs (Iwasawa et al. 2009).

Figures 1.13 and 1.14 show the synthetic spectra of a thermal plasma in ionization equilibrium at $kT = 0.7$ and 3 keV, respectively (Smith et al. 2001). The continuum is produced by two processes: free-free emission (Bremsstrahlung), and radiative recombination continua (RRC). Bremsstrahlung emission is produced by electrons being accelerated by the electric field originated by the ions in the plasma. The RRC is produced by the photons emitted in re-combinations of ions with free electrons. The energy of the RRC photons is the ionization potential of the ion (I) plus the free electron energy (Maxwell-Boltzmann distribution with temperature kT). In thermal plasmas both energies are comparable and thus broad RRC features are produced. Conversely, in photoionized plasmas $kT \ll I$ thus the RRC is very sharp (Liedahl &

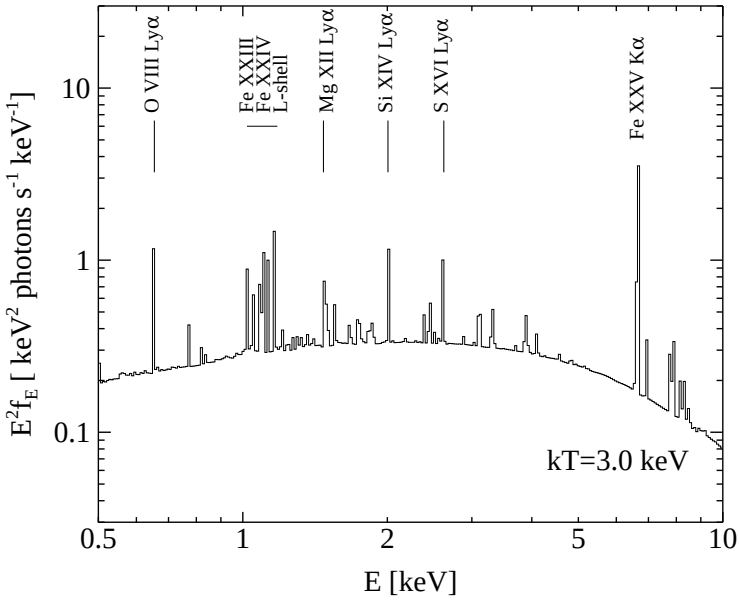

Figure 1.14: Synthetic spectrum of a hard ($kT = 3\,\mathrm{keV}$) thermal plasma calculated using the code `APEC` (Smith et al. 2001). The strongest emission lines are labeled.

Paerels 1996).

The critical densities of the emission lines are high ($n_\mathrm{c} > 10^{14}\,\mathrm{cm}^{-3}$). Thus for the diffuse gas in galaxies the low density approximation, where all collisional excitations produce radiative transitions, can be used.

The spectrum of the soft plasma is dominated by atomic emission lines, mainly from highly ionized iron (Fe XVII and Fe XVIII) and oxygen (O VIII). The strength of these emission lines provides a direct measurement of the relative element abundances. The Fe Kα emission line at 6.7 keV is the strongest feature in the spectrum of the hard plasma. Indeed, the detection of this emission line is an evidence for the presence of hot gas in galaxies (Cappi et al. 1999; Ballo et al. 2004). Note, however, that this emission line can also be produced by AGN (see next section).

1.3.2 Active Galactic Nuclei

AGN are very bright X-ray sources. They emit about 5–10 % of their energy in the X-ray spectral range (Marconi et al. 2004). AGN have X-ray luminosities in the range 10^{41}–$10^{44}\,\mathrm{erg\,s^{-1}}$ in Seyfert galaxies and can reach more than $10^{48}\,\mathrm{erg\,s^{-1}}$ in quasars. This large X-ray luminosity is produced by mass accretion onto the super-massive black hole (SMBH) located at the galaxy centers.

The accretion disk around the SMBH is the origin of the X-ray emission. The thermal component (blackbody with kT ~0.1–0.3 keV) observed in the soft X-ray spectra of AGN is thought to be produced in this accretion disk. In addition, they show a power-law component extending up to 100 keV. This power-law spectrum is believed to be produced by the inverse Compton scattering of lower energy photons (optical and UV) by energetic particles around the accretion disk. At the same time, high-energy photons are scattered by low-energy electrons (Compton scattering) in the colder regions of the accretion disk and the gas around the AGN. This produces an emission bump at 20–30 keV, as well as the fluorescent Fe Kα emission line at 6.4 keV. The emission from photoionized plasma is also seen in the soft X-ray spectra of AGN.

According to the AGN unified model (Antonucci 1993; Urry & Padovani 1995), apart from the accretion disk, SMBH are surrounded by an obscuring torus of dust and gas and a number of gas clouds. Our line of sight toward the SMBH determines the observational characteristics of AGN. They are classified in two groups, Type 1 and Type 2 AGN. Type 2 are those AGN observed through the obscuring torus, while in Type 1 we can see directly the central engine.

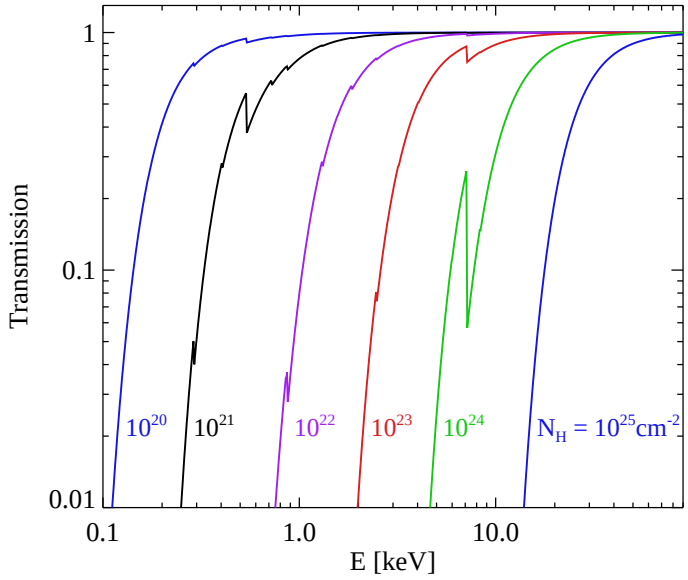

Figure 1.15: X-ray transmission for different hydrogen column densities ($N_{\rm H}$). The corresponding $N_{\rm H}$ of each curve are indicated in the figure. The transmission curves are calculated using the Tuebingen-Boulder ISM absorption model (Wilms et al. 2000).

The different obscuration in Type 1 and 2 AGN are clearly observed in the X-ray spectra. Figure 1.15 shows the transmission curves for various hydrogen column densities ($N_{\rm H}$). Additionally the Galactic $N_{\rm H}$ can affect the observed X-ray emission of

AGN. At high galactic latitudes it is in the range 10^{20}–$10^{21}\,\mathrm{cm}^{-2}$, and thus it modifies the soft X-ray emission below $E < 0.5\,\mathrm{keV}$. Type 1 AGNs have N_H comparable to the Galactic value. However, most Type 2 AGNs have $N_\mathrm{H} > 10^{23}\,\mathrm{cm}^{-2}$, so they are completely obscured at $E < 2\,\mathrm{keV}$ (Risaliti et al. 1999).

AGNs with N_H larger than the inverse of the Thomson cross section, that is $N_\mathrm{H} > 1.5 \times 10^{24}\,\mathrm{cm}^{-2}$, are known as Compton-thick. In these AGNs the nuclear radiation is only visible above 10 keV, although they can be identified by a strong Fe Kα emission and the reflected continuum emission from the AGN (Comastri 2004). In fact, in Compton-thick AGNs the EW of the Fe Kα emission line is usually $> 1\,\mathrm{keV}$. This is caused by the different gas column densities that affect the AGN continuum and the emission line. The X-ray continuum in a Compton-thick AGN is highly absorbed below 10 keV by the gas around the AGN. The 6.4 keV Fe Kα emission line, on the other hand, is produced in regions far from the AGN with an absorbing column density in our line of sight significantly lower than that of the continuum (e.g., Jiménez-Bailón et al. 2005). Moreover, the Fe Kα luminosity is a good proxy of the AGN intrinsic luminosity (e.g., Levenson et al. 2006).

1.4 Thesis Project

Although the mid-IR and X-ray properties of local LIRGs are understood on a broad sense, previous works suffer from several biases. Up until now most of the mid-IR studies of local LIRGs were done only for a few bright and well-known LIRGs. At the time of submission of our *Spitzer* guaranteed time observer (GTO) program proposing to observe a sample of LIRGs with the Infrared Spectrograph (IRS) much of our knowledge of the mid-IR spectroscopic properties of local IR-bright galaxies came from *ISO* (e.g., Genzel et al. 1998; Tran et al. 2001) and early results with *Spitzer* (Armus et al. 2004, 2006). However, the majority of the *ISO* works focused on samples of local IR-bright galaxies or starburst galaxies, and only included a few luminous LIRGs [$\log(L_\mathrm{IR}/L_\odot)$,$> 11.8$, see e.g., Genzel et al. 1998; Verma et al. 2003]. Likewise, previous X-ray studies of local LIRGs were biased toward the most luminous objects in this spectral range and thus included mostly LIRGs hosting a bright AGN.

This thesis presents a detailed study of the mid-IR and X-ray emission properties of a sample of local LIRGs. In particular we use a complete volume limited sample of local LIRGs ($0.009 < z < 0.017$). The sample was drawn from the *IRAS* Revised Bright Galaxy Sample (RBGS; Sanders et al. 2003). It was described by Alonso-Herrero et al. (2006) and Alonso-Herrero et al. (2011). In Chapter 2 we give a summary of its main properties.

We used both imaging and spectroscopic mid-IR *Spitzer* data. For the X-ray analysis we used *XMM-Newton* and *Chandra* data. We obtained part of the *Spitzer* spectroscopic data through two GTO programs as well as X-ray data for LIRGs without bright AGN through two *XMM-Newton* guest observer programs. In addition we used *Spitzer*, *XMM-Newton*, and *Chandra* archival data. This thesis can be divided in three topics as follows:

- **Mid-IR High-ionization Lines from AGN and Star-forming Galaxies**
  (U)LIRGs are mainly powered by star-formation, although the contribution of the AGN increases with increasing $L_{\rm IR}$. The mid-IR spectral range is well suited to detect AGNs in obscured systems due to the reduced extinction at these wavelengths. Indeed, using mid-IR indicators Alonso-Herrero et al. (2011) and Petric et al. (2011) have calculated that the AGN luminosity accounts for 10 % of the bolometric luminosity of the LIRG class. For this type of studies the mid-IR properties of a typical AGN need to be known. Therefore as a first step to disentangle the AGN and star-formation activity in the mid-IR we study a sample of 426 galaxies, including quasars, Seyferts, LINERs, and H II galaxies using their mid-IR *Spitzer*/IRS spectra. In Chapter 3 we analyze the emission from the mid-IR high-ionization emission lines in these galaxies. The contribution from the AGN and star-formation to the [Ne III]15.56 μm and [O IV]24.9 μm emission lines are also estimated.

- **Spatially Resolved Mid-IR Emission of Local LIRGs**
  LIRGs are a cosmologically important class of galaxies. Recent works using *Spitzer* data reveal that they dominate the SFR density of the universe at $0.6 < z < 1.5$ (e.g., Le Floc'h et al. 2005; Pérez-González et al. 2005). Moreover the mid-IR spectra of high-redshift ULIRGs, which dominate the SFR density at $z > 1.5$, resembles those of local starbursts and LIRGs, but several order of magnitude more luminous (Farrah et al. 2008). This may be explained if star-formation in high-redshift ULIRGs takes place in few kpc scales, like in local starbursts/LIRGs, instead of in compact regions (< 1 kpc) as in local ULIRGs. In Chapter 4 we study the spatial distribution of the mid-IR emission in local LIRGs with extended star formation to help us understand their more distant counterparts. We use *Spitzer*/IRS spectral mapping observations of a sample of 15 local LIRGs. These data provide both spectral and spatial information similar to an integral field unit (IFU) observation. We analyze the emission of the mid-IR continuum, PAH bands, ionized gas ([Ne II], [Ne III], [S III], and [S IV]), and molecular gas (warm H_2), as well as the 9.7 μm silicate feature.

- **X-ray Emission of Local LIRGs**
  A large fraction of the luminosity produced by an AGN is emitted in the X-ray range. Thus if a bright AGN is present in a galaxy strong X-ray emission is expected. However star-forming regions also emit X-rays. An intense burst of star-formation can reach X-ray luminosities comparable to those of a low-luminosity AGN or an obscured (Compton-thick) AGN. In (U)LIRGs both AGN and star-formation activity are common. We use the X-ray emission together with the mid-IR emission to investigate the relative contributions to the bolometric luminosity of the AGN and star-formation in local LIRGs. In Chapter 5 we present the study of the *XMM-Newton* and *Chandra* X-ray observations of a sample of 27 local LIRGs. We look for the presence of an obscured AGN measuring the Fe Kα emission line at 6.4 keV. We also compare the soft (0.5–2 keV) and hard (2–10 keV) emissions of these LIRGs with those expected from the SFR vs. X-ray emission observed in local starbursts.

Chapter 2

Sample, Observations and Data Reduction

In this chapter we present the sample of local LIRGs studied in this thesis. Then we describe the mid-IR observations obtained with the Spitzer infrared spectroscopy (IRS) and with IRAC and MIPS imaging instruments. We explain in detail the Spitzer data reduction and analysis. Finally we describe the data reduction of the CCD X-ray and the UV/optical imaging data obtained with XMM-Newton.

2.1 The Sample

Most of the work in this thesis is concerned with the study of the IR and X-ray properties of local LIRGs. Our sample is the volume limited sample of local LIRGs (40 Mpc$< d <$70 Mpc) defined by Alonso-Herrero et al. (2006). This sample was drawn from the *IRAS* RBGS (Sanders et al. 2003). The RBGS is a complete flux limited sample that includes all the extragalactic objects with a 60 μm flux density greater than 5.24 Jy and Galactic latitude $|b| > 5\,^{\circ}$. Alonso-Herrero et al. (2006) imposed the following selection criteria: $v_{\rm hel} = 2750$–$5200\,{\rm km\,s^{-1}}$ and $11.05 < \log(L_{\rm IR}/L_{\odot}=) < 11.88$. The redshift criterion was chosen to allow for Paα imaging with the F190N narrow-band filter of *HST*/NICMOS. The Alonso-Herrero et al. (2006) sample was representative of the local population of LIRGs and complete to a 77 % level.

Additionally we extended the Alonso-Herrero et al. (2006) sample to include all the galaxies in the *IRAS* RBGS that fulfill their selection criteria but were not included in their sample (mostly Seyfert galaxies; see also Alonso-Herrero et al. 2011). We note that MCG−03-34-063, which is part of IRAS F13197−1627 with MCG−03-34-064 (Surace et al. 2004), is at $6394\,{\rm km\,s^{-1}}$ (from NED) and does not meet the distance criterion of our sample. Two galaxies, NGC 5743 and NGC 7769 were not originally included in the *IRAS* RBGS. However, both galaxies were discussed by Surace et al. (2004),

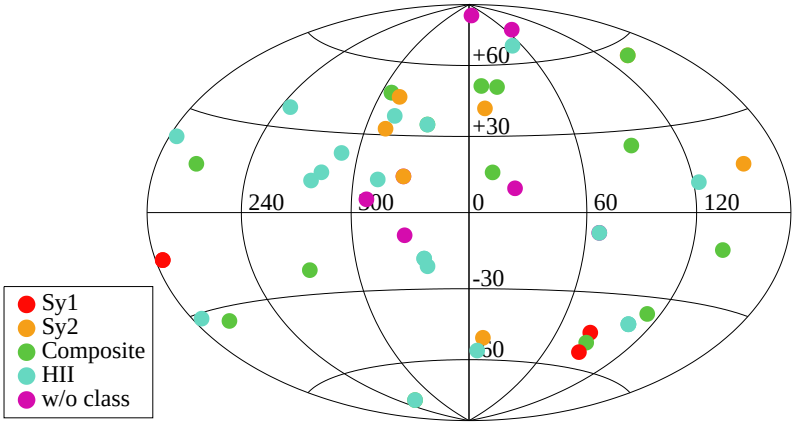

Figure 2.1: Distribution of the LIRGs in our sample in Galactic coordinates in Aitoff projection. Galaxy colors indicate the nuclear activity classification. The numbers on the curves are the Galactic longitude and latitude in degrees.

and are in interaction with RBGS *IRAS* sources. NGC 5743 is paired with NGC 5734 and shows a diffuse Hα extension toward NGC 5734 (Dopita et al. 2002). NGC 7769 is part of the NGC 7771/NGC 7770 group, and there is evidence that NGC 7769 is undergoing a direct encounter with NGC 7771 (Nordgren et al. 1997). We therefore included them in our sample.

The sample is presented in Table 2.1. It contains 45 *IRAS* sources (53 individual galaxies), with eight of them being interacting galaxies, pairs of galaxies or galaxies with companions unresolved by *IRAS*. Figure 2.1 shows the classification and distribution in Galactic coordinates of the LIRGs in our sample. The individual *IRAS* flux densities of these eight *IRAS* systems were recovered using image reconstruction techniques by Surace et al. (2004). When this was not possible with the *IRAS* images we took advantage of the better angular resolution of the *Spitzer*/MIPS 24 μm images. We assumed that the $L_{\rm IR}$ fraction of each component is proportional to the MIPS 24 μm flux density fraction.

We searched in the literature for the nuclear activity classification from optical spectroscopy. For the 45 galaxies of the sample with an activity class, we find that most of them are H II (47 %) or composite systems (31 %). Composite galaxies are likely to be a combination of AGN activity and star-formation. 22 % of the galaxies are classified as Seyfert, 3 as Type 1 and 7 as Type 2. We show in Figure 2.2 the activity class distribution of the sample. In addition we detected the high-ionization [Ne V] emission lines, which indicates the presence of an AGN (see Chapter 3), in the mid-IR spectra of 1 galaxy without optical classification and in 2 galaxies classified as

H II in the optical. This line is also detected in 8 out of 10 of the Seyfert LIRGs.

Yuan et al. (2010) investigated the nuclear activity of the LIRGs in the Bright Galaxy Sample[1] (BGS) using optical spectroscopy. They found that the fraction of starbursts and composite galaxies are 30 and 35 %, respectively, whereas 30 % are Seyfert galaxies (see Figure 1.2). These fractions are similar to those of our sample.

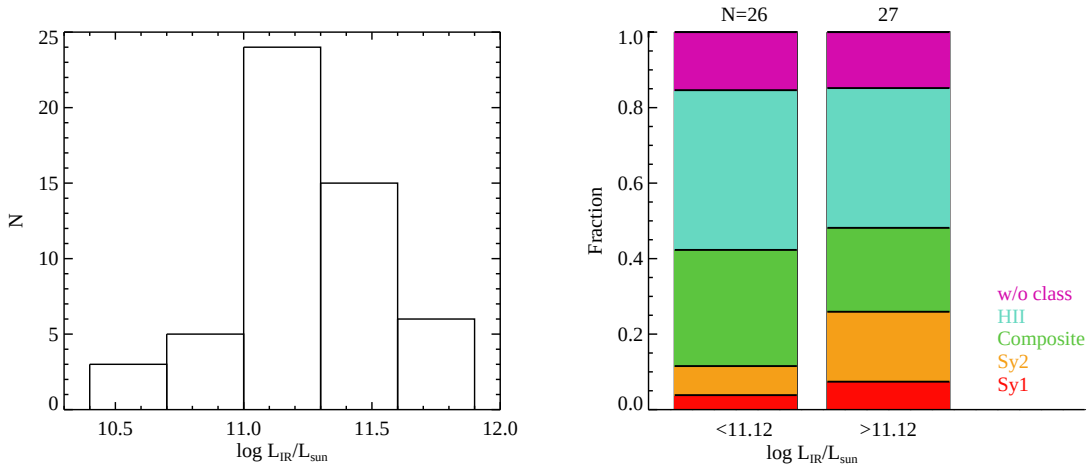

Figure 2.2: *Left panel*: Distribution of the $L_{\rm IR}$ of the individual galaxies in our sample of LIRGs. The median $\log(L_{\rm IR}/L_{\odot})$ is 11.12. *Right panel*: Nuclear activity class of the LIRGs in our sample as function of the $L_{\rm IR}$. The color of the histogram indicates the activity class as in Figure 2.1.

The $\log(L_{\rm IR}/L_{\odot})$ of the sample is in the range 10.4–11.7 and the median is 11.12. Therefore the low-luminosity end of the LIRG class is well represented. The distribution of the $L_{\rm IR}$ is shown in the left panel of Figure 2.2. The median distance is 65 Mpc. At this distance $1''$ corresponds to ∼300 pc. Due to the redshift criterion only 4 LIRGs with $v_{\rm hel} < 2750\,{\rm km\,s^{-1}}$ in the RBGS are not in our sample. Therefore our sample of LIRGs includes 91 % of the *IRAS* systems with $\log(L_{\rm IR}/L_{\odot}),> 11.05$ within 75 Mpc.

In Chapters 4 and 5 we studied two subsamples of LIRGs drawn from the parent sample described here. The galaxies included in these two subsamples are marked in Table 2.1. Both subsamples are representative of the properties of the parent sample in terms of $L_{\rm IR}$ and nuclear activity. Most of these LIRGs are also included in the statistical study presented in Chapter 3.

[1]The BGS is similar to the RBGS but compiled using earlier versions of the *IRAS* catalogs.

Table 2.1: The Volume Limited Sample of Local LIRGs

Galaxy Name	*IRAS* Name	$v_{\rm hel}$ ($\rm km\,s^{-1}$)	Dist. (Mpc)	$\log L_{\rm IR}$ ($L_\odot$)	Ref. IR	Nuclear Spect. Class[a]	Ref. Class	Mapping Sample	X-ray Sample
NGC23	IRAS F00073+2538	4478	64.7	11.11	A1	composite	B1		✓
MCG+12-02-001	IRAS F00506+7248	4722	68.3	11.48	A1	H II	B1		
NGC633	IRAS F01341−3735	5128	74.2	10.64	A2	composite	B2		
ESO297-G012	″	5183	75.0	11.06	A2	H II	B3		
UGC1845	IRAS F02208+4744	4601	66.5	11.12	A1	composite	B1		
UGC2982	IRAS F04097+0525	5355	77.6	11.23	A1	H II	B4		
NGC1614[b]	IRAS F04315−0840	4778	69.1	11.67	A1	composite	B2		✓
CGCG468-002 NED01	IRAS F05054+1718	5268	76.3	10.55	A3	Sy1, [Ne V]	B5, B6		
CGCG468-002 NED02	″	4951	71.6	10.83	A3	···	···		
UGC3351	IRAS F05414+5840	4433	64.1	11.26	A1	Sy2	B7		
NGC2369	IRAS F07160−6215	3196	46.0	11.13	A1	composite	B8	✓	✓
NGC2388	IRAS F07256+3355	4078	58.9	11.23	A1	H II	B1		
MCG+02-20-003	IRAS F07329+1149	4908	71.0	11.11	A1	composite	B1		
NGC3110	IRAS F10015−0614	5014	72.6	11.29	A1	H II	B2	✓	✓
NGC3256	IRAS F10257−4339	2790	40.1	11.66	A1	H II	B9	✓	✓
ESO264-G057	IRAS F10567−4310	5141	74.4	11.05	A1	H II	B10		
NGC3690	IRAS F11257+5850	3057	44.0	11.43	A4	Sy2	B11	✓	✓
IC694	″	3098	44.6	11.58	A4	LINER	B11	✓	✓
ESO320-G030	IRAS F11506−3851	3038	43.7	11.22	A1	H II	B8	✓	✓
MCG−02-33-098 W	IRAS F12596−1529	4714	69.1	10.96	A2	composite	B2		
MCG−02-33-098 E	″	4775	69.1	10.48	A2	H II	B2		
IC860	IRAS F13126+2453	3859	55.7	11.12	A1	no	B1		✓
MCG−03-34-064	IRAS F13197−1627	5009	72.5	11.09	A2	Sy2, [Ne V]	B2, B12		✓

Table 2.1: *Continued*

Galaxy Name	*IRAS* Name	$v_{\rm hel}$ (km s^{-1})	Dist. (Mpc)	log $L_{\rm IR}$ ($L_\odot$)	Ref. IR	Nuclear Spect. Class[a]	Ref. Class	Mapping Sample	X-ray Sample
NGC5135	IRAS F13229−2934	4074	58.8	11.27	A1	Sy2, [Ne V]	B2, B12	✓	✓
ESO173-G015	IRAS 13242−5713	2948	42.4	11.57	A1	···	···		
IC4280	IRAS F13301−2356	4843	70.1	11.01	A1	H II	B8		
UGC8739	IRAS F13470+3530	5000	72.3	11.05	A1	no	B14		
ESO221-IG010	IRAS F13478−4848	3084	44.4	10.92	A1	H II	B8		
NGC5653	IRAS F14280+3126	3513	50.7	10.98	A1	H II	B2		✓
NGC5734	IRAS F14423−2039	3998	57.7	11.00	A2	composite	B8		✓
NGC5743	IRAS F14423−2042	4121	59.5	10.84	A2	H II, [Ne V]	B8, B12		✓
IC4518W	IRAS F14544−4255	4720	68.2	11.15	A3	Sy2, [Ne V]	B10, B12		✓
IC4518E	″	4518	66.3	10.28	A3	no	B8	✓	
Zw049.057	IRAS F15107+0724	3858	55.7	11.21	A1	composite	B14	✓	✓
NGC5936	IRAS F15276+1309	3977	57.4	11.00	A1	composite	B1		
NGC5990	IRAS F15437+0234	3756	54.2	10.98	A1	Sy2, [Ne V]	B2, B6		
NGC6156	IRAS 16304−6030	3253	46.9	11.12	A1	[Ne V]	B6		
···	IRAS F17138−1017	5161	74.7	11.39	A1	composite	B2	✓	
···	IRAS 17578−0400	3931	56.7	11.31	A1	···	···		
IC4686[b]	IRAS F18093−5744	4948	71.6	10.98	A3	H II	B2		✓
IC4687	″	5105	73.9	11.30	A3	H II	B2	✓	✓
IC4734	IRAS F18341−5732	4623	66.8	11.27	A1	H II	B10		✓
NGC6701	IRAS F18425+6036	3896	56.2	11.03	A1	composite	B1	✓	
NGC6921[b]	IRAS 20264+2533	4327	62.5	10.37	A2	no	B13		
MCG+04-48-002	″	4199	60.6	10.96	A2	H II, [Ne V]	B6, B13		✓
NGC7130	IRAS F21453−3511	4837	70.0	11.38	A1	Sy2, [Ne V]	B2, B12	✓	✓

Table 2.1: *Continued*

Galaxy Name	*IRAS* Name	$v_{\rm hel}$ ($\rm km\,s^{-1}$)	Dist. (Mpc)	log $L_{\rm IR}$ ($L_\odot$)	Ref. IR	Nuclear Spect. Class[a]	Ref. Class	Mapping Sample	X-ray Sample
IC5179	IRAS F22132−3705	3363	48.5	11.18	A1	H II	B2	✓	✓
NGC7469	IRAS F23007+0836	4840	70.0	11.64	A1	Sy1, [Ne V]	B1, B12		✓
NGC7591	IRAS F23157+0618	4907	71.0	11.11	A1	composite	B1	✓	
NGC7679	IRAS 23262+0314	5162	74.7	11.12	A1	Sy1, [Ne V]	B2, B6		✓
NGC7769	IRAS F23485+1952	4158	60.0	10.90	A2	composite	B14		✓
NGC7770	IRAS F23488+1949	4128	59.6	10.80	A3	H II	B2		✓
NGC7771	″	4277	61.8	11.33	A3	H II	B1	✓	✓

Notes. The heliocentric velocities are derived from the high-resolution *Spitzer*/IRS spectra. The $L_{\rm IR}$ was calculated as defined in Table 1.1. [(a)] Classification from optical spectroscopy. Composite galaxies are likely to be a combination of AGN activity and star-formation. In this column "no" indicates that no classification was possible from the optical spectroscopic data. [(b)] Not observed with the IRS and the IRS observation of NGC 1614 is not well centered at its nucleus. Their heliocentric velocities are from NED.

References. (A1) Sanders et al. (2003); (A2) Surace et al. (2004); (A3) Alonso-Herrero et al. (2011) from MIPS 24 μm data; (A4) Charmandaris et al. (2002); (B1) Alonso-Herrero et al. (2009a); (B2) Yuan et al. (2010); (B3) Kewley et al. (2001); (B4) Veilleux et al. (1995); (B5) Kollatschny et al. (2008); (B6) Petric et al. (2011); (B7) Baan et al. (1998); (B8) This work. See Section 2.1.1; (B9) Lípari et al. (2000); (B10) Corbett et al. (2003); (B11) García-Marín et al. (2006); (B12) Pereira-Santaella et al. (2010b); (B13) Masetti et al. (2006); (B14) Parra et al. (2010).

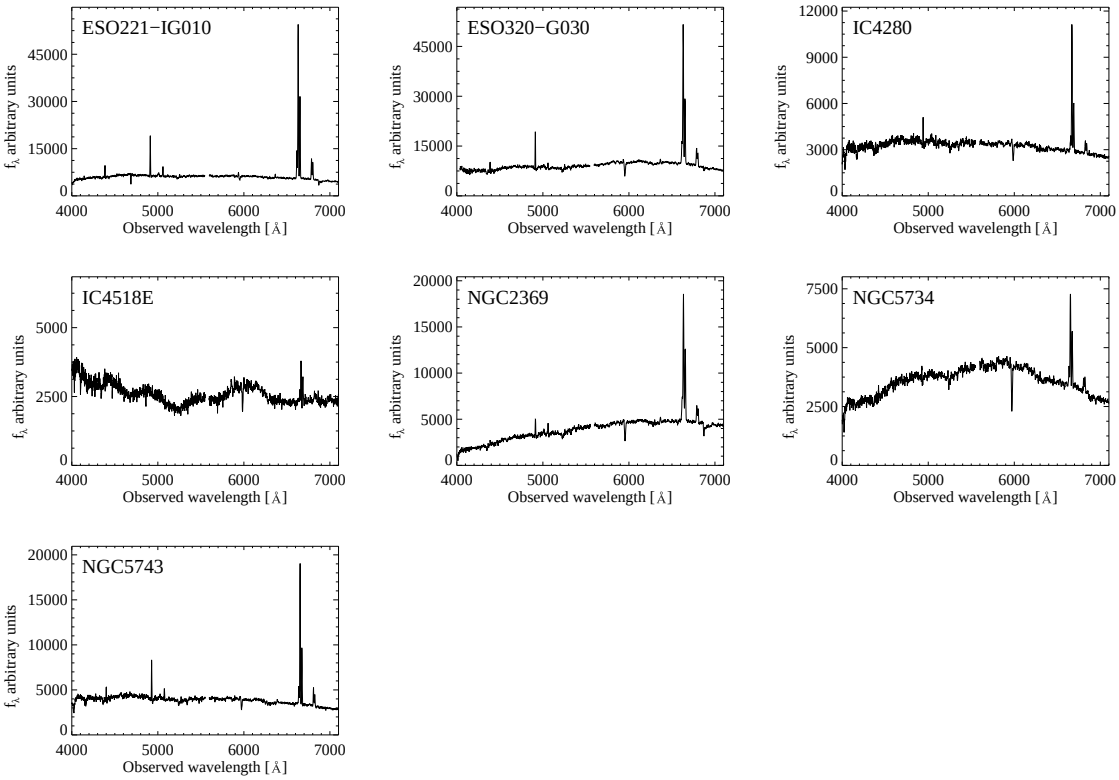

Figure 2.3: Observed optical spectra of 7 LIRGs from the 6dFGS database.

2.1.1 Optical Classification

The optical spectra of seven galaxies in our sample of LIRGs without a previous activity classification were obtained as part of the six-degree Field (6dF) Galaxy Survey (6dFGS DR3; Jones et al. 2004, 2009).

The optical spectra were obtained with the 6dF multi-object fibre spectrograph on the United Kingdom Schmidt Telescope (UKST) from 2001 to 2006. The fiber angular diameter is 6.″7, which means that at the distance of these LIRGs it covers the central ∼2 kpc of the galaxies (i.e., similar to the physical regions covered by the Veilleux et al. 1995 spectra of local LIRGs). Each object was observed with two gratings in the V (3900–5600 Å) and R (5400–7500 Å) bands for at least 1 hr and 0.5 hr, respectively. These two spectra were later spliced to obtain the final object spectrum. The spectral resolution is 5–6 Å in V and 9–12 Å in R. Although the spectra are not accurately flux-calibrated, they can be used to calculate ratios of emission lines close in wavelength (see Lee et al. 2011). The spectra of the 7 LIRGs are shown in Figure 2.3.

We measured the Hβ, [O III]λ5007 Å, Hα, and [N II]λ6584 Å emission lines in the

Table 2.2: Observed optical emission line ratios and classification

Galaxy Name	[N II]/Hα	[O III]/Hβ	Class.
NGC2369	0.58	1.00	composite
ESO320-G030	0.48	0.20	H II
IC4280	0.41	<0.40	H II
ESO221-IG010	0.50	0.28	H II
NGC5734	0.59	1.10	composite
NGC5743	0.43	0.35	H II
IC4518E	0.57	...	...

spectra by fitting a Gaussian to each emission line. The measured [N II]/Hα and [O III]/Hβ line ratios are listed in Table 2.2. We did not correct Hβ for stellar absorption, so the calculated [O III]/Hβ ratio should be considered as an upper limit.

To determine the nuclear activity of these galaxies, we used the standard optical diagnostic diagram [N II]λ6584 Å/Hα vs. [O III]λ5007 Å/Hβ (Baldwin et al. 1981). We adopted the boundaries between H II, AGN, and composite galaxies of Kewley et al. (2006). The diagram for these LIRGs is shown in Figure 2.4 and the adopted classifications are listed in Table 2.2. Neither the Hβ nor the [O III]λ5007 emission lines are detected in IC 4518E and, therefore we do not plot this galaxy in Figure 2.4. We did not detect the [O III]λ5007 Å emission line in the spectrum of IC 4280, so we plotted the upper limit of the [O III]/Hβ ratio in Figure 2.4. This does not affect the H II activity classification of this galaxy (see Figure 2.4).

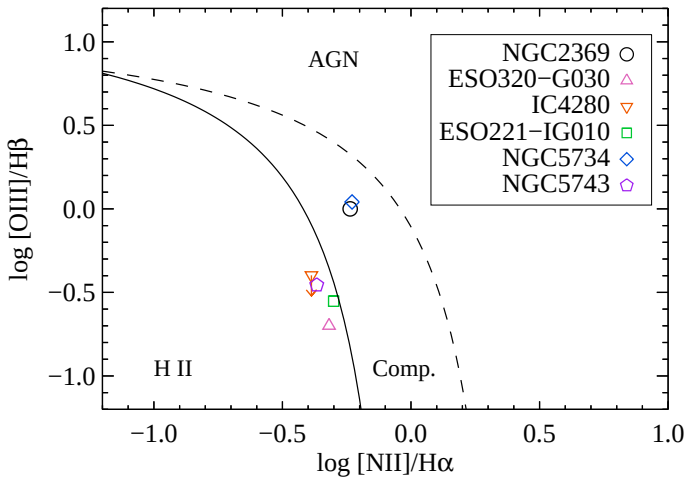

Figure 2.4: [N II]λ6584/Hα versus [O III]λ5007/Hβ diagnostic diagram for the nuclear spectra of 6 LIRGs. The black lines show the empirical separation between H II, AGN, and composite galaxies of Kewley et al. (2006).

2.2 Mid-IR *Spitzer* Imaging and Spectroscopy

Spitzer is an IR space telescope launched in August 2003 (Werner et al. 2004). It is the NASA's Great Observatory for IR astronomy. The telescope primary mirror diameter is 85 cm and it was cooled down to 5.5 K with helium. There are three scientific instruments onboard *Spitzer*: the InfraRed Array Camera (IRAC); the InfraRed Spectrograph (IRS); and the Multiband Imaging Photometer for *Spitzer* (MIPS). They provide imaging and spectroscopy in the wavelength range from 3.6 to 160 μm.

The cryogenic mission lasted 5.7 years, until the helium depletion in May 2009. In July 2009 the *Spitzer* Warm Mission began and only the shortest wavelength IRAC channels operate. The Warm Mission will be probably extended until the end of 2013.

2.2.1 *Spitzer*/ IRS Spectroscopy

IRS is the spectrograph onboard *Spitzer* (Houck et al. 2004). It covers the wavelength range from 5.2 to 38.0 μm with 4 different modules. Two high spectral resolution modules ($R \sim 600$): short-high (SH; 9.9–19.6 μm) and long-high (LH; 18.7–37.2 μm), and two low spectral resolution ($R \sim 60$–120) modules: short-low (SL1; 7.4–14.5 μm, SL2; 5.2–7.7 μm) and long-low (LL1; 19.5–38.0 μm, LL2; 14.0–21.3 μm). The low-resolution modules are grating spectrographs with two long-slit apertures, one for each spectral order. On the other hand, the high-resolution modules are cross-dispersed echelle spectrographs with a single slit each one. The sizes of the IRS slits and the plate scale of each module are listed in Table 2.3. IRS also has two small imaging sub-arrays: the blue peak-up (15.8 μm) and the red peak-up (22.3 μm). The peak-up sub-arrays are mainly used for the IRS target acquisition, although they are capable of obtaining science images as well. IRS has four 128×128 pixel detectors, two Si:As arrays that operate in the 5–26 μm range for the SH and SL modules, and two Si:Sb arrays operating in the 14–40 μm range for the LL and LH modules. The peak-up sub-arrays are part of the SL detector.

IRS has two operating modes: the staring mode and the mapping mode. In the staring mode the target is placed in the slit for a certain amount of integration time. The observation is divided into various cycles with a duration (ramp time) of up to 480 s, depending on the module. During each cycle the detectors are read non-destructively a number of times that depends on the ramp duration and the module used. In this mode the target is placed at two slit positions (nods) to allow for the correction of cosmic rays and detector artifacts. In the mapping mode IRS observes a grid of positions around the central target. The size and number of steps in the parallel and perpendicular to the slit directions can be defined for each observation. In the mapping mode

Table 2.3: *Spitzer*/IRS Characteristics

IRS Module	R	Plate Scale ($''$ pix^{-1})	Slit Width ($''$)	Slit Length ($''$)
SL	60–120	1.8	3.6	57
LL	60–120	5.1	10.5	168
SH	600	2.3	4.7	11.3
LH	600	4.5	11.1	22.3

Notes. Table adapted from the IRS Instrument Handbook.

the observations are also divided into various cycles but the target is only placed at one slit position unlike in the staring mode. The mapping mode provides spectral and spatial information simultaneously. Further details regarding the IRS operation can be found the IRS Instrument Handbook.

We obtained IRS spectral mapping observations of 15 of the LIRGs in our sample through two *Spitzer* GTO programs P30577 and P40479 (PI: G. H. Rieke) during years 2006, 2007, and 2009. In addition, most of the galaxies were observed in the staring mode as part of the Great Observatories All-sky LIRG Survey (GOALS) legacy program (Armus et al. 2009). The observing logs of the staring and mapping observations are listed in Table 2.4.

2.2.1.1 Staring Mode

We started the data reduction with the basic calibrated data (BCD) retrieved from the *Spitzer* archive. The raw data consist of data cubes with N planes (one for each non-destructive read) of 128×128 pixels. Then, the *Spitzer*/IRS pipeline performs low-level processing of the raw data producing the BCD (128×128 pixels images). The pipeline processing includes bias and dark current subtraction, ramp fitting, flat-field correction, and telescope pointing reconstruction (see the IRS Data Handbook for details).

We used the BCD processed by the pipeline version S18.7. Example BCD images are shown in Figure 2.5. Bad pixels were corrected using the IDL package `IRSCLEAN`. Dedicated background observations are not needed for the low-resolution modules (SL and LL) because the separation on the sky between the two orders of each module is larger than the size of the galaxies in our sample. That is, when order 1 is on the galaxy, order 2 is observing the background and vice versa. The SH and LH slits are too small to allow for background subtraction. We used dedicated background observations when available. For those galaxies without them, we estimated the sky background

Table 2.4: Log of *Spitzer*/IRS Observations

Target	AOR[a]	Target	AOR[a]
Staring			
NGC23	20348672	UGC8739	20345856
MCG+12-02-001	20371712	ESO221-IG010	20371200
NGC633/ESO297-G012	20342272	NGC5653	20333312
UGC1845	20338432	NGC5734/5743	20311040
UGC2982	20365312	IC4518W	21929984
NGC1614	3757056[b]	NGC5936	20310016
CGCG468-002 NED01/NED02	20322048	NGC5990	20344576
UGC3351	20332800	NGC6156	20317952
NGC2388	14837760	IRAS17578-0400	20352000
MCG+02-20-003	20353280	IC4734	20339200
ESO264-G057	20347904	NGC6701	20341760
NGC3690/IC694	12247808	MCG+04-48-002	20349184
MCG-02-33-098 W/E	20318464	NGC7469	3755008
IC860	6652416	NGC7591	10512384
MCG-03-34-064	20367616	NGC7679	20350720
ESO173-G015	20328448	NGC7769/7770/7771	20318720
IC4280	20350208		
Spectral Mapping – GTO program			
NGC2369	17659392	Zw049.057	17661184
NGC3110	17659648	IRASF17138−1017	17661440
NGC3256	17659904	IC4687	17665024
NGC3690[c]	17660160	NGC6701	21928448
IC694[c]	17660416	NGC7130	17661696
ESO320-G030	17660672	IC5179	17661952
NGC5135	17660928	NGC7591	21928960
IC4518E	21927936	NGC7771	21929472

Notes. [(a)] Astronomical Observation Request key. [(b)] The staring observation of NGC1614 is not well centered at its nucleus. [(c)] NGC 3690 and IC 694 are the two components, western and eastern respectively, of the interacting system Arp 299

emission by combining the background spectra from the low-resolution modules. Note however, that the sky subtraction is not fundamental to measure emission lines and it just improves the final quality of the spectra by removing rogue pixels.

Finally we extracted the spectra using the standard modules included in the *Spitzer* IRS Custom Extraction (SPICE) package provided by the *Spitzer* Science Center (SSC). Four modules are used in extraction process: `profile`, `ridge`, `extract`, and

`irs_tune`. The first two modules, `profile` and `ridge`, are used to find the peak of spatial profile for each wavelength. Then, the `extract` module uses a wavelength dependant aperture centered at the spatial emission peak to extract the source spectrum. The `extract` module accounts for the curvature of the spectrum in the spatial and dispersed directions. The last step is the flux calibration that is performed by the `irs_tune` module. We assumed a point source calibration for our galaxies, since they are dominated by the nuclear emission that is only partially resolved at the spatial resolution of IRS (3–6″). The flux calibration is based on the comparison of observations of standard stars with their model spectra. The primary calibrators are HR 7341 and HR 6688 for the low- and high-resolution modules respectively. Figure 2.6 shows the typical spectrum of a star-forming LIRG.

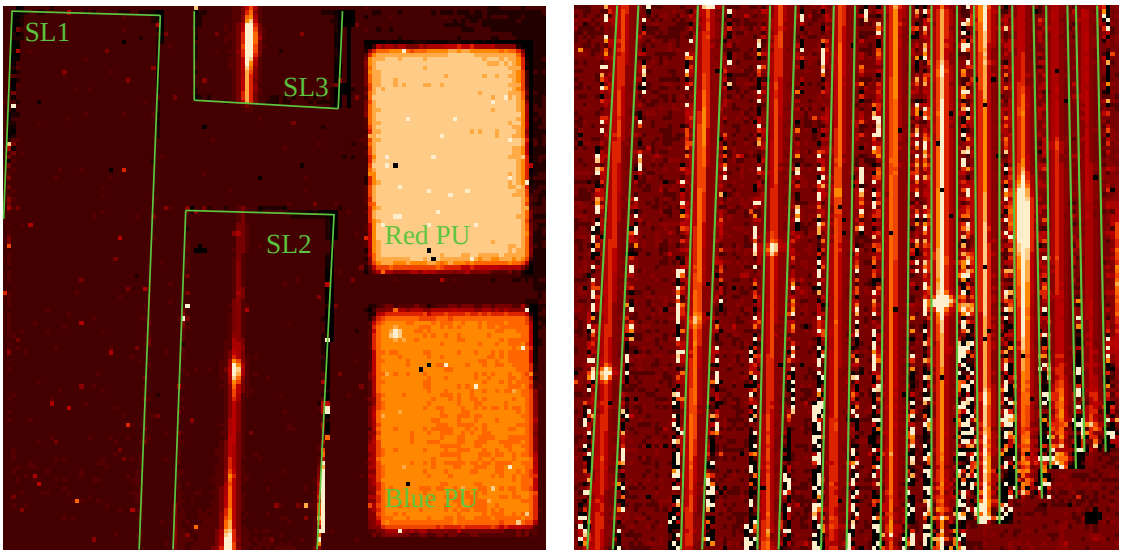

Figure 2.5: *Spitzer*/IRS BCD images. The left panel shows a typical short-low module observation. The two spectral orders, SL1 and SL2, the bonus order SL3, and the two peak-up sub-arrays are marked. The target was centered at the SL2 order while the SL1 order and the peak-up sub-arrays were observing the sky. The right panel shows a short-high module observation. The 10 echelle orders are marked. In both panels the dispersion direction is approximately along the y axis.

2.2.1.2 Spectral Mapping Mode

The *Spitzer*/IRS spectral maps of our sample of LIRGs were made by moving the telescope pointing position perpendicular to the long axis of the slit with a step size half of the slit width. The SL, LL and LH slits are long enough to cover the full region of interest with just one slit length. Due to the smaller size of SH slit, parallel steps

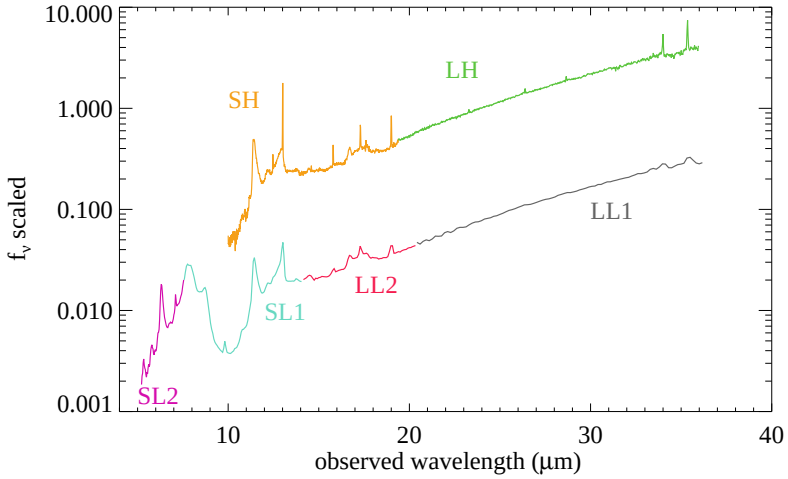

Figure 2.6: Example of a *Spitzer*/IRS spectrum of a LIRG dominated by star-formation. The labels and line colors indicate the different IRS modules. Both high-resolution (SH and LH modules) and low-resolution (SL1, SL2, LL1, and LL2 modules) spectra are plotted.

Table 2.5: *Spitzer*/IRS Mapping Observation Details

IRS Module	Pixel Size (″)	Ramp (s)	Number of Cycles	Step Size ⊥ (″)	Step Size ∥ (″)
SL1, SL2	1.85	14	2	1.8	···
LL1, LL2	4.46	14	2	5.25	···
SH	2.26	30	2	2.35	5.65
LH	4.46	60	4	5.55	···

were also needed. The parallel step size was half of the slit length. This strategy produced maps with a redundancy per pixel of 2 for SL, LL and LH, and 4 for SH. Table 2.5 details the integration time, pixel size and step size for each IRS module. The maps cover at least the central 20″×20″ to 30″×30″ of the galaxies. Figure 2.7 shows an example mapping observation. We obtained dedicated background observations for LH by observing a region 2′ away from the galaxy. Dedicated SH sky observations are available only for the galaxies observed under the program P40479.

Similar to the staring observation we started the data reduction with the BCD. To build the data cubes we used the Cube Builder for IRS Spectra Maps (CUBISM; Smith et al. 2007a). CUBISM is an IDL tool that combines slit observations to create spectral cubes. Within CUBISM we masked bad pixels and subtracted the sky background. Dedicated sky background observations with the high-resolution modules were used when available. For the low-resolution modules we proceeded as with the staring

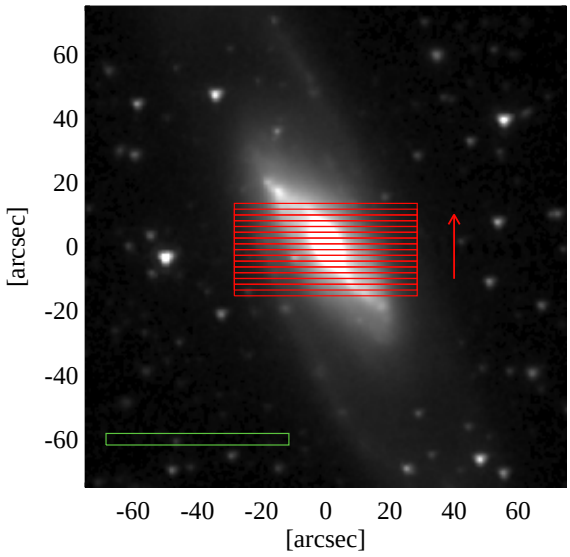

Figure 2.7: Example *Spitzer*/IRS mapping observation using the SL module. The position of the slit for the different telescope pointings is shown in red. The red arrow points in the telescope scanning direction. Note that the step size is half the slit width. For reference the size of the SL slit is shown in green in the lower left corner. The background image corresponds to the *Spitzer*/IRAC 3.6 μm image of NGC 2369.

observations (see Section 2.2.1.1).

The nuclear spectra of the galaxies were extracted using a $13\farcs4 \times 13\farcs4$ aperture. This is the angular resolution of the long wavelength modules. Since the data cubes are calibrated as extended sources, we applied a wavelength dependant aperture correction to the mapping nuclear spectra in order to obtain spectra comparable to those observed in staring mode. To calculate this aperture correction we used the mapping observations of standard stars (HR 7341, HR 6606, HR 6688, and HR 2491; see Section 2.2.1.3).

2.2.1.3 The Point Spread Function of IRS Spectral Mapping Observations

When comparing maps of lines or features, at different wavelengths, the variation of the Point Spread Function (PSF) size can be significant. The *Spitzer*/IRS PSF is much less studied than that of the other *Spitzer* instruments, although it is possible to generate synthetic IRS PSF using the STinyTim program (Krist 2002). This is useful for staring observations, but the spectral mapping observation mode introduces extra issues, such as the cube assembly from staring observations, wavelength calibration uncertainties, that cannot be easily taken into account using the modeled PSF. Because of this, a better way to characterize the IRS PSF of the spectral mapping observation

Table 2.6: Log of IRS Mapping Calibration Observations

IRS Module	AOR	Target	Step Size $\perp$ ($''$)	Step Size $\parallel$ ($''$)
SL1, SL2	16295168	HR 7341	0.6	15.5
LL1, LL2	16463104	HR 6606	1.7	46.0
SH	16294912	HR 6688	0.8	0.8
SH	16340224	sky		
LH	16101888	HR 2491	1.7	1.7
LH	116088320	sky		

mode is to use the mapping observations of calibration stars available in the *Spitzer* archive. Previously, Kóspál et al. (2008) studied the factor that should be applied to correct for flux losses when the slit is not centered properly on a point source. We extend this analysis to characterize the variations of the PSF.

To do this, we used the same data sets as Kóspál et al. (2008), of spectral mapping observations of calibration stars. These observations were taken with the same instrument configuration used for the galaxies studied in this paper, but with much smaller steps between pointings, i.e. the calibration observations have a better spatial information of the PSF. Details of the observations are listed in Table 2.6.

After obtaining BCD files processed by the *Spitzer* pipeline (version 15.3 for SH and SL modules, and version 17.2 for LH and LL modules), we built the spectral cubes with CUBISM (Smith et al. 2007a). The sky emission was subtracted using dedicated background observations. To take advantage of the better spatial information of the calibration observations, we set the pixel size in the final cube to be the size of the step in the perpendicular direction[2] (see Table 2.6). We did this for all IRS modules, however we only present the results for the SH, SL1 and SL2 modules, because the other modules (LH, LL1 and LL2), are heavily affected by fringing patterns and their PSF is not well reproduced by a Gaussian.

In order to study the PSF core variations we fitted each plane of the cube using a 2-D Gaussian. We allowed different values of the Full Width Half Maximum (FWHM) for each axis of the Gaussian, but the axis orientation is fixed and aligned with the parallel and perpendicular directions. By doing this we obtained the FWHM and centroid of the PSF at every wavelength. These values are represented in Figure 2.8.

The undulating pattern of the FWHM and the centroid in the modules SL1 and SL2

[2]In this Section we use the terms: "perpendicular" and "parallel" direction. They refer to the direction along the spectral dispersion axis and the spatial axis of the slit, respectively.

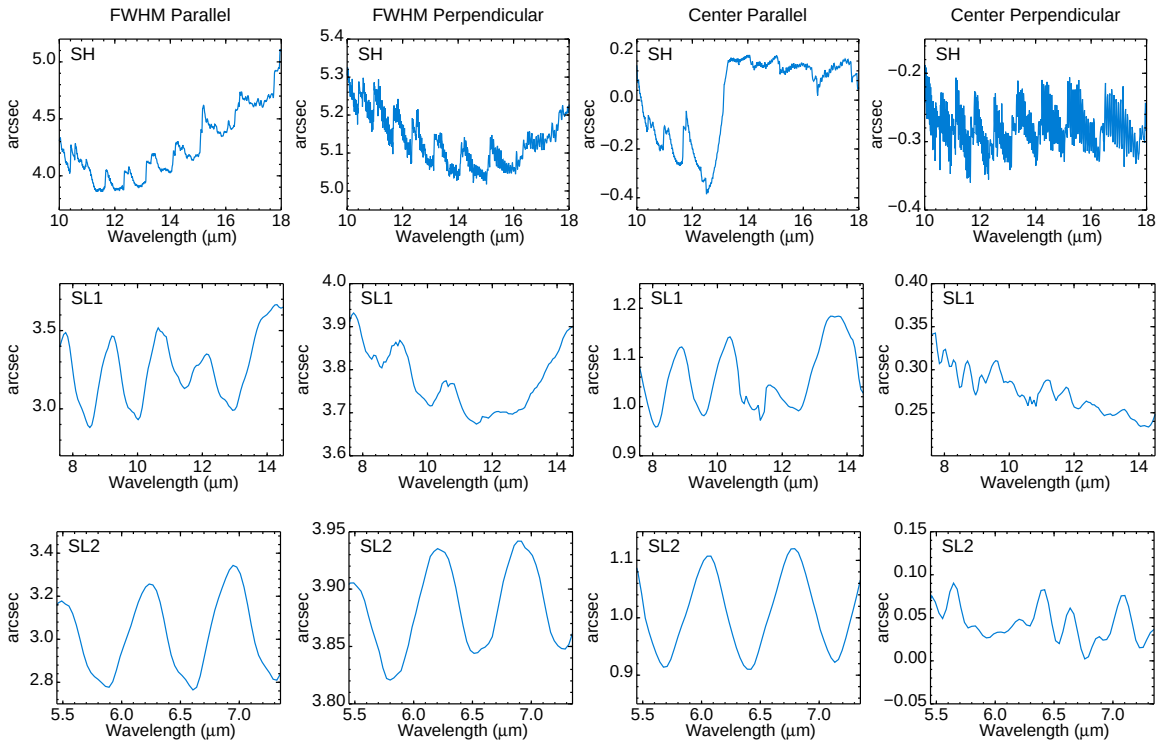

Figure 2.8: Full Width at Half Maximum (FWHM) and centroid position of the PSF of the modules SH, SL1 and SL2. Parallel and perpendicular directions are represented. We have calculated these values by fitting a 2-D Gaussian.

is originated by several causes: (1) The spectral axis is not aligned with the detector, consequently to extract the spectra is necessary to resample the original image. This resampling process produces this kind of periodic patterns. (2) The algorithm used to build the data cubes (see Smith et al. 2007a for details) does not try to correct for this effect. In any case, these variations are small: <10 % for the FWHM and <0.2 arcsec for the centroid position.

The PSF core is slightly asymmetric for all modules. The FWHM in the perpendicular direction is larger than the FWHM in parallel direction, which has an almost constant value. A possible explanation to this is the way CUBISM builds the cubes. It assumes that there is no spatial information in the dispersion (or perpendicular) direction and the spatial information in that direction comes from different telescope pointings (for more details see Smith et al. 2007a). The averaged values of the FWHM of each module are listed in Table 2.7.

The variation of the centroid position in SL modules is small. The 1σ deviation around the average centroid position are 0.07 and 0.02 arcsec for the parallel and perpendicular direction respectively, that is a twentieth of the SL pixel size. These

Table 2.7: Measured FWHM of the *Spitzer*/IRS PSF in Spectral Mapping Mode

Module	FWHM Perpendicular (″)	FWHM Parallel (″)
SH	5.16 ± 0.08	4.31 ± 0.37
SL1	3.76 ± 0.07	3.27 ± 0.21
SL2	3.88 ± 0.04	3.02 ± 0.17

variations can be attributed to small telescope pointing errors and S/N limitation. The position of the centroid in the SH module shows variations that cannot be explained just by instrumental pointing error or a limited signal-to-noise. The 1-σ deviation in the perpendicular direction is 0.03 arcsec, but in the parallel direction the variation is one order of magnitude larger (0.2 arcsec) and shows a clear wavelength dependency. The most probable cause for this, is an error in the position and/or angle of the extraction aperture. However this effect (0.6 arcsec) is small when compared with the SH pixel size (2.26 arcsec).

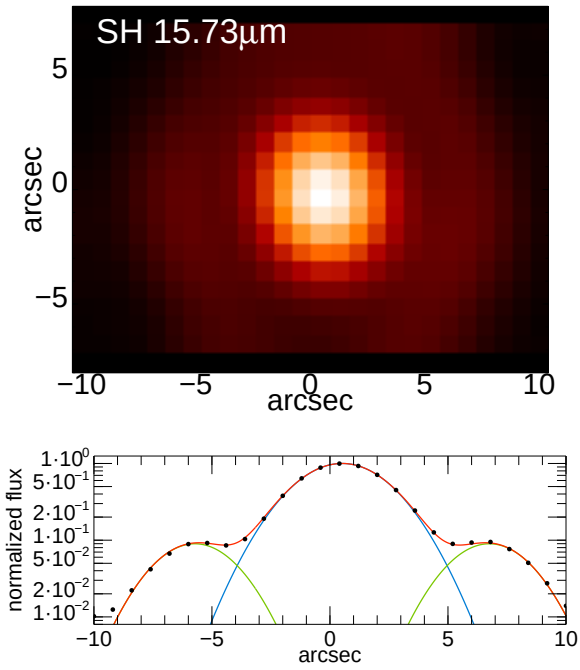

Figure 2.9: Upper panel: PSF of the SH module at 15.73 μm. Lower Panel: Fit of the PSF profile at the central row. The blue line is the Gaussian used to fit the PSF core. The green line is the fit of the diffraction ring. The red line is the sum of both components.

We studied the variations of the diffraction rings in the SH module. We fitted the central row of the cube for each wavelength using a Gaussian for the PSF core and two

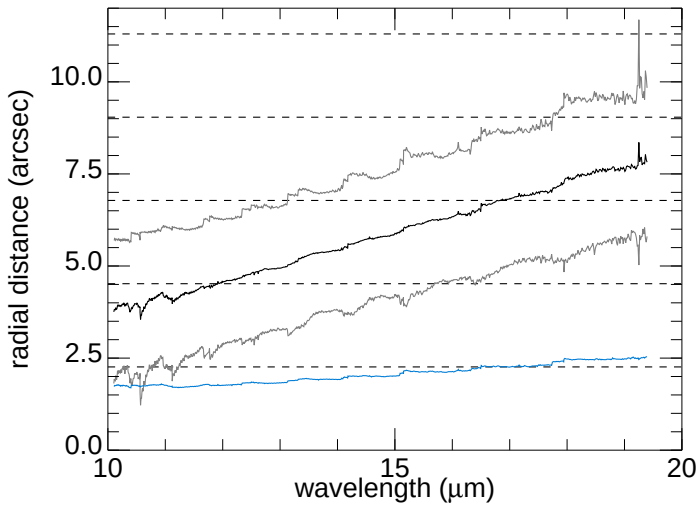

Figure 2.10: Position of the diffraction ring in the SH module (black solid line). The position of the half-maximum of the diffraction ring is shown in gray. For comparison, the blue line is the half width at half maximum of the PSF core. The dashed black lines represent the pixel size of the SH module.

Gaussians for the only diffraction ring detected. These two Gaussians have the same FWHM and they are symmetrically placed around the PSF core position. Figure 2.9 shows a fit example. The results of the fits are summarized in the Figure 2.10. The FWHM of the diffraction ring, that does not depend on the wavelength, is 3.6 $\pm$ 0.3 arcsec. Instead the position of the ring depends linearly on wavelength.

The relative value of the diffraction ring peak respect to the PSF core peak, depends slightly on wavelength. At 10 μm it is 11% of the core peak value and at 19 μm it is 9%.

When calculating feature ratios, the point spread function variations (FWHM and centroid), could originate artifacts. For the SL module these variations are less than one tenth of the pixel size and should not affect feature ratios. For the SH module the major source of uncertainty is the centroid position, but the difference is only one fourth of the pixel size. Since these variations are very small compared with the pixel size, they do not affect the calculated feature ratios. Diffraction rings can produce artifacts in the feature ratios too. They cause inaccurate ratio values 3 or 4 pixels away from the center of the point source in the SH module. For extended sources the situation is more complex because it is not possible to know where the diffraction ring will appear. However, comparing the spatial profiles of the features and the underlying continuum, as we do in this paper, helps determine if the ratio values are real or artifacts.

2.2.2 *Spitzer* Imaging

IRAC (Fazio et al. 2004) and MIPS (Rieke et al. 2004) are the two imaging instruments onboard *Spitzer*[3]. They provide imaging from 3.6 to 160 μm. IRAC works in the shorter wavelength range, 3.6–8.0 μm, whereas MIPS covers the longer wavelength range from 24 to 160 μm.

2.2.2.1 *Spitzer*/IRAC

IRAC provides 4 broad-band imaging bands centered at 3.6, 4.5, 5.8, and 8.0 μm (Fazio et al. 2004). The system throughput for each band is shown in Figure 2.11. Each band has its own detector of 256 × 256 pixels with a field of view of 5.′2×5.′2 (the pixel size is 1.″2 for the four detectors). Two nearly adjacent fields are observed simultaneously, one with the 3.6 and 5.8 μm detectors and the other with the 4.5 and 8.0 μm detectors. The 3.6 and 4.5 μm channels use InSb detector arrays, while the 5.8 and 8.0 μm use Si:As arrays. The FWHM of the PSF varies from 1.″4 to 1.″7, so the PSF is undersampled. The dithering patterns used in IRAC observations improve the PSF sampling and reduce the effect of bad pixels and cosmic rays.

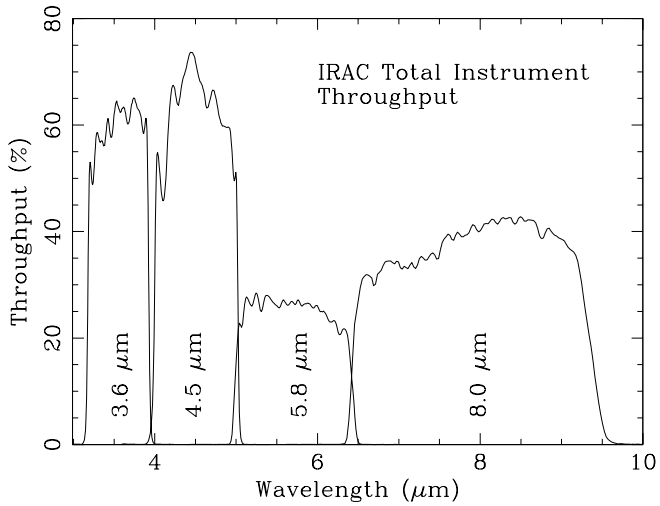

Figure 2.11: IRAC system total throughput. It includes transmission of the telescope, IRAC optics and quantum efficiency of the detectors. Figure from Fazio et al. (2004).

The only operating mode IRAC consists of pointing the telescope at the desired field and integrate. For the full array mode the standard integration times vary from 2 to 100 s. For the subarray mode (32 × 32 pixels) the readout is faster, from 0.02 to 0.4 s.

[3]IRS also has imaging capabilities in two bands centered at 15.8 and 22.3 μm, see Section 2.2.1.

This mode is used for bright sources. During each integration N non-destructive reads are performed. N depends on the integration time. The ramp fitting is done onboard by the IRAC electronics, therefore a single image is generated for each integration. In the high-dynamic range (HDR) mode one short exposure is taken before a long exposure in order to maximize the dynamic range of the observation.

2.2.2.2 *Spitzer*/MIPS

MIPS is the long-wavelength imager onboard *Spitzer*. It provides imaging in three bands at 24, 70, and 160 μm and low-resolution spectroscopy ($R \sim 15$–25) between 55 and 95 μm (Rieke et al. 2004). Figure 2.12 shows the instrument response for each band. It has 3 detectors, one for each imaging band. The 24 μm detector is a Si:As array with 128×128 pixels of size $\sim 2\farcs5$. For the 70 μm a 32×32 pixels Ge:Ga array is used, although due to a cabling problem half of the array is very noisy so the effective array size is 16×32 pixels. The pixel size is $\sim 5\farcs3$ or $\sim 9\farcs9$ depending on the observing mode. The 160 μm detector is a 2×20 pixels Ge:Ga array, the size of the pixels is $\sim 16''$. The low-resolution spectroscopy (spectral energy distribution mode) uses the 70 μm detector. MIPS is diffraction limited in all bands. The FWHM of the PSF are 6, 18, and $40''$ for the 24, 70, and 160 μm bands, respectively. They are well sampled by the detectors. The 24 and 160 μm detectors cover two nearby non-overlapping fields of view of $5' \times 5'$, whereas the field of view of the 70 μm detector depends on the observing mode.

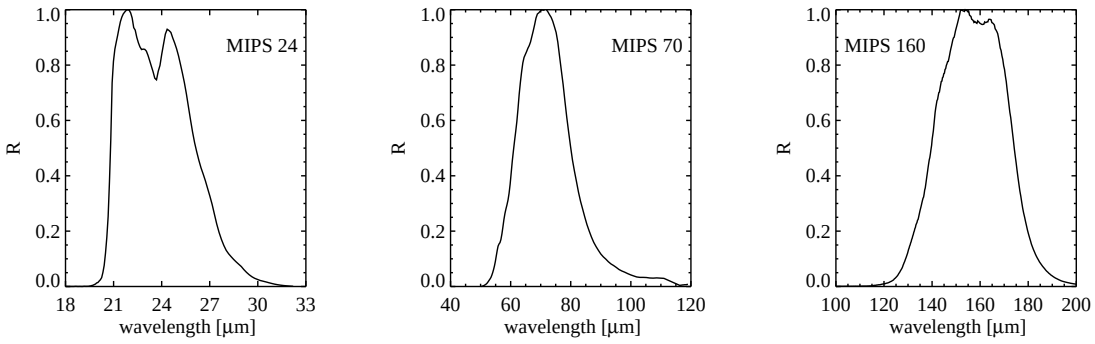

Figure 2.12: MIPS system response. It includes the detector and filter response. Figure adapted from the MIPS Instrument Handbook.

The 24 μm detector is read non-destructively every 0.5 s. The total integration time is 3, 4, 10, or 30 s. The ramp fitting is done onboard and only the slope image and the difference image between the two first reads are stored. The difference image is

Table 2.8: Log of *Spitzer* Imaging Observations

Target	IRAC AOR[a]	MIPS AOR[a]	Target	IRAC AOR[a]	MIPS AOR[a]
NGC23	12293120	12294144	UGC8739	12379904	12332288
MCG+12-02-001	12330752	12331776	ESO221-IG010	12336128	12337408
NGC633/ESO297-G012	12323584	12295424	NGC5653	12302848	12344576
UGC1845	12359680	12360704	NGC5734/5743	12358912	12307712
UGC2982	12295680	12296192	IC4518W/E	12301568	12302336
NGC1614	4327680	4346112	Zw049.057	12359168	12359936
CGCG468-002 NED01/NED02	12343040	12317440	NGC5936	12327680	12328704
UGC3351	12356352	12357888	NGC5990	12291072	12292352
NGC2369	12310528	12312064	NGC6156	12335872	12336640
NGC2388	12339712	12324352	IRASF17138-1017	12353536	12355328
MCG+02-20-003	12361984	···	IRAS17578-0400	12307200	12351744
NGC3110	12337152	12337920	IC4686/4687	12327168	12371456
NGC3256	3896832	3902464	IC4734	12366336	12367616
ESO264-G057	12360192	12360960	NGC6701	12375552	12345600
NGC3690/IC694	3898880	3904256	NGC6921/MCG+04-48-002	12370944	12344832
ESO320-G030	12343552	12345088	NGC7130	12367360	4858880
MCG-02-33-098 W/E	12356608	12372480	IC5179	12360448	12366080
IC860	12325632	12326400	NGC7469	3898368	3904000
MCG-03-34-064	12308480	12355072	NGC7591	12380928	12333568
NGC5135	12372992	4864768	NGC7679	12320512	12320256
ESO173-G015	12315904	1231692	NGC7769/7770/7771	12325888	12347648
IC4280	12309760	12311296			

Notes. [(a)] Astronomical Observation Request key.

used to replace saturated pixels in the slope image. The 70 and 160 μm arrays are read non-destructively as well, but the full data cubes are stored and the ramp fitting is performed in ground.

MIPS has 3 main operating modes: scan map, photometry, and spectral energy distribution (SED). The scan map mode is used to map large areas. The telescope scans the sky at a constant rate and the scan mirror is used to freeze the images in the arrays for the integration. In the photometry mode the telescope points at the target and integrates. Small offsets to the telescope pointing and scan mirror motions are applied to dither the images. The SED mode provides a far-IR low-resolution long-slit spectra. The size of the slit is $20''\times3\farcm8$.

2.2.2.3 Imaging Data Reduction

Spitzer imaging data were obtained, mainly as part of the GOALS legacy program (Armus et al. 2009), for the LIRGs in our sample. These galaxies were observed using all the IRAC and MIPS imaging bands. In this thesis we use the 4 IRAC bands but only the MIPS 24 μm band. The observing log is shown in Table 2.8.

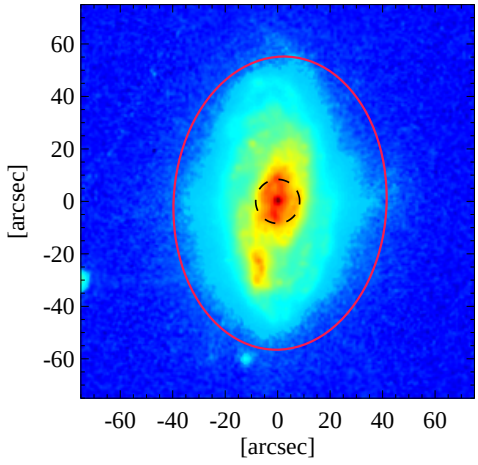

Figure 2.13: Example *Spitzer*/IRAC aperture photometry. Over the IRAC 8.0 μm image of IC 5179 we plot the apertures used to measure the the galaxy integrated flux (solid red ellipse) and the nuclear flux (dashed black circle).

We retrieved the BCD from the *Spitzer* archive. The IRAC BCD processing includes corrections for the instrumental response (pixel response, linearization, etc.), dark and flat fielding corrections, and flux calibration based on standard stars. Similarly the BCD processing of the 24 μm MIPS includes dark subtraction, linearity correction, flat field, replacement of saturated pixels with those of the difference image and flagging of cosmic ray hits (see the IRAC and MIPS Instrument Handbooks for further details).

We combined the BCD images into mosaics using the MOsaicker and Point source EXtractor (MOPEX) software provided by the SSC using the standard parameters. This is done in two steps: overlap and mosaicking. Each of them performed by the scripts `overlap.pl` and `mosaic.pl` provided by MOPEX. The overlap modules calculate the additive correction needed to bring all the images to a common background level. First, bright objects are masked, then the input images are projected into a common output grid and the background offsets are calculated. The mosaic modules create a mosaic of the observed region combining the BCD images. The BCD images are interpolated into the output grid and geometric distortions are corrected. Cosmic ray hits and bad pixels are detected and they are later ignored during the final BCD frames combination (see the MOPEX User's Guide for details on the data reduction). We set the pixel size of the output mosaic to half of the detector physical pixel size, that is 0.″6 for the IRAC images and 1.″2 for the 24 μm MIPS images. The IRAC and MIPS images of the LIRGs are shown in Appendix 2.A.

2.2.2.4 Photometry

We measured the integrated flux of our LIRGs using an elliptical aperture which encompasses the emission of the galaxy. This ellipse was calculated by fitting the emission of the galaxy (3σ over the background) in the 8 μm band. This corresponds to the emission with a surface brightness larger than 0.06 Mj sr^{-1} at 8 μm. For the IRAC images we applied the extended source aperture correction to the integrated fluxes as described in the IRAC Instrument Handbook. This correction accounts for the diffuse scattering of the emission across the IRAC focal plane. It is larger in the 5.8 and 8.0 μm bands (up to 25–35 %) than in the 3.6 and 4.5 μm bands (5–10 %).

To measure the nuclear flux we used aperture photometry. The aperture size was set to a physical aperture of radius 2 kpc at the distance of the galaxy. Since all the galaxies in our sample are at comparable distances the aperture size is similar for all of them ($\sim$6″). Figure 2.13 shows an example of the apertures used. The nuclear emission of most of the our LIRGs are only partially resolved, therefore we applied an aperture correction. The exact value of the aperture correction was obtained by interpolating the corrections from the Instrument Handbooks to the used aperture. This method can overestimate the nuclear flux of the galaxies, up to 10 %, depending on the exact spatial distribution of the nuclear sources. However there is a very good agreement between the nuclear fluxes obtained from the image photometry and synthetic fluxes derived from the nuclear spectra. The measured nuclear and integrated fluxes are listed in Table 2.9.

Table 2.9: *Spitzer* Photometry of Local LIRGs

Galaxy Name	$F_{3.6\mu m}$ [mJy]		$F_{4.5\mu m}$ [mJy]		$F_{5.8\mu m}$ [mJy]		$F_{8.0\mu m}$ [mJy]		$F_{24\mu m}$ [mJy]	
	Nuc.	Int.	Nuc.	Int.	Nuc.	Int.	Nuc.	Int.	Nuc.	Int.
NGC23	51	110	34	74	100	160	290	410	730	860
MCG+12-02-001	36	59	32	52	140	190	430	560	2900	3100
NGC633	19	41	16	31	46	78	130	220	440	990
ESO297-G012	15	20	11	14	40	49	120	140	630	630
UGC1845	41	52	30	38	110	110	330	310	860	860
UGC2982	27	66	19	49	79	180	250	540	350	610
NGC1614	68	96	57	76	240	280	740	790	5700	5600
CGCG468-002-NED01	36	46	33	40	52	63	90	100	340	340
CGCG468-002-NED02	9	15	9	13	32	39	92	110	710	710
UGC3351	42	91	31	68	97	190	270	510	460	660
NGC2369	73	160	56	120	180	260	500	670	1600	1800
NGC2388	45	66	35	49	130	140	370	390	1600	1600
MCG+02-20-003	19	26	27	33	93	97	190	200	...	...
NGC3110	26	85	19	61	76	200	230	580	520	950
NGC3256	200	310	180	260	790	980	2300	2700	11000	12000
ESO264-G057	14	50	11	35	37	96	120	280	440	580
ESO320-G030	63	91	45	64	170	180	490	490	8100	17000
MCG-02-33-098	12	37	10	28	38	76	120	210	1700	1700
IC860	13	21	9	14	16	22	41	48	940	1100
MCG-03-34-064	60	80	100	120	200	250	400	460	850	820
NGC5135	65	130	64	110	170	210	410	520	2600	2600
ESO173-G015	66	150	66	120	250	370	720	1000	1800	2000
IC4280	21	72	14	49	46	140	140	400	4600	6000

Table 2.9: *Continued*

Galaxy Name	$F_{3.6\mu m}$ [mJy]		$F_{4.5\mu m}$ [mJy]		$F_{5.8\mu m}$ [mJy]		$F_{8.0\mu m}$ [mJy]		$F_{24\mu m}$ [mJy]	
	Nuc.	Int.	Nuc.	Int.	Nuc.	Int.	Nuc.	Int.	Nuc.	Int.
UGC8739	19	54	14	40	40	110	110	300	240	470
ESO221-IG010	41	110	29	74	110	230	310	630	130	320
NGC5653	40	94	27	67	99	210	310	610	1000	1500
NGC5734	51	110	34	74	90	170	260	460	480	1100
NGC5743	22	52	16	37	55	110	160	300	360	560
IC4518W	37	65	52	68	96	140	180	250	250	420
IC4518E	12	53	8	36	23	55	63	140	140	1100
Zw049.057	12	16	9	11	28	31	77	85	1000	1000
NGC5936	27	70	19	51	73	160	220	450	530	520
NGC5990	87	140	88	130	150	210	300	450	780	1000
NGC6156	44	180	31	120	69	320	210	890	970	1200
IRASF17138-1017	34	74	28	55	120	150	350	400	1100	2000
IRAS17578-0400	20	33	15	25	67	78	190	210	1700	1600
IC4686	10	13	8	10	22	29	63	78	640	640
IC4687	35	56	27	42	130	180	400	510	1400	2800
IC4734	27	64	21	47	65	110	190	300	890	890
NGC6701	36	96	26	69	74	160	210	430	990	1000
MCG+04-48-002	43	72	38	59	140	170	370	430	720	990
NGC7130	31	89	32	72	83	160	220	440	83	81
IC5179	56	170	40	120	170	390	520	1100	610	690
NGC7469	140	180	160	190	320	410	750	950	1600	1800
NGC7591	22	60	16	42	39	97	110	270	1100	1800
NGC7679	34	53	25	40	94	130	280	380	4900	4900

Table 2.9: *Continued*

Galaxy Name	$F_{3.6\mu m}$ [mJy]		$F_{4.5\mu m}$ [mJy]		$F_{5.8\mu m}$ [mJy]		$F_{8.0\mu m}$ [mJy]		$F_{24\mu m}$ [mJy]	
	Nuc.	Int.	Nuc.	Int.	Nuc.	Int.	Nuc.	Int.	Nuc.	Int.
NGC7769	24	98	15	65	23	130	58	330	580	660
NGC7770	16	26	17	24	43	56	100	130	750	840
NGC7771	50	170	38	120	110	240	310	620	900	1700

Notes. Nuclear and integrated observed fluxes. The nuclear fluxes corresponds to the flux in the central 4 kpc. The fluxes at 3.6, 4.5, 5.8, and 8.0 μm were measured in the *Spitzer*/IRAC images. The 24 μm flux was obtained from the *Spitzer*/MIPS images. We applied the corrections described in Section 2.2.2.4.

2.3 *XMM-Newton* Observations

XMM-Newton is an ESA space telescope. It was launched in December 1999 and it is expected to work at least until 2015. It carries three co-aligned X-ray Wolter type-I telescopes and a 30 cm optical/UV telescope.

XMM-Newton has three science instruments: the European Photon Imaging Camera (EPIC); the Reflection Grating Spectrograph (RGS); and the Optical Monitor (OM). The two X-ray instruments, EPIC and RGS, provide X-ray imaging and low-resolution X-ray spectroscopy, and high-resolution X-ray spectroscopy, respectively. OM provides optical/UV imaging and grism spectroscopy. EPIC and RGS are sensitive in the X-ray ranges 0.15–12 keV and 0.35–2.5 keV, respectively. The OM bandpass is 1800–6000 Å. Further details can be found in the *XMM-Newton* User Handbook. All the instruments are operated together, so simultaneous X-ray and optical/UV observations are acquired.

We obtained new *XMM-Newton* data for 9 galaxies (proposals 55046 and 60160). We also found X-ray data for 12 more galaxies in the *XMM-Newton* archive . Our proposal was focused on galaxies classified as H II galaxies based on their optical spectra whereas most of the galaxies from the archive are active galaxies (Seyfert and LINER activity). The observation IDs and effective exposure times are shown in Table 2.10. In addition we used *Chandra* data from the literature for 6 LIRGs.

2.3.1 EPIC X-ray Imaging and Low-resolution Spectroscopy

EPIC consists of 3 CCD cameras. Two of them are Metal Oxide Semiconductor (MOS) arrays and the third is a pn array. Each camera is located at one of the X-ray telescopes. The MOS cameras (MOS1 and MOS2) share the telescope with the two RGS arrays, thus they receive 44 % of the reflected light.

The pn and MOS cameras are composed by 12 and 7 CCD chips, respectively. One of the chips of the MOS1 camera stopped recording events after the impact of a micrometeorite. The MOS1 camera continued working but with this CCD chip switched off. The pixel size of the MOS and pn cameras are $1\farcs1$ and $4\farcs1$, respectively. The field of view is $\sim 30'$ and the cameras are sensitive in the range 0.15–12 keV with a low spectral resolution ($E/\Delta E \sim 20$–50). The on-axis angular resolution is $6''$. The shape and size of the PSF vary with the off-axis angle (distance from the center of the field of view). The PSF shape becomes more elongated and its size increases with increasing off-axis angle.

The pn and MOS cameras have three operating modes: full-frame, window, and timing modes. Each mode has a different field of view and time resolution. High time

Table 2.10: Log of the *XMM-Newton* Observations

Galaxy Name	Obs. ID.	Exposure[a] (ks)
New *XMM-Newton* Observations		
NGC2369	0550460101	24.3
NGC3110	0550460201	15.9
ESO320-G030	0550460301	23.9
NGC5734/5743	0601600101	27.0
IC4686/4687	0550460601	26.5
IC4734	0550460701	18.6
IC5179	0550460801	22.0
Archival *XMM-Newton* Observations		
NGC1614	0150480201	21.8
NGC3256	0300430101	125.6
NGC3690/IC694	0112810101	17.1
MCG−03-34-064	0206580101	42.7
”	0506340101[b]	...
IC4518W	0406410101	22.8
MCG+04-48-002	0312192301	11.4
NGC7469	0112170301	23.0
NGC7679	0301150501	17.9
NGC7769/7770/7771	0093190301	30.0

Notes. [(a)] Exposure time after flare removal. [(b)] Only used for the *XMM-Newton*/OM UVW2 image of MCG−03-34-064.

resolution is important to avoid photon pile-up[4] in bright sources. In the full-frame mode the complete CCDs are read. This mode covers the whole field of view, but has the lowest time resolution. Window modes are similar to full-frame mode but only a partial region of the CCDs is read with a higher time resolution. In the timing mode the highest time resolution is achieved, but the part of the spatial information is lost. The CCD chips also are sensitive to optical and UV light. To prevent contamination from this light three optical blocking filters (thin, medium, and thick filters) are available to use when a bright optical source is observed ($m_{\rm V} < 12$). The soft X-ray range ($< 2\,$keV) sensitivity is reduced when these filters are used.

[4]Photon pile-up occurs when more than one X-ray photon arrives at one camera pixel between two readouts.

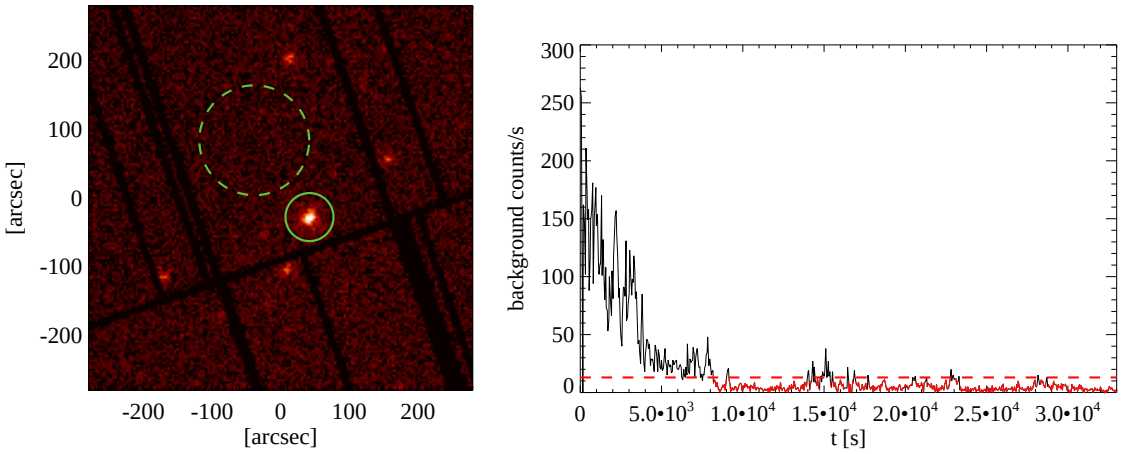

Figure 2.14: Example *XMM-Newton* high-background filtering. The left panel shows the EPIC/pn image of ESO 320-G030. The solid green circle indicates the aperture used to extract the source spectrum. The region encircled by the dashed green line is the background region. The right panel shows the background light-curve. The dashed red line marks the threshold count rate used to filter out high-background periods. The intervals in black were filtered out due to the high-background count rate.

EPIC Data Reduction

In general H II-like LIRGs are not bright X-ray sources. Therefore most of the observations were obtained in the full-frame mode. We retrieved from the *XMM-Newton* archive the Observation Data Files (ODF). We reduced the observation data files (ODF) using Science Analysis Software (SAS) version 10.0.2. First we used the SAS *epproc* and *emproc* tasks to generate the calibrated event files from the raw EPIC pn and MOS data, respectively.

A circular aperture (d$\sim$15″ depending on the source extent) was used to extract the spectra of the galaxies. We estimated the backgrounds from a region close to the source in the same CCD and free of any contaminating source. The background regions were $\sim$4–5 times larger than the aperture used for the galaxies. Then we created the background and background+source light-curves that we used to filter out high-background periods. The background count rate threshold was chosen to just filter out those high-background periods that would not increase the S/N ratio of the source (see Appendix A of Piconcelli et al. 2004).

For the pn data we considered single and double pixel events (PATTERN $\leq$ 4). We rejected events close to the CCD borders or to bad pixels (#XMMEA_EP). For the MOS we also considered triple and quadruple pixel events (PATTERN $\leq$ 12) and we used the recommended expression (#XMMEA_EM) to filter the events. The energy

redistribution matrices were generated with `rmfgen` and `arfgen`. We rebinned the combined MOS spectrum (MOS1 and MOS2 spectra) and the pn spectrum to obtain at least 20 counts in each spectral bin using `grppha`. Likewise we obtained X-ray images of the galaxies using the pn calibrated event files.

2.3.2 RGS High-resolution X-ray Spectroscopy

The RGS consists of two grating spectrographs. Each one is located at a different *XMM-Newton* X-ray telescope and shares the X-ray light with the MOS cameras. They cover the energy range 0.35–2.5 keV (5–38 Å) with high spectral resolution ($R \sim 100$–500). Each RGS camera has 9 MOS CCD chips. Two of these CCDs failed due to electronic components errors. In the cross-dispersion direction the field of view is $5'$. RGS is a slitless spectrograph therefore the spectral resolution is degraded for extended objects (size $> 20''$).

Most of our LIRGs are weak in the X-ray range. Therefore owing to the low number of counts in the RGS data we could only extract the RGS spectra for few galaxies: NGC 3256, MCG−03-34-064, and NGC 7469. We did not analyze them in this work. The spectra of MCG−03-34-064 and NGC 7469 are analyzed in detail by Miniutti et al. (2007) and Blustin et al. (2003), respectively.

2.3.3 OM Optical and UV Imaging

The *XMM-Newton* 30 cm optical/UV telescope is co-aligned with the X-ray telescopes. It provides simultaneous optical/UV imaging and spectroscopic observations of the X-ray targets. It has 6 broad-band filters (V 5430 Å, B 4500 Å, U 3440 Å, UVW1 2910 Å, UVM2 2310 Å, and UVW2 2120 Å) covering from 1800 Å to 6000 Å for imaging. In addition, two grism are used for low-resolution ($R \sim 250$) spectroscopy in the optical and UV spectral ranges. The OM detector is a micro-channel plate with 256×256 pixels. The pixel size is $4''$. The position of the photons entering the pixels is determined onboard using a centroiding algorithm which subsamples each pixel into 8×8 pixels of size $\sim 0.5''$. Therefore the final array has 2048×2048 pixels and covers a field of view of $17'$. The FWHM of the PSF is $1''.4$–$2''.4$ depending on the wavelength.

The operating modes of OM are the imaging mode and the fast mode. In the imaging mode OM produces integrated images with no timing information. Note that the complete field of view cannot be observed in a single OM exposure due to the limited on-board memory. However multiple exposures with different windows can be used to cover the full field of view. In the fast mode event lists with timing and location information of individual photons are produced instead of images. These two operating

modes can be used with the imaging filters and the grisms.

OM Data Reduction

Simultaneously with the X-ray observations we obtained optical and UV images of the galaxies using the *XMM-Newton*/OM with all available filters (V 5430 Å, B 4500 Å, U 3440 Å, UVW1 2910 Å, UVM2 2310 Å, and UVW2 2120 Å). We used the SAS script `omichain` for the data reduction. This script processes the OM ODF files and produces calibrated images taking into account the telescope tracking information and the flat-fielding corrections. For some filters there was more than one exposure that we combined to increase the S/N ratio.

2.A *Spitzer* IRAC and MIPS Images

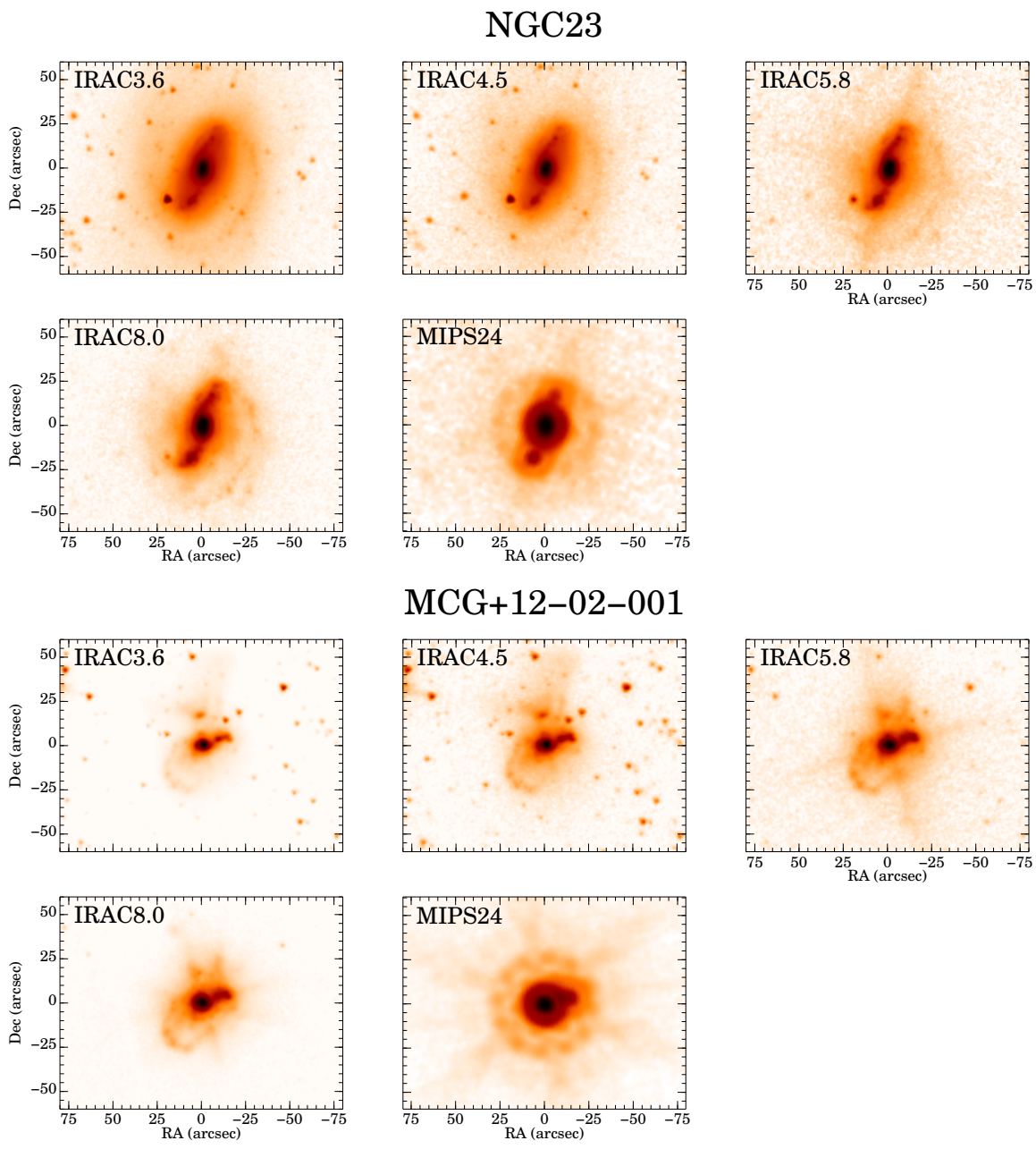

Figure 2.15: *Spitzer*/IRAC 3.6, 4.5, 5.8, and 8.0 μm and *Spitzer*/MIPS 24 μm images of the sample of LIRGs. All images are shown in a logarithm scale. North is up and east is to the left. In galaxy systems the first and second components of the system are identified with the numbers 1 and 2, respectively, in the 3.6 μm image.

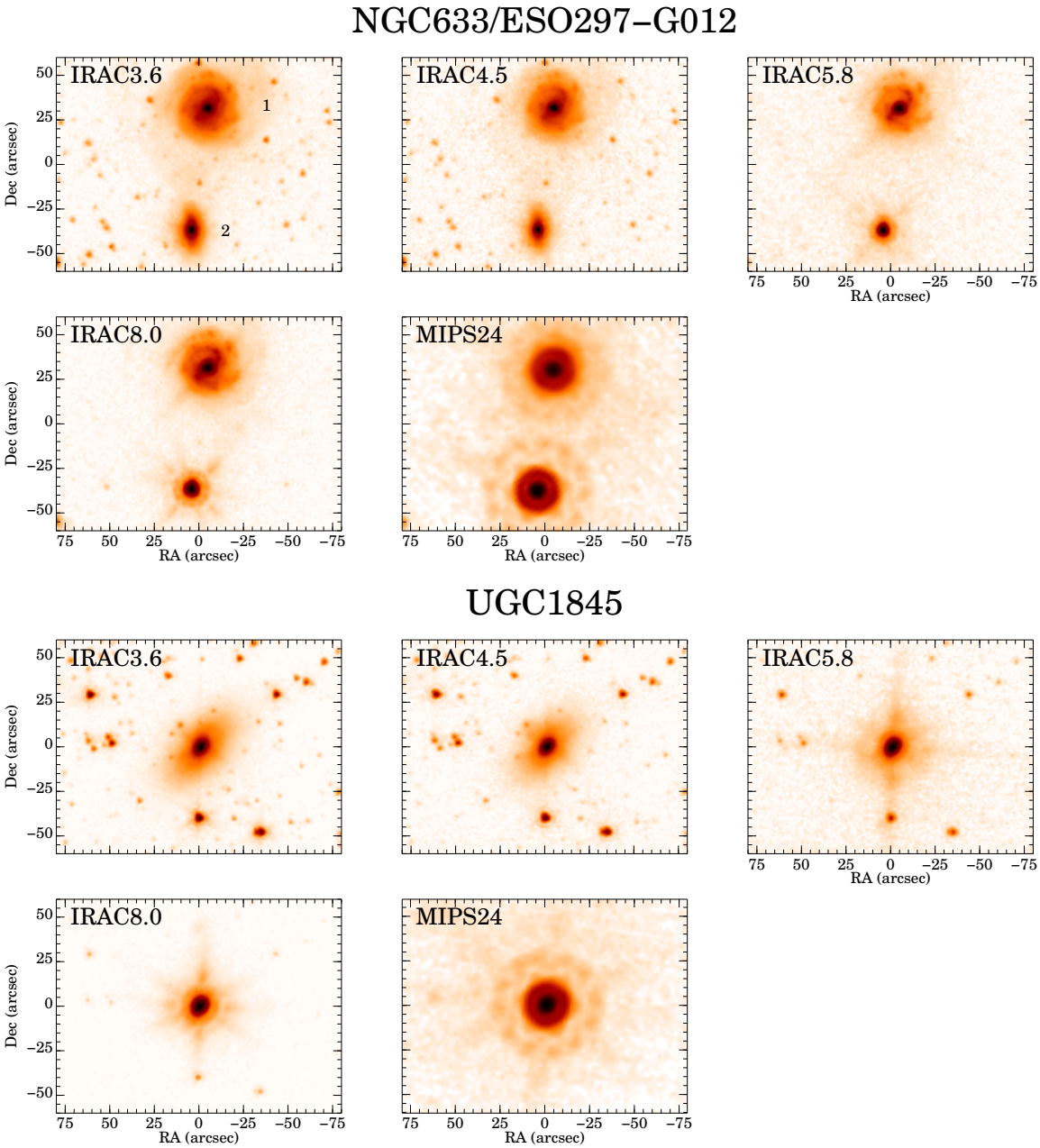

Figure 2.15: *Continued.*

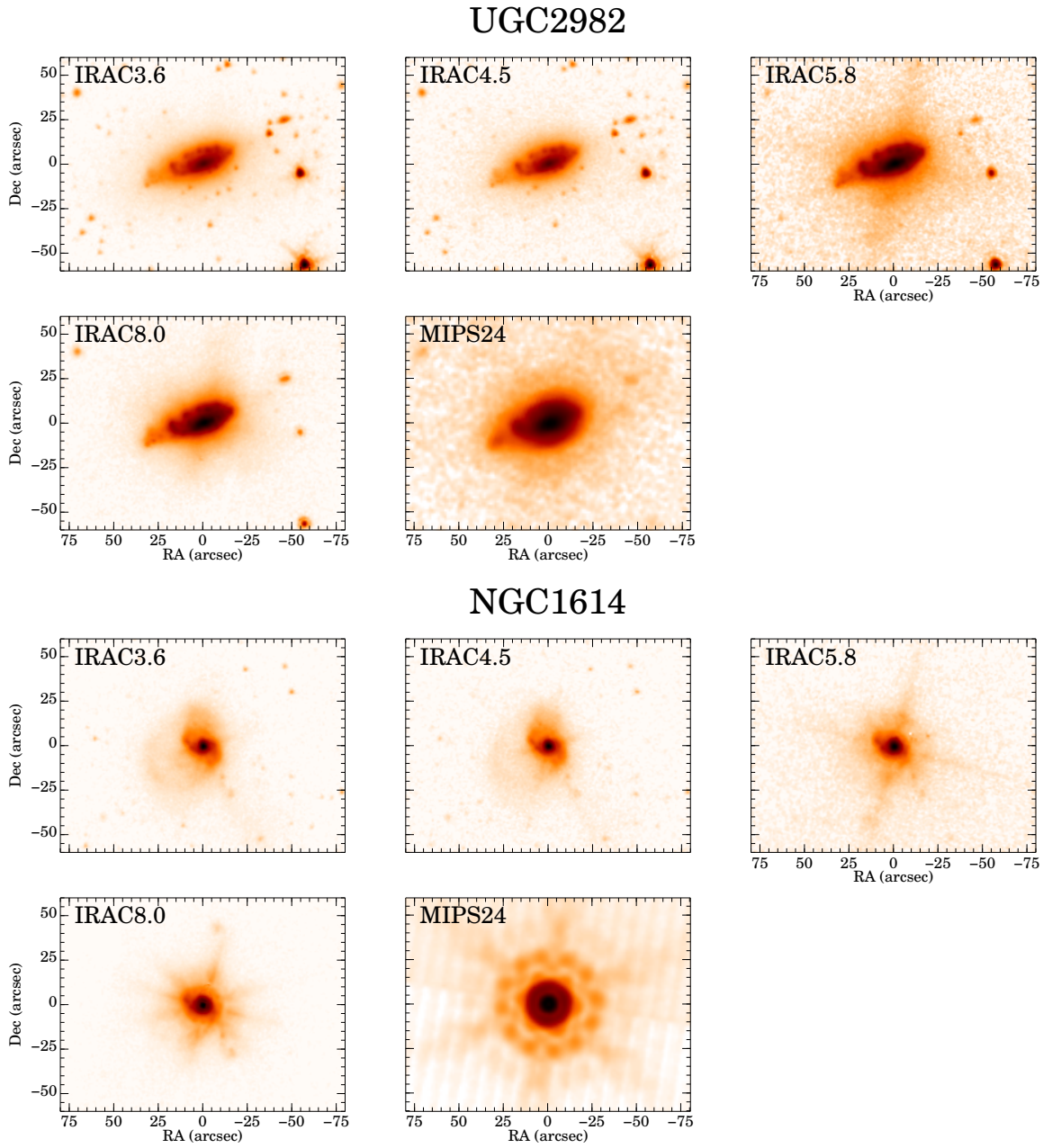

Figure 2.15: *Continued.*

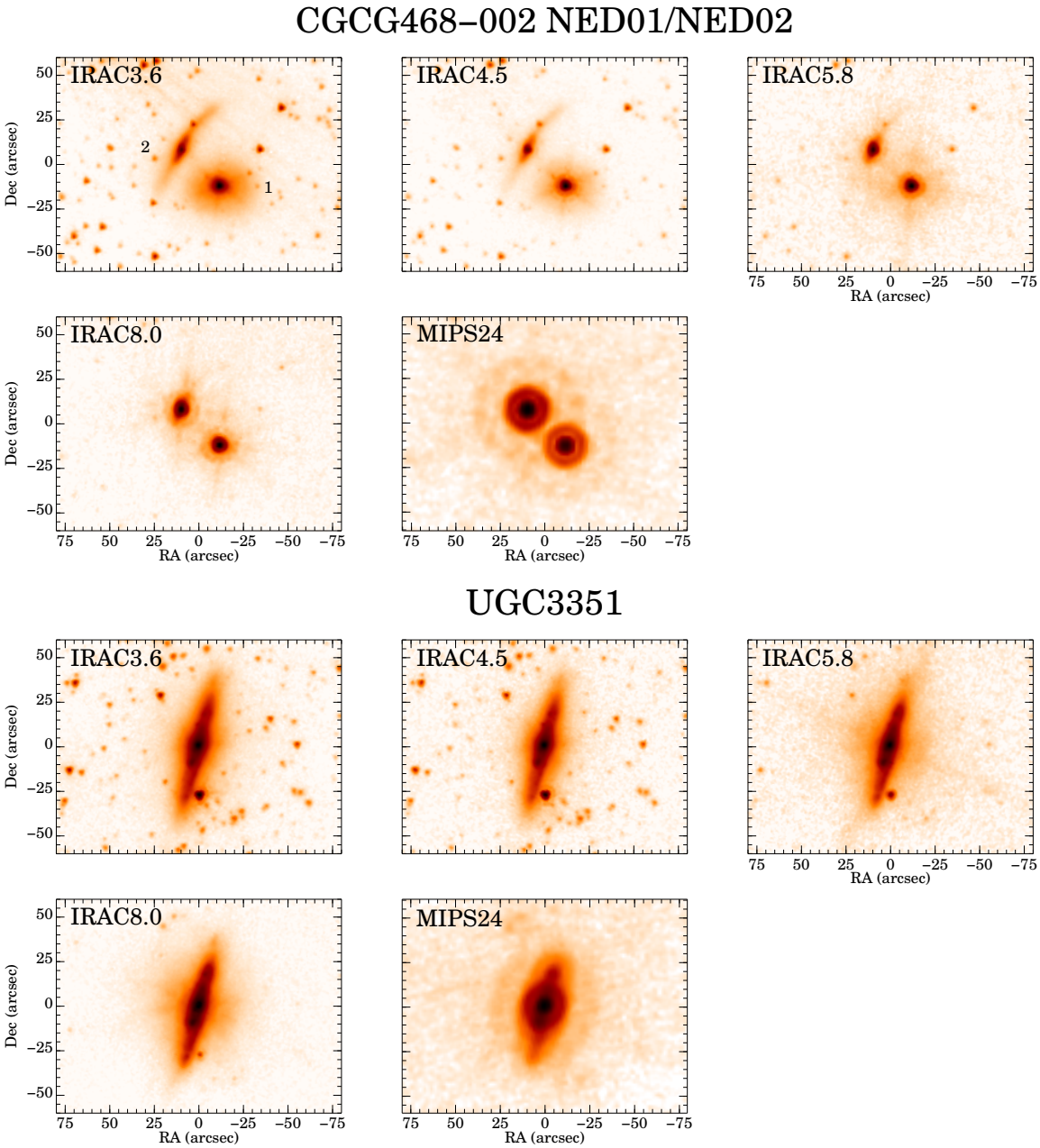

Figure 2.15: *Continued.*

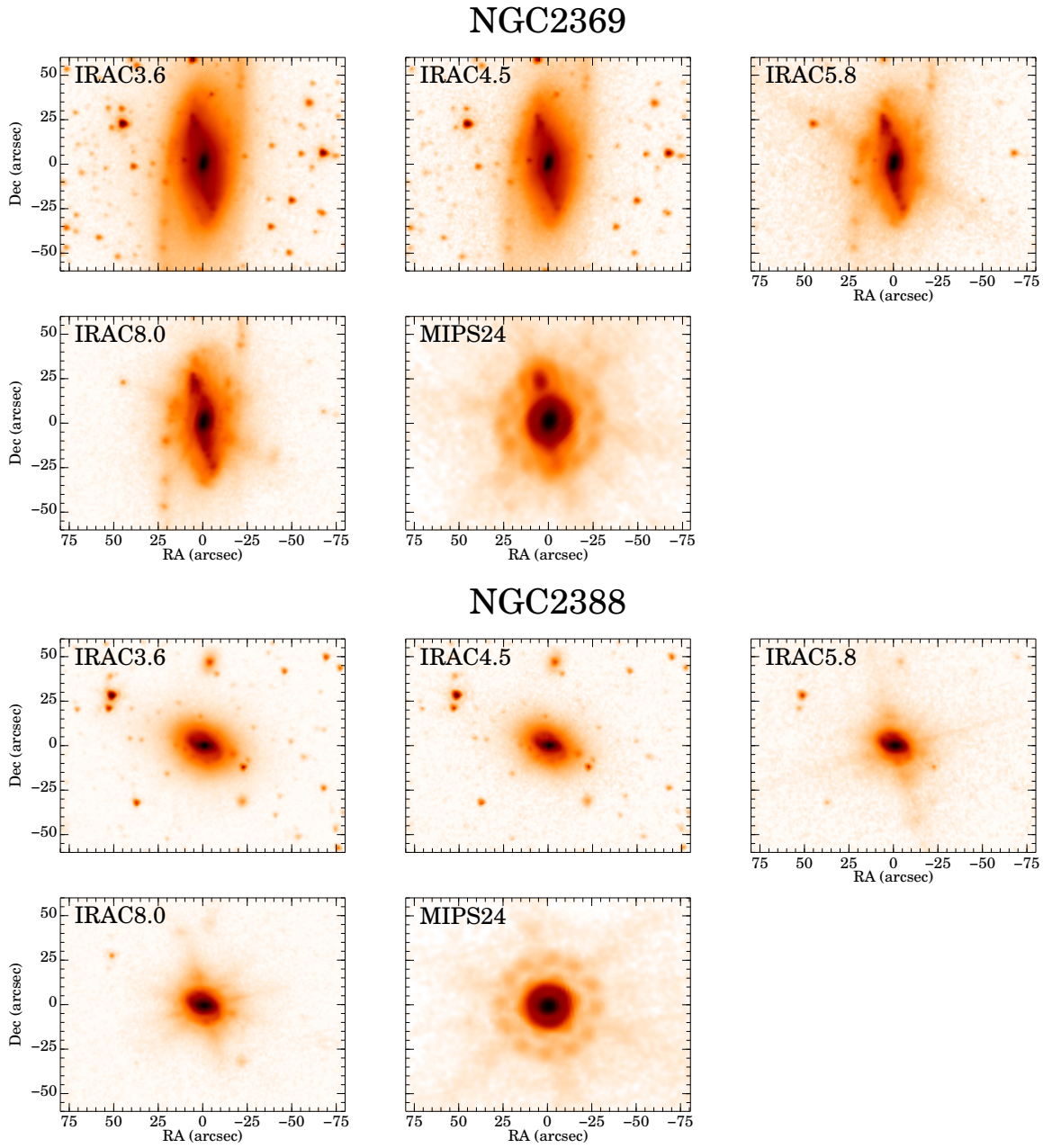

Figure 2.15: *Continued.*

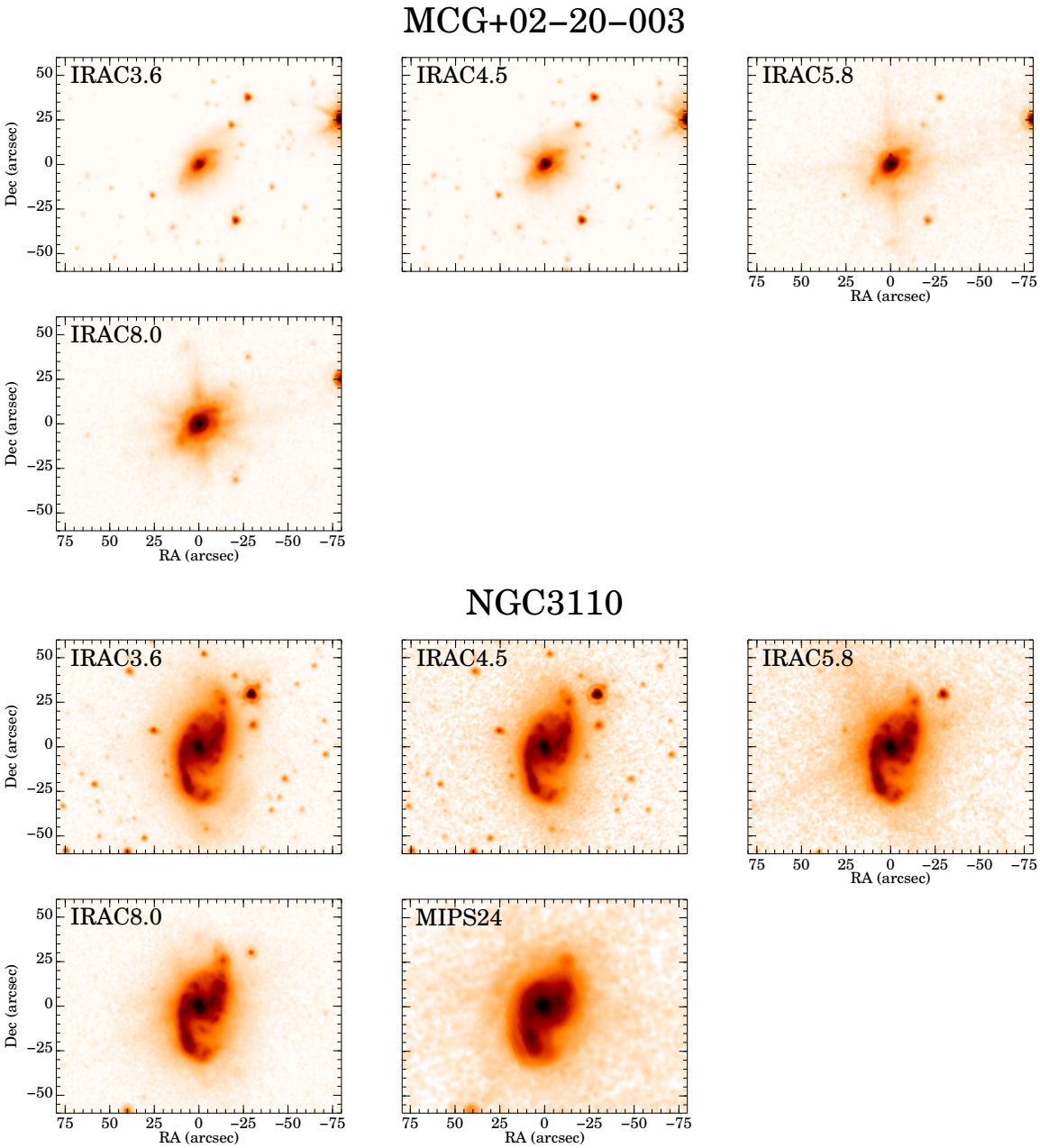

Figure 2.15: *Continued.*

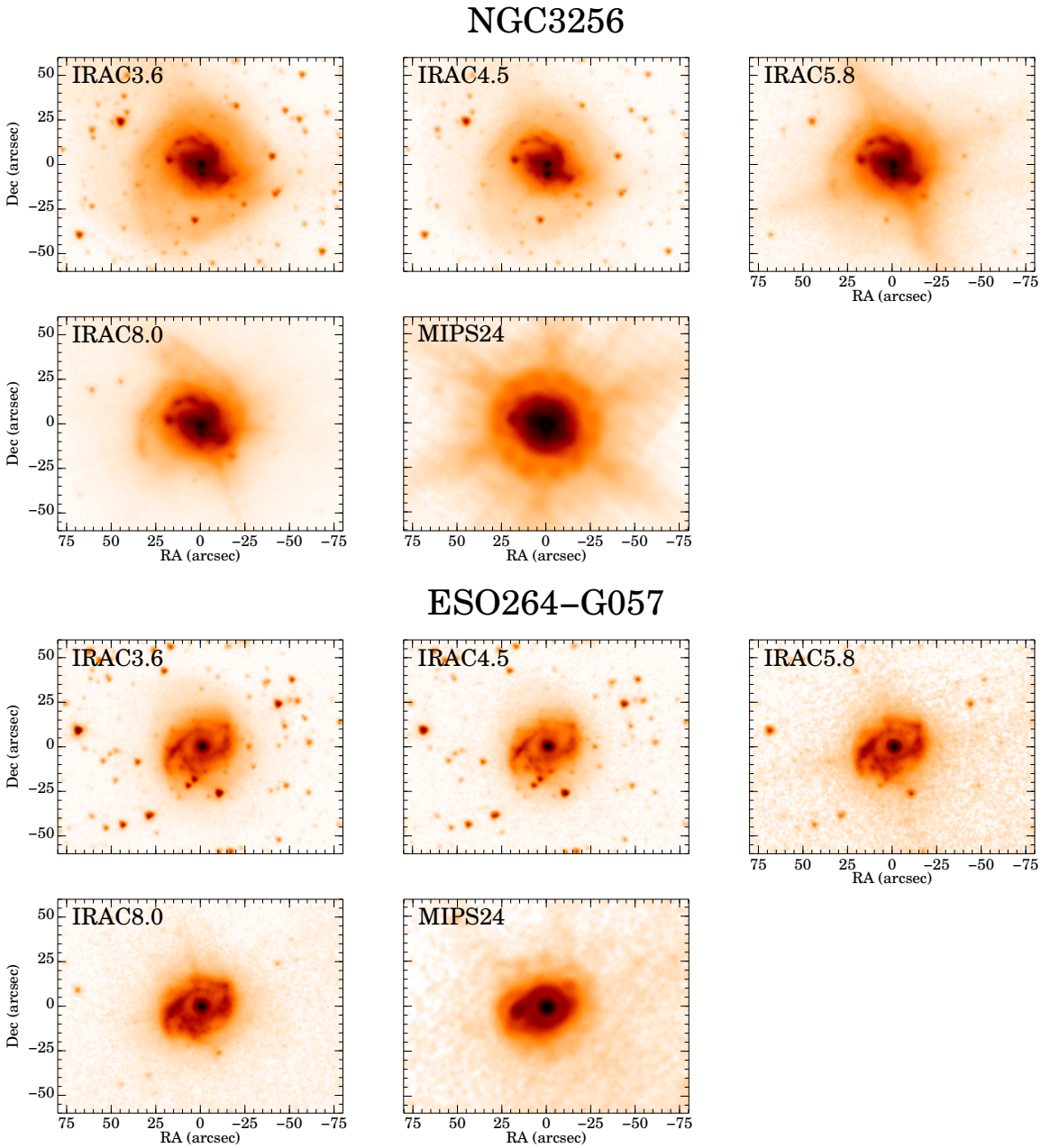

Figure 2.15: *Continued.*

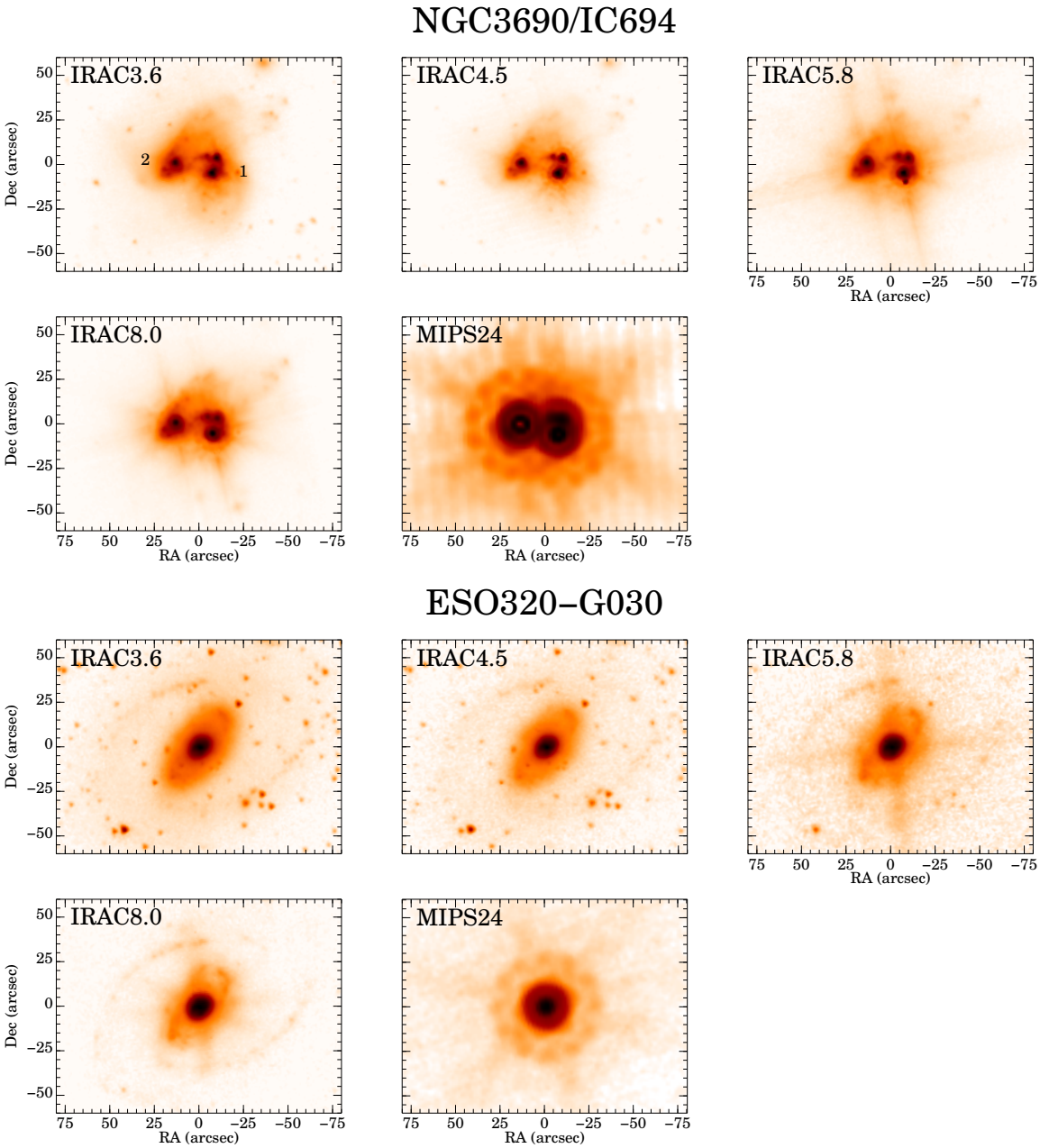

Figure 2.15: *Continued.*

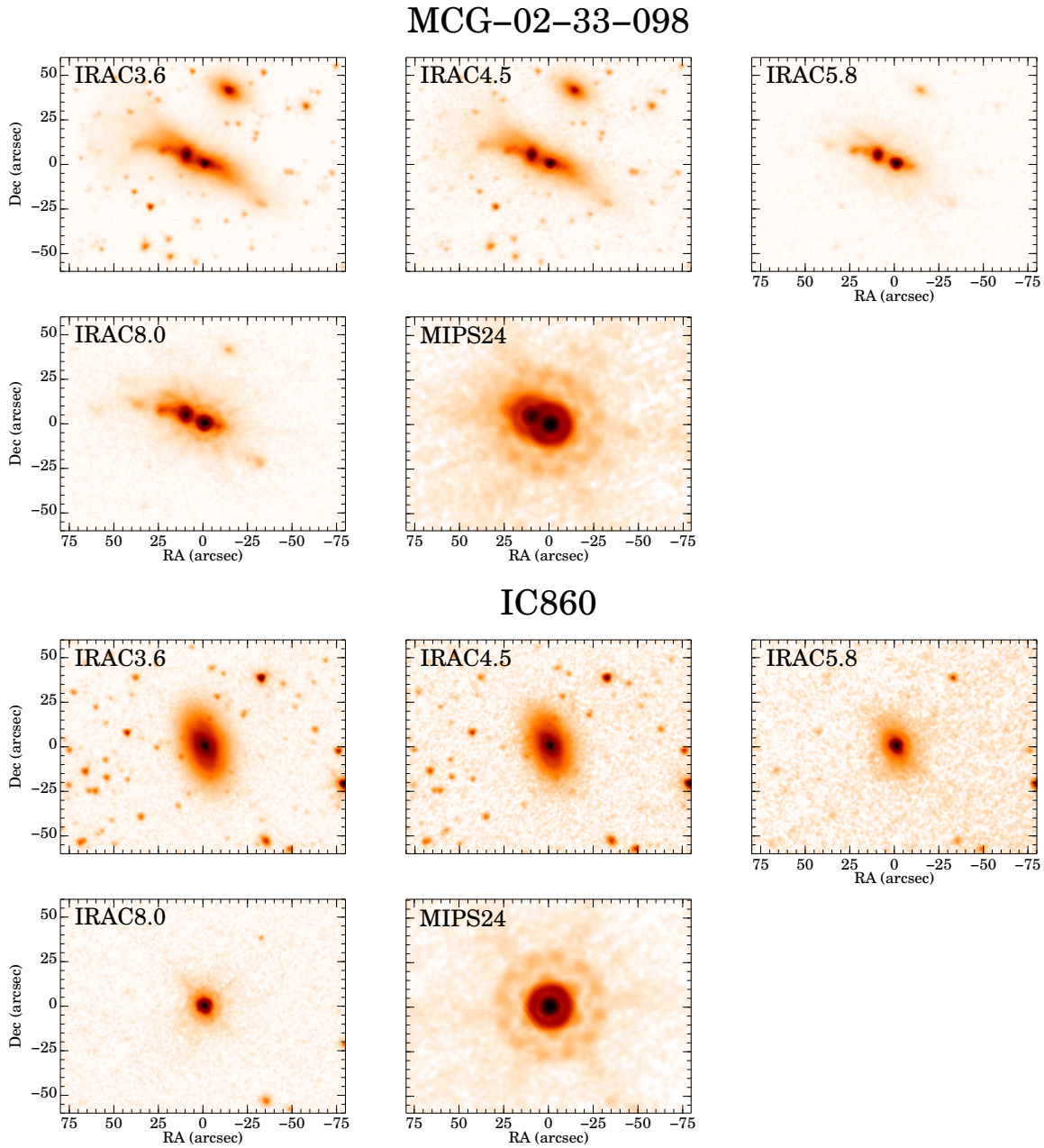

Figure 2.15: *Continued.*

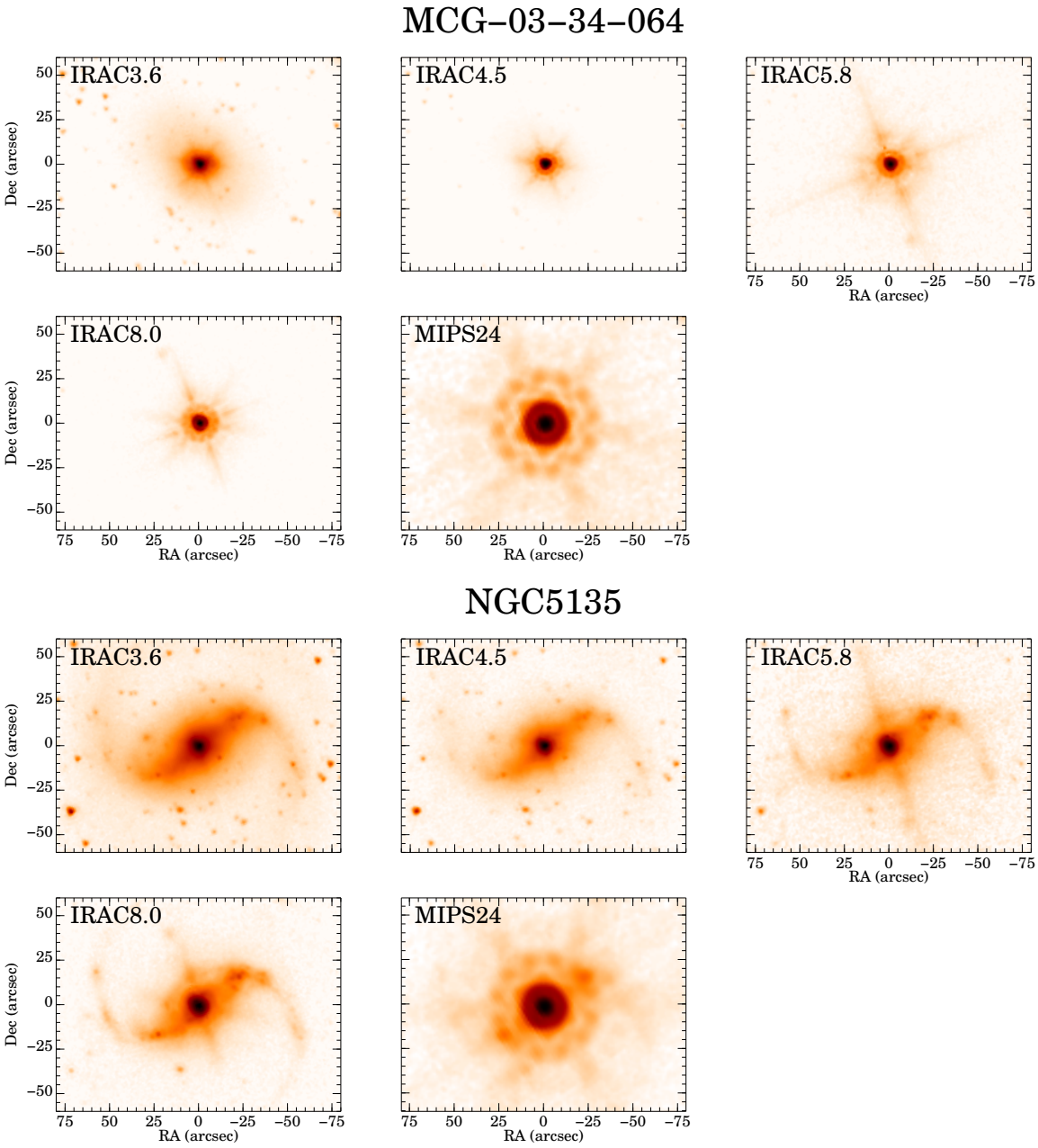

Figure 2.15: *Continued.*

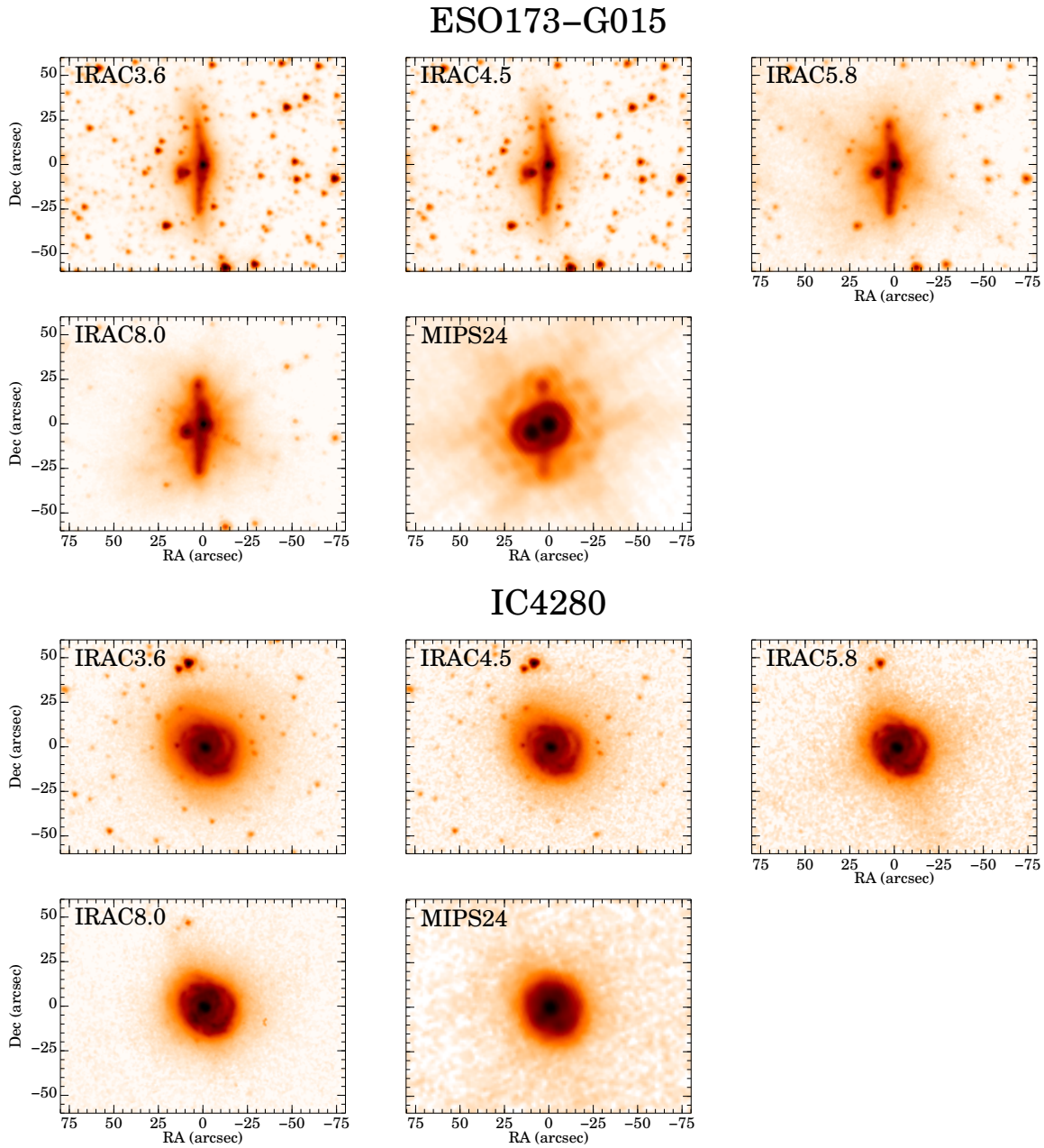

Figure 2.15: *Continued.*

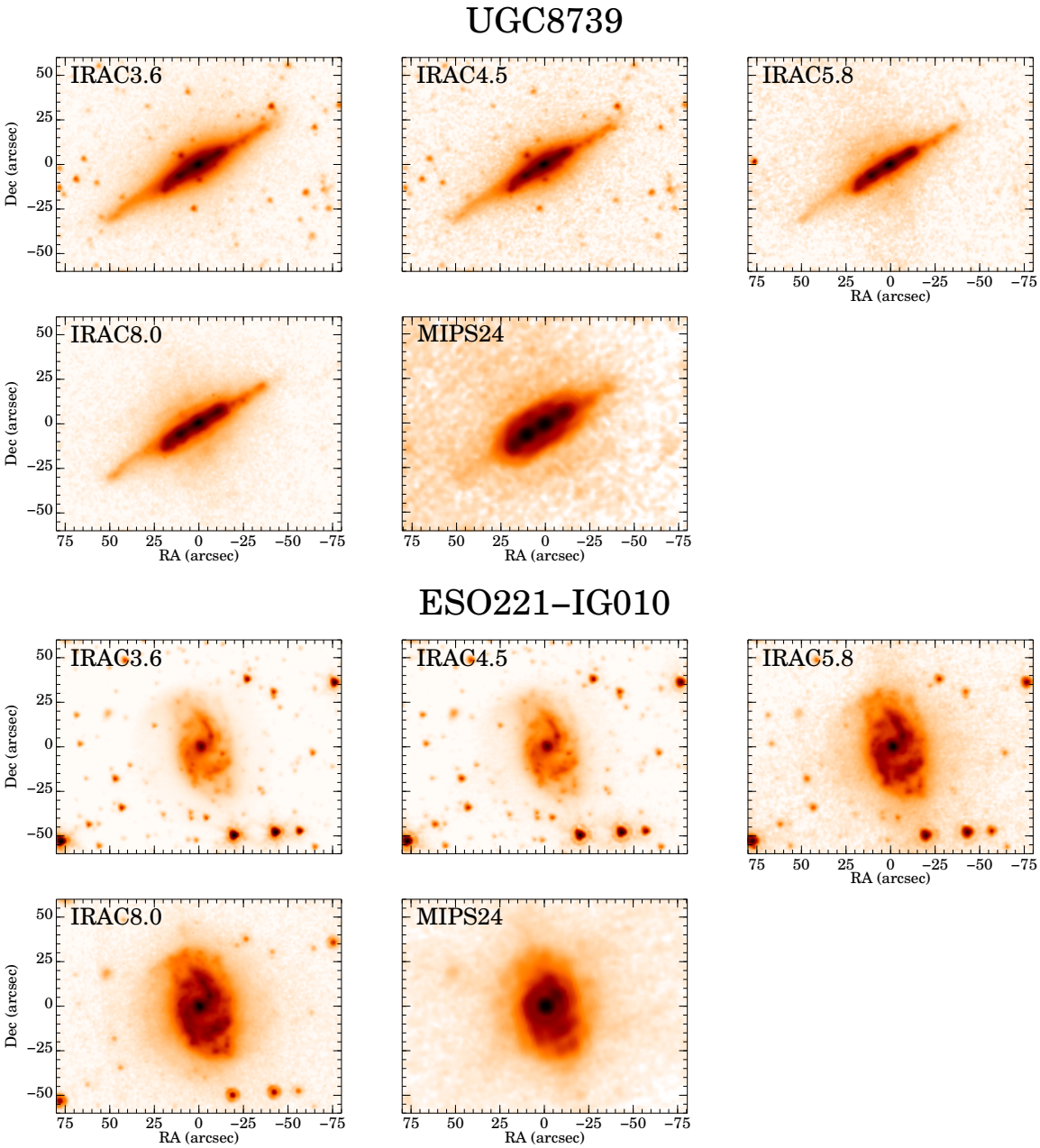

Figure 2.15: *Continued.*

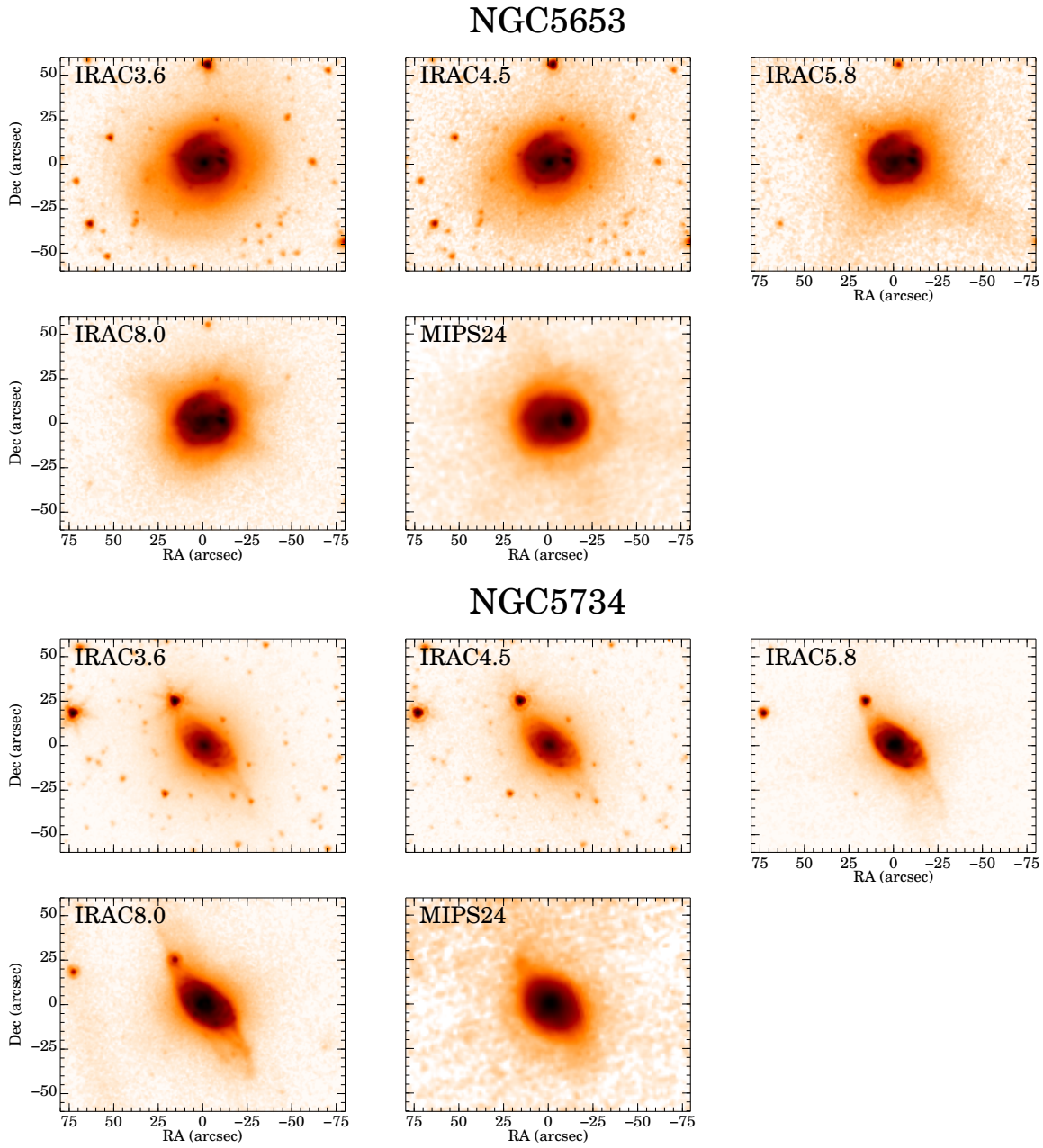

Figure 2.15: *Continued.*

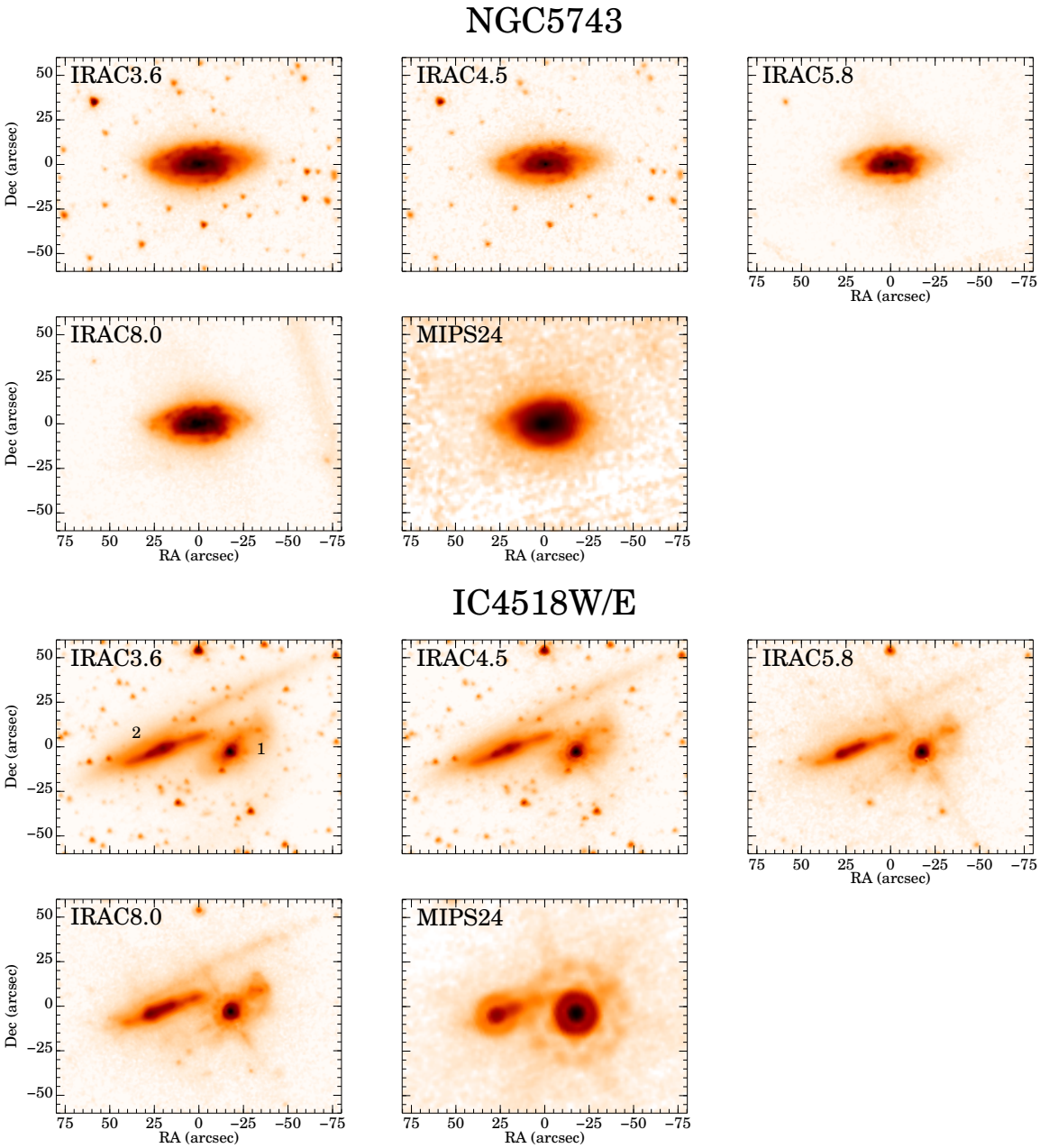

Figure 2.15: *Continued.*

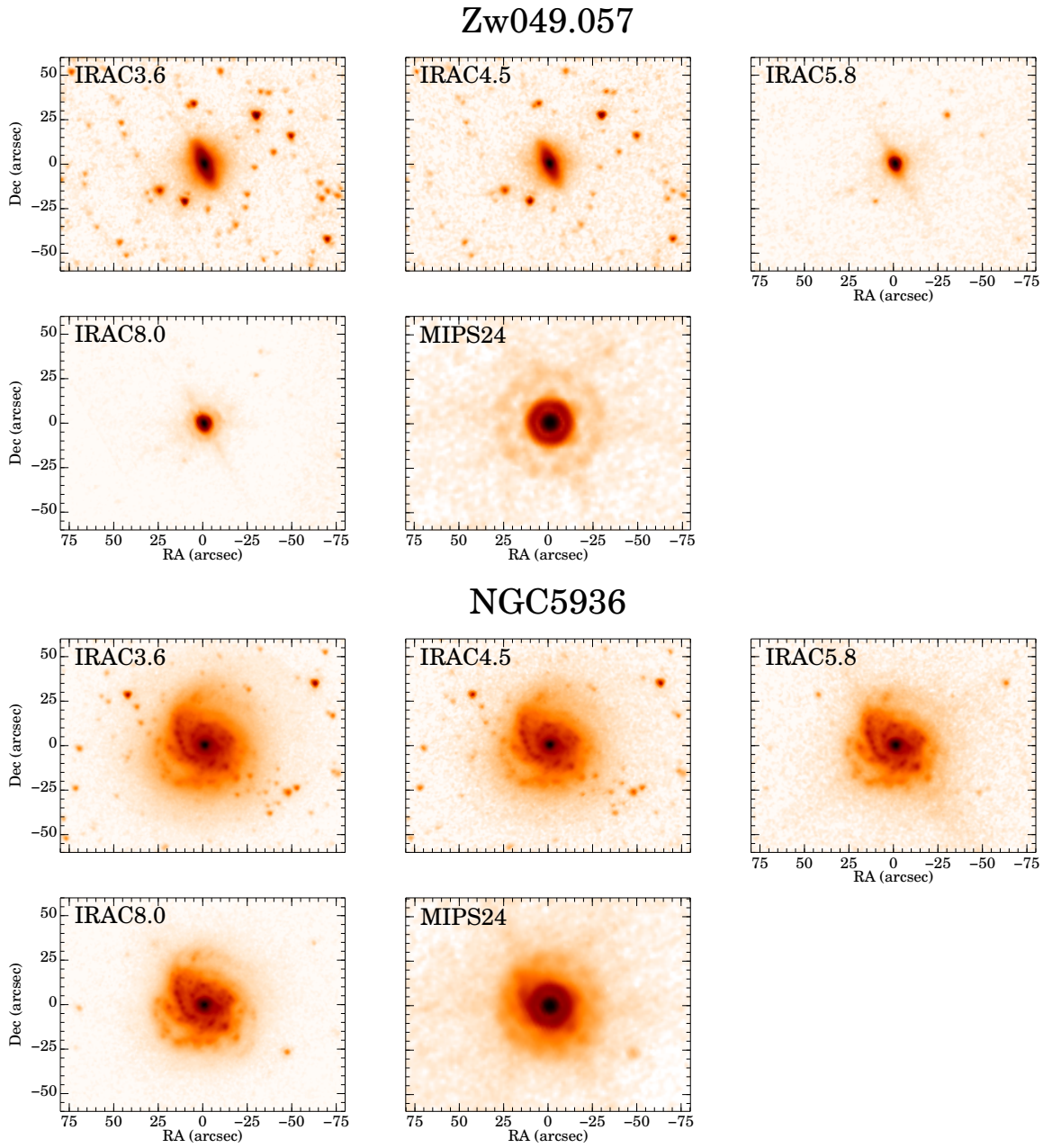

Figure 2.15: *Continued.*

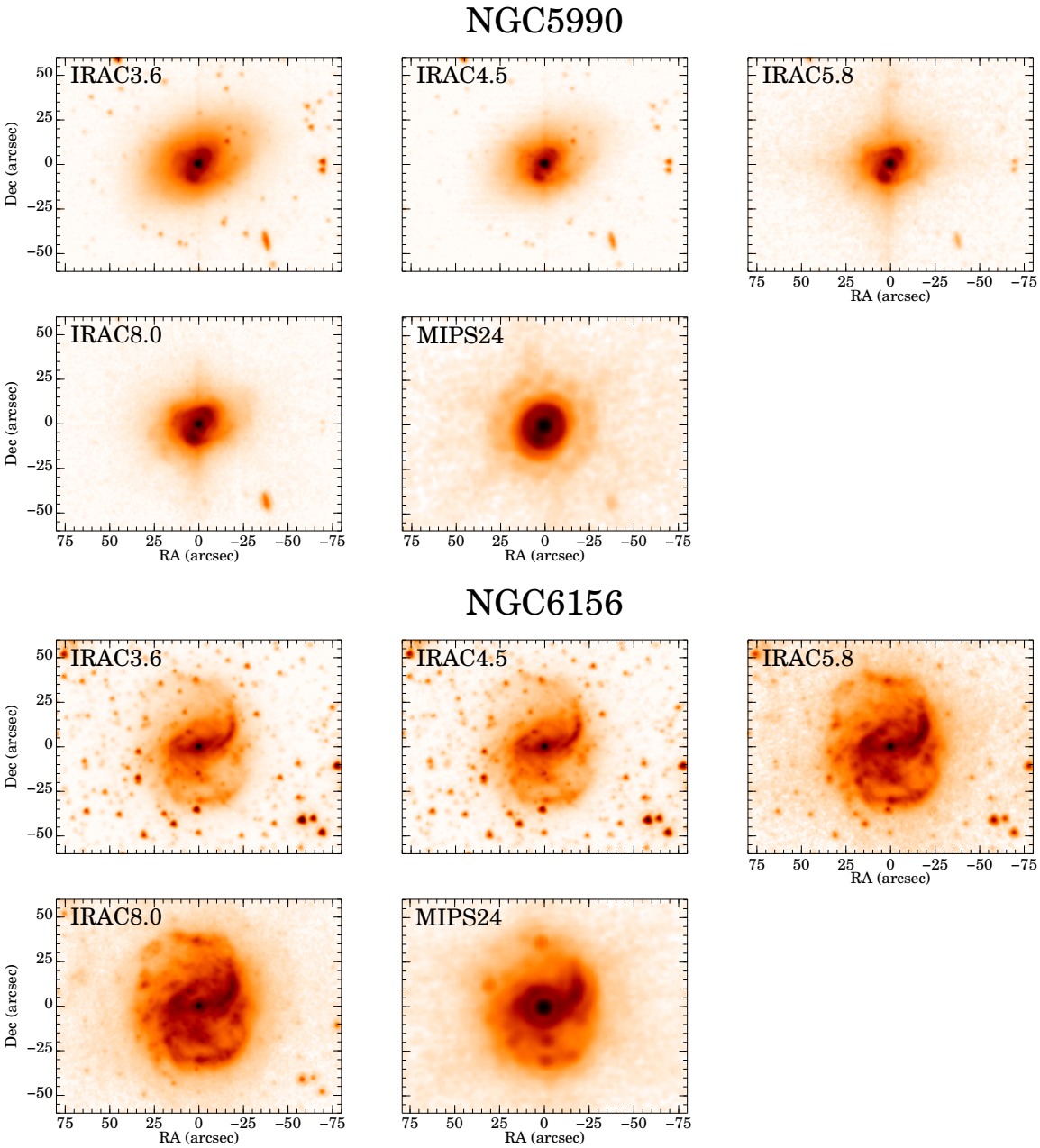

Figure 2.15: *Continued.*

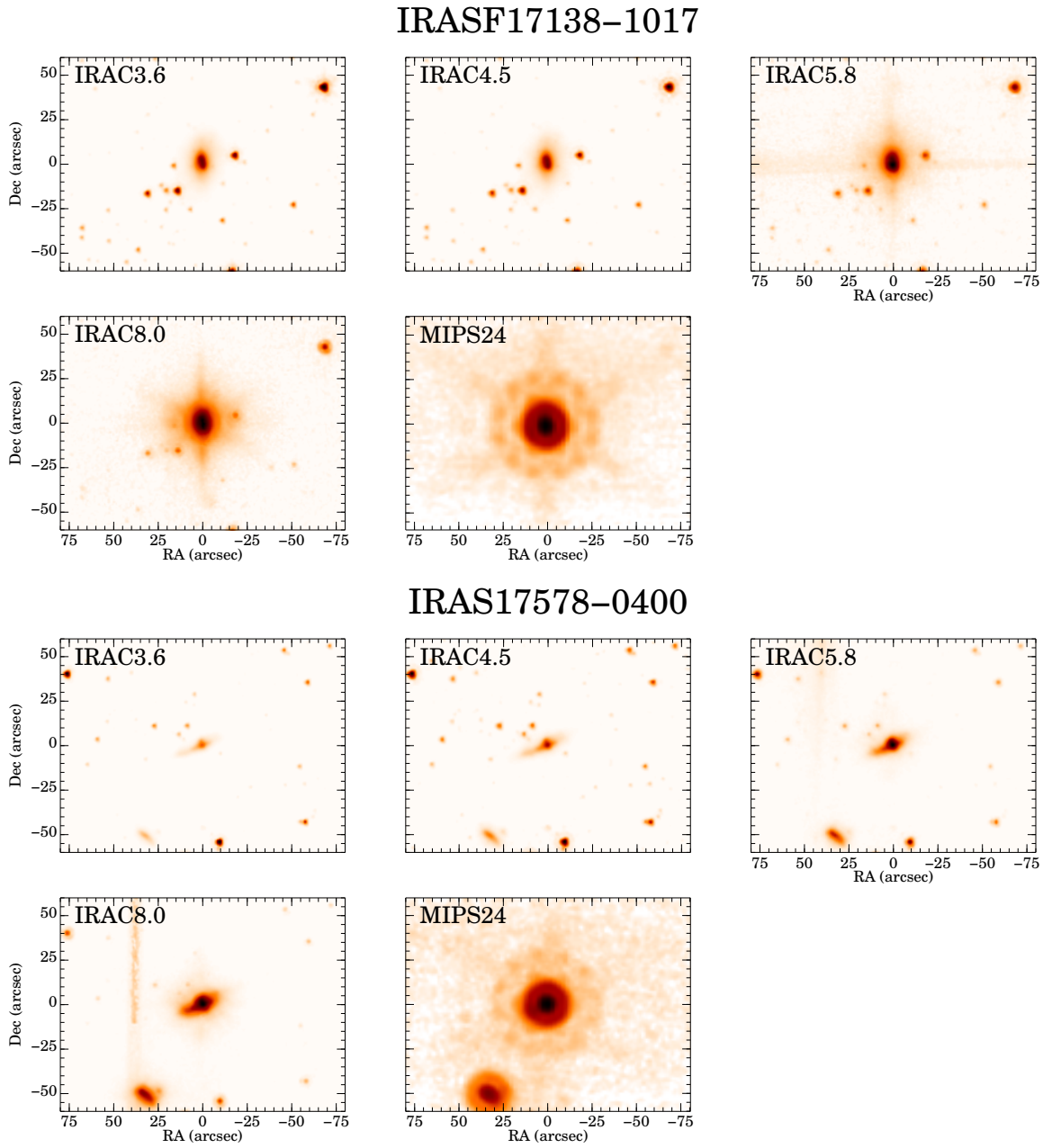

Figure 2.15: *Continued.*

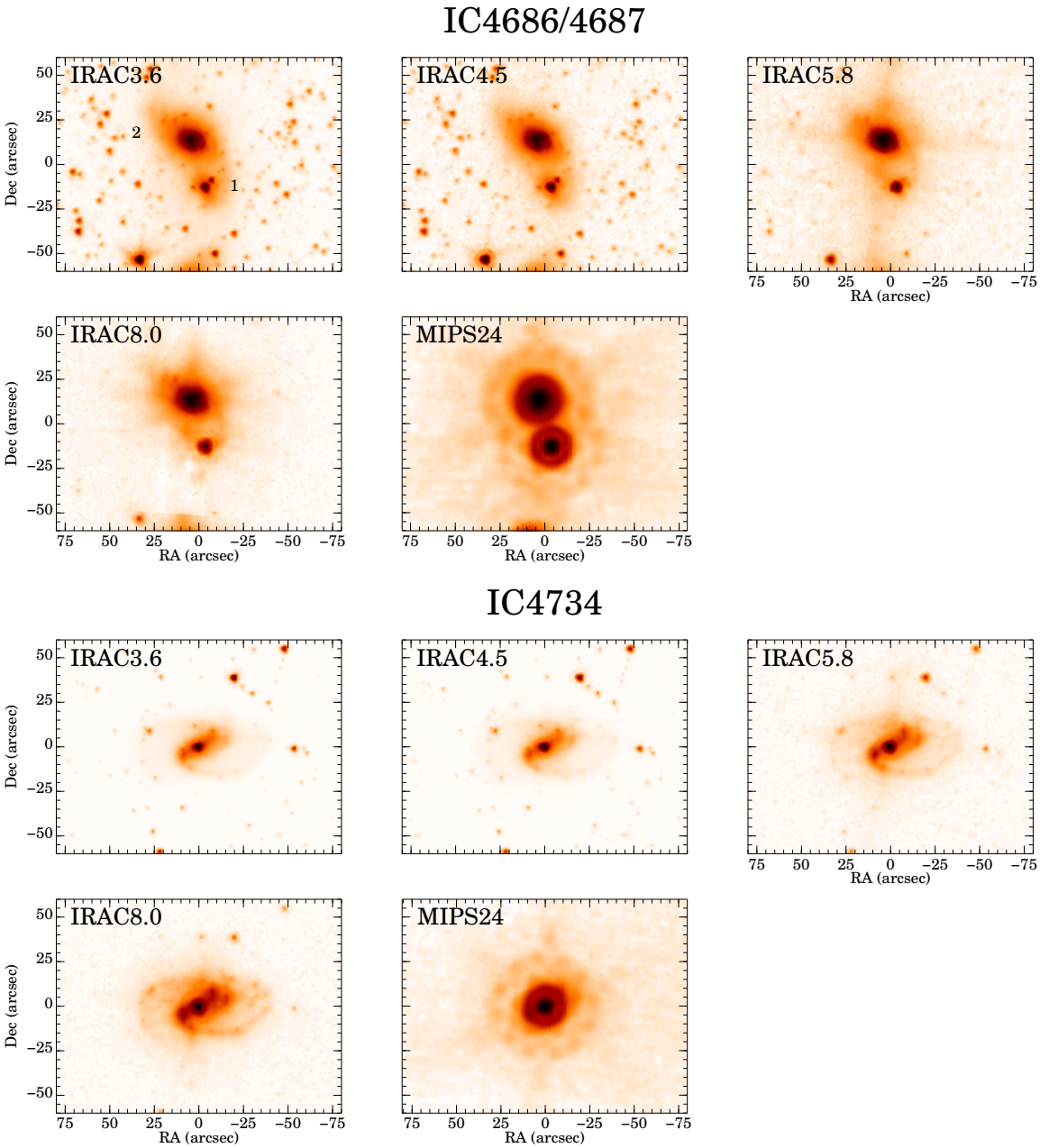

Figure 2.15: *Continued.*

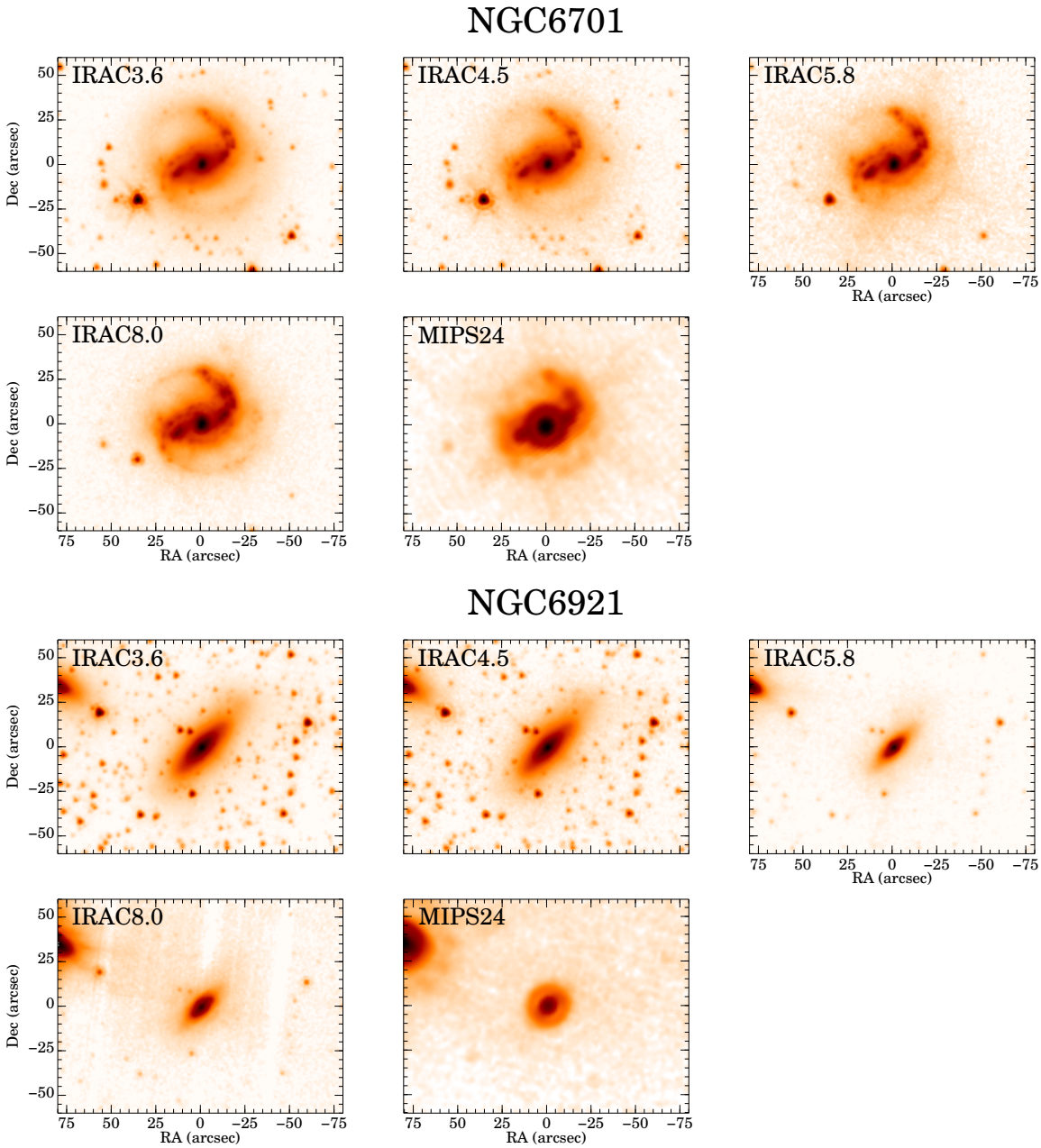

Figure 2.15: *Continued.*

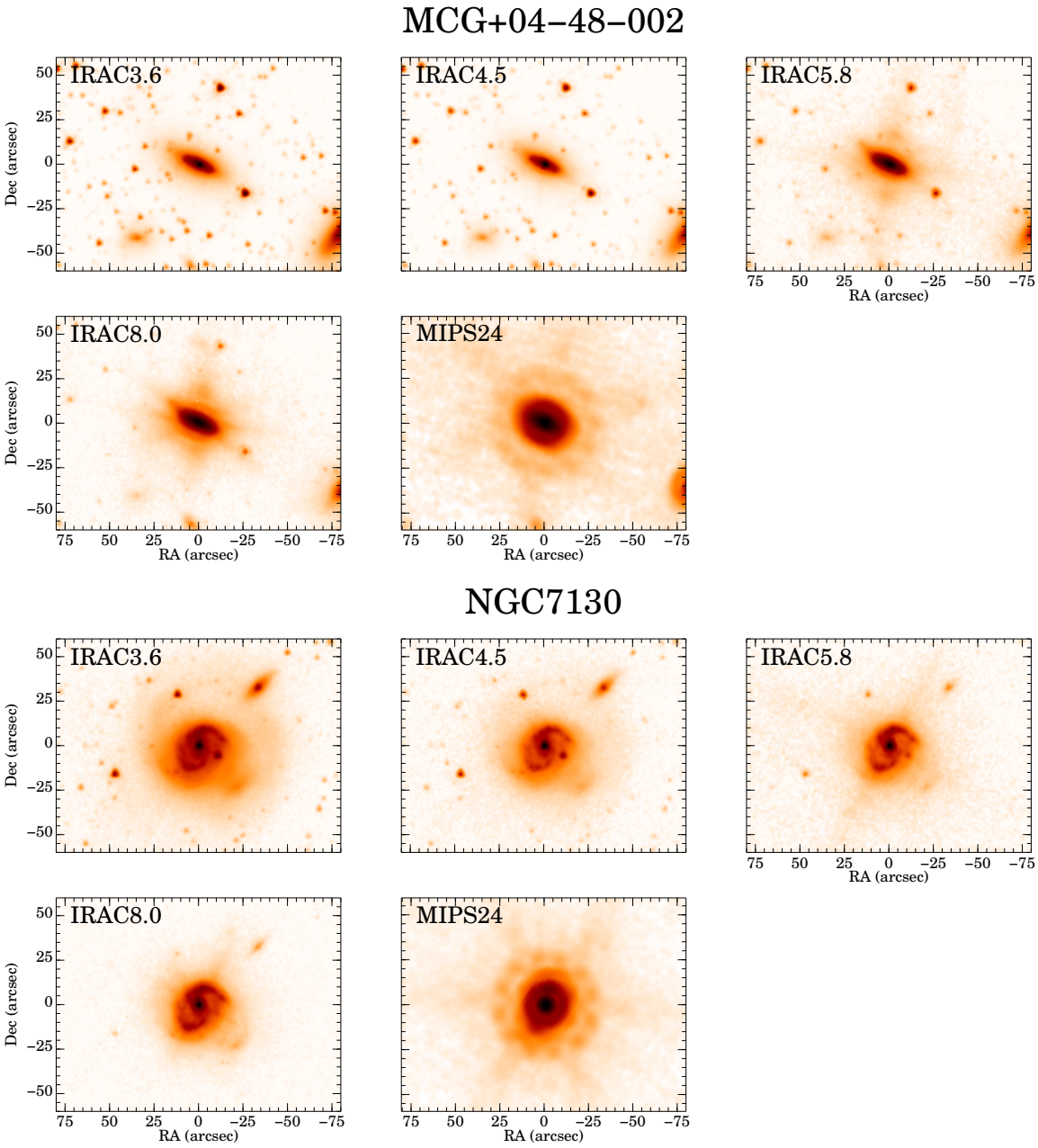

Figure 2.15: *Continued.*

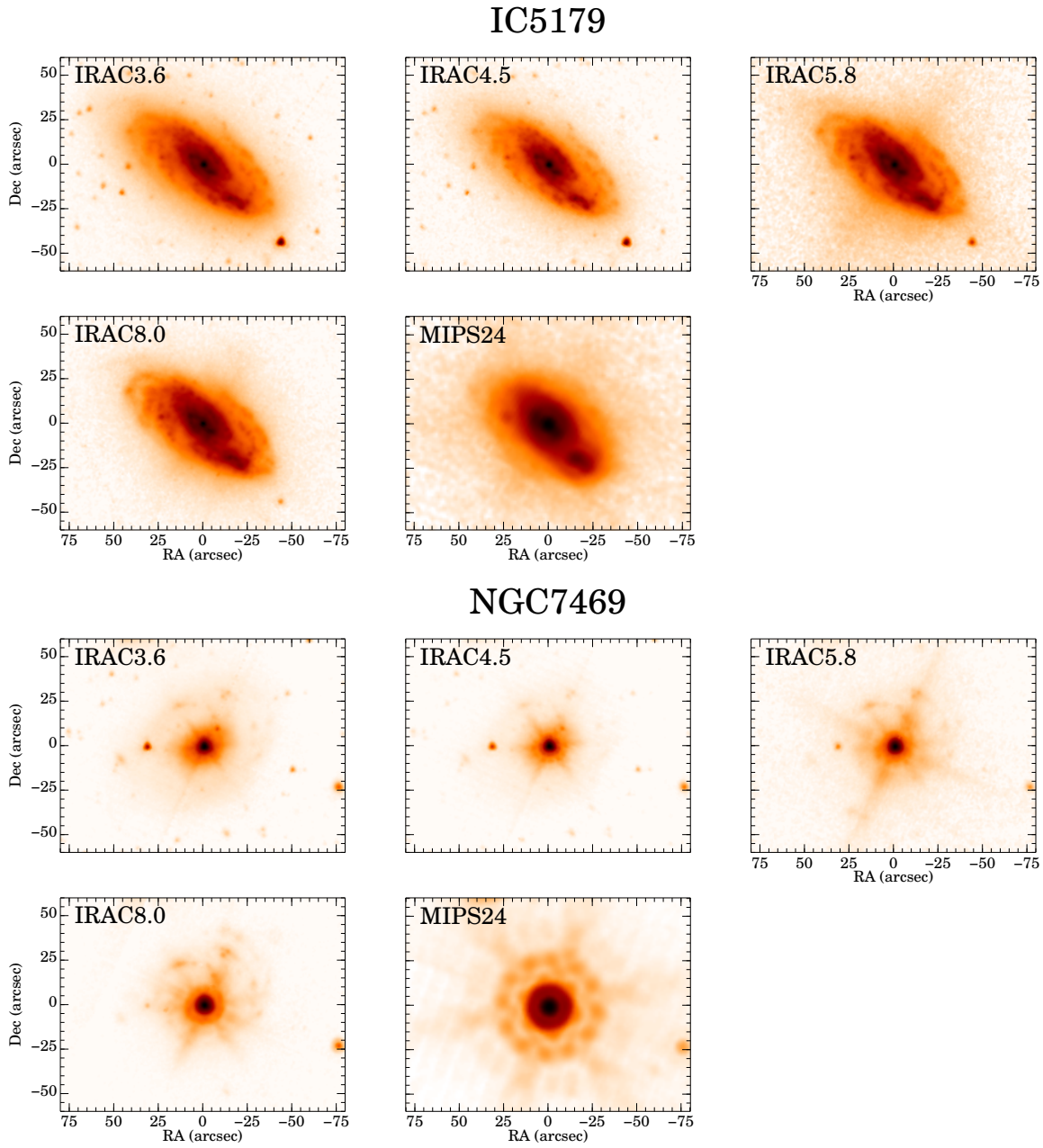

Figure 2.15: *Continued.*

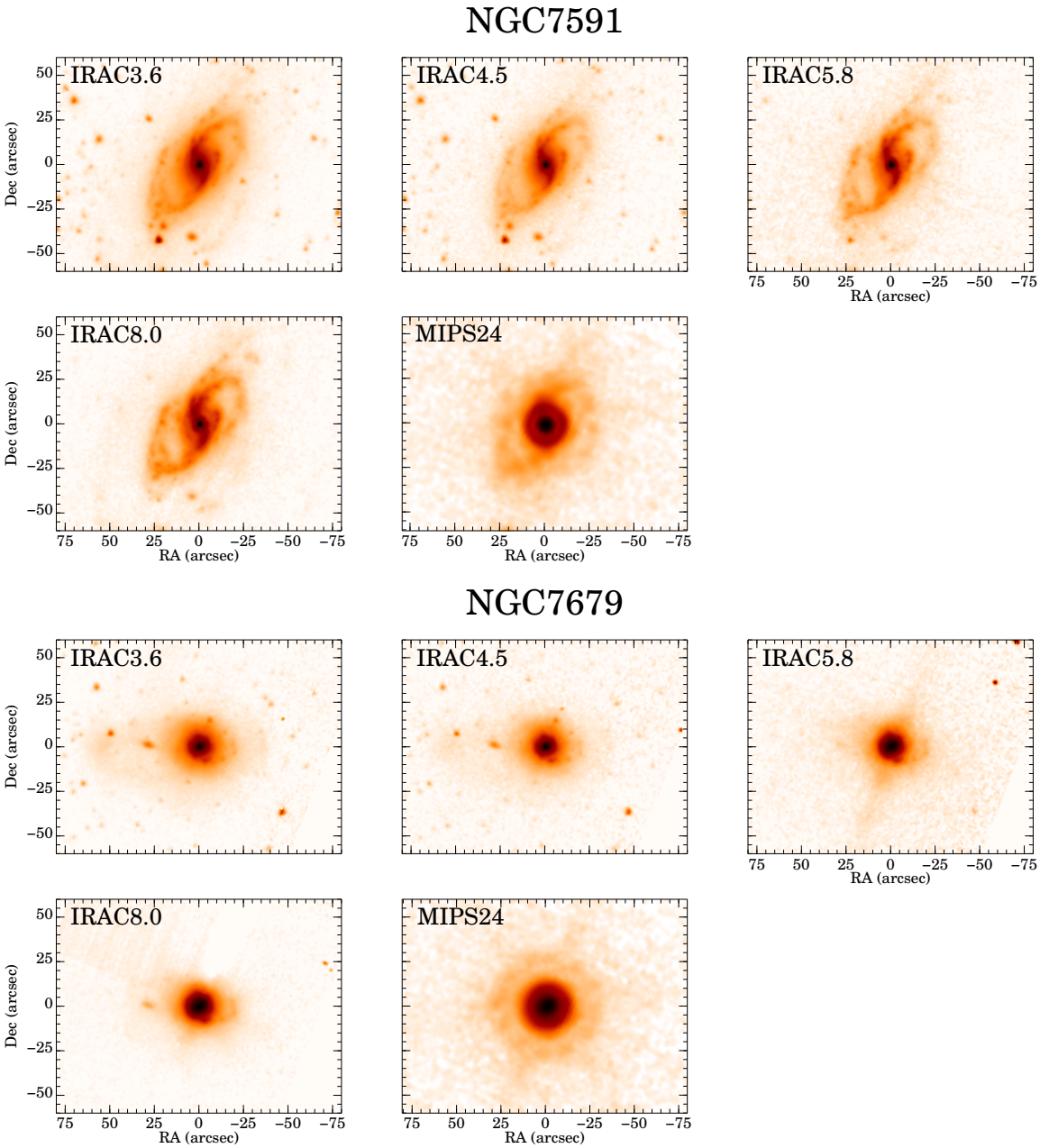

Figure 2.15: *Continued.*

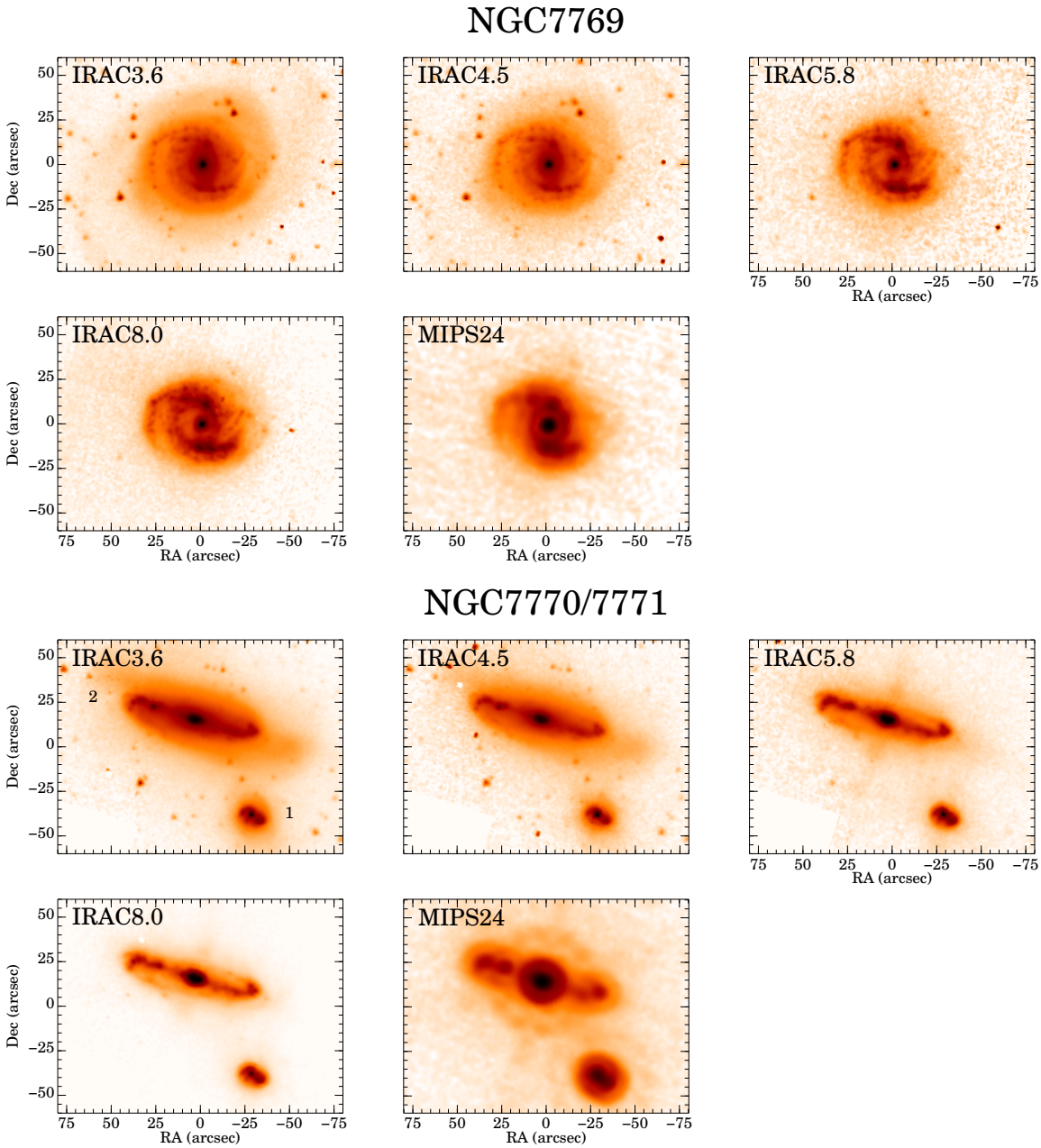

Figure 2.15: *Continued.*

Chapter 3

The Mid-IR High-ionization Lines from AGN and SF

We compiled Spitzer/Infrared Spectrograph spectroscopic data of 426 galaxies including quasars, Seyferts, LINERs and H II galaxies to investigate the relationship among the mid-IR emission lines. There is a tight linear correlation between the [Ne V]14.3 μm and 24.3 μm (97.1 eV) and the [O IV]25.9 μm (54.9 eV) high-ionization emission lines. The correlation also holds for these high-ionization emission lines and the [Ne III] 15.56 μm (41 eV) emission line, although only for active galaxies. We used these correlations to calculate the [Ne III] excess due to star formation in Seyfert galaxies. We also estimated the [O IV] luminosity due to star formation in active galaxies and determined that it dominates the [O IV] emission only if the contribution of the active nucleus to the total luminosity is below 5 %. We find that the active galactic nucleus dominates the [O IV] emission in most Seyfert galaxies, whereas star-formation adequately explains the observed [O IV] emission in optically classified H II galaxies. Finally we computed photoionization models to determine the physical conditions of the narrow line region where these high-ionization lines originate. The estimated ionization parameter range is –2.8 < log U < –2.5 and the total hydrogen column density range is 20 < log $n_{\rm H}$ (cm^{-2}) < 21.

3.1 Introduction

Primarily through measurements in the optical, AGNs have been categorized as Type 1 or 2, respectively with and without very broad emission lines. The unification model (Antonucci 1993; Urry & Padovani 1995) successfully explains this behavior in terms of a dusty circumnuclear torus that hides the broad-line region (BLR) from our line of sight for Type 2 AGN. It also appears that extinction in the host galaxy can hide the BLR (e.g., Maiolino & Rieke 1995; Alonso-Herrero et al. 2003) in some active

galaxies. Extinction therefore affects the optical properties of AGN in fundamental ways. These effects can be minimized by studying these objects using IR emission lines, both to test the predictions of the unification model and to characterize AGNs in a uniform way. Toward this end, we have used mid-IR observations with IRS on *Spitzer* to examine the behavior of a large sample of AGN.

Important high-ionization lines accessible in the mid-IR include [Ne V] (97.1 eV) at 14.32 and 24.32 μm, [O IV] (54.9 eV) at 25.89 μm, and [Ne III] (41 eV) at 15.56 μm. Because of their very high ionization potential, the [Ne V] lines are considered to be reliable signposts for an AGN (Genzel et al. 1998; Armus et al. 2007). These lines have been used to estimate the accretion power in the local universe (Tommasin et al. 2010) and to identify low-luminosity AGNs in local galaxies (Satyapal et al. 2008; Goulding & Alexander 2009). However, they are also produced in SNR (Oliva et al. 1999; Smith et al. 2009), PN (Pottasch et al. 2009), and W-R stars (Schaerer & Stasińska 1999). Although the [Ne V] luminosities of these objects are low, $\sim 10^{34}$ erg s^{-1} (Smith et al. 2009; Pottasch et al. 2009), several thousands of them might also produce detectable [Ne V] emission.

Despite the lower ionization potential of [O IV], the 25.89 μm emission line appears to be an accurate indicator of AGN power, since it correlates well with the hard (> 14 keV) X-ray luminosity (Meléndez et al. 2008a; Rigby et al. 2009; Diamond-Stanic et al. 2009) and the mid-IR [Ne V] emission lines (Dudik et al. 2009; Weaver et al. 2010). However, this line also appears in the spectra of starburst galaxies with no other evidence for AGN (Lutz et al. 1998a; Bernard-Salas et al. 2009), where it is attributed to Wolf–Rayet stars (Crowther et al. 1999; Schaerer & Stasińska 1999) and/or to shocks (Allen et al. 2008; Lutz et al. 1998a).

The [Ne III] 15.56 μm line is excited by young, massive stars (Verma et al. 2003; Brandl et al. 2006; Beirão et al. 2006, 2008; Ho & Keto 2007; Bernard-Salas et al. 2009; Alonso-Herrero et al. 2009b; Pereira-Santaella et al. 2010a). Nonetheless, it seems to be a reasonably good proxy for AGN luminosity, at least for reasonably high luminosities (Gorjian et al. 2007; Dudik et al. 2009; Meléndez et al. 2008a; Tommasin et al. 2008). Quantifying when its excitation is dominated by an active nucleus would allow it to be used in concert with the other high-ionization lines to probe conditions in the neighborhoods of AGNs.

In this chapter we present a statistical study of the behavior of these lines in a sample of 426 galaxies. The data are compiled from the literature on high spectral resolution ($R \sim 600$) IRS measurements, as well as our own new measurements of low-luminosity Seyfert galaxies and LIRGs.

Table 3.1: Summary of the Sample

Type	N	[Ne V]14.3 μm	[Ne V]24.3 μm	[O IV]
QSO	28	22	16	25
Seyfert 1	76	59	42	63
Seyfert 2	125	89	69	101
LINER	55	10	6	27
H II/starburst	110	4	2	59
Unknown	32	2	1	7
Total	426	186	136	282

Notes. N is the number of galaxies of each type. For each type we give the number of detections of the [Ne V] 14.32 μm, [Ne V] 24.32 μm and [O IV] 25.89 μm emission lines.

3.2 The Sample

The sample contains 426 galaxies (Table 3.5) for which high spectral resolution ($R \sim 600$) *Spitzer*/IRS spectra were available, either in the literature (Weedman et al. 2005; Ogle et al. 2006; Farrah et al. 2007; Gorjian et al. 2007; Tommasin et al. 2008, 2010; Veilleux et al. 2009; Dale et al. 2009; Bernard-Salas et al. 2009; Goulding & Alexander 2009; Alonso-Herrero et al. 2011), in the *Spitzer* archive or observed through the programs 40936 and 50597 (PI: G. H. Rieke). AGN type classifications were taken from NASA Extragalactic Database (NED). We designated only pure cases as Type 2 and included within Type 1 all intermediate cases (i.e., 1.2, 1.5, 1.8, 1.9) based on observations and modeling of the nuclear spectra energy distributions (Alonso-Herrero et al. 2003; Ramos Almeida et al. 2009). We could not find the nuclear activity classification for 32 of the galaxies. The sample includes 28 QSOs, 76 Seyfert 1, 125 Seyfert 2, 55 LINERs and 110 H II or starburst galaxies (see Table 3.1). The luminosity of the active galaxies ranges from QSO (QUEST sample, Veilleux et al. 2009) to typical Seyfert galaxies (12 μm sample, Rush et al. 1993; Tommasin et al. 2010), relatively low-luminosity Seyferts (RSA sample, Maiolino & Rieke 1995; Ho et al. 1997; Diamond-Stanic et al. 2009) and LINERs (Sturm et al. 2006). According to their IR luminosities 71 sample members are classified as local LIRGs and 54 as ULIRGs. We note that the majority of LIRGs in the sample described in Chapter 2 are included here. We found in the RBGS catalog (Sanders et al. 2003; Surace et al. 2004) the *IRAS* fluxes for 196 of our galaxies which we used to calculate their $L_{\rm IR}$ as defined in Sanders & Mirabel (1996).

Note that the LINER group includes very different galaxies. IR-bright LINERs

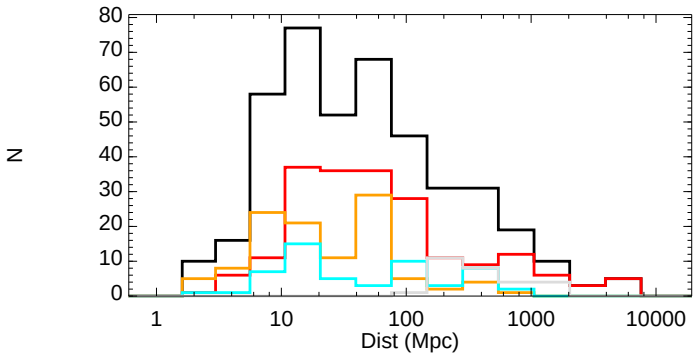

Figure 3.1: Distribution of the galaxy distances of the complete sample (black), QSO (gray), Seyfert 1 and 2 galaxies (red), LINERs (blue) and H II galaxies (orange).

($L_{\rm IR}/L_{\rm B} \gtrsim 1$) have infrared SEDs similar to starbursts, although high-ionization lines and hard X-ray cores are detected in some, suggesting the presence of an AGN. In comparison, IR-faint LINERs ($L_{\rm IR}/L_{\rm B} \lesssim 1$) seem to be powered by an AGN (Sturm et al. 2006; Satyapal et al. 2004).

Figure 3.1 shows the distance distribution of the sample. The median distance is 60 Mpc and most (68 %) of the galaxies are between 15 and 400 Mpc.

3.3 Measurements

In addition to results from the literature, we utilized the measurements for the 88 galaxies of the RSA sample observed with the IRS high spectral resolution modules. These data were reduced as described in Chapter 2.

We used a Gaussian profile to fit the emission lines in the spectra. For nine galaxies (NGC 777, NGC 3254, NGC 3486, NGC 3941, NGC 4138, NGC 4378, NGC 4472, NGC 4698, and NGC 5631) we were not able to measure any spectral feature due to the low S/N ratio of the spectra. They are not listed in Table 3.5 nor included in the analyzed sample.

Table 3.1 includes the number of detections of the [Ne V] 14.32 μm, [Ne V] 24.32 μm and [O IV] 25.89 μm emission lines and in Table 3.2 we show the observed median line ratios for each galaxy type both for galaxies from the literature and those analyzed by us. Note that there are four detections of the [Ne V] 14.32 μm line and two of the [Ne V] 24.32 μm line in galaxies classified as H II. For these galaxies (NGC 613, NGC 1792, NGC 3621, and NGC 5734) the detection of the [Ne V] lines is the only evidence of AGN activity. We decided to keep their H II classification because: (1) the AGN may be extremely obscured or of very low luminosity and, thus, the nuclear spectra might

Table 3.2: Median Line Ratios

	Median Ratio				
Ratio	QSO	Sy1	Sy2	LINER	H II
[O IV] 25.89 μm/[Ne V] 24.32 μm	3.3±1.2*	3.6±0.6	3.5±0.6	3.7±1.0*	4.1±1.3*
[O IV] 25.89 μm/[Ne V] 14.32 μm	3.6±0.9	3.5±1.0	3.5±1.3	4.8±2.0*	4.4±2.0*
[Ne V] 24.32 μm/[Ne V] 14.32 μm	1.0±0.3*	1.1±0.3	1.0±0.3	1.3±0.3*	4.7±4.1*
[Ne III] 15.56 μm/[Ne V] 14.32 μm	1.7±0.5	1.9±0.6	2.0±0.7	5.3±3.7*	6.8±1.7*
[Ne II] 12.81 μm/[Ne V] 14.32 μm	0.7±0.4	1.6±0.7	2.0±1.1	28±14*	57±42*
[Ne III] 15.56 μm/[O IV] 25.89 μm	0.5±0.2	0.6±0.2	0.9±0.4	2.3±1.1	4.2±2.4
[Ne II] 12.81 μm/[O IV] 25.89 μm	0.2±0.1	0.5±0.3	1.1±0.9	6±2	22±16
[Ne III] 15.56 μm/[Ne II] 12.81 μm	2.0±1.0	1.2±0.6	0.8±0.4	0.3±0.2	0.17±0.07

Notes. Median ratios and uncertainties for each type of galaxies. The uncertainty is calculated as the median absolute deviation (should be multiplied by 1.48 to obtain the standard deviation).
$^{(\star)}$ These values are calculated with less than 20 galaxies.

be dominated by star formation features; and (2) these lines are also detected in SNR, PN and W-R stars which could be the origin of the [Ne V] emission in these galaxies.

Table 3.2 gives the median and deviation of all the line ratios we discuss in this Chapter for each type of galaxy. The line fluxes for all the galaxies are listed in Table 3.5.

3.4 The Mid-IR High-Ionization Emission Lines

3.4.1 The [O IV] versus [Ne V] correlations

The [Ne V] 24.32 μm and the [O IV] 25.89 μm emission lines are commonly detected in active galaxies (Lutz et al. 1998b; Genzel et al. 1998; Tommasin et al. 2010). The detection of the former is considered a good indicator of AGN activity because of its high ionization potential. However using the [O IV] 25.89 μm line as an AGN tracer is not as straightforward. For optically classified Seyfert galaxies the [O IV] 25.89 μm luminosity is a good proxy for the AGN intrinsic luminosity (Diamond-Stanic et al. 2009; Meléndez et al. 2008a) and there is a good correlation between the [Ne V] 24.32 μm and the [O IV] 25.89 μm emission in AGNs (Dudik et al. 2009; Weaver et al. 2010). However, the [O IV] 25.89 μm line is also produced by W-R stars (Schaerer & Stasińska 1999) and is observed in starburst galaxies with no other evidence for the presence of an AGN (Lutz et al. 1998a; Bernard-Salas et al. 2009).

The left panel of Figure 3.2 shows the tight correlation between the [Ne V] 24.32 μm and [O IV] 25.89 μm lines spanning at least five orders of magnitude in luminosity ($38 < \log L_{[\mathrm{O\ IV}]}\,(\mathrm{erg\,s^{-1}}) < 43$). We do not find any dependence between the optical classification of the nuclear activity and this correlation. This implies that the ionization parameter is similar in type 1 and 2 Seyfert galaxies (see Section 3.7). The slope of the best fit to the luminosity data is 0.96±0.02 with a 0.14 dex dispersion. It is reasonable to assume a linear correlation between these two emission lines, and this yields a ratio [O IV] 25.89 μm/[Ne V] 24.32 μm = 3.5, with an rms scatter of 0.8.

The [Ne V] 24.32 μm line is detected in ∼50 % of the optically classified Seyfert galaxies (see Table 3.1). However, for a considerable number of galaxies we have the [O IV] 25.89 μm measurement and an upper limit for the [Ne V] 24.32 μm flux. We plot these fluxes and upper limits (middle panel of Figure 3.2) for all the galaxies. The upper limits to the [Ne V] 24.32 μm flux are compatible with the correlation for most of the Seyfert galaxies. However, the [O IV] 25.89 μm line is detected in more than 50 % of the H II galaxies in our sample. In 90% of these galaxies, the sensitivity of the [Ne V] 24.32 μm measurement (or upper limits) is inadequate to probe whether the [O IV] emission is associated with a hidden AGN.

In short, we find that the [O IV] 25.89 μm luminosity is well correlated with the intrinsic AGN luminosity (i.e., [Ne V] luminosity) for Seyfert galaxies and quasars with $L_{[\mathrm{O\ IV}]} > 10^{39}\,\mathrm{erg\,s^{-1}}$ to, at least, $L_{[\mathrm{O\ IV}]} \sim 10^{43}\,\mathrm{erg\,s^{-1}}$. For lower luminosities the fraction of the [O IV] 25.89 μm emission produced by star formation may be considerable. Thus the [O IV] 25.89 μm may not be an accurate tracer of the AGN luminosity for galaxies with $L_{[\mathrm{O\ IV}]} < 10^{39}\,\mathrm{erg\,s^{-1}}$(Goulding & Alexander 2009).

The linear correlation also holds for the [Ne V] 14.32 μm and the [O IV] 25.89 μm luminosities (Figure 3.3), although the dispersion is larger ([O IV] 25.89 μm/[Ne V] 14.32 μm = 3.4, with an rms scatter of 1.4 assuming a linear fit).

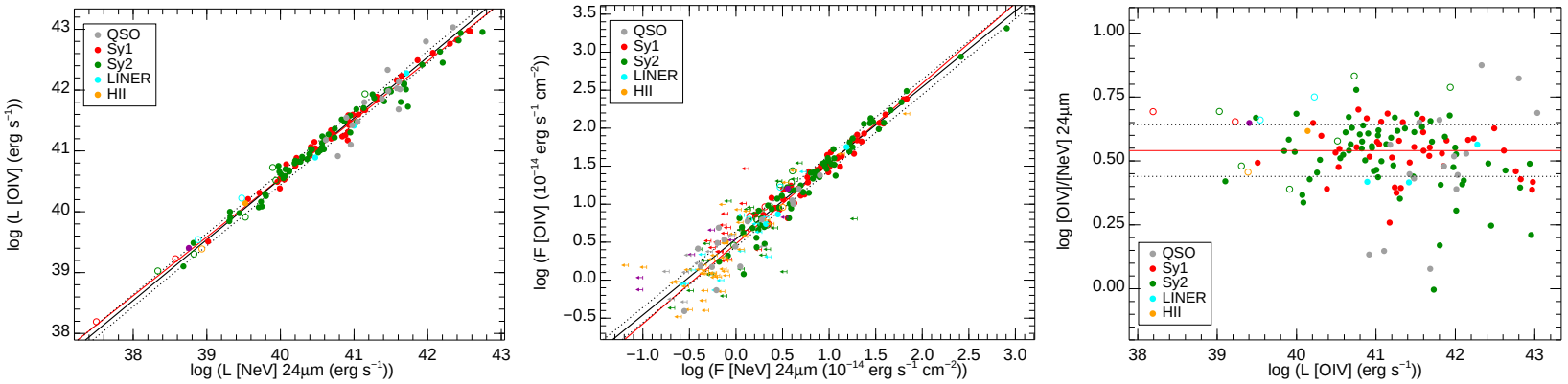

Figure 3.2: Relationship between the [O IV] 25.89 μm and [Ne V] 24.32 μm luminosities (left) and fluxes (middle). The red line is the best fit and the black line the best linear fit. The dashed lines mark the 1σ deviation. QSO are plotted as gray circles, Sy1 as red circles, Sy2 as green circles, LINERs as blue circles, H II galaxies as orange circles and those galaxies without a classification as purple circles. The open symbols mark the galaxies with star formation which may contribute to the [O IV] 25.89 μm emission (see Section 3.4.2 and the right panel of Figure 3.4). The right panel shows the [O IV] 25.89 μm/[Ne V] 24.32 μm ratio vs. the [O IV] 25.89 μm luminosity. The solid red line is the ratio obtained from the linear fit and the dashed lines mark the 1σ deviation.

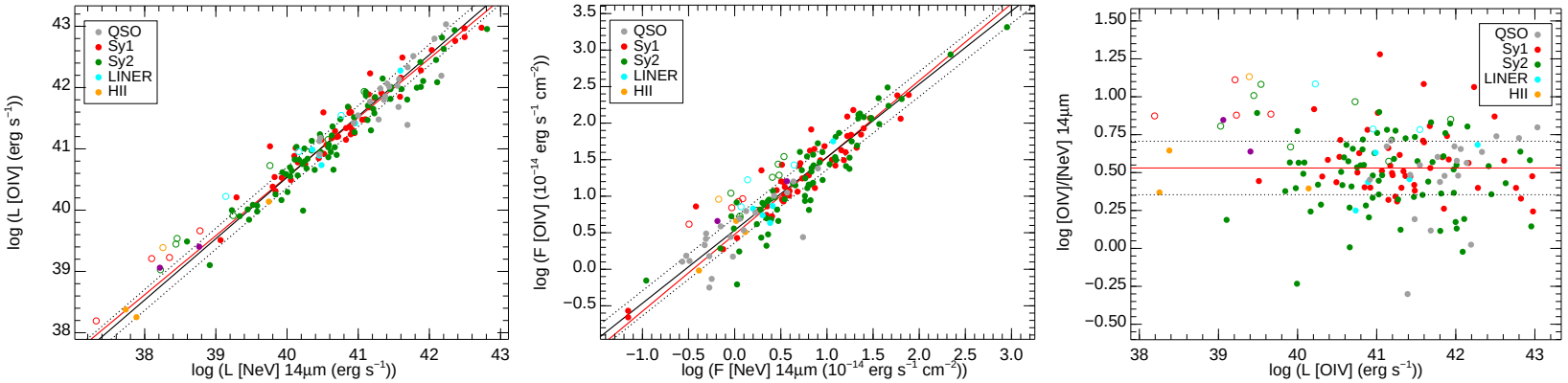

Figure 3.3: Relationship between the [O IV] 25.89 μm and [Ne V] 14.32 μm luminosities (left) and fluxes (middle). The right panel shows the [O IV] 25.89 μm/[Ne V] 14.32 μm ratio vs. the [O IV] 25.89 μm luminosity. Symbols are as in Figure 3.2.

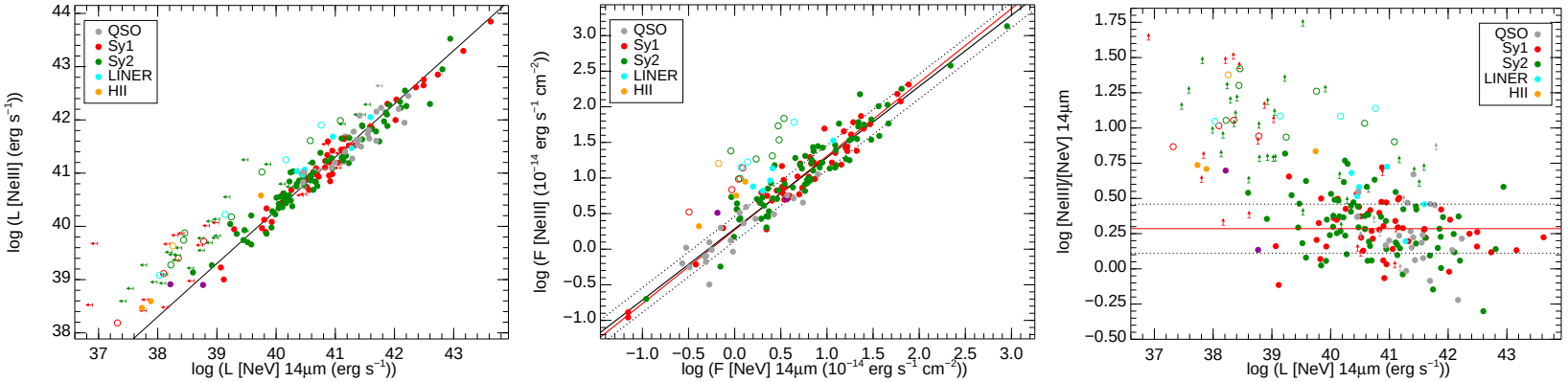

Figure 3.4: Relation between the [Ne III] 15.56 μm and [Ne V] 14.32 μm emission. Galaxy symbols are as in Figure 3.2. The open symbols mark those galaxies above 3σ the [Ne V] 14.32 μm vs. [Ne III] 15.56 μm flux correlation. The black line in the left panel is the ratio obtained from the flux correlation. In the left panel only are included the [Ne V] 24.32 μm upper limits of the QSO and Seyfert galaxies.

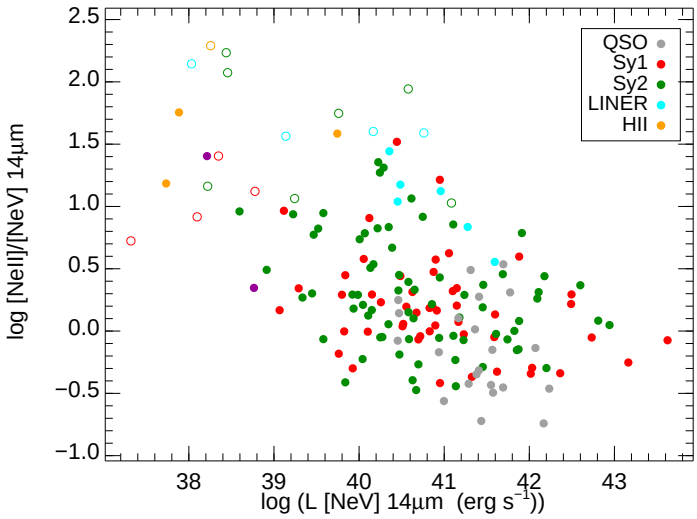

Figure 3.5: [Ne II] 12.81 μm/[Ne V] 14.32 μm ratio vs. [Ne V] 14.32 μm luminosity. Symbols are as in Figure 3.4.

3.4.2 The [Ne III] and [Ne II] emission lines

Due to the intermediate ionization potential of Ne^{+2} (41.0 eV), the [Ne III] 15.56 μm emission line may be produced by young stars or by AGNs. This line is observed in star forming galaxies (Verma et al. 2003; Brandl et al. 2006; Beirão et al. 2006, 2008; Ho & Keto 2007; Bernard-Salas et al. 2009; Dale et al. 2009; Pereira-Santaella et al. 2010a), and it is also correlated with the AGN intrinsic luminosity (Gorjian et al. 2007; Deo et al. 2007; Tommasin et al. 2008; Meléndez et al. 2008b).

The middle panel of Figure 3.4 shows the relation between the observed flux of the [Ne III] 15.56 μm and [Ne V] 14.32 μm emission lines for our sample of AGNs and for the 4 H II galaxies with [Ne V] detections. We compare these lines because they are close in wavelength and the effect of differential extinction is minimized. It is clear that some galaxies have an excess of [Ne III] 15.56 μm emission relative to that of the [Ne V] 14.32 μm, which we attribute to star formation (see Section 3.5). Therefore to obtain the fit to the data we use the outliers resistant linear fit algorithm provided by the IDL function ROBUST_LINEFIT. The slope of this fit is 1.02±0.02 with a scatter of about 0.2 dex around the fit. The result is consistent with a simple correlation; by fixing the slope to unity, we obtain the ratio [Ne III] 15.56 μm/[Ne V] 14.32 μm = 1.9, with rms scatter of 0.8. This correlation was previously reported by Gorjian et al. (2007), although they found a slight dependence of the ratio with the [Ne V] 14.32 μm luminosity (slope 0.89). Their sample included 53 X-ray selected AGNs with [Ne V] 14.32 μm luminosities between 10^{39} and 10^{43} erg s^{-1}. The larger number of galaxies in

our sample allows us to minimize the contribution of the galaxies contaminated by star formation to the fit and the luminosity dependence of the correlation is substantially reduced. Where the AGN clearly dominates, the points fall around the line determined for the whole sample by ROBUST_LINEFIT, thus supporting our interpretation that this fit determines the relationship for AGNs in general.

The [Ne II] 12.81 μm emission traces young (< 10 Myr) star formation (Roche et al. 1991; Thornley et al. 2000; Verma et al. 2003; Rigby & Rieke 2004; Snijders et al. 2007; Ho & Keto 2007; Díaz-Santos et al. 2010). The ionization potential of this emission line is 21 eV and thus it is mainly produced in H II regions. Figure 3.5 shows that the scatter in the [Ne II] 12.81 μm/[Ne V] 14.32 μm ratio (0.7 dex) is larger than that found in the other line ratios, for the lower AGN luminosities there is a large scatter. There is a weak trend of [Ne II] 12.81 μm/[Ne V] 14.32 μm ratios decreasing with increasing AGN luminosity. Assuming that there is an intrinsic ratio for AGN, this behavior implies that the AGN does not dominate the [Ne II] 12.81 μm output and that there is a wide range of star formation rates contributing to its luminosity. However, for the most luminous objects ($\log L_{[\mathrm{Ne\ V}]14\mu\mathrm{m}}$ (erg s^{-1}) > 41.5), the smaller scatter indicates that the relative contribution of the AGN to the total [Ne II] 12.81 μm excitation is higher.

Sturm et al. (2002) determined that the pure AGN [Ne V] 14.32 μm/[Ne II] 12.81 μm ratio is 1.1, but we find many Seyfert galaxies with higher ratios. In our sample the largest [Ne V] 14.32 μm/[Ne II] 12.81 μm ratio is $\sim$5.5, which is compatible with the largest ratio predicted by narrow line region (NLR) photoionization models (Groves et al. 2006, their Figure 11). With our data (Figure 3.5) we are not able to determine the pure AGN ratio, which also depends on the ionization parameter (Groves et al. 2006), but it is likely that it is between that found by Sturm et al. (2002) and the largest ratio in our sample.

The [O IV] 25.89 μm/[Ne II] 12.81 μm ratio can be used to separate AGNs from star-forming galaxies (Genzel et al. 1998; Sturm et al. 2002; Peeters et al. 2004b; Dale et al. 2009). We plot this ratio versus the [O IV] 25.89 μm luminosity in Figure 3.6. Most of the active galaxies have ratios larger than 0.35 whereas the ratios for H II galaxies are lower than 0.05 (Figure 5 of Dale et al. 2009). LINERs appear in the region between these ratios (Figure 3.6). A considerable number of H II galaxies also have [O IV] 25.89 μm/[Ne II] 12.81 μm ratios above 0.05. The [Ne V] lines are not detected for them although their upper limits are compatible with the [O IV] 25.89 μm versus [Ne V] correlations and thus a low-luminosity AGN could be the origin of the [O IV] 25.89 μm emission. The large scatter in the [O IV] 25.89 μm/[Ne II] 12.81 μm ratio, due to the different star formation rates in the AGNs, does not allow us to determine the

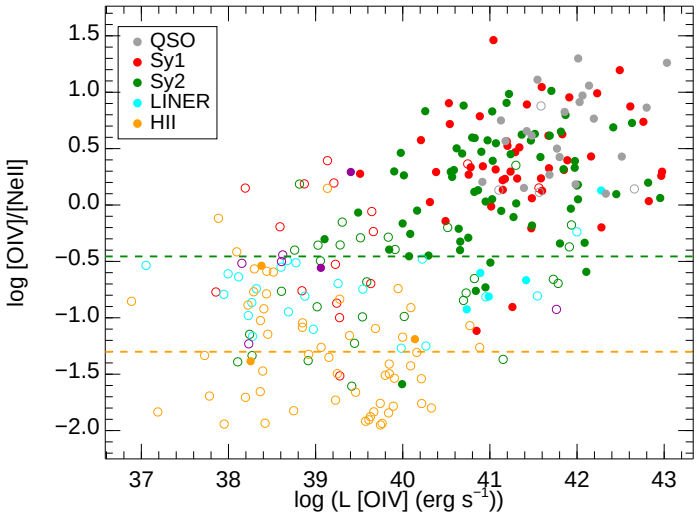

Figure 3.6: [O IV] 25.89 μm/[Ne II] 12.81 μm ratio vs. [O IV] 25.89 μm luminosity. Galaxy symbols are as in Figure 3.2. The dashed orange ([O IV]/[Ne II] = 0.05) and green ([O IV]/[Ne II] = 0.35) lines are the boundaries of the H II and Seyfert galaxies respectively.

value of the pure AGN ratio. The largest [O IV] 25.89 μm/[Ne II] 12.81 μm ratios that we find in AGNs are $\sim$10.

3.5 Star-formation Contributions to the Mid-IR High-Ionization Emission Lines

3.5.1 [O IV] Contamination by Star Formation

In Figures 3.2 and 3.3 there are few outliers above the [O IV] 25.89 μm versus [Ne V] correlations. Most of them are represented by open symbols, which indicate that their [Ne III] 15.56 μm/[Ne V] 14.32 μm ratios (see Section 3.5.2) are larger than those found in AGN dominated galaxies (QSO, Sy1 and Sy2). It is likely that the [O IV] 25.89 μm emission of these galaxies is contaminated by star formation. We now compare the [O IV] 25.89 μm emission of star forming regions and AGN. The [O IV] 25.89 μm/[Ne II] 12.81 μm ratio in star forming regions is < 0.05 (Section 3.4.2). Taking this upper limit and using the relation between the [Ne II] 12.81 μm luminosity and the total infrared (8–1000 μm) luminosity ($L_{\rm IR}$) from Ho & Keto (2007) we obtain the following relation for star-forming galaxies.

$$\log L_{[\rm O\ IV]}\ (\rm erg\ s^{-1}) < \log L_{\rm IR}\ (\rm erg\ s^{-1}) - 4.7 \pm 0.6 \qquad (3.1)$$

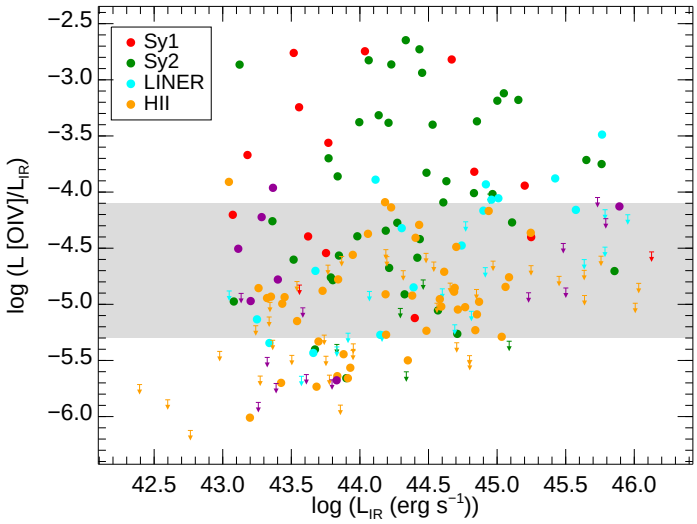

Figure 3.7: [O IV] 25.89 μm/$L_{\rm IR}$ ratio vs. $L_{\rm IR}$. Galaxy symbols are as in Figure 3.2. The shaded region is the upper limit to the [O IV] 25.89 μm/$L_{\rm IR}$ ratio of star-forming galaxies. Galaxies above this region need an AGN contribution to the [O IV] 25.89 μm emission in order to explain the observed ratio.

Rigby et al. (2009) calculated the ratio between the total AGN luminosity and the [O IV] 25.89 μm emission. We use the ratio for type 1 AGNs (∼2500) because the hard X-ray ($E > 10$ keV) emission used for the bolometric corrections may be affected by extinction in Seyfert 2s (Rigby et al. 2009).

$$\log L_{[\rm O\ IV]}\ ({\rm erg\ s^{-1}}) = \log L_{\rm AGN}\ ({\rm erg\ s^{-1}}) - 3.4 \pm 0.4 \qquad (3.2)$$

Then, combining both relations we find that the luminosity due to star formation, $L_{\rm IR}$, has to be at least 20 times brighter than the AGN luminosity (i.e., AGN contribution to the total luminosity below 5 %) for the star formation to dominate the [O IV] 25.89 μm emission.

We note that the number of H II galaxies falls rapidly above log $L_{[\rm O\ IV]}$ (erg s^{-1}) = 40.2 (see Figure 3.6). Assuming that star formation dominates the [O IV] 25.89 μm emission at this luminosity in these galaxies, the equivalent infrared luminosity ($L_{\rm IR}$) would be $2{\times}10^{11}\,L_{\odot}$. This value of the $L_{\rm IR}$ seems reasonable since most of the H II galaxies with log $L_{[\rm O\ IV]}$ (erg s^{-1}) between 39.6 and 41.0 are classified as LIRGs. The $L_{\rm IR}$ limit calculated above is one order of magnitude larger than $L_{\star}$ (Takeuchi et al. 2003) so the reason for the lower number of H II galaxies above this [O IV] 25.89 μm luminosity can be that the space density of luminous star forming galaxies decreases rapidly with increasing luminosity.

Out of the 196 galaxies with estimates for $L_{\rm IR}$, [O IV] 25.89 μm is detected in 122.

Only 2±2 % of the H II galaxies have [O IV] 25.89 μm luminosities 1σ above those expected from their $L_{\rm IR}$. Likewise star formation can explain the observed [O IV] 25.89 μm luminosities for 9±4 % of the Seyfert galaxies (Figure 3.7). Thus the [O IV] 25.89 μm emission of Seyferts is generally dominated by the AGN, whereas for optically classified H II galaxies star formation is likely to be the origin of the [O IV] 25.89 μm emission.

3.5.2 The [Ne III] Excess

The [Ne III] 15.56 μm emission may be produced by star formation and/or AGN. In this section, we try to quantify the contribution of each one to the total [Ne III] 15.56 μm output. For this purpose we used the correlations between [Ne V] 14.32 μm, [O IV] 25.89 μm, and [Ne III] 15.56 μm (see Section 3.4). Combining the typical [O IV]/[Ne V] 14.32 μm and [Ne III] 15.56 μm/[Ne V] 14.32 μm ratios found in AGN we estimate a ratio [Ne III]/[O IV] = 0.6, with rms scatter of 0.3 for AGNs[1], or log [Ne III]/[O IV] = −0.22. This estimated ratio is very similar to that obtained using a linear fit between the [Ne III] 15.56 μm and [O IV] 25.89 μm luminosities (Table 3.2). The median of this ratio for H II galaxies is 4.7, or log [Ne III]/[O IV] = 0.67, which is ∼8 times larger than that estimated for active galaxies. Figure 3.8 shows that the observed ratio for Seyfert galaxies and QSOs falls around the predicted value for AGN. Only a small fraction (4 %) of the H II galaxies have [Ne III] 15.56 μm/[O IV] 25.89 μm ratios in the AGN range. It is also apparent that H II galaxies, a large fraction of LINERs and some Seyfert galaxies have an excess of [Ne III] 15.56 μm relative to their [O IV] 25.89 μm emission which can also be attributed to star formation.

We find that the four H II galaxies with [Ne V] 14.32 μm detections have the [Ne III] 15.56 μm/[Ne V] 14.32 μm and [Ne II] 12.81 μm/[Ne V] 14.32 μm ratios much larger than those of Seyfert galaxies (Table 3.2). This indicates that the star formation contribution is larger than that in Seyfert galaxies. Thus as suggested in Section 3.2 the AGN does not dominate the nuclear spectra of these galaxies.

As can be seen in the left panel of Figure 3.4, most of the outliers (galaxies more than 3σ above the [Ne V] 14.32 μm versus [Ne III] 15.56 μm flux correlation) have $L_{\rm [Ne\ III]} < 10^{42}\,{\rm erg\,s^{-1}}$. That is, for the most luminous objects the AGN dominates the [Ne III] 15.56 μm emission. Using the relation by Ho & Keto (2007) that relates star formation rate (SFR) and the luminosity of the [Ne II] 12.81 μm and [Ne III] 15.56 μm emission lines and assuming a [Ne III] 15.56 μm/[Ne II] 12.81 μm ratio = 0.3 (see Section 3.5.3) we find that the SFR of the outliers is between 0.1 and 100 $M_\odot\,{\rm yr^{-1}}$.

[1] In this section the term "AGN" refers to galaxies classified as QSO or Seyfert.

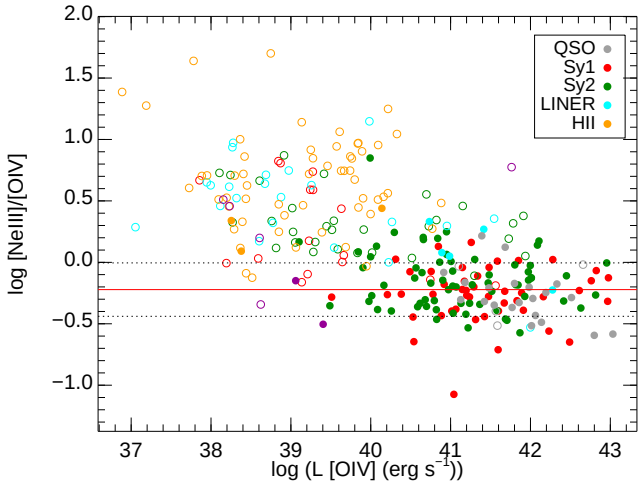

Figure 3.8: [Ne III] 15.56 μm/[O IV] 25.89 μm ratio vs. [O IV] 25.89 μm luminosity. Galaxy symbols are as in Figure 3.2. The solid red line is the [O IV] 25.89 μm/[Ne III] 15.56 μm ratio calculated from the linear fit to the [O IV] 25.89 μm vs. [Ne III] 15.56 μm luminosities. The dotted black lines are the 1σ deviation.

3.5.3 The [Ne III] 15.56 μm/[Ne II] 12.81 μm Ratio

The [Ne III] 15.56 μm/[Ne II] 12.81 μm ratio traces the hardness of the radiation field and the age of the stellar population (Rigby & Rieke 2004; Snijders et al. 2007). Figure 3.9 compares the [Ne III] 15.56 μm/[Ne II] 12.81 μm ratio observed in H II galaxies (median 0.2) with that observed in Seyfert galaxies with star formation[2] (median 0.6). The larger ratio found in Seyfert galaxies can be explained if the AGN contributes noticeably to the total [Ne III] 15.56 μm emission but not to the [Ne II] 12.81 μm emission (see Section 3.4.2). By assuming this we calculate the star formation [Ne III] 15.56 μm/[Ne II] 12.81 μm ratio in these Seyfert galaxies using the non-AGN [Ne III] 15.56 μm emission that we estimated using the method described in Section 3.6. The median of this ratio becomes ∼0.3, which is somewhat larger than that found in pure H II galaxies but it is in the range of the observed ratio in this class of galaxies (Brandl et al. 2006).

3.6 Comparison of Star Formation in Seyfert 1 and 2 Galaxies

The AGN unification scenario predicts that there should be no differences between the star formation activity in Seyfert 1 and 2 galaxies. A number of studies compared

[2]Those with excess [Ne III] 15.56 μm.

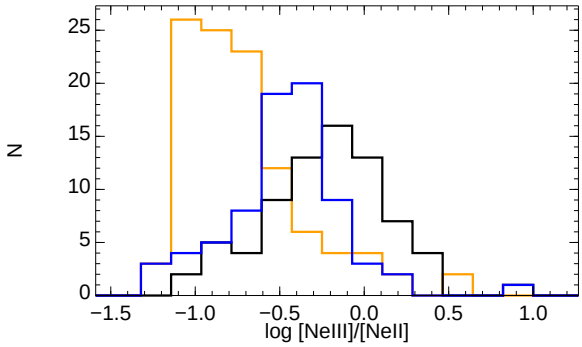

Figure 3.9: Distribution of the [Ne III] 15.56 μm/[Ne II] 12.81 μm ratio. The orange histogram corresponds to the observed ratios in H II galaxies, black corresponds to the observed ratios in active galaxies with star formation ([Ne III] 15.56 μm/[O IV] 25.89 μm ratios > 0.9). The blue histogram shows the ratios calculated for Seyfert galaxies after subtracting the AGN contribution to the [Ne III] 15.56 μm emission.

the star formation rates in Seyfert 1 and 2 galaxies. Some of them found enhanced star formation activity in Seyfert 2 with respect Seyfert 1 galaxies, for a given AGN luminosity (Maiolino et al. 1995; Buchanan et al. 2006; Deo et al. 2007; Meléndez et al. 2008b), whereas others did not find any differences between the two types (Kauffmann et al. 2003; Imanishi & Wada 2004). However, as discussed by Shi et al. (2009), the different methods used to study the star formation activity are sensitive to different stellar age ranges. Therefore these apparently contradictory results may be consistent with each other. The [Ne III] 15.56 μm line is sensitive to young (< 5 Myr) massive star formation (Rigby & Rieke 2004; Snijders et al. 2007). Studies using this line (and the [Ne II] 12.81 μm line) found that star formation is enhanced in Seyfert 2 galaxies (Deo et al. 2007; Meléndez et al. 2008b). Kauffmann et al. (2003) did not find differences between Seyfert 1 and Seyfert 2 star formation, but their method (the 4000Å break and the Hδ stellar absorption) was sensitive to stellar populations older than 100 Myr (Shi et al. 2009). The same applies to the PAH features used by Imanishi & Wada (2004), which can be affected by the presence of the AGN (Diamond-Stanic & Rieke 2010, and references therein).

It is also important to use the appropriate indicator for the AGN luminosity. We will use the [O IV] 25.89 μm emission, as it is a good isotropic indicator (Rigby et al. 2009; Diamond-Stanic et al. 2009), as long as the AGN dominates the [O IV] 25.89 μm emission as we showed in Section 3.5.1.

We estimate the star formation contribution to the [Ne III] 15.56 μm emission by using the observed [O IV] 25.89 μm/[Ne III] 15.56 μm ratio and subtracting the estimated AGN contribution from the total [Ne III] 15.56 μm line strength. Further details

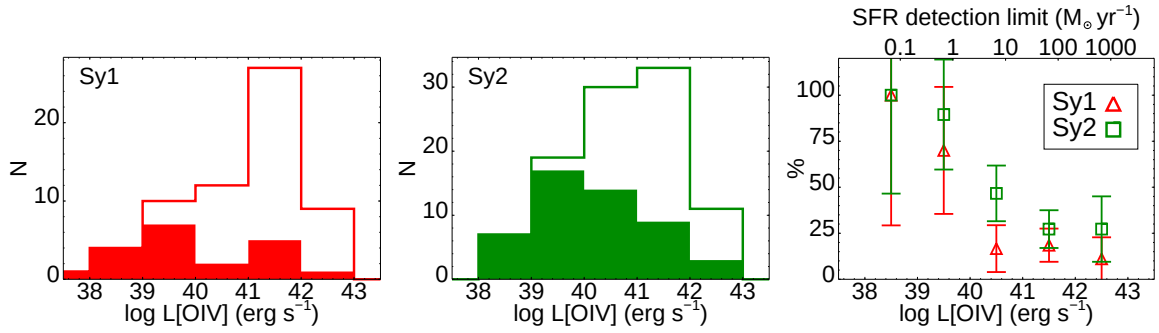

Figure 3.10: Distribution of the [O IV] 25.89 μm luminosities of the Seyfert 1 (left) and 2 (middle) galaxies. The filled histograms are the galaxies with a [Ne III] 15.56 μm excess. The right panel compares the fraction of type 1 and 2 Seyferts with a [Ne III] 15.56 μm excess for each luminosity bin. We used Poisson statistical errors to estimate the uncertainties of the fractions. The scale on the upper part of the right panel gives the lower limit to the SFR that can be detected with our method for each AGN luminosity bin.

are provided in Appendix 3.A. We used the [O IV] 25.89 μm/[Ne III] 15.56 μm instead of the [O IV] 25.89 μm/[Ne II] 12.81 μm ratio because we could not calculate the typical AGN [O IV] 25.89 μm/[Ne II] 12.81 μm ratio due to the larger relative contribution of star formation activity to the [Ne II] 12.81 μm emission (Section 3.4.2). We only subtract this contribution from those active galaxies more than 1σ above the typical AGN [Ne III] 15.56 μm/[O IV] 25.89 μm ratio (see Section 3.5.2 and Figure 3.8), since the galaxies below this ratio are presumably dominated by the AGN and their star formation activity, if any, is masked. This criterion basically selects only those active galaxies with at least 25 % of the [Ne III] 15.56 μm emission arising from star formation. In our sample 45 % of the AGNs with the [O IV] 25.89 μm line detected have excess [Ne III] 15.56 μm emission due to star formation. The right panel of Figure 3.10 shows that the fraction of Seyfert 2s with star formation is slightly higher than that of Seyfert 1s. In all the luminosity bins except for one, the difference in the fraction with a [Ne III] 15.56 μm excess is less than 2σ significant. However, for the overall proportion of [Ne III] 15.56 μm excess detections, the Fisher's exact test indicates that there is a probability of less than 0.03 that the incidence of this behavior is the same in the Sy1 and Sy2 samples. Therefore, the full sample in our study supports, with a moderate statistical significance, previous indications that Sy2 host galaxies tend to have higher rates of star formation than Sy1 hosts. However the full sample is heterogeneous and may be subject to a number of biases. For example, it includes a number of radio galaxies, which are known to have low star formation rates – in fact none of the radio galaxies have [Ne III] 15.56 μm excess. It also contains ULIRGs with Seyfert spectral

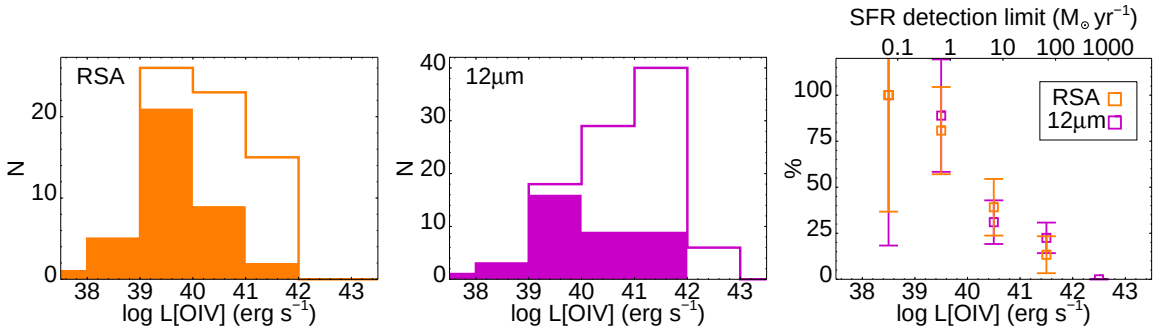

Figure 3.11: Distribution of the [O IV] 25.89 μm luminosities for the RSA sample (left panel) and 12 μm sample (middle panel). Symbols are as in Figure 3.10.

characteristics, most of which do have [Ne III] 15.56 μm excess. The observed differences depend to some extent on the relative number of galaxies in these two classes. In the following section, we discuss this trend in two relatively complete but smaller subsamples where the biases should be reduced.

3.6.1 Results for the 12 μm sample and the RSA samples

At this point we study separately the 12 μm sample and the RSA sample. Both are complete samples of Seyfert galaxies selected with homogeneous criteria. The former is selected based on their *IRAS* 12 μm fluxes whereas the latter is selected based on the optical magnitude of the host galaxy. Given the different selection criteria they they might be affected by star formation in different ways.

As can be seen from Table 3.3 and Figure 3.11, the fraction of galaxies with a [Ne III] 15.56 μm excess in the RSA sample is higher (by a factor of 1.4) than in the 12 μm sample. The lower number of galaxies with a [Ne III] 15.56 μm excess in the 12 μm sample is because the galaxies of this sample are brighter and the sensitivity to star formation of our method is reduced at high [O IV] 25.89 μm luminosities. Both effects are clearly seen in Figure 3.11. First, the RSA sample contains a larger fraction of low luminosity Seyferts ($L_{[\mathrm{O\ IV}]} \leq 10^{40}\,\mathrm{erg\,s^{-1}}$) than the 12 μm sample. Second, for each AGN luminosity, we are sensitive to a different SFR limit. In other words, for the brightest Seyferts we are only sensitive to SFR above 100 $M_\odot\,\mathrm{yr}^{-1}$, while for low luminosity AGN we are sensitive to SFR $> 0.1\,M_\odot\,\mathrm{yr}^{-1}$. We note that the fraction of galaxies with star formation in each luminosity bin is similar for both samples (right panel of Figure 3.11).

In both samples the fraction of Seyfert 2s with [Ne III] 15.56 μm excess is slightly larger than that of Seyfert 1s. However, due to the small size of the samples the

Table 3.3: Fraction of Galaxies with a [Ne III] Excess in the RSA and 12 μm Samples

Type	12 μm sample	RSA
Seyfert 1	15/45	12/25
Seyfert 2	23/52	25/45
Total	38/97	37/70

Notes. In this table we only include galaxies with the [O IV] 25.89 μm and [Ne III] 15.56 μm emission lines detected. Some galaxies are common to both samples.

statistical significance of this excess is low. Based on the two sample Kolmogorov-Smirnov test, the probability for these differences being due to chance is 0.25 and 0.4 for the 12 μm and RSA samples respectively.

3.7 Line Ratios and Models

We studied the physical conditions in the NLR of the AGNs with the photoionization code MAPPINGSIII (Groves et al. 2004a). We used a radiation pressure dominated model that includes the effects of dust. For the input parameters we followed the prescription given by Groves et al. (2006). Briefly, we assumed a plane parallel geometry and solar abundances. We modeled the input ionizing spectrum with two power-laws with exponential cutoffs (Nagao et al. 2001). We explored the effect of the variations in the total hydrogen column density ranging from log $n_{\rm H}$ (cm^{-2}) = 19.0 to 22.0. This range was chosen since it reproduces the observed line ratios and is in good agreement with the hydrogen column density determined using UV and X-ray observations (Crenshaw et al. 2003). For each hydrogen column density we varied the total pressure (P/k) and the incident ionizing flux (I_0). The values for the total pressure are log P/k (K cm^{-3}) = 6, 7, 8, 9. These correspond to electron densities, as traced by [S II]λ6716Å/λ6731Å, of $\sim$ <10^1, 10^2, 10^3 and > 10^4 cm^{-3} respectively. The explored range for the ionizing flux is I_0 = 0.1 to 0.55. The incident ionizing flux is scaled by the factor 2.416×[$(P/k)/10^6$] erg cm^{-2} s^{-1} which gives a range in the ionization parameter, log U, from $\sim$ –3 to –2.

3.7.1 The [Ne V] ratio

Figure 3.12 shows the ratio between the two [Ne V] emission lines available in the mid-infrared. The critical densities of the [Ne V] 14.32 μm and [Ne V] 24.32 μm lines are 3.5×10^4 cm^{-3} and 6.2×10^3 cm^{-3}, respectively (Osterbrock & Ferland 2006), thus they

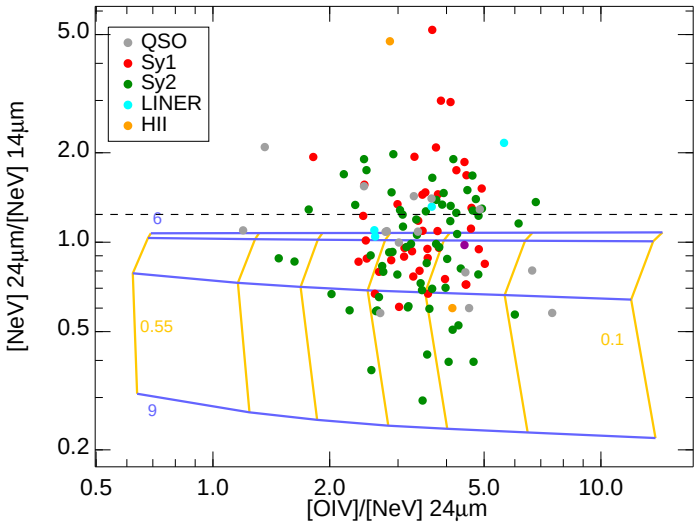

Figure 3.12: Predicted [Ne V] 24.32 μm/[Ne V] 14.32 μm ratio vs. [O IV] 25.89 μm/[Ne V] 24.32 μm. Galaxy symbols are as in Figure 3.2. The dashed black line indicates the low density limit calculated at 10000 K for the [Ne V] 24.32 μm/[Ne V] 14.32 μm ratio (galaxies above this line have densities below the low density limit). The blue lines trace constant pressure and the orange lines constant ionization parameter (I_0). The input parameters for the model are log P/k = 6, 7, 8, 9 and I_0 = 0.1, 0.15, 0.20, 0.25, 0.32, 0.4, 0.55 for constant hydrogen column density log $n_{\rm H}$ (cm^{-2}) = 20.3. The galaxy symbols are as in Figure 3.2.

can be used to trace the density of the NLR . We find, however, that a large fraction of the galaxies (∼30 %) lie above the low-density limit ratio. This issue and its possible cause are discussed in detail by Dudik et al. (2007) and also addressed by Tommasin et al. (2010) for a sample of Seyfert galaxies. Dudik et al. (2007) concluded that the ratios above the low density limit are due to differential extinction from the obscuring torus, and thus can indicate the inclination angle to our line of sight. However, similar to Baum et al. (2010), we do not find any significant difference between the proportion of Seyfert 1 and 2 galaxies above the low density limit, as would be predicted by this hypothesis.

We calculated the $A_{24.3}/A_{14.3}$ ratio to quantify the extinction needed to move the points above the low density limit ratio to this value (which would be a lower limit to the extinction since the real ratio may be lower than the low density limit). The ratios are summarized in Table 3.4 for some infrared extinction laws. As can be seen depending on the extinction law chosen the extinction can increase or decrease the [Ne V] 24.32 μm/[Ne V] 14.32 μm ratio. Since the construction of an extinction law implies some interpolation we also used direct measurements of $A_{24}/A_{\rm K}$ and $A_{15}/$

Table 3.4: Extinction at 24 μm Relative to that at 14 μm

Extinction Law	A_{24}/A_{14}
Rosenthal[a]	1.25
McClure $0.3 < A_{\rm K} < 1$[b]	0.83
McClure $1 < A_{\rm K} < 7$[b]	0.83
Chiar Galactic Center[c]	1.38
Chiar Local ISM[c]	0.97

[(a)] Rosenthal et al. 2000. [(b)] McClure 2009. [(c)] Chiar & Tielens 2006.

$A_{\rm K}$.[3] Jiang et al. (2006) measured the extinction at 15 μm and found $A_{15}/A_{\rm K} = 0.40$, although it ranges from 0.25 to 0.55. For the $A_{24}/A_{\rm K}$ ratio the range is 0.28 to 0.65 for different $A_{\rm K}$ bins (Chapman et al. 2009) and the average value is ∼0.5 (Chapman et al. 2009; Flaherty et al. 2007). From these measurements we estimate $A_{24.3}/A_{14.3}$ = 1.2±0.3. Again it is close to unity and it is not clear if the extinction would increase or decrease the [Ne V] ratio. Moreover the extinction is nearly neutral between the lines with all the extinction laws and therefore there is very little potential effect on the ratio unless the extinction is extremely large.

We also checked if aperture effects can explain the large values of this ratio. The [Ne V] 14.32 μm line is observed with the IRS Short-High module (5.″7×11.″3), whereas the [Ne V] 24.32 μm is observed with the IRS Long-High module (11.″1×22.″3). We would expect a correlation between the [Ne V] 24.32 μm/[Ne V] 14.32 μm ratio and the distance if the [Ne V] emission region was larger than the SH slit. However, we do not find this correlation and thus rule out any aperture bias.

Alternatively, the atomic parameters for the Ne^{+4} ion may not be sufficiently accurate for the comparison with these observations, and the calculated low-density limit may be incorrect.

3.7.2 Ionization parameter

In Figure 3.12 we plot the model grid together with the data. In this plot we vary the ionizing flux, I_0, and the total pressure, P/k, for a constant total hydrogen column density [$\log n_{\rm H}\,({\rm cm}^{-2}) = 20.3$]. We see that the [Ne V] ratio can be used to measure the pressure. However the pressure (or density) values derived from this ratio have some issues, since a considerable fraction of galaxies are above the low density limit ratio (Section 3.7.1).

[3]From the extinction laws, the difference between these A values and those at 14.3 μm and 24.3 μm would be small (∼5%).

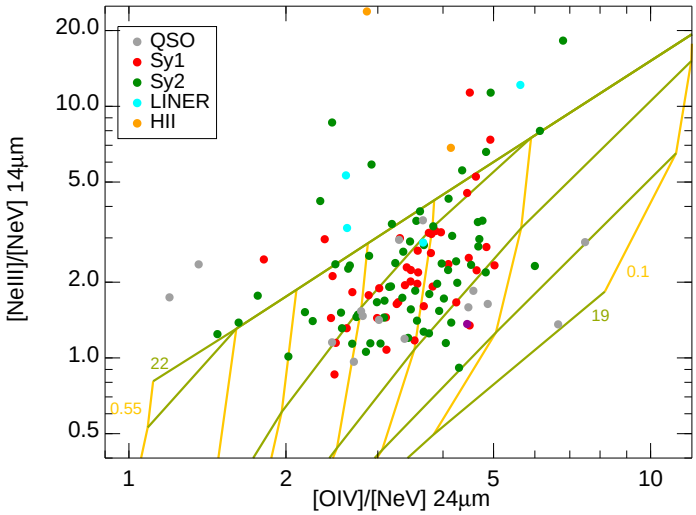

Figure 3.13: Predicted [Ne III] 15.56 μm/[Ne V] 14.32 μm ratio vs. [O IV] 25.89 μm/[Ne V] 24.32 μm. The green lines trace constant hydrogen column density and the orange lines constant ionization parameter. The input parameters for the model are $\log n_{\rm H}\,({\rm cm}^{-2})$ = 19.0, 20.0, 20.3, 20.6, 21.0, 22.0 and I_0 = 0.1, 0.15, 0.20, 0.25, 0.32, 0.4, 0.55 for constant pressure ($\log P/k = 8$). The galaxy symbols are as in Figure 3.2.

Also, Figure 3.12 shows that the [O IV] 25.89 μm/[Ne V] 24.32 μm ratio traces the ionization parameter. The [O IV] 25.89 μm/[Ne V] 24.32 μm ratio spans a narrow range (less than 1 dex) which is related to the tight correlation found between the [O IV] 25.89 μm and [Ne V] 24.32 μm luminosities (Section 3.4). This implies a very small range for the ionization parameter (-2.8 $<$ $\log U$ $<$ -2.5). This range is similar to that found when modeling the optical [O III] and Hβ emission (Baskin & Laor 2005; Kraemer et al. 1999). The critical density of the [O III] lines is larger than that of these mid-IR lines and for instance the Baskin & Laor (2005) models predict electron densities $\log n_{\rm e}\,({\rm cm}^{-3})$ = 5.8$\pm$0.7 well above the critical density of the mid-IR lines studied here. Thus it is possible that these lines are produced in different gas clouds.

3.7.3 Hydrogen column density

We use the [Ne III] 15.56 μm and the [Ne V] 14.32 μm lines to estimate the total hydrogen (H I + H II) column density, $n_{\rm H}$. The [Ne V] 14.32 μm line is produced in the inner part of the NLR while the [Ne III] 15.56 μm is produced in a more external region. Thus the [Ne III] 15.56 μm/[Ne V] 14.32 μm ratio is subject to change depending on the column density. As expected, the models predict larger [Ne III] 15.56 μm/[Ne V] 14.32 μm ratios for larger $n_{\rm H}$.

In Figure 3.13 we plot the model grid together with the observed ratios. The

[Ne III] 15.56 μm/[Ne V] 14.32 μm ratio is not sensitive to column densities larger than $\log n_{\rm H}\,({\rm cm}^{-2}) > 21$. We find that the column density for most of the galaxies is in the range $20.3 < \log n_{\rm H}\,({\rm cm}^{-2}) < 21$. There is no difference between the predicted hydrogen column density for type 1 and 2 galaxies. This column density range is compatible with the values derived from UV observations although lower than that determined using X-ray data (Crenshaw et al. 2003). A few galaxies are above the model grid. The [Ne III] 15.56 μm/[Ne V] 14.32 μm ratio of these galaxies is larger than that predicted by the models. As we proposed in Sections 3.4.2 and 3.5.2, star formation acting in these galaxies is likely producing the extra [Ne III] 15.56 μm emission.

3.8 Conclusions

We studied a sample of 426 galaxies observed with the *Spitzer*/IRS spectrograph in the high resolution mode. Our analysis includes published data for QSO, Seyfert, LINER and H II galaxies as well as unpublished measurements for the RSA Seyfert sample and LIRGs. We explored the relationship between the high-ionization ([Ne V] 14.32 μm, [Ne V] 24.32 μm and [O IV] 25.89 μm) and intermediate ionization ([Ne III] 15.56 μm and [Ne II] 12.81 μm) emission lines present in the mid-IR spectra. The median ratios for each class of galaxies are listed in Table 3.2. The main results are as follows:

1. There is a tight linear correlation between the fluxes and luminosities of the high-ionization emission lines [O IV] 25.89 μm and [Ne V] 24.32 μm. This correlation spans 5 orders of magnitude ($38 < \log L_{[\rm Ne\ V]24}\,({\rm erg\ s}^{-1}) < 43$), ranging from LINERs, low-luminosity Seyfert galaxies, types 1 and 2, to QSOs. The typical [O IV] 25.89 μm/[Ne V] 24.32 μm ratio for AGNs is 3.5, with rms scatter of 0.8. The correlation also holds between the [O IV] 25.89 μm and the [Ne V] 14.32 μm lines, although the scatter is larger. The typical [O IV] 25.89 μm/[Ne V] 14.32 μm ratio for AGNs is 3.4, with rms scatter of 1.4.

2. There is also a good linear correlation between the [Ne III] 15.56 μm and the [Ne V] 14.32 μm fluxes and luminosities for Seyfert galaxies and QSO. The [Ne III] 15.56 μm/[Ne V] 14.32 μm ratio is 1.9, with rms scatter of 0.8. Using this correlation and the previous one we calculated the typical [Ne III] 15.56 μm/[O IV] 25.89 μm ratio for AGNs of 0.6, with rms scatter of 0.3.

3. We calculate the [O IV] 25.89 μm emission due to star formation ($\log L_{[\rm O\ IV]}\,({\rm erg\ s}^{-1}) < \log L_{\rm IR}\,({\rm erg\ s}^{-1}) - 4.7 \pm 0.6$) and estimate that it may dominate the total [O IV]

25.89 μm emission when the intrinsic AGN luminosity is a factor of 20 smaller than the star forming luminosity. In general, we find that the [O IV] 25.89 μm emission is dominated by the AGN in Seyfert galaxies, whereas star formation can explain the [O IV] 25.89 μm emission of optically classified H II galaxies.

4. We do not find any significant difference between the mid-IR high-ionization emission lines in type 1 and 2 Seyfert galaxies. Either there are no differences in the conditions in the NLR of the two AGN types, or the effects associated with the different line of sight (i.e., dust extinction) are minimized in the mid-infrared spectra.

5. We find that a significant number of Seyfert galaxies from the 12 μm sample (30 %) and the RSA sample (40 %) show evidence for excess [Ne III] 15.56 μm emission relative to their [O IV] 25.89 μm emission associated with star formation. The larger fraction in the RSA sample is explained because the RSA sample contains a larger fraction of low-luminosity AGNs ($L_{[\mathrm{O\ IV}]} < 10^{41}\,\mathrm{erg\,s^{-1}}$) in which these star formation excesses are easier to detect.

6. The fraction of Seyfert 2 galaxies with [Ne III] 15.56 μm excess is larger than that of Seyfert 1 with a moderate statistical significance in the full sample, although this sample may be affected by several bias. However, when we consider the 12 μm or RSA Seyfert samples separately, these differences are not statistically significant due to the smaller size of these samples.

7. A considerable fraction (30 %) of the galaxies have [Ne V] 24.32 μm/[Ne V] 14.32 μm ratios above the low-density limit. We did not find a connection between the Seyfert type and the ratio of galaxies above the limit. We are not able to explain this in terms of differential extinction.

8. Our modeling shows that the nebular conditions in the NLRs are remarkably similar among all the AGNs in our sample. This similarity allows us to compare conditions critically in the NLRs of the type 1 and 2 galaxies. There appear to be no significant overall differences, consistent with the unified model. We constrained the ionization parameter in the range $-2.8 < \log U < -2.5$ and the hydrogen column density $20 < \log n_{\mathrm{H}}\,(\mathrm{cm^{-2}}) < 21$.

The relationships presented in this Chapter provide an important benchmark for the interpretation of the current and future mid-IR observations of AGNs and star forming galaxies with *Spitzer*/IRS and in the future with *JWST*/MIRI.

3.A Calculating the AGN Contribution

In this appendix we explain briefly the method used in Sections 3.5 and 3.6 to calculate the star formation fraction of the [Ne III] 15.56 μm emission.

The total [Ne III] 15.56 μm emission includes two components, one from the AGN and the other from star formation (SF).

$$[\text{Ne III}] = [\text{Ne III}]_{\text{SF}} + [\text{Ne III}]_{\text{AGN}} \tag{3.3}$$

If we assume that all the [O IV] 25.89 μm is produced by the AGN, we can use the typical [Ne III] 15.56 μm/[O IV] 25.89 μm ratio observed in Seyfert galaxies with low SF (Figure 3.8) to estimate the amount of [Ne III] 15.56 μm emission coming from the AGN.

$$[\text{Ne III}] = [\text{Ne III}]_{\text{SF}} + [\text{O IV}] \times \left(\frac{[\text{Ne III}]}{[\text{O IV}]}\right)_{\text{AGN}}. \tag{3.4}$$

Finally we obtain the fraction of [Ne III] 15.56 μm from SF.

$$\frac{[\text{Ne III}]_{\text{SF}}}{[\text{Ne III}]} = 1 - \frac{[\text{O IV}]}{[\text{Ne III}]} \times \left(\frac{[\text{Ne III}]}{[\text{O IV}]}\right)_{\text{AGN}}. \tag{3.5}$$

This method can be applied as well to other line ratios. The only assumption is that one of the lines in the ratio is uniquely produced by the AGN while the SF and AGN contribute to the other line (e.g., the [Ne III] 15.56 μm and [Ne V] lines). Also note that this method makes use of a typical AGN ratio and; thus the estimated star formation contribution to an emission line for a single object will be uncertain and dependent on the ionization parameter.

3.B Mid-Infrared Emission Line Fluxes

Table 3.5: Mid-Infrared Emission Line Fluxes

Name	R.A.[a] (J2000.0)	Decl.[a] (J2000.0)	Dist.[b] (Mpc)	Spect. Class.[a]	[Ne II] 12.81 μm	[Ne V] 14.32 μm	[Ne III] 15.56 μm	[Ne V] 24.32 μm	[O IV] 25.89 μm	Ref.
Mrk 335 [d]	00 06 19.5	+20 12 10	113	Sy1	0.25	0.38	0.61	2.0	7.2	4
NGC 23	00 09 53.4	+25 55 25	64.5	H II	96	<0.50	13	<0.44	1.4	2
NGC 24	00 09 56.5	–24 57 47	7.30	···	3.1	<0.88	1.3	···	<0.42	5
Mrk 938 [d]	00 11 06.5	–12 06 26	85.3	Sy2	52	<2.2	6.4	<0.37	<0.66	4
IRAS F00188–0856	00 21 26.5	–08 39 26	600	LINER	4.7	<0.18	0.69	<1.6	<0.90	3
IRAS 00198–7926 [d]	00 21 53.6	–79 10 07	329	Sy2	6.2	12	14	11	33	4
PG 0026+129	00 29 13.6	+13 16 03	672	QSO	0.23	0.47	0.79	<0.33	2.1	1
ESO 012-G021 [d]	00 40 46.2	–79 14 24	144	Sy1	12	3.2	6.4	4.6	16	4
IRAS F00397–1312	00 42 15.5	–12 56 02	1329	H II	4.4	<0.20	2.7	<1.5	<1.2	3
NGC 253	00 47 33.1	–25 17 17	2.50	H II	2832	<21	205	<73	155	8
Mrk 348 [d]	00 48 47.1	+31 57 25	65.1	Sy2	16	5.8	20	4.9	18	4
NGC 278	00 52 04.3	+47 33 01	11.4	···	18	<0.070	3.0	<0.59	<0.62	7
PG 0050+124	00 53 34.9	+12 41 36	273	QSO	1.9	5.5	4.5	<2.1	2.7	1
IRAS 00521–7054 [d]	00 53 56.1	–70 38 04	310	Sy2	5.8	5.8	8.1	2.4	8.6	4
MCG +12-02-001	00 54 03.6	+73 05 11	68.1	H II	242	<1.00	43	<1.4	3.8	2
UGC 556	00 54 50.3	+29 14 47	66.1	H II	40	<0.21	7.1	<0.73	<1.6	2
NGC 337	00 59 50.1	–07 34 40	22.4	H II	19	<0.74	8.0	···	<0.49	5
ESO 541-IG012 [d]	01 02 17.5	–19 40 08	253	Sy2	1.9	2.2	2.0	1.2	5.0	4
IRAS 01003–2238	01 02 50.0	–22 21 57	550	H II	3.1	<0.30	1.3	<0.30	<0.30	3
3C 33	01 08 52.9	+13 20 13	269	Sy2	3.9	2.0	5.3	···	8.1	6
NGC 404	01 09 27.0	+35 43 04	3.24	LINER	3.1	<0.16	1.7	<0.31	0.90	2

Table 3.5: *Continued*

Name	R.A.[a] (J2000.0)	Decl.[a] (J2000.0)	Dist.[b] (Mpc)	Spect. Class.[a]	[Ne II] 12.81 μm	[Ne V] 14.32 μm	[Ne III] 15.56 μm	[Ne V] 24.32 μm	[O IV] 25.89 μm	Ref.
NGC 424 [d]	01 11 27.6	–38 05 00	50.8	Sy2	8.7	16	18	6.4	26	4
NGC 526A [d]	01 23 54.4	–35 03 55	83.0	Sy1	5.8	6.3	10	5.9	19	4
NGC 513 [d]	01 24 26.9	+33 47 58	85.0	Sy2	13	1.9	4.4	1.1	6.5	4
NGC 520	01 24 35.1	+03 47 32	30.2	H II	45	<0.64	7.5	<1.4	8.1	8
NGC 584	01 31 20.8	–06 52 05	20.0	···	···	<0.92	1.7	···	<0.30	5
NGC 613	01 34 18.2	–29 25 06	15.0	H II	131	0.67	16	3.2	9.1	7
NGC 633	01 36 23.4	–37 19 17	74.2	H II	50	<0.50	6.1	<0.59	1.9	2
NGC 628	01 36 41.8	+15 47 00	7.30	···	6.2	<1.00	···	···	<0.38	5
IRAS 01364–1042	01 38 52.9	–10 27 11	215	H II	7.9	<0.32	1.5	<0.60	<0.91	2
NGC 660	01 43 02.4	+13 38 42	12.1	H II	346	<0.57	37	<4.5	28	2
Mrk 573	01 43 57.8	+02 20 59	73.8	Sy2	···	18	24	···	<79	6
III Zw 035	01 44 30.5	+17 06 05	120	···	3.8	<0.17	0.19	<1.9	<1.3	2
IRAS 01475–0740 [d]	01 50 02.7	–07 25 48	76.7	Sy2	14	6.4	9.9	1.9	6.5	4
3C 55	01 57 10.5	+28 51 37	4522	Sy2	···	1.1	2.0	···	···	6
Mrk 1014	01 59 50.2	+00 23 40	781	Sy1	6.6	7.4	9.7	5.0	13	3
NGC 788 [c]	02 01 06.4	–06 48 55	58.9	Sy2	6.1	5.3	14	7.9	23	2
NGC 855	02 14 03.6	+27 52 37	9.60	···	5.5	<0.72	···	···	<0.40	5
NGC 891	02 22 33.4	+42 20 56	8.60	H II	8.6	<0.040	0.84	<0.62	<1.0	7
Mrk 1034 NED01 [d]	02 23 18.9	+32 11 18	148	Sy1	19	<1.1	1.5	<0.59	<0.77	4
Mrk 1034 NED02 [d]	02 23 22.0	+32 11 49	148	Sy1	35	1.1	3.6	<0.60	2.7	4
UGC 1845	02 24 08.0	+47 58 11	66.7	H II	106	<0.59	11	<0.82	3.1	2
ESO 545-G013 [d]	02 24 40.6	–19 08 31	148	Sy1	10	4.8	11	3.2	12	4
NGC 925	02 27 16.9	+33 34 45	9.10	H II	10	<1.0	5.1	···	<0.36	5

Table 3.5: *Continued*

Name	R.A.[a] (J2000.0)	Decl.[a] (J2000.0)	Dist.[b] (Mpc)	Spect. Class.[a]	[Ne II] 12.81 μm	[Ne V] 14.32 μm	[Ne III] 15.56 μm	[Ne V] 24.32 μm	[O IV] 25.89 μm	Ref.
NGC 931 [d]	02 28 14.5	+31 18 41	72.2	Sy1	5.5	14	15	14	43	4
NGC 1055	02 41 45.2	+00 26 35	11.3	Sy2	26	<0.19	2.6	<0.58	1.2	7
NGC 1068 [c] [d]	02 42 40.7	–00 00 47	16.3	Sy2	461	895	1355	808	2061	2
NGC 1056 [d]	02 42 48.3	+28 34 27	22.1	Sy2	34	<1.8	10	<1.2	1.4	4
NGC 1058 [c]	02 43 30.0	+37 20 28	7.42	Sy2	1.0	<0.46	···	<0.33	<0.50	2
UGC 2238	02 46 17.5	+13 05 44	94.5	H II	65	<0.47	10	<2.6	5.5	2
NGC 1097 [c] [d]	02 46 19.1	–30 16 29	17.7	Sy1	165	<0.74	20	<2.4	5.0	2
IRAS 02438+2122	02 46 39.1	+21 35 10	102	LINER	18	<0.33	1.6	<2.2	<2.6	2
NGC 1125 [d]	02 51 40.3	–16 39 03	47.2	Sy2	16	5.1	16	9.7	40	4
NGC 1142 [d]	02 55 12.2	–00 11 00	126	Sy2	17	0.92	5.4	1.8	5.3	4
Mrk 1066	02 59 58.6	+36 49 14	51.9	Sy2	···	18	52	···	···	6
MCG –02-08-039 [d]	03 00 30.6	–11 24 56	131	Sy2	3.9	6.6	9.8	5.2	14	4
NGC 1194 [d]	03 03 49.1	–01 06 13	58.9	Sy2	3.8	4.3	7.4	3.8	15	4
NGC 1204	03 04 39.9	–12 20 28	64.8	H II	54	<0.34	5.0	<2.0	<1.6	2
NGC 1222	03 08 56.7	–02 57 18	32.3	H II	81	<0.57	89	<0.78	9.9	8
3C 79	03 10 00.1	+17 05 58	1295	Sy2	···	0.11	0.20	···	0.70	6
NGC 1241 [c] [d]	03 11 14.6	–08 55 19	58.5	Sy2	14	2.5	8.4	1.5	4.8	2
NGC 1266	03 16 00.8	–02 25 38	30.0	LINER	29	<0.92	9.7	···	<1.4	5
NGC 1291	03 17 18.6	–41 06 29	10.8	H II	5.2	<0.86	7.2	···	1.4	5
IRAS F03158+4227	03 19 12.4	+42 38 28	631	···	5.8	<1.1	0.94	<1.4	<1.8	3
NGC 1275 [c]	03 19 48.2	+41 30 42	76.2	Sy2	43	<1.2	21	<2.5	9.6	2
NGC 1316	03 22 41.7	–37 12 29	24.3	LINER	13	<0.61	11	···	2.6	5
NGC 1320 [d]	03 24 48.7	–03 02 32	38.3	Sy2	9.6	11	14	7.5	27	4

Table 3.5: *Continued*

Name	R.A.[a] (J2000.0)	Decl.[a] (J2000.0)	Dist.[b] (Mpc)	Spect. Class.[a]	[Ne II] 12.81 μm	[Ne V] 14.32 μm	[Ne III] 15.56 μm	[Ne V] 24.32 μm	[O IV] 25.89 μm	Ref.
NGC 1365 [c] [d]	03 33 36.4	–36 08 25	23.9	Sy1	156	19	61	40	151	2
NGC 1358 [c]	03 33 39.7	–05 05 21	58.2	Sy2	5.1	3.5	8.2	<1.6	9.1	2
NGC 1377	03 36 39.1	–20 54 08	25.2	H II	4.1	<1.9	2.6	···	<1.7	5
NGC 1386 [c] [d]	03 36 46.2	–35 59 57	12.5	Sy2	14	37	39	34	97	2
NGC 1404	03 38 51.9	–35 35 39	18.5	···	1.4	<0.97	1.00	···	<0.35	5
NGC 1433 [c] [d]	03 42 01.6	–47 13 19	15.4	Sy2	···	<1.6	···	<1.9	<6.9	2
NGC 1448	03 44 31.9	–44 38 41	11.5	···	8.2	3.7	5.0	3.6	16	7
IC 342	03 46 48.5	+68 05 46	4.60	H II	615	<2.4	37	<4.9	<7.7	8
IRAS 03450+0055 [d]	03 47 40.2	+01 05 14	136	Sy1	1.1	<1.5	1.8	<1.9	2.5	4
NGC 1482	03 54 38.9	–20 30 08	23.2	H II	457	<2.6	56	···	<6.4	5
IRAS 03521+0028	03 54 42.2	+00 37 03	724	LINER	2.8	<0.45	1.3	<0.48	<0.90	3
NGC 1512	04 03 54.3	–43 20 55	11.8	H II	31	<1.1	4.7	···	<0.83	5
3C 109	04 13 40.4	+11 12 13	1589	Sy1	0.030	0.070	0.11	···	0.27	6
IC 2056	04 16 24.5	–60 12 24	13.8	···	13	<0.16	2.2	<0.10	0.75	7
NGC 1559	04 17 35.8	–62 47 01	12.7	···	15	<0.44	2.3	<0.36	<0.69	7
NGC 1566 [c] [d]	04 20 00.4	–54 56 16	21.3	Sy1	15	1.1	9.6	<1.9	8.4	2
NGC 1569	04 30 49.1	+64 50 52	4.60	Sy1	19	<0.38	188	<1.4	29	7
3C 120 [d]	04 33 11.1	+05 21 15	145	Sy1	7.8	17	28	29	123	4
Mrk 618 [d]	04 36 22.2	–10 22 33	156	Sy1	16	3.9	5.4	<1.3	10	4
IRAS F04385–0828 [d]	04 40 55.0	–08 22 22	65.4	Sy2	14	2.3	7.1	<1.4	8.6	4
NGC 1667 [c] [d]	04 48 37.1	–06 19 11	65.9	Sy2	10.0	<0.32	6.9	1.7	6.3	2
NGC 1705	04 54 13.5	–53 21 39	5.10	H II	3.2	<0.91	12	···	2.5	5
ESO 033-G002 [d]	04 55 59.0	–75 32 28	78.6	Sy2	2.1	6.3	9.2	5.3	14	4

Table 3.5: *Continued*

Name	R.A.[a] (J2000.0)	Decl.[a] (J2000.0)	Dist.[b] (Mpc)	Spect. Class.[a]	[Ne II] 12.81 μm	[Ne V] 14.32 μm	[Ne III] 15.56 μm	[Ne V] 24.32 μm	[O IV] 25.89 μm	Ref.
NGC 1792	05 05 14.4	–37 58 50	12.5	H II	23	0.41	2.1	<0.25	0.96	7
NGC 1808	05 07 42.3	–37 30 47	12.6	Sy2	177	<0.91	17	<8.4	<9.5	7
ESO 362-G018 [d]	05 19 35.8	–32 39 27	53.8	Sy1	12	3.3	7.5	2.6	8.9	4
IRAS F05189–2524	05 21 01.5	–25 21 45	190	Sy2	21	18	18	12	24	3
IRAS 05187–1017	05 21 06.5	–10 14 46	126	LINER	10	<0.15	1.9	<0.66	<0.92	2
ESO 253-G003 [d]	05 25 18.1	–46 00 21	188	Sy2	16	6.8	18	7.2	24	4
UGC 3351	05 45 47.9	+58 42 03	64.1	H II	67	<0.50	9.6	<0.31	0.83	2
UGCA 116	05 55 42.6	+03 23 31	11.6	H II	6.0	<0.28	117	<1.1	8.5	7
IRAS F05563–3820 [d]	05 58 02.0	–38 20 04	149	Sy1	3.9	2.5	4.8	<0.79	5.3	4
IRAS F06035–7102	06 02 54.0	–71 03 10	358	H II	7.0	<0.48	1.7	<0.81	<3.0	3
ESO 121-G006	06 07 29.9	–61 48 27	14.5	···	16	0.65	3.2	<0.59	4.6	7
Mrk 3	06 15 36.4	+71 02 15	60.6	Sy2	100	64	179	···	214	6
NGC 2146	06 18 37.7	+78 21 25	16.5	H II	625	<2.8	91	<3.7	19	8
UGCA 127	06 20 55.7	–08 29 44	10.2	···	9.3	<0.15	1.5	<0.97	3.4	7
IRAS F06206–6315	06 21 01.2	–63 17 23	421	Sy2	6.6	2.3	2.9	2.0	3.0	3
NGC 2273 [c]	06 50 08.7	+60 50 44	26.5	Sy2	40	4.5	19	6.1	14	2
Mrk 6 [d]	06 52 12.3	+74 25 37	81.7	Sy1	28	9.4	49	10	48	4
IRAS 07145–2914	07 16 31.2	–29 19 28	25.8	Sy2	···	83	168	···	···	6
NGC 2369	07 16 37.7	–62 20 37	46.2	H II	124	<0.51	10	<0.91	1.8	2
NGC 2388	07 28 53.4	+33 49 08	58.9	H II	121	<1.2	9.8	<0.79	1.4	2
MCG +02-20-003	07 35 43.4	+11 42 33	71.1	H II	60	<0.47	6.3	<0.53	<1.2	2
NGC 2403	07 36 51.4	+65 36 09	3.20	H II	5.1	<0.71	2.1	···	<0.36	5
Mrk 9 [d]	07 36 57.0	+58 46 13	176	Sy1	3.2	2.2	1.9	2.2	5.6	4

Table 3.5: *Continued*

Name	R.A.[a] (J2000.0)	Decl.[a] (J2000.0)	Dist.[b] (Mpc)	Spect. Class.[a]	[Ne II] 12.81 μm	[Ne V] 14.32 μm	[Ne III] 15.56 μm	[Ne V] 24.32 μm	[O IV] 25.89 μm	Ref.
3C 184	07 39 24.5	+70 23 10	6559	Sy2	0.19	0.17	0.65	···	···	6
Mrk 79 [d]	07 42 32.8	+49 48 34	96.7	Sy1	10	6.6	20	13	42	4
ESO 209-G009	07 58 15.4	–49 51 15	11.8	···	9.8	<0.26	1.4	<0.12	<0.29	7
IRAS F07598+6508	08 04 33.1	+64 59 48	703	···	3.9	<0.75	2.5	<3.0	<1.8	3
3C 196	08 13 36.0	+48 13 02	5572	Sy1	···	0.30	0.46	···	···	6
IRAS 08311–2459	08 33 20.6	–25 09 33	460	Sy1	24	12	23	9.8	26	3
UGC 4459	08 34 07.2	+66 10 54	2.78	···	···	<0.89	0.98	···	<0.37	5
NGC 2623	08 38 24.1	+25 45 16	77.4	Sy2	56	2.7	15	2.2	9.6	8
NGC 2639 [c] [d]	08 43 38.1	+50 12 20	44.6	Sy1	8.9	<0.45	4.9	<0.82	1.8	2
PG 0838+770	08 44 45.3	+76 53 09	615	QSO	0.41	0.32	0.56	<0.19	1.3	1
PG 0844+349	08 47 42.5	+34 45 04	287	QSO	0.42	0.30	1.0	0.42	1.5	1
NGC 2681	08 53 32.7	+51 18 49	12.5	···	6.9	<0.15	3.4	<0.36	2.2	7
NGC 2685 [c]	08 55 34.7	+58 44 03	12.7	Sy2	···	<0.28	···	<0.22	0.43	2
NGC 2655 [c] [d]	08 55 37.7	+78 13 23	20.2	Sy2	13	<1.3	7.2	<1.3	<8.0	2
IRAS F08572+3915	09 00 25.4	+39 03 54	259	···	7.2	<0.75	2.0	<5.4	<6.0	3
IRAS 09022–3615	09 04 12.7	–36 27 01	269	···	57	<2.4	40	<3.6	6.7	3
NGC 2798	09 17 22.9	+41 59 59	26.2	H II	215	<1.9	33	···	<5.1	5
Mrk 704 [d]	09 18 26.0	+16 18 19	128	Sy1	···	3.9	5.6	<3.7	12	4
NGC 2841	09 22 02.6	+50 58 35	14.1	LINER	5.7	<4.5	6.7	···	0.78	5
NGC 2915	09 26 11.5	–76 37 34	3.80	H II	3.2	<0.75	11	···	0.45	5
NGC 2903	09 32 10.1	+21 30 03	8.30	H II	182	<0.82	14	<0.94	<1.7	7
UGC 5101	09 35 51.7	+61 21 11	172	LINER	34	2.6	14	2.8	7.3	3
NGC 2992 [c] [d]	09 45 42.1	–14 19 34	33.2	Sy2	46	22	61	28	131	2

Table 3.5: *Continued*

Name	R.A.[a] (J2000.0)	Decl.[a] (J2000.0)	Dist.[b] (Mpc)	Spect. Class.[a]	[Ne II] 12.81 μm	[Ne V] 14.32 μm	[Ne III] 15.56 μm	[Ne V] 24.32 μm	[O IV] 25.89 μm	Ref.
NGC 2976	09 47 15.5	+67 54 59	3.60	H II	7.4	<0.99	2.8	···	<0.31	5
NGC 3059	09 50 08.2	–73 55 19	14.2	···	27	<0.18	3.1	<0.69	<1.5	7
Mrk 1239 [d]	09 52 19.1	–01 36 43	86.7	Sy1	9.4	3.4	9.4	3.2	16	4
NGC 3049	09 54 49.6	+09 16 15	23.9	H II	39	<0.89	6.0	···	<1.00	5
NGC 3031 [c] [d]	09 55 33.2	+69 03 55	3.64	Sy1	27	<0.50	21	<1.4	4.5	2
M 82	09 55 52.7	+69 40 45	3.60	H II	506	<0.89	81	<15	46	7
Holmberg IX	09 57 32.0	+69 02 45	2.64	···	···	<0.64	···	···	<0.38	5
NGC 3081 [c]	09 59 29.5	–22 49 34	34.3	Sy2	12	30	34	39	118	2
3C 234 [d]	10 01 49.5	+28 47 08	897	Sy2	···	2.3	3.4	2.9	9.0	4
NGC 3079 [c] [d]	10 01 57.8	+55 40 47	16.2	Sy2	108	0.91	24	<0.89	11	2
NGC 3110	10 04 02.1	–06 28 29	72.4	H II	75	<0.68	9.9	<0.62	1.2	2
PG 1001+054	10 04 20.1	+05 13 00	771	QSO	0.40	<0.21	0.21	<0.30	0.52	1
NGC 3175	10 14 42.1	–28 52 19	13.4	H II	34	<0.35	2.5	<0.86	1.1	7
IC 2560 [c]	10 16 18.7	–33 33 49	41.7	Sy2	16	19	36	18	56	2
NGC 3147 [c] [d]	10 16 53.7	+73 24 02	40.3	Sy2	4.5	<0.59	3.4	<0.91	<2.5	2
NGC 3185 [c]	10 17 38.6	+21 41 17	17.7	Sy2	9.6	1.0	3.6	1.8	8.2	2
NGC 3190	10 18 05.6	+21 49 55	20.9	LINER	8.3	<0.67	4.8	···	0.93	5
NGC 3184	10 18 17.0	+41 25 27	11.1	H II	18	<0.83	2.2	···	<0.29	5
NGC 3198	10 19 54.9	+45 32 59	13.7	···	15	<1.00	0.81	···	<0.32	5
NGC 3227 [c] [d]	10 23 30.6	+19 51 54	15.7	Sy1	66	23	74	18	70	2
NGC 3245	10 27 18.4	+28 30 26	18.2	H II	9.9	<0.21	3.0	<0.76	0.71	2
NGC 3256	10 27 51.3	–43 54 13	40.1	H II	780	<1.9	119	<7.9	<20	2
NGC 3265	10 31 06.8	+28 47 48	23.2	H II	30	<0.78	5.4	···	<0.71	5

Table 3.5: *Continued*

Name	R.A.[a] (J2000.0)	Decl.[a] (J2000.0)	Dist.[b] (Mpc)	Spect. Class.[a]	[Ne II] 12.81 μm	[Ne V] 14.32 μm	[Ne III] 15.56 μm	[Ne V] 24.32 μm	[O IV] 25.89 μm	Ref.
NGC 3281 [c]	10 31 52.1	–34 51 13	49.6	Sy2	17	47	58	46	173	2
Mrk 33	10 32 31.9	+54 24 03	22.9	H II	59	<1.0	45	···	0.89	5
3C 244.1	10 33 34.0	+58 14 35	2353	Sy2	1.4	0.60	0.30	···	···	6
NGC 3310	10 38 45.9	+53 30 12	19.8	H II	28	<0.25	28	<1.0	4.0	8
IRAS 10378+1109	10 40 29.2	+10 53 18	641	LINER	3.5	<1.1	0.60	<2.4	2.0	3
NGC 3351	10 43 57.7	+11 42 13	9.30	H II	219	<2.3	18	···	2.5	5
NGC 3368	10 46 45.7	+11 49 11	10.5	LINER	4.3	<0.29	2.8	<0.74	0.99	7
NGC 3393	10 48 23.5	–25 09 43	56.2	Sy2	···	42	95	···	···	6
IRAS F10565+2448	10 59 18.1	+24 32 34	190	H II	64	<1.00	7.6	<0.90	<1.2	3
NGC 3511 [d]	11 03 23.8	–23 05 12	15.9	Sy1	8.7	<0.49	1.00	<1.7	<1.8	4
NGC 3507	11 03 25.4	+18 08 07	14.2	LINER	3.7	<0.12	1.4	<0.55	<0.21	2
3C 249.1	11 04 13.7	+76 58 58	1619	Sy1	···	0.090	0.14	···	<0.23	6
NGC 3521	11 05 48.6	–00 02 09	10.1	H II	14	<0.95	7.4	···	2.2	5
NGC 3516 [c] [d]	11 06 47.5	+72 34 06	38.0	Sy1	7.2	7.3	16	9.5	44	2
ESO 265-G007	11 07 49.6	–46 31 27	11.7	···	2.6	<0.41	1.1	<1.2	<1.0	7
NGC 3556	11 11 31.0	+55 40 26	13.9	H II	21	<0.37	3.2	<1.2	<1.5	8
IRAS F11095–0238	11 12 03.4	–02 54 22	495	LINER	6.1	<0.48	1.9	<1.8	<0.90	3
IRAS F11119+3257	11 14 38.9	+32 41 33	920	Sy1	3.0	0.75	2.0	<0.90	1.9	3
NGC 3621	11 18 16.5	–32 48 50	6.60	H II	16	1.0	5.7	···	4.6	5
NGC 3627	11 20 15.0	+12 59 29	9.40	Sy2	23	<0.92	8.5	···	1.7	5
NGC 3628	11 20 17.0	+13 35 22	10.00	LINER	126	0.90	10	<1.0	<2.4	8
MCG +00-29-023 [d]	11 21 12.3	–02 59 03	109	Sy2	47	<1.0	4.4	<5.4	<6.0	4
PG 1119+120	11 21 47.1	+11 44 18	222	QSO	0.46	1.7	2.7	1.3	5.9	1

Table 3.5: *Continued*

Name	R.A.[a] (J2000.0)	Decl.[a] (J2000.0)	Dist.[b] (Mpc)	Spect. Class.[a]	[Ne II] 12.81 μm	[Ne V] 14.32 μm	[Ne III] 15.56 μm	[Ne V] 24.32 μm	[O IV] 25.89 μm	Ref.
NGC 3642	11 22 17.9	+59 04 28	22.3	LINER	2.8	<0.11	0.97	<0.54	<0.18	2
NGC 3660 [d]	11 23 32.3	–08 39 30	53.1	Sy2	6.5	0.98	1.5	1.7	3.6	4
IRAS 11215–2806 [c]	11 24 02.8	–28 23 15	59.5	Sy2	1.5	2.6	5.2	2.8	12	2
NGC 3675	11 26 08.6	+43 35 09	12.7	H II	8.1	<0.23	2.2	<0.48	<0.58	7
IC 694	11 28 27.3	+58 34 42	44.5	H II	294	<1.6	69	<4.7	<19	2
NGC 3690	11 28 32.2	+58 33 44	44.0	Sy2	151	<1.5	77	<4.6	21	2
PG 1126-041	11 29 16.7	–04 24 07	269	QSO	1.4	4.3	5.2	4.7	16	1
NGC 3726	11 33 21.1	+47 01 45	14.5	H II	5.5	<0.41	0.43	<0.52	<0.44	7
NGC 3735 [c] [d]	11 35 57.3	+70 32 08	38.9	Sy2	9.4	7.1	13	9.8	37	2
NGC 3773	11 38 12.9	+12 06 43	11.9	H II	18	<0.81	16	···	0.36	5
NGC 3783 [c]	11 39 01.7	–37 44 18	41.6	Sy1	18	16	27	12	40	2
NGC 3884	11 46 12.2	+20 23 29	101	LINER	1.5	<0.12	0.86	<0.72	<0.72	2
NGC 3898	11 49 15.4	+56 05 03	16.1	H II	1.0	<0.13	1.3	<0.51	0.40	2
NGC 3938	11 52 49.5	+44 07 14	13.3	H II	5.4	<0.66	1.0	···	0.25	5
ESO 320-G030	11 53 11.7	–39 07 48	43.6	H II	110	<0.53	11	<1.6	<0.88	2
NGC 3949	11 53 41.7	+47 51 31	13.6	H II	5.8	<0.11	1.1	<0.11	1.5	7
NGC 3976 [c]	11 55 57.6	+06 45 02	36.0	Sy2	2.3	<0.26	1.1	<0.35	0.73	2
NGC 3982 [c] [d]	11 56 28.1	+55 07 30	15.2	Sy2	9.2	3.0	6.7	1.7	4.6	2
NGC 3998	11 57 56.1	+55 27 12	14.6	LINER	11	<0.18	6.9	<0.65	0.74	2
NGC 4013	11 58 31.4	+43 56 47	13.8	H II	13	<0.090	2.8	<0.89	<1.0	7
NGC 4036	12 01 26.8	+61 53 44	19.1	LINER	4.4	<0.060	2.8	<0.37	1.4	2
NGC 4051 [c] [d]	12 03 09.6	+44 31 52	9.27	Sy1	17	11	16	10	32	2
IRAS F12018+1941	12 04 24.5	+19 25 09	813	LINER	3.0	<0.80	0.35	<0.10	<0.63	3

Table 3.5: *Continued*

Name	R.A.[a] (J2000.0)	Decl.[a] (J2000.0)	Dist.[b] (Mpc)	Spect. Class.[a]	[Ne II] 12.81 μm	[Ne V] 14.32 μm	[Ne III] 15.56 μm	[Ne V] 24.32 μm	[O IV] 25.89 μm	Ref.
NGC 4085	12 05 22.7	+50 21 10	14.6	H II	23	<0.15	2.9	<0.92	<0.44	7
NGC 4088	12 05 34.2	+50 32 20	13.4	H II	37	<0.39	2.5	<0.50	0.73	8
NGC 4125	12 08 06.0	+65 10 26	22.9	LINER	2.3	<0.62	3.3	···	0.75	5
IRAS 12071–0444	12 09 45.1	–05 01 13	600	Sy2	5.2	2.9	5.1	3.7	6.6	3
NGC 4151 [c] [d]	12 10 32.6	+39 24 20	14.0	Sy1	131	77	205	68	244	2
NGC 4157	12 11 04.4	+50 29 04	13.3	H II	12	<0.070	1.4	<0.70	1.1	7
NGC 4192	12 13 48.3	+14 54 01	19.3	H II	19	<0.18	4.7	<0.48	1.6	2
NGC 4194	12 14 09.5	+54 31 36	40.3	Sy2	165	3.0	54	4.0	27	8
PG 1211+143	12 14 17.7	+14 03 12	368	QSO	0.32	<0.43	0.73	<0.56	2.4	1
NGC 4236	12 16 42.1	+69 27 45	4.36	···	···	<1.5	···	···	<0.23	5
NGC 4235 [c]	12 17 09.9	+07 11 29	33.5	Sy1	3.8	<0.43	3.3	<0.54	3.3	2
Mrk 766 [d]	12 18 26.5	+29 48 46	55.9	Sy1	23	21	24	18	46	4
NGC 4254	12 18 49.6	+14 24 59	16.6	H II	53	<0.92	6.1	···	2.5	5
NGC 4258 [c]	12 18 57.5	+47 18 14	6.60	Sy1	12	<1.3	8.1	<0.82	7.5	2
NGC 4278	12 20 06.8	+29 16 50	9.17	LINER	5.4	<0.23	3.9	<0.29	0.88	2
NGC 4321	12 22 54.9	+15 49 20	14.3	LINER	152	<1.2	18	···	<1.9	5
Mrk 52	12 25 42.8	+00 34 21	30.1	H II	29	<0.57	3.8	<0.83	1.3	8
NGC 4388 [c] [d]	12 25 46.7	+12 39 43	36.3	Sy2	75	45	106	68	308	2
NGC 4395 [c]	12 25 48.9	+33 32 48	4.33	Sy1	4.9	0.93	6.8	1.4	6.9	2
NGC 4419	12 26 56.4	+15 02 50	17.2	H II	36	<0.46	8.5	<1.0	<1.6	2
NGC 4435	12 27 40.5	+13 04 44	11.9	H II	6.8	<0.24	2.1	<0.67	1.1	2
NGC 4450	12 28 29.6	+17 05 05	16.6	LINER	3.5	<0.53	2.1	···	0.63	5
NGC 4457	12 28 59.0	+03 34 14	12.4	LINER	7.8	<0.18	3.2	<0.47	2.2	2

Table 3.5: *Continued*

Name	R.A.[a] (J2000.0)	Decl.[a] (J2000.0)	Dist.[b] (Mpc)	Spect. Class.[a]	[Ne II] 12.81 μm	[Ne V] 14.32 μm	[Ne III] 15.56 μm	[Ne V] 24.32 μm	[O IV] 25.89 μm	Ref.
3C 273	12 29 06.7	+02 03 08	755	Sy1	1.5	3.4	6.0	2.9	8.5	3
NGC 4477 [c]	12 30 02.2	+13 38 11	19.3	Sy2	3.2	<0.33	2.8	<3.5	1.3	2
NGC 4490	12 30 36.4	+41 38 37	10.5	···	3.5	<0.10	3.5	<0.10	1.1	7
NGC 4486	12 30 49.4	+12 23 28	17.0	Sy2	6.9	<0.19	5.4	<0.57	1.2	2
NGC 4501 [c d]	12 31 59.2	+14 25 13	32.7	Sy2	5.0	<0.47	4.7	<0.43	2.5	2
PG 1229+204	12 32 03.6	+20 09 29	283	QSO	0.61	0.91	1.3	0.99	2.8	1
NGC 4536	12 34 27.1	+02 11 17	14.4	H II	386	<1.2	60	···	<7.9	5
NGC 4507 [c]	12 35 36.6	–39 54 33	50.9	Sy2	30	12	29	8.6	34	2
NGC 4552	12 35 39.8	+12 33 22	15.9	LINER	1.7	<0.89	2.9	···	<0.53	5
NGC 4559	12 35 57.7	+27 57 35	10.3	H II	8.3	<1.0	2.3	···	0.12	5
NGC 4565 [c d]	12 36 20.8	+25 59 15	18.1	Sy1	2.6	0.32	3.3	<0.82	4.1	2
NGC 4569	12 36 49.8	+13 09 46	16.6	LINER	36	<0.93	16	···	2.9	5
NGC 4579 [c d]	12 37 43.5	+11 49 05	21.5	Sy1	23	<0.40	12	<0.68	3.2	2
NGC 4593 [c d]	12 39 39.4	–05 20 39	38.8	Sy1	6.8	3.5	7.4	5.4	13	2
NGC 4594 [c d]	12 39 59.4	–11 37 23	15.7	Sy1	14	<0.55	16	<0.71	2.4	2
NGC 4602 [d]	12 40 36.9	–05 07 58	36.5	Sy1	7.6	0.82	0.63	<1.2	<2.3	4
TOL 1238-364 [c d]	12 40 52.9	–36 45 21	47.7	Sy2	42	9.0	27	3.5	17	2
NGC 4625	12 41 52.7	+41 16 26	9.20	···	5.9	<0.84	1.2	···	<0.26	5
NGC 4631	12 42 08.0	+32 32 29	8.10	H II	133	<0.52	30	···	3.0	5
NGC 4639 [c]	12 42 52.4	+13 15 26	14.0	Sy1	0.84	<0.27	1.1	<0.28	<1.2	2
NGC 4666	12 45 08.6	–00 27 42	21.5	LINER	35	<0.30	8.3	1.4	6.3	2
NGC 4676	12 46 10.1	+30 43 55	94.0	H II	28	<0.25	4.7	<0.33	1.4	8
PG 1244+026	12 46 35.2	+02 22 08	213	QSO	0.94	0.53	1.2	1.1	1.5	1

Table 3.5: *Continued*

Name	R.A.[a] (J2000.0)	Decl.[a] (J2000.0)	Dist.[b] (Mpc)	Spect. Class.[a]	[Ne II] 12.81 μm	[Ne V] 14.32 μm	[Ne III] 15.56 μm	[Ne V] 24.32 μm	[O IV] 25.89 μm	Ref.
NGC 4725 [c d]	12 50 26.6	+25 30 03	17.4	Sy2	1.2	<0.38	2.4	<0.50	1.8	2
NGC 4736	12 50 53.1	+41 07 13	5.00	LINER	13	<0.81	14	···	3.3	5
NGC 4748 [d]	12 52 12.5	–13 24 53	63.4	Sy1	7.4	6.7	16	20	82	4
IRAS F12514+1027	12 54 00.8	+10 11 12	1667	Sy2	2.3	1.9	2.7	1.7	2.7	3
Mrk 231	12 56 14.2	+56 52 25	186	Sy1	20	<3.0	3.0	<18	<9.5	3
NGC 4826	12 56 43.7	+21 40 57	5.00	Sy2	105	<1.3	23	···	4.3	5
NGC 4818	12 56 48.9	–08 31 31	9.40	H II	185	<1.2	14	<2.0	<1.6	8
NGC 4922 [d]	13 01 24.9	+29 18 40	103	LINER	36	2.4	9.2	<1.9	4.3	2
MCG –02-33-098-W	13 02 19.7	–15 46 03	68.1	H II	67	<0.51	12	<0.79	<1.2	2
MCG –02-33-098-E	13 02 20.4	–15 45 59	68.9	H II	32	<0.58	12	<0.61	1.2	2
NGC 4941 [c d]	13 04 13.1	–05 33 05	15.9	Sy2	13	7.2	24	6.9	26	2
NGC 4939 [c]	13 04 14.4	–10 20 22	44.8	Sy2	8.1	12	24	17	65	2
NGC 4945 [c]	13 05 27.5	–49 28 05	8.19	Sy2	586	3.4	69	<5.1	35	2
PG 1302-102	13 05 33.0	–10 33 19	1422	QSO	0.36	0.49	0.66	0.39	2.6	1
UGC 8201	13 06 24.9	+67 42 25	3.68	···	···	<0.75	···	···	<0.24	5
NGC 4968 [d]	13 07 06.0	–23 40 37	42.6	Sy2	25	18	34	11	34	4
PG 1307+085	13 09 47.0	+08 19 48	739	QSO	0.40	0.56	0.98	0.62	0.74	1
NGC 5005 [c d]	13 10 56.2	+37 03 33	13.8	Sy2	37	<1.1	13	<1.2	4.6	2
PG 1309+355	13 12 17.8	+35 15 21	893	QSO	0.51	0.27	1.3	<0.30	<0.49	1
NGC 5033 [c d]	13 13 27.5	+36 35 38	12.4	Sy1	31	1.2	14	2.0	9.2	2
IC 860	13 15 03.5	+24 37 07	55.8	H II	3.6	<0.14	0.68	<0.48	<0.62	2
IRAS 13120–5453	13 15 06.3	–55 09 22	136	Sy2	150	1.7	18	<20	6.4	3
NGC 5055	13 15 49.3	+42 01 45	7.80	LINER	22	<0.95	9.6	···	2.3	5

Table 3.5: *Continued*

Name	R.A.[a] (J2000.0)	Decl.[a] (J2000.0)	Dist.[b] (Mpc)	Spect. Class.[a]	[Ne II] 12.81 μm	[Ne V] 14.32 μm	[Ne III] 15.56 μm	[Ne V] 24.32 μm	[O IV] 25.89 μm	Ref.
UGC 8387	13 20 35.3	+34 08 22	101	H II	113	<0.54	19	<2.3	6.2	2
NGC 5104	13 21 23.1	+00 20 32	80.0	LINER	43	<0.39	5.1	<1.2	2.4	2
MCG –03-34-064 [d]	13 22 24.5	–16 43 42	71.7	Sy1	56	63	119	38	115	4
NGC 5128 [c]	13 25 27.6	–43 01 08	7.85	Sy2	197	23	150	28	135	2
NGC 5135 [c d]	13 25 44.1	–29 50 01	58.9	Sy2	112	14	58	18	73	2
NGC 5194 [c d]	13 29 52.7	+47 11 42	6.77	Sy2	44	3.0	34	3.9	19	2
NGC 5195	13 29 59.6	+47 15 58	8.00	LINER	18	<1.0	6.9	···	<1.9	5
3C 286	13 31 08.3	+30 30 32	5399	Sy1	···	0.75	0.69	···	···	6
NGC 5218	13 32 10.4	+62 46 03	41.1	H II	45	<0.16	4.9	<0.57	<2.3	2
MCG –06-30-015 [d]	13 35 53.8	–34 17 44	33.4	Sy1	5.0	5.0	5.9	7.4	26	4
IRAS F13342+3932	13 36 24.1	+39 17 31	866	Sy1	5.7	3.5	5.0	4.2	10	3
NGC 5236	13 37 00.9	–29 51 55	3.60	H II	503	<0.61	29	<1.2	5.7	7
Mrk 266 [d]	13 38 17.5	+48 16 37	116	Sy2	57	8.0	28	11	53	8
NGC 5273 [c]	13 42 08.3	+35 39 15	15.2	Sy1	2.0	<1.5	3.4	<0.88	4.9	2
Mrk 273	13 44 42.1	+55 53 12	167	LINER	42	12	34	15	56	3
IRAS F13451+1232	13 47 33.4	+12 17 24	565	Sy2	5.0	<1.0	5.1	<2.1	2.1	3
IC 4329A [d]	13 49 19.3	–30 18 34	69.6	Sy1	28	29	57	35	117	4
PG 1351+640	13 53 15.8	+63 45 45	402	QSO	1.8	<0.92	2.7	<1.00	<0.90	1
NGC 5347 [d]	13 53 17.8	+33 29 26	33.6	Sy2	4.2	2.1	4.1	<1.7	7.6	4
NGC 5371	13 55 39.9	+40 27 42	37.1	LINER	1.7	<0.090	1.1	<0.32	<0.50	2
Mrk 463	13 56 02.9	+18 22 19	222	Sy1	9.3	18	41	20	69	3
NGC 5395 [c]	13 58 38.0	+37 25 28	50.3	Sy2	···	<0.54	···	<0.31	<0.18	2
NGC 5398	14 01 21.6	–33 03 49	10.8	···	···	<0.50	···	···	<0.31	5

Table 3.5: *Continued*

Name	R.A.[a] (J2000.0)	Decl.[a] (J2000.0)	Dist.[b] (Mpc)	Spect. Class.[a]	[Ne II] 12.81 μm	[Ne V] 14.32 μm	[Ne III] 15.56 μm	[Ne V] 24.32 μm	[O IV] 25.89 μm	Ref.
NGC 5408	14 03 20.9	–41 22 39	4.85	H II	···	<0.93	1.2	···	<0.51	5
NGC 5427 [c]	14 03 26.1	–06 01 50	37.5	Sy2	10	1.7	5.1	1.2	4.2	2
NGC 5474	14 05 01.6	+53 39 44	6.40	H II	···	<0.83	···	···	<0.31	5
IRAS F14070+0525	14 09 31.3	+05 11 31	1341	Sy2	1.8	<0.15	0.58	<0.60	<1.5	3
3C 295	14 11 20.6	+52 12 09	2571	Sy2	0.060	0.070	0.050	···	···	6
Circinus [c]	14 13 09.9	–65 20 20	6.09	Sy2	427	219	379	261	871	2
NGC 5506 [c] [d]	14 13 14.9	–03 12 27	26.1	Sy1	81	58	151	63	239	2
PG 1411+442	14 13 48.3	+44 00 13	411	QSO	0.36	0.96	0.92	0.55	1.5	1
NGC 5548 [d]	14 17 59.5	+25 08 12	74.5	Sy1	8.5	5.4	7.3	3.9	17	4
PG 1426+015	14 29 06.6	+01 17 06	392	QSO	1.3	1.2	2.3	0.75	3.4	1
NGC 5653	14 30 10.4	+31 12 55	50.6	H II	70	<0.55	5.9	<0.25	<1.2	2
NGC 5643 [c]	14 32 40.8	–44 10 28	16.9	Sy2	38	25	56	30	121	2
Mrk 817 [d]	14 36 22.1	+58 47 39	138	Sy1	3.8	1.9	4.6	3.6	6.5	4
IRAS F14348–1447	14 37 38.4	–15 00 22	378	LINER	11	<0.21	2.6	<1.5	<3.3	3
NGC 5713	14 40 11.5	–00 17 20	29.4	H II	127	<0.80	17	···	2.8	5
IRAS F14378–3651	14 40 59.0	–37 04 32	306	LINER	11	<0.90	1.2	<2.3	<3.8	3
PG 1440+356	14 42 07.5	+35 26 22	358	QSO	4.1	1.3	3.9	1.9	6.3	1
NGC 5728 [c]	14 42 23.9	–17 15 11	40.9	Sy2	28	22	53	27	116	2
3C 303.1	14 43 14.9	+77 07 28	1358	Sy2	0.040	<0.020	0.070	···	0.090	6
NGC 5734	14 45 09.1	–20 52 13	58.0	H II	77	<0.96	8.2	<0.23	0.93	2
NGC 5743	14 45 11.0	–20 54 48	59.7	H II	50	1.3	8.9	0.78	3.2	2
PG 1448+273	14 51 08.8	+27 09 26	292	QSO	0.51	2.7	3.1	4.1	10	1
IC 4518W	14 57 41.2	–43 07 55	68.5	Sy1	40	25	49	24	85	2

Table 3.5: *Continued*

Name	R.A.[a] (J2000.0)	Decl.[a] (J2000.0)	Dist.[b] (Mpc)	Spect. Class.[a]	[Ne II] 12.81 μm	[Ne V] 14.32 μm	[Ne III] 15.56 μm	[Ne V] 24.32 μm	[O IV] 25.89 μm	Ref.
IC 4518E	14 57 44.6	–43 07 53	65.4	H II	18	<0.63	1.7	<0.26	0.33	2
3C 309.1	14 59 07.6	+71 40 19	5833	Sy2	···	0.30	0.40	···	···	6
IRAS F15001+1433	15 02 31.9	+14 21 35	781	Sy2	6.8	1.1	2.6	0.66	1.7	3
PG 1501+106	15 04 01.2	+10 26 16	158	QSO	3.6	8.0	11	8.0	24	1
NGC 5866	15 06 29.5	+55 45 47	15.1	H II	7.8	<0.97	4.9	···	0.93	5
IRAS F15091–2107 [d]	15 11 59.8	–21 19 01	198	Sy1	12	8.5	16	8.1	31	4
CGCG 049-057	15 13 13.1	+07 13 31	55.8	H II	20	<0.58	1.5	<0.82	<0.59	2
NGC 5899 [c] [d]	15 15 03.2	+42 02 59	37.0	Sy2	11	6.8	16	6.7	22	2
NGC 5907	15 15 53.8	+56 19 43	12.1	H II	6.1	<0.0100	1.3	<0.070	1.6	7
VV 705	15 18 06.3	+42 44 36	178	···	62	<0.33	14	<0.79	<2.8	2
IRAS F15206+3342	15 22 38.0	+33 31 35	580	H II	13	<0.40	21	<1.5	<2.4	3
NGC 5929 [d]	15 26 06.2	+41 40 14	35.8	Sy2	13	1.1	9.8	2.2	5.3	4
IRAS 15250+3609	15 26 59.4	+35 58 37	245	LINER	10	<1.2	2.7	<2.4	<1.5	3
NGC 5936	15 30 00.8	+12 59 21	57.1	H II	82	<0.81	6.1	<0.63	1.1	2
3C 321	15 31 43.5	+24 04 19	441	Sy2	···	0.70	0.57	···	1.9	6
NGC 5953	15 34 32.4	+15 11 37	28.9	LINER	51	1.4	17	3.0	17	2
Arp 220	15 34 57.1	+23 30 11	78.2	H II	65	<2.9	7.8	<14	<21	3
IRAS 15335–0513	15 36 11.7	–05 23 52	119	H II	32	<0.19	6.1	<0.95	<1.4	2
3C 323.1	15 47 43.5	+20 52 16	1341	Sy1	0.12	<0.060	0.11	···	0.17	6
MCG –02-40-004 [d]	15 48 25.0	–13 45 27	110	Sy2	16	6.1	8.5	3.1	13	4
IRAS F15462–0450	15 48 56.8	–04 59 33	460	Sy1	7.4	<0.30	1.4	<1.0	<3.6	3
IRAS FSC15480–0344 [d]	15 50 41.5	–03 53 18	133	Sy2	5.6	6.1	9.4	8.9	35	4
3C 330	16 09 36.6	+65 56 43	3170	Sy2	···	0.40	0.40	···	···	6

Table 3.5: *Continued*

Name	R.A.[a] (J2000.0)	Decl.[a] (J2000.0)	Dist.[b] (Mpc)	Spect. Class.[a]	[Ne II] 12.81 μm	[Ne V] 14.32 μm	[Ne III] 15.56 μm	[Ne V] 24.32 μm	[O IV] 25.89 μm	Ref.
IRAS F16090–0139	16 11 40.5	–01 47 05	631	LINER	7.8	<0.12	2.0	<2.0	<1.4	3
PG 1613+658	16 13 57.2	+65 43 09	605	QSO	3.9	1.1	3.3	0.65	4.9	1
IRAS 16164–0746	16 19 11.8	–07 54 02	102	LINER	47	1.2	14	<1.2	7.2	2
PG 1617+175	16 20 11.3	+17 24 27	520	QSO	0.29	<0.17	0.36	0.28	0.39	1
3C 334	16 20 21.8	+17 36 23	3212	Sy1	0.66	1.2	1.6	···	···	6
PG 1626+554	16 27 56.1	+55 22 31	626	QSO	0.069	<0.069	0.11	<0.16	<0.20	1
3C 343	16 34 33.8	+62 45 35	6510	Sy1	0.70	0.83	1.4	···	···	6
NGC 6221 [c]	16 52 46.1	–59 13 07	20.8	Sy2	196	<1.6	24	<3.1	20	2
NGC 6240	16 52 58.9	+02 24 03	105	LINER	171	4.4	61	<5.7	27	3
NGC 6285	16 58 24.0	+58 57 21	82.3	H II	18	<0.080	3.0	<0.48	1.2	2
NGC 6286	16 58 31.4	+58 56 10	79.2	LINER	29	<0.43	3.3	1.6	<0.75	2
PG 1700+518	17 01 24.8	+51 49 20	1505	QSO	1.2	<0.23	1.6	<0.43	1.7	1
3C 351	17 04 41.4	+60 44 30	1988	Sy1	0.100	0.22	0.21	···	···	6
IRAS 17138–1017	17 16 35.8	–10 20 39	74.6	H II	124	<0.81	20	<1.3	<3.4	2
NGC 6300 [c]	17 16 59.5	–62 49 14	15.9	Sy2	11	13	15	9.1	31	2
IRAS F17179+5444	17 18 54.4	+54 41 48	698	Sy2	4.5	2.2	2.9	0.82	2.1	3
IRAS 17208–0014	17 23 22.0	–00 17 00	190	H II	41	<1.00	8.1	<3.2	<2.4	3
NGC 6500	17 55 59.8	+18 20 17	43.1	LINER	4.8	<0.11	2.6	<0.49	<0.35	2
IC 4687	18 13 39.6	–57 43 31	73.8	H II	146	<0.80	45	<1.2	2.5	2
IC 4710	18 28 38.0	–66 58 56	9.00	···	0.88	<1.0	4.3	···	<0.30	5
3C 381	18 33 46.3	+47 27 02	771	Sy1	0.060	0.070	0.13	···	0.22	6
ESO 103-G035	18 38 20.3	–65 25 39	56.2	Sy2	···	18	41	···	···	6
IC 4734	18 38 25.7	–57 29 25	66.7	H II	65	<0.48	6.1	<0.66	<1.8	2

Table 3.5: *Continued*

Name	R.A.[a] (J2000.0)	Decl.[a] (J2000.0)	Dist.[b] (Mpc)	Spect. Class.[a]	[Ne II] 12.81 μm	[Ne V] 14.32 μm	[Ne III] 15.56 μm	[Ne V] 24.32 μm	[O IV] 25.89 μm	Ref.
NGC 6701	18 43 12.5	+60 39 12	56.2	H II	73	<0.59	7.0	<0.63	2.1	2
NGC 6744	19 09 46.1	–63 51 27	9.90	LINER	1.1	<0.030	1.5	<0.13	<0.73	7
ESO 593-IG008	19 14 30.9	–21 19 07	218	···	32	<0.72	8.9	<0.29	<0.78	2
ESO 141-G055 [d]	19 21 14.2	–58 40 13	158	Sy1	2.2	2.2	5.6	1.6	7.3	4
IRAS F19254–7245	19 31 21.4	–72 39 18	283	Sy2	31	<2.8	13	<1.6	6.3	3
IRAS F19297–0406	19 32 21.3	–03 59 56	392	H II	18	<0.92	2.5	<2.2	<0.90	3
NGC 6814 [c]	19 42 40.6	–10 19 24	22.4	Sy1	7.2	3.2	15	6.1	27	2
NGC 6810 [d]	19 43 34.4	–58 39 20	29.2	Sy2	103	<1.1	13	<2.3	2.5	4
NGC 6860 [d]	20 08 46.9	–61 06 00	64.5	Sy1	5.6	2.8	6.7	2.4	12	4
IRAS F20087–0308	20 11 23.9	–02 59 50	490	LINER	14	<0.75	1.6	<1.9	<1.6	3
IRAS F20100–4156	20 13 29.5	–41 47 34	610	H II	7.3	<0.48	2.8	<1.3	<4.8	3
NGC 6890 [d]	20 18 18.1	–44 48 25	34.8	Sy2	11	5.8	6.6	3.8	10	4
NGC 6946	20 34 52.3	+60 09 14	6.80	H II	430	<1.5	39	···	<7.2	5
NGC 6951 [c]	20 37 14.1	+66 06 20	19.8	Sy2	40	<1.8	11	<2.0	8.2	2
Mrk 509 [c] [d]	20 44 09.7	–10 43 24	151	Sy1	11	5.1	16	7.4	28	2
IRAS F20414–1651	20 44 18.2	–16 40 16	397	LINER	6.8	1.00	1.6	<1.5	<1.8	3
IC 5063 [d]	20 52 02.3	–57 04 07	49.0	Sy2	27	30	66	24	114	4
IRAS F20551–4250	20 58 26.8	–42 39 00	190	H II	13	<0.75	2.8	<1.5	<2.0	3
Mrk 897 [d]	21 07 45.8	+03 52 40	115	Sy2	24	1.1	4.4	<0.80	0.62	4
3C 433	21 23 44.5	+25 04 11	470	Sy2	1.9	2.7	5.2	···	<7.9	6
PG 2130+099	21 32 27.8	+10 08 19	283	QSO	1.4	3.7	5.7	4.0	11	1
NGC 7130 [c] [d]	21 48 19.5	–34 57 04	69.8	Sy2	82	7.1	27	4.2	15	2
NGC 7177	22 00 41.2	+17 44 17	16.1	H II	4.2	<0.11	1.5	<0.48	0.54	2

Table 3.5: *Continued*

Name	R.A.[a] (J2000.0)	Decl.[a] (J2000.0)	Dist.[b] (Mpc)	Spect. Class.[a]	[Ne II] 12.81 μm	[Ne V] 14.32 μm	[Ne III] 15.56 μm	[Ne V] 24.32 μm	[O IV] 25.89 μm	Ref.
NGC 7172 [c d]	22 02 01.9	–31 52 11	37.2	Sy2	31	8.9	17	11	40	2
B2 2201+31A	22 03 15.0	+31 45 38	1523	QSO	0.096	0.53	0.32	<0.22	0.56	1
IRAS F22017+0319 [d]	22 04 19.2	+03 33 50	274	Sy2	5.9	8.3	14	9.4	29	4
NGC 7213 [c d]	22 09 16.2	–47 10 00	25.8	Sy1	24	<0.94	13	<0.73	2.4	2
IC 5179	22 16 09.1	–36 50 37	48.4	H II	113	<0.44	11	<0.81	2.0	2
PG 2214+139	22 17 12.3	+14 14 20	297	QSO	0.23	0.27	0.63	<0.31	1.3	1
NGC 7252	22 20 44.8	–24 40 41	66.4	H II	42	<0.33	3.7	<0.51	1.3	8
3C 445 [d]	22 23 49.6	–02 06 12	251	Sy1	2.3	2.0	6.2	5.8	23	4
ESO 602-G025	22 31 25.5	–19 02 04	110	LINER	44	1.6	7.6	<2.3	6.8	2
NGC 7314 [c d]	22 35 46.2	–26 03 00	20.6	Sy1	8.3	17	24	22	67	2
NGC 7331	22 37 04.1	+34 24 56	14.5	LINER	19	<0.52	10	···	3.0	5
MCG –03-58-007 [d]	22 49 37.1	–19 16 26	138	Sy2	8.5	6.6	9.3	3.9	8.8	4
IRAS F22491–1808	22 51 49.3	–17 52 23	354	···	5.4	<0.45	1.9	<0.90	<2.4	3
PG 2251+113	22 54 10.4	+11 36 38	1709	QSO	0.17	0.49	0.80	0.63	3.1	1
NGC 7410 [c]	22 55 00.9	–39 39 40	24.0	Sy2	3.7	<1.1	···	<1.9	<12	2
NGC 7469 [c d]	23 03 15.6	+08 52 26	69.8	Sy1	250	15	45	13	31	2
MCG –02-58-022	23 04 43.5	–08 41 08	213	Sy1	···	2.4	8.6	···	···	6
CGCG 453-062	23 04 56.5	+19 33 08	109	LINER	22	2.0	6.6	2.1	5.5	2
NGC 7479 [c d]	23 04 56.6	+12 19 22	34.2	Sy2	9.4	<2.4	5.8	<2.8	4.9	2
NGC 7496 [c d]	23 09 47.3	–43 25 40	22.8	Sy2	46	<0.41	6.3	<0.98	<0.48	2
IRAS F23128–5919	23 15 46.8	–59 03 15	199	Sy2	27	2.6	20	3.0	18	3
NGC 7552	23 16 10.8	–42 35 05	21.0	LINER	834	<3.6	70	···	<10	5
NGC 7591	23 18 16.3	+06 35 08	70.7	LINER	56	<0.62	5.5	<0.76	<0.54	2

Table 3.5: *Continued*

Name	R.A.[a] (J2000.0)	Decl.[a] (J2000.0)	Dist.[b] (Mpc)	Spect. Class.[a]	[Ne II] 12.81 μm	[Ne V] 14.32 μm	[Ne III] 15.56 μm	[Ne V] 24.32 μm	[O IV] 25.89 μm	Ref.
NGC 7582 [c] [d]	23 18 23.5	–42 22 14	22.7	Sy2	248	36	102	60	220	2
NGC 7590 [c] [d]	23 18 54.8	–42 14 20	23.0	Sy2	6.8	<0.36	3.7	<0.52	3.0	2
IRAS F23230–6926	23 26 03.6	–69 10 18	490	LINER	7.4	<0.75	2.0	<1.2	<1.5	3
NGC 7674 [d]	23 27 56.7	+08 46 44	127	Sy2	20	21	35	17	49	4
IRAS F23253–5415	23 28 06.1	–53 58 31	610	Sy2	5.5	<0.33	1.9	1.2	1.2	3
NGC 7714	23 36 14.1	+02 09 18	38.2	LINER	103	<1.0	77	<1.8	5.5	8
IRAS F23365+3604	23 39 01.3	+36 21 08	287	LINER	8.6	<0.80	0.73	<0.54	<2.0	3
NGC 7743 [c]	23 44 21.1	+09 56 02	24.3	Sy2	4.1	<0.28	4.2	0.95	2.9	2
CGCG381-051 [d]	23 48 41.7	+02 14 23	134	Sy2	19	<0.70	1.4	<1.2	<1.3	4
NGC 7769	23 51 04.0	+20 09 01	60.2	H II	13	<0.66	3.4	<0.34	0.41	2
NGC 7771	23 51 24.9	+20 06 42	61.9	H II	108	<0.71	8.8	<0.51	1.2	2
PG 2349-014	23 51 56.1	–01 09 13	840	QSO	1.4	0.71	2.0	<0.96	3.9	1
IRAS F23498+2423	23 52 26.0	+24 40 16	1046	Sy2	3.2	1.1	2.7	2.0	5.0	3
NGC 7793	23 57 49.8	–32 35 27	3.80	H II	10	<1.0	2.6	···	<0.32	5

Notes. Fluxes are expressed in units of 10^{-14} erg cm^{-2} s^{-1}. [(a)] Coordinates and optical spectroscopic classification from NED. [(b)] We calculated the distance from the redshift assuming a flat cosmology with $H_0 = 70$ km s^{-1}Mpc^{-1}, $\Omega_{\rm M} = 0.3$, and $\Omega_\Lambda = 0.7$. Except for the galaxies from Dale et al. (2009), Bernard-Salas et al. (2009) and Goulding & Alexander (2009) for which we used the distances adopted by these authors. [(c)] Member of the RSA sample. [(d)] Member of the 12 μm sample.

References. (1) Veilleux et al. (2009); (2) This work; (3) Farrah et al. (2007); (4) Tommasin et al. (2008, 2010); (5) Dale et al. (2009); (6) Gorjian et al. (2007); (7) Goulding & Alexander (2009); (8) Bernard-Salas et al. (2009).

Chapter 4

Spatially Resolved Observations with *Spitzer*/IRS

We present results from the Spitzer/IRS spectral mapping observations of 15 local LIRGs. In this chapter we investigate the spatial variations of the mid-IR emission which includes: fine structure lines, molecular hydrogen lines, PAH features, continuum emission and the 9.7 μm silicate feature. We also compare the nuclear and integrated spectra. The behavior of the integrated PAH emission and 9.7 μm silicate feature is similar to that of local starburst galaxies. We also find that the minima of the [Ne III] 15.56 μm/[Ne II] 12.81 μm ratio tends to be located at the nuclei and its value is lower than that of H II regions in our LIRGs and nearby galaxies. It is likely that increased densities in the nuclei of LIRGs are responsible for the smaller nuclear [Ne III] 15.56 μm/[Ne II] 12.81 μm ratios. This includes the possibility that some of the most massive stars in the nuclei are still embedded in ultracompact H II regions. In a large fraction of our sample the 11.3 μm PAH emission appears more extended than the dust 5.5 μm continuum emission. We find a dependency of the 11.3 μm PAH/7.7 μm PAH and [Ne II] 12.81 μm/11.3 μm PAH ratios with the age of the stellar populations. Smaller and larger ratios respectively indicate recent star formation. Finally we find that the [Ne II] 12.81 μm velocity fields for most of the LIRGs in our sample are compatible with a rotating disk at ∼kpc scales, and they are in a good agreement with Hα velocity fields.

4.1 Introduction

Thanks to the high sensitivity of IRS on board *Spitzer*, we can, for the first time, study systematically the mid-IR properties of (U)LIRGs, both locally and at high-z. The majority of IRS local studies have, so far, focused on the properties of starburst galaxies (Smith et al. 2007b; Brandl et al. 2006) and ULIRGs (Armus et al. 2007;

Farrah et al. 2007). The latter class of galaxies includes a large variety of physical and excitation conditions. For instance, most of these local ($z < 0.3$) ULIRGs are powered predominantly by compact starburst events, although a substantial active galactic nucleus (AGN) contribution is present in about half of them (Imanishi et al. 2007; Farrah et al. 2007; Nardini et al. 2008).

Although ULIRGs at $z \sim 2$ extend to even higher luminosities than local ones, their mid-IR spectra are similar to those of local starbursts, rather than to local ULIRGs (Rigby et al. 2008; Farrah et al. 2008). A similar behavior is found for high-z sub-millimeter galaxies (Pope et al. 2007; Menéndez-Delmestre et al. 2009). This behavior may indicate that star formation in IR-bright galaxies at $z \sim 2$ takes place over larger scales (a few kpc) than in local ULIRGs, where most of the IR emission arises from very compact regions (sub-kiloparsec scales, see e.g., Soifer et al. 2000; Farrah et al. 2007).

As a result, local LIRGs may provide important insights to the behavior of high-redshift ULIRGs. Their star-formation is often distributed over a substantial fraction of the galaxy (e.g., Alonso-Herrero et al. 2006), and in any case is usually not embedded at the high optical depths characteristic of the nuclear star-forming regions in local ULIRGs. To make good use of this analogy requires observations that map the local LIRGs to get an understanding of their global properties as well as to provide a better comparison with the observations of high-z galaxies, where the entire galaxy is encompassed in the IRS slit. The spectral mapping mode of *Spitzer*/IRS is well suited for this purpose, since it can provide both the nuclear and integrated spectra of local galaxies, enabling study of the spatial distribution of the spectral features that make up the integrated spectrum.

In this chapter we analyze IRS spectral mapping observations of a sample of 15 LIRGs with extended Paα (i.e., SF) emission.

4.2 The Sample

The galaxies studied here were selected from the sample of local LIRGs described in Chapter 2 and Alonso-Herrero et al. (2006), which was drawn from the *IRAS* Revised Bright Galaxy Sample (RBGS, Sanders et al. 2003). From this sample we selected 15 galaxies (Table 4.1) with extended emission in the NICMOS Paα images to be mapped with the IRS spectrograph. This selection criterion does not introduce any bias in the luminosity, distance and nuclear activity distributions of the mapped galaxies as compared to the parent sample. The remaining galaxies in the sample have been observed using the IRS staring mode as part of different programs. The latter is

Table 4.1: Galaxies with *Spitzer*/IRS Spectral Mapping Observations

Target	R.A.[a] (J2000.0)	Decl.[a] (J2000.0)	D_L[b] (Mpc)	Scale (pc arcsec^{-1})	$\log L_{IR}$ ($L_\odot$)	Spect. class[c]
NGC 2369	07 16 37.75	-62 20 37.5	46.0	220	11.1	comp.
NGC 3110	10 04 02.12	-06 28 29.1	72.6	350	11.3	H II
NGC 3256	10 27 51.28	-43 54 13.5	40.1	190	11.7	H II
NGC 3690*	11 28 30.80	+58 33 44.0	44.0	220	11.8	Sy2
IC 694*	11 28 33.80	+58 33 46.5	″	″	″	LINER
ESO320-G030	11 53 11.72	-39 07 48.7	43.7	210	11.2	H II
NGC5135	13 25 44.06	-29 50 01.2	58.8	280	11.3	Sy2
IC4518E	14 57 44.80	-43 07 53.0	66.3	320	10.3	no
Zw049.057	15 13 13.12	+07 13 31.7	55.7	270	11.2	comp.
IRASF17138−1017	17 16 35.80	-10 20 39.4	74.7	360	11.4	comp.
IC4687	18 13 39.83	-57 43 31.2	73.9	360	11.3	H II
NGC6701	18 43 12.46	+60 39 12.0	56.2	270	11.0	comp.
NGC7130	21 48 19.40	-34 57 04.9	70.0	340	11.4	Sy2
IC5179	22 16 09.09	-36 50 37.5	48.5	230	11.2	H II
NGC7591	23 18 16.28	+06 35 08.9	71.0	340	11.1	comp.
NGC7771	23 51 24.88	+20 06 42.6	61.8	300	11.3	H II

(*) NGC 3690 and IC 694 are the two components, western and eastern respectively, of the interacting system Arp 299 (a) Coordinates of the nucleus of the galaxy. (b) Luminosity distance. (c) Classification of the nuclear activity from optical spectroscopy. Composite indicates intermediate AGN/H II classification.

analyzed by Alonso-Herrero et al. (2011). The interacting galaxy Arp 299 was studied in detail by Alonso-Herrero et al. (2009b) and will be included in the appropriate comparisons and figures in this chapter.

Most of the nuclei of the LIRGs in our sample are classified as H II region-like from optical spectroscopy, three galaxies have a Seyfert classification and five are classified as composite (intermediate between H II and AGN, see Alonso-Herrero et al. 2009a). The infrared luminosity of the sample ranges from $10^{11.0}$ to $10^{11.8}\,L_\odot$. The main properties of the galaxies are summarized in Table 4.1.

4.3 Analysis

4.3.1 SL Spectral Maps

Using the SL cubes generated by CUBISM we constructed maps of the 5.5 μm continuum, and the most prominent PAH features in this module (6.2 μm PAH, 7.7 μm PAH

and 11.3 μm PAH). To build them we used our own IDL procedures. First we extracted one-dimensional spectra from the cubes by averaging the spectra over a 2×2 pixel aperture and then by moving with a 1 pixel step until the whole field of view was covered. The 2×2 pixel extraction box allows us to increase the signal-to-noise ratio (S/N) of the one-dimensional spectra, with only a slight loss of angular resolution (see below and Section 2.2.1.3). Once we obtained the one-dimensional spectra, for each pixel we did the following. To create the 5.5 μm continuum map, we integrated the flux between the rest-frame 5.3 μm and 5.7 μm wavelengths (in this section all wavelengths refer to rest-frame wavelengths). For the PAH maps, first we fitted the local continuum using a linear fit. The continuum pivots were set by averaging the spectrum over a ∼0.2 μm interval centered at 5.75 μm and 6.7 μm for the 6.2 μm PAH, at 7.2 μm and 8.2 μm for the 7.7 μm PAH, and at 10.6 μm and 11.8 μm for the 11.3 μm PAH. After subtracting the continuum, we integrated the flux in the wavelength ranges between 5.9 and 6.5 μm 7.3 and 7.9 μm and 10.8 and 11.6 μm for the 6.2, 7.7 and 11.3 μm PAH features, respectively. We derived the flux uncertainty of these maps with the statistical uncertainties provided by CUBISM. To avoid noisy pixels, we required the feature peak to be at least above 1σ to plot that pixel in the map, where σ is the continuum noise. The SL spectral maps of our sample are shown in Figure 4.18.

The angular resolution (FWHM) of the SL spectral maps is ∼4.″5. This is the resolution when we use 2×2 boxes to construct the maps, as opposed to that measured from the standard star observations (see Section 2.2.1.3). For the distances of our galaxies corresponds to ∼1 kpc (the exact scale for each galaxy is given in Table 4.1). In Section 2.2.1.3 we give full details on how the angular resolution of the spectral maps was derived.

We constructed maps of different PAH ratios by dividing the PAH maps obtained as described above. To avoid noisy pixels in the ratio maps we imposed further restrictions, and only those pixels with S/N ratio greater than 4 are plotted in the PAH ratio maps. Figures 4.19 and 4.20 show the 11.3 μm PAH/6.2 μm PAH and 11.3 μm PAH/ 7.7 μm PAH ratios, respectively.

4.3.2 SH Spectral Maps

We used the SH cubes to measure the brightest fine structure emission lines: [S IV] 10.51 μm, [Ne II] 12.81 μm, [Ne III] 15.56 μm, [S III] 18.71 μm, and the molecular hydrogen lines, H_2 S(2) at 12.3 μm and H_2 S(1) at 17.0 μm. First we extracted one-dimensional spectra using the same method as for the low-resolution cubes. Then we used the IDL package MPFIT (Markwardt 2009) to fit simultaneously a first-order

polynomial to the continuum and a Gaussian to the line. The fit was over a wavelength range of $\sim$0.4 μm centered at the line wavelength. The spectral resolution, $R \sim 600$, is sufficiently high to allow us to separate the emission lines from the broad PAH bands. However, to improve the continuum determination, we used extra Gaussian profiles to fit the PAH features close to the emission lines (e.g., the 12.7 μm PAH feature next to the [Ne II]). To avoid noisy pixels in the maps, we required. (1) a S/N > 2 in the continuum range; and (2) the line peak to be at least 1σ above the continuum noise for the pixel to be shown in the corresponding map.

We also constructed an 11.3 μm PAH feature map by the same procedure as for SL cubes, but with the high-resolution spectra. A 15 μm continuum was obtained by integrating the flux between 14.9 μm and 15.1 μm. We required a signal above 1σ to plot a pixel in these two maps.

The SH spectral maps are shown in Figure 4.21 together with the *HST*/NICMOS continuum-subtracted Paα maps of Alonso-Herrero et al. (2006).

We constructed [S III] 18.71 μm/[Ne II] 12.81 μm, [Ne III] 15.56 μm/[Ne II] 12.81 μm and [Ne II] 12.81 μm/11.3 μm PAH ratio maps by dividing the flux maps. The variation of the PSF size with wavelength within each module is negligible (see Section 2.2.1.3), and therefore we divided the flux maps directly without attempting to correct for this small effect (we only built ratio maps of lines observed with the SH module). We imposed stricter conditions to plot a pixel in a ratio map than those used for the line maps; only pixels with a flux measurement $> 3\sigma$, for both features, were included in the ratio maps. The maps of the SH line ratios are shown in Figure 4.21. The angular resolution of the SH maps is $\sim$6 arcsec. This corresponds to physical scales between $\sim$1 kpc, for the nearest galaxies, and $\sim$2 kpc for the most distant ones.

4.3.3 Nuclear, Integrated and Extranuclear One-dimensional Spectra

We extracted one-dimensional spectra of the nuclei as well as of the integrated galaxy. To extract the nuclear spectra we used a $5\farcs5 \times 5\farcs5$ square aperture centered at the nuclear coordinates (Table 4.1). This aperture corresponds to physical scales between 1 and 2 kpc, depending on the galaxy. We set the orientation of the aperture aligned with the R.A. and decl. axis. We used the same aperture for both low and high–resolution data cubes. To obtain the integrated spectrum we summed the flux of the cube. We excluded those pixels with the 11.3 μm PAH flux (15 μm continuum) below 1σ to avoid adding too much noise to the low-resolution (high-resolution) integrated spectra. This threshold is the same as that required to plot a pixel in the 11.3 μm PAH

and 15 μm continuum maps of Figures 4.18 and 4.21, respectively. The physical scale of the integration area varies from galaxy to galaxy. The approximated physical sizes are listed in Tables 4.3 and 4.5 for the low- and high-resolution maps respectively. They are of the order of 10×8 kpc. Although the extraction regions are slightly different for each module, the flux differences are only ∼10%–20%.

We plot the integrated spectra in Figure 4.1. The nuclear spectra was presented by (Alonso-Herrero et al. 2011), together with the nuclear spectra of the rest of the sample.

In Figure 4.2 (right), we show a comparison of the nuclear and extranuclear low -resolution spectra normalized at 14 μm for four of the galaxies. We selected these galaxies because in their spectral maps (left panel of Figure 4.2) it is possible to identify extranuclear H II regions and extract their spectra. All the spectra, nuclear and extranuclear, show bright PAH features and fine structure lines. The variations of the spectral features from galaxy to galaxy and within a galaxy are relatively small, at least when compared to those observed in ULIRGs (Armus et al. 2007) or those observed in star-forming galaxies with different metallicities (Engelbracht et al. 2008). That is, the comparison of the spectra shows that these LIRGs have a more or less uniform shallow silicate absorption and relatively high-metallicity.

The PAH ratios, PAH EW and silicate depth measured in the nuclear and integrated low-resolution spectra are listed in Tables 4.3 and 4.2. Tables 4.5 and 4.4 show respectively the integrated and nuclear fine structure line fluxes in the high-resolution spectra.

4.3.4 Silicate Feature Maps

Amorphous silicate grains present a broad feature centered at 9.7 μm that can be measured from the SL cubes. We used a method similar to that proposed by Spoon et al. (2007) to measure the observed silicate strength. First, we extracted one-dimensional spectra from the cube as described in Section 4.3.1. For each spectrum, we estimated the continuum expected at 10 μm by fitting a power law through the feature-free continuum pivots at 5.5 μm and 13 μm. Then we compared the estimated continuum and the measured flux using the following expression:

$$S_{\rm Si} = ln \frac{f_{\rm obs}(10\,\mu{\rm m})}{f_{\rm cont}(10\,\mu{\rm m})} \tag{4.1}$$

where $S_{\rm Si}$ is the silicate strength. When the silicate strength is negative, the silicate feature is in absorption, whereas a positive silicate strength indicates that the feature is seen in emission.

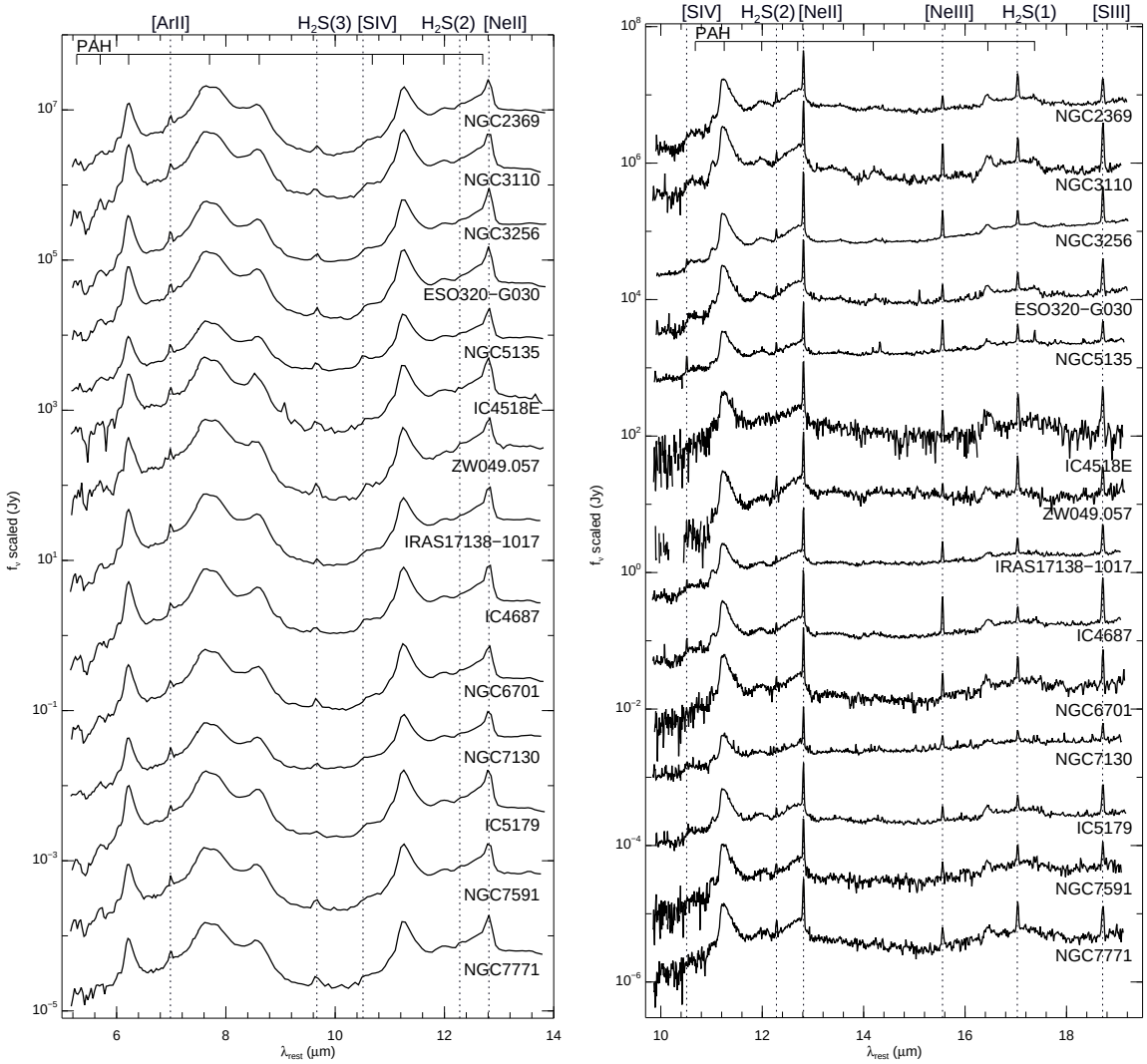

Figure 4.1: Rest-frame SL (left panel) and SH (right panel) integrated spectra of the sample. The Arp 299 spectra was shown in Alonso-Herrero et al. (2009b). The fluxes have been scaled for better comparison. The scale factors are, starting from the top galaxy, 2×10^{7}, 6×10^{6}, 1.2×10^{5}, 1.5×10^{5}, 2×10^{4}, 3×10^{4}, 7×10^{3}, 1×10^{2}, 8, 1, 1×10^{-1}, 1×10^{-2}, 5×10^{-3}, 2×10^{-4} for the left panel and 1×10^{7}, 2×10^{6}, 2×10^{4}, 2×10^{3}, 5×10^{3}, 2×10^{2}, 2, 2×10^{-1}, 5×10^{-2}, 2×10^{-3}, 2×10^{-4}, 2×10^{-4}, 1×10^{-5} for the right panel.

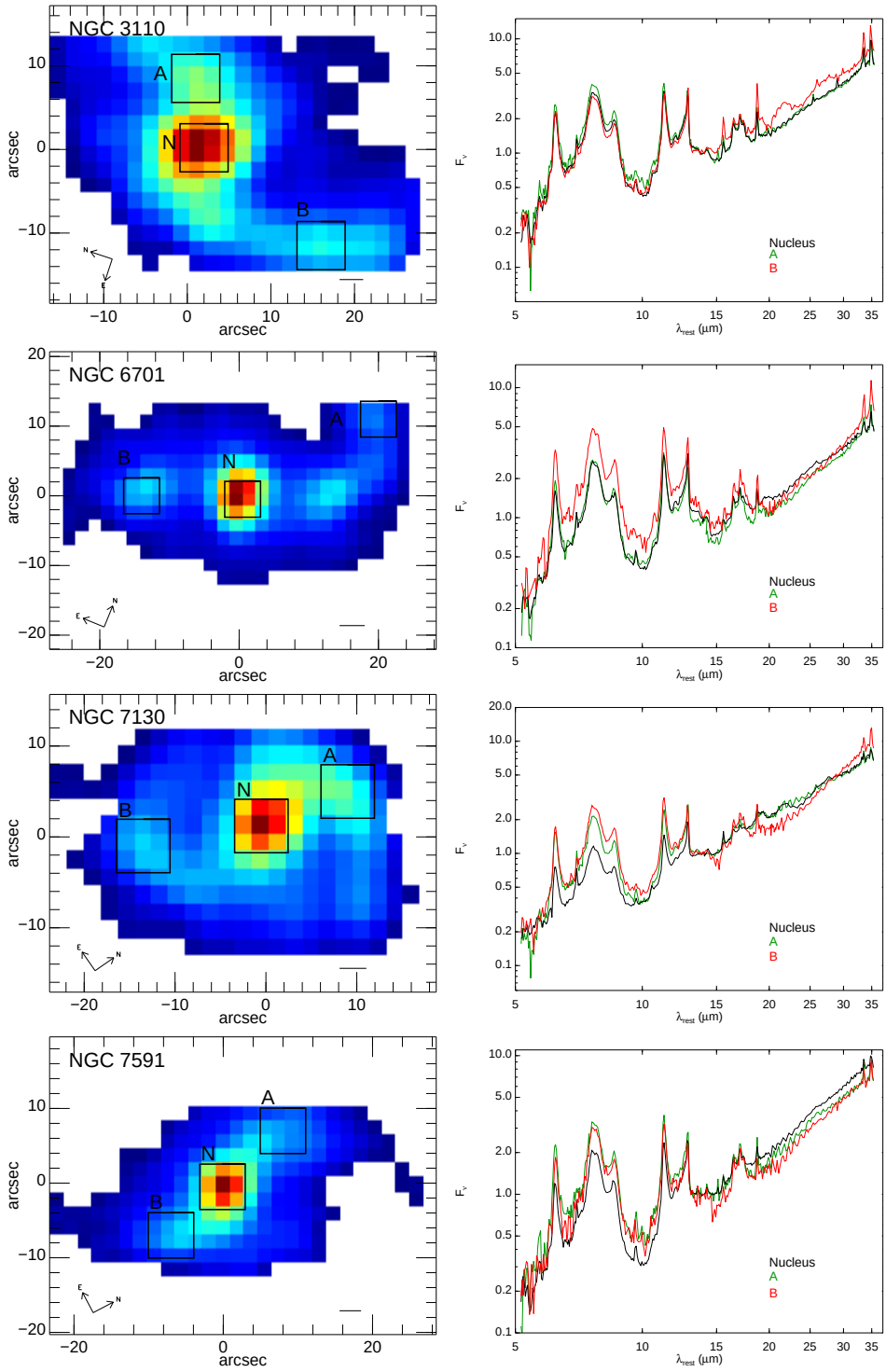

Figure 4.2: Left: *Spitzer*/IRS SL spectral maps of the 7.7 μm PAH feature. The image orientation is indicated on the maps for each galaxy. The scale represents 1 kpc. The black squares are the positions and sizes of the extraction apertures. Right: Low-resolution spectra normalized at 14 μm.

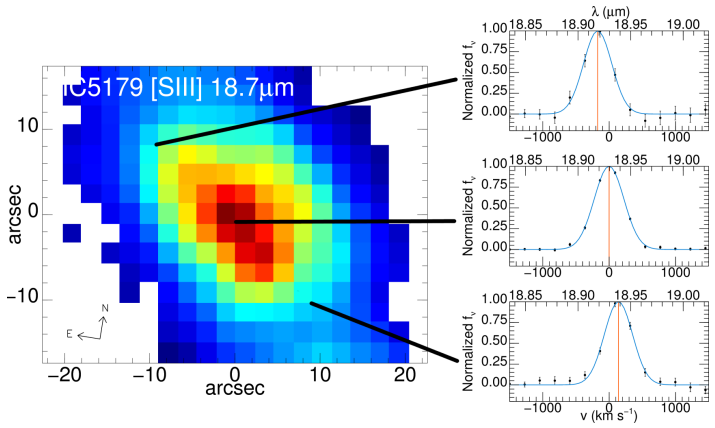

Figure 4.3: Left panel is the map of the [S III] 18.71 μm line flux of IC 5179. The right panels show the fit to this line for three selected regions of this galaxy.

We estimated the flux at 10 μm instead of 9.7 μm (the maximum of the feature) to avoid a possible contamination by the molecular hydrogen emission line H_2 S(3) at 9.67 μm.

There are several factors that affect the accuracy of the silicate strength measurement. The most important source of uncertainty is the continuum estimate, because of the presence of broad PAH bands in the spectra. We selected continuum pivots similar to those used by Spoon et al. (2007), so that we can make meaningful comparisons with their results. The $S_{\rm Si}$ is equivalent to the optical depth of the silicate absorption ($\tau_{\rm Si}$) defined in Rieke & Lebofsky (1985). Alternatively, a more accurate way to measure the silicate optical depth is to fit all the features (PAHs, emission lines and dust continuum) present in the spectrum as PAHFIT does (Smith et al. 2007b). However, to avoid ambiguities between the PAH strength and the silicate absorption, the entire low-resolution spectral range (5.2 μm–38 μm) is desirable. At longer wavelengths (>14.5 μm) the pixel size is about 2.5 times larger than at shorter wavelengths and since we are interested in the spatial distribution of the silicate feature we decided to use the first method to estimate the continuum. To compared these methods, first we fitted the integrated spectra using PAHFIT, assuming a foreground screen dust geometry to obtain the $\tau_{9.7}$, and then we compared this value with the measured $S_{\rm Si}$. We found that both quantities are well correlated.

Keeping in mind that the main source of uncertainty of the silicate strength measurements is the continuum determination, we estimated that the typical values of the statistical uncertainty are ∼0.05 for the nuclei and less than ∼0.15 for the extranuclear regions. The maps of the silicate feature strength are presented in Figure 4.22.

4.3.5 SH Velocity Fields

The SH spectra were also used for rough determination of velocities. Figure 4.3 shows an example of line fitting for selected regions of IC 5179 to illustrate the detection of variations in the line position, even with the relatively low spectral resolution of the SH module.

Since the spectral resolution, $R \sim 600$, is lower than that of most kinematic studies, we tested the validity of the velocities with synthetic spectra. We created these spectra to simulate an unresolved spectral line as seen by the SH module and then we tried to recover the original line parameters. The EW of the simulated lines was similar to the observed ones. We added noise to the spectra to match the continuum S/N ratio of the maps. The continuum S/N ratio, for most of the galaxies, is in the range ∼60–100 at the nuclei and ∼3–10 at the external regions. To allow for the effect of the telescope pointing uncertainties, we distorted the wavelength scale by ∼5 % (estimated from the pointing information in the BCD file headers). We found that this effect limits the accuracy of the velocity determination to $\pm 10\,\mathrm{km\,s^{-1}}$, independent of the S/N ratio of the spectra. For extended sources, which fill uniformly the slit, the wavelengths are more stable, and then the uncertainty due to the pointing inaccuracy would be lower. The galaxies studied here are not point sources, neither uniformly extended sources, thus this uncertainty estimation is an upper limit. Including the uncertainty in the absolute wavelength calibration (equivalent to 10 % of a pixel), we found the minimum uncertainty to be $\pm 20\,\mathrm{km\,s^{-1}}$. We therefore conclude that the uncertainty in the velocity field is in the range of 10–30 $\mathrm{km\,s^{-1}}$, depending on the pointing accuracy achieved and the S/N ratio of an individual spectrum. Thus, we consider that variations in the velocity maps larger than $\sim 20\,\mathrm{km\,s^{-1}}$ are likely to be real. Figure 4.23 shows the velocity fields derived for the [Ne II] 12.81 μm and H_2 S(1) emission lines; they range up to a total gradient of $\sim 200\,\mathrm{km\,s^{-1}}$ and hence include a substantial amount of information about the sources.

4.4 The Silicate Feature

4.4.1 Spatially Resolved Measurements

LIRGs are known to contain highly obscured regions ($A_V \simeq 4$–50 mag, see e.g., Veilleux et al. 1995; Genzel et al. 1998; Alonso-Herrero et al. 2000, 2006), usually coincident with the nuclei of the galaxies. Assuming an extinction law and a dust distribution geometry the silicate strength can be converted into a visual extinction.

The maps of the silicate feature of our sample are shown in Figure 4.22. In a large

fraction of the systems (80 %) the most obscured regions appear to be coincident with the nuclei. In other cases, the nuclear regions appear to be slightly less obscured than the surrounding regions (e.g., NGC 7130) or they show a complicated morphology (e.g., IRAS 17138−1017, NGC 7771, IC 4687). We note that the spectra used for measuring the strength of the silicate feature are averaged over ∼1 kpc scales, and thus some of the real variations seen on smaller scales using ground-based mid-IR observations are smoothed out (e.g., the highly obscured southern nucleus of NGC 3256, see Díaz-Santos et al. 2008).

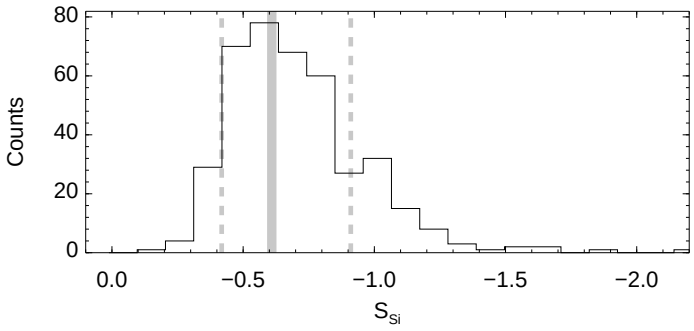

Figure 4.4: Histogram of the spatially resolved measurements of the silicate strength for all galaxies measured in boxes of 2×2 pixel. The solid gray line indicates the median silicate strength. The dashed gray lines define the range including 68 % of the data points.

Figure 4.4 shows the distribution of the silicate strengths measured from the spatially resolved maps for all the galaxies. They are in the range ∼0 to ∼ −2.0, with a median of −0.61. The strengths of the majority of the LIRGs are moderate ($S_{\rm Si} \sim -0.4$ to −0.9), and intermediate between those observed in starburst galaxies (Brandl et al. 2006) and ULIRGs (Spoon et al. 2007; Sirocky et al. 2008).

If we assume a foreground screen of dust, the silicate absorption strength can be expressed in terms of the optical extinction ($A_{\rm V}$) using the conversion factor $A_{\rm V}/S_{\rm Si} = 16.6$ (Rieke & Lebofsky 1985). We then find that the median $A_{\rm V}$ of the spatially resolved measurements is ∼10 mag. The most extincted region in our sample of LIRGs is the nuclear region of IC 694, also known as Arp 299-A (see also Alonso-Herrero et al. 2009b), with $A_{\rm V} \sim 37$ mag. The foreground screen assumption gives the minimum extinction compatible with the measurements. Most of the spatially resolved measurements (68 %) are in the range of −0.4 to −0.9. This range is much narrower than that observed in the nuclear regions of ULIRGs ($0 > S_{\rm Si} > -4$; Spoon et al. 2007). The similarity of the silicate absorption strengths among our sample members suggests that they may be in part a product of radiative transfer in dusty regions. We can approximate this possibility by assuming that the dust and emission sources are

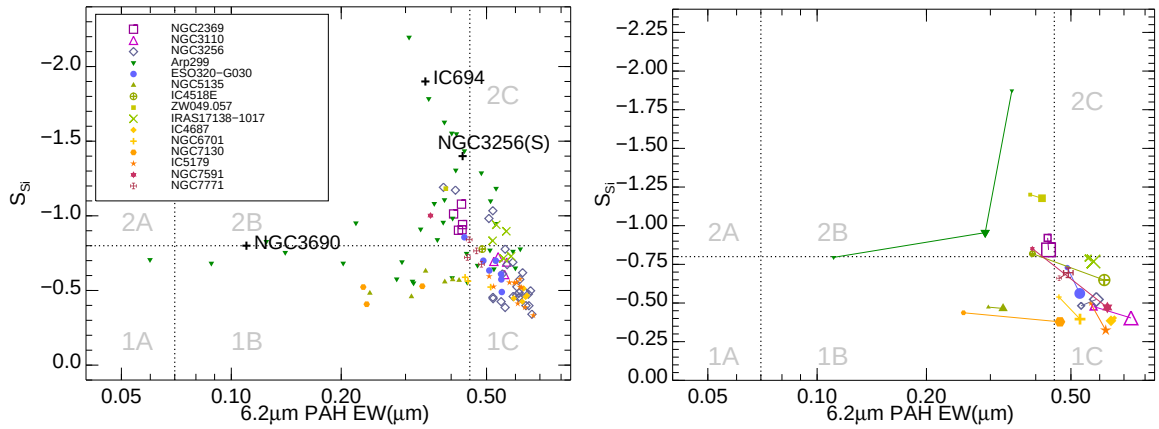

Figure 4.5: $S_{\rm Si}$ vs. the 6.2 μm PAH equivalent width (EW) diagram, similar to that presented by Spoon et al. (2007). Top: spatially resolved measurements for our sample of LIRGs using a 2×2 pixel box (3.″7×3.″7 aperture). The black crosses are the two nuclei of Arp 299 (IC 694 and NGC 3690) and the southern nucleus of NGC 3256. Bottom: Nuclear (5.″5×5.″5 aperture) and integrated values of each galaxy. The small symbols correspond to the nuclear value and the large symbols to the integrated galaxy. Nuclear and integrated are connected by a line to guide the eye. In both panels, following Spoon et al. (2007), the parameter space is divided into six classes out of their nine classes. Class 1A is populated by unobscured AGNs. They have featureless spectra with a shallow silicate feature. Class 1C corresponds to pure starbursts (PAH dominated spectra). The spectra of a galaxy in the class 1B are intermediate between the AGN spectra and the pure starburst. Classes 2B and 2C have a deeper silicate absorption, so do classes 3A and 3B (not plotted here). The majority of ULIRGs not dominated by an AGN lie in these classes.

mixed. The resulting median $A_{\rm V}$ is then ∼20 mag, about 2 times greater than for the foreground screen geometry.

The nuclear and integrated values of the silicate strength are listed in Tables 4.2 and 4.3. For all the galaxies, we find that the integrated strength of the silicate feature is smaller than, although comparable to, the nuclear one. The nuclear silicate strengths range from −0.4 to −1.9, although most of them are larger than −1.0. The integrated strength is $-0.3 < S_{\rm Si} < -1.2$, somewhat shallower than the nuclear strength. The LIRGs with the largest variations between the nuclear and integrated silicate features are NGC 3256, Arp 299, NGC 7130, and NGC 7591.

4.4.2 The $S_{\rm Si}$ versus 6.2 μm PAH EW Diagram

Spoon et al. (2007) presented a diagram using the EW of 6.2 μm PAH feature and the silicate strength to provide a general classification of infrared galaxies. ULIRGs

appear distributed along two branches. The horizontal branch is populated by unobscured AGNs (QSO and Sy1) in the left-hand side of the diagram (class 1A) and by starburst galaxies in the right-hand side (class 1C) of the diagram. The diagonal branch goes from deeply obscured nuclei (class 3A) to unobscured starbursts (class 1A).

In Figure 4.5 we present a similar diagram for our sample of LIRGs. The left panel shows the spatially resolved measurements of our sample of LIRGs. Most of them appear in this diagram at the region where both branches intercept. The nuclear and surrounding regions of galaxies classified as Seyferts using optical spectroscopy (NGC 5135: Sy2, NGC 7130: Sy2, and Arp 299-B1: Sy2, see Table 4.1) are located in the 1B region (intermediate between AGN and starbursts), in agreement with their well-known composite nature. NGC 6701 and NGC 7591 are classified as composite objects which is likely to be a combination of an AGN and star-formation activity (see Alonso-Herrero et al. 2009a). Both nuclei appear quite close to region 1B. The two most obscured nuclei in the sample, Arp 299-A and the southern nucleus of NGC 3256, and their neighboring regions, are in the upper part of the diagonal branch populated by ULIRGs, although they do not reach the silicate strengths of the deeply embedded ULIRG nuclei.

The comparison between the nuclear and integrated values (the right panel of Figure 4.5) shows that the integrated spectra tend to have lower silicate strengths and larger 6.2 μm PAH EWs. We find that on average the integrated 6.2 μm PAH EW is $\sim$30 % larger than the nuclear values, whereas the integrated silicate strength is $\sim$15 % lower than that found in the nuclei. That is, the integrated values move the galaxies to the pure starburst class region (1C) in this diagram. In the case of all the active galaxies of the sample, the nucleus is not sufficiently bright as to dominate the integrated mid-infrared spectrum and the dominant contribution from star formation, which is extended over several kpc (see Alonso-Herrero et al. 2006, 2009b,a) makes the integrated spectrum look more starburst-like.

4.5 Fine Structure Emission Lines

4.5.1 Morphology

Although the limited spatial resolution ($\sim$ 1 kpc) of the SH maps does not allow us to study the galaxy morphologies in great detail, it is possible to analyze general trends. The exact spatial distribution of the emission lines depends on the physical conditions and the age of the dominating stellar population in each region. In Appendix 4.C we

discuss the galaxies individually.

Figure 4.21 shows the SH spectral maps of the most prominent features, as well as those of the 15 μm continuum. The [Ne II] 12.81 μm, [Ne III] 15.56 μm, and [S III] 18.71 μm fine structure lines have an overall morphology similar to that of the 15 μm continuum. We detect [S IV] 10.51 μm emission in only five systems. In two of them (NGC 7130 and NGC 5135), the [S IV] 10.51 μm emission mainly comes from the active nuclei (Díaz-Santos et al. 2010). Our data do not allow us to determine whether there is a low surface brightness [S IV] 10.51 μm emission, associated with H II regions, in these two galaxies due to the relatively low flux of this line. In the other three cases, NGC 3256, IC 4687, and Arp 299 (for the last galaxy, see Alonso-Herrero et al. 2009b), the emission is more extended and we attribute it to the H II regions seen in the Paα and/or Hα images.

We find that the neon emission ([Ne II] 12.81 μm and [Ne III] 15.56 μm) and the 15 μm continuum are spatially resolved. We calculated the ratio between the nuclear (circular aperture of radius 1 kpc; depending on the distance the aperture radius varies between 1.5 and 3 pixels)[1] and the integrated neon line emission and 15 μm continuum emission for our galaxies, we also used the uncertainty maps to estimate the statistical uncertainty of these ratios (Table 4.6). On average the uncertainty of the ratio is $\sim$6 %. These are upper limits to the relative contribution of the nucleus to the total emission of the galaxy as in some cases the IRS maps do not cover the full extent of the galaxy. In general the emission arising from the central 2 kpc accounts for less than 50 % of the total emission for the neon lines and the continuum, indicating that the star formation is extended over several kpc. We note however that the LIRGs in this work were selected because they show extended Paα emission (Section 4.2), and thus, this result needs to be confirmed for a complete sample of LIRGs.

The combined luminosities of the [Ne II] 12.81 μm and [Ne III] 15.56 μm lines are good tracers of the star formation rate in galaxies (Ho & Keto 2007), so a good morphological correspondence is expected between them and Hα. To further explore the behavior of the neon emission, Figure 4.6 compares the IRS neon spectral maps with Hα images[2] of Hattori et al. (2004) for NGC 3110 and NGC 7771. The SH and Hα maps of NGC 3110 show emission from the nuclear region and from H II regions in the spiral arms. The [Ne III] 15.56 μm emission (also the [S III] 18.71 μm emission) from these H II regions is comparable to the emission arising from the nucleus, while [Ne II]

[1]The physical size of the nuclear aperture was chosen so it corresponds to the minimum spatial resolution of the most distant galaxy in the sample.

[2]The Hα images were degraded to the *Spitzer*/IRS SH angular resolution, pixel size, and orientation.

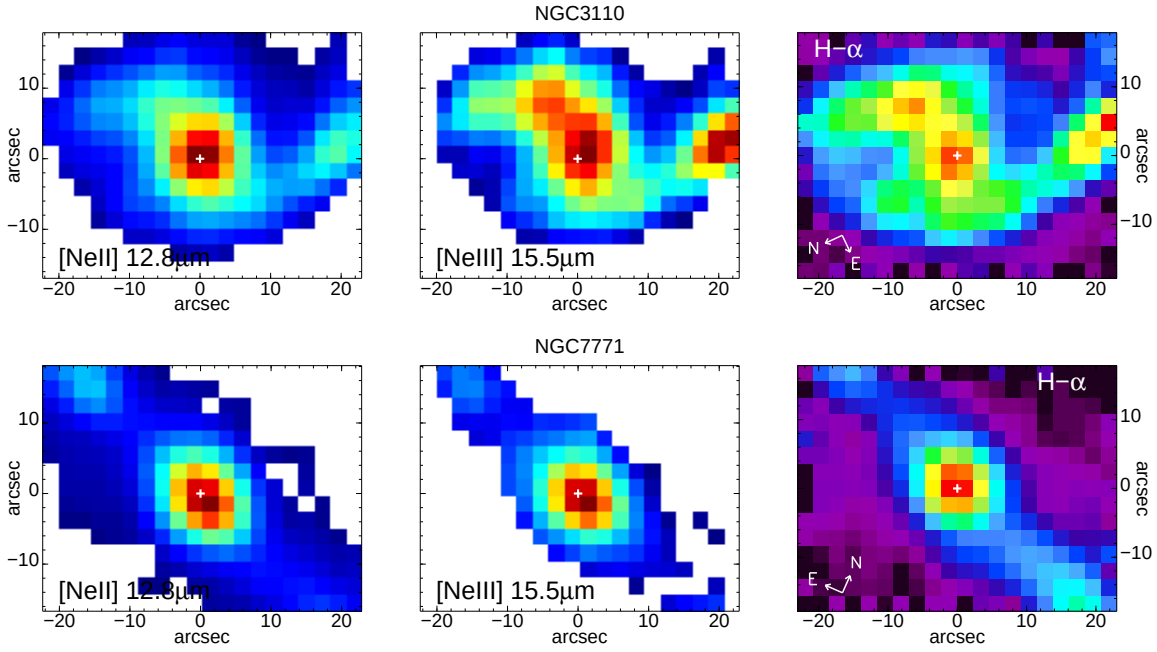

Figure 4.6: Comparison of the [Ne II] 12.81 μm and [Ne III] 15.56 μm maps with Hα images from Hattori et al. (2004) for NGC 3110 and NGC 7771. The image orientation for each galaxy is shown on the Hα image. All the maps are shown in a square root scale.

12.81 μm is more concentrated around the nucleus. We note, however, that the Hα image is not corrected for extinction. This is especially important in the nuclear region ($S_{\rm Si} \sim -0.48$, see Table 4.2, $A_{\rm V} \sim 8$ mag) as it is the most extincted region in this galaxy. For NGC 7771, the [Ne II] 12.81 μm [Ne III] 15.56 μm, and Hα emissions show similar morphologies, both in the nuclear ring of star formation (seen in the Paα image, Figure 4.21, but not resolved by the IRS spectral maps), and the extra-nuclear H II regions, as well as in the diffuse regions between them. These two examples illustrate that at least from a qualitative point of view and on the scales probed here, the Hα, [Ne II] 12.81 μm, and [Ne III] 15.56 μm lines are tracing the same young ionizing stellar populations (see Ho & Keto 2007 for a quantitative assessment).

4.5.2 Spatially Resolved Line Ratios

4.5.2.1 The [Ne III] 15.56 μm/[Ne II] 12.81 μm Line Ratios

The spectral maps of the [Ne III] 15.56 μm/[Ne II] 12.81 μm line ratios for our sample of LIRGs are shown in Figure 4.21. In most cases the nuclei have the lowest [Ne III] 15.56 μm/[Ne II] 12.81 μm ratios, while the circumnuclear regions and H II regions tend to show higher ratios (see also Figure 4.7). With the exception of three cases with

an active nucleus (NGC 3690, NGC 5135 and NGC 7130), the nuclear values of the [Ne III] 15.56 μm/[Ne II] 12.81 μm ratio are all in the range of 0.06–0.10 (with three exceptions near 0.2, IC 694, IRAS17138-1017, and IC 4687, see Table 4.4). Excluding the galaxies hosting an AGN, the median nuclear ratio is 0.08. The extra-nuclear values are between 0.06 and 1, while the integrated values (see Table 4.5) are between 0.08 and 0.5. Thornley et al. (2000) find a similar range for the integrated ratios for an additional four LIRGs. This ratio ranges from 0.02 to 6 in starburst galaxies (Verma et al. 2003; Dale et al. 2006, 2009). For the H II galaxies, the nuclear [Ne III] 15.56 μm/[Ne II] 12.81 μm ratio is a factor $\sim$2–3 smaller than those measured in the extranuclear regions.

A similar behavior of increasing [Ne III] 15.56 μm/[Ne II] 12.81 μm ratios with increasing galactocentric distances has been observed in the nearby galaxies NGC 253 (Devost et al. 2004) and M82 (Beirão et al. 2008), although the physical scales probed are different ($\sim$80 pc in these two galaxies, $\sim$1 kpc in our sample of LIRGs). Galactic H II regions follow the same trend, with H II regions at increasing distances from the galactic nucleus showing larger [Ne III] 15.56 μm/[Ne II] 12.81 μm ratios (Giveon et al. 2002).

Note that we did not correct this ratio for extinction. This correction however, only produces variations in the ratio of 5–15 % for the typical extinction of our sample ($S_{\rm Si} \sim -0.6$, that is $A_{\rm V} \sim$10 mag). The correction (positive or negative) depends on the adopted extinction law (see Farrah et al. 2007).

The strength of [Ne III] 15.56 μm relative to [Ne II] 12.81 μm decreases with increasing metallicity, increasing age of the stellar population and increasing nebular density (e.g., Snijders et al. 2007). In accordance with the luminosity- and mass-metallicity relations, LIRGs are characterized by uniformly relatively high-metallicity (in many cases super-solar), with some indications of slightly (factor of two) reduced levels in their nuclei (Rupke et al. 2008). The Snijders et al. (2007) models predict a $\sim$3 times larger [Ne III] 15.56 μm/[Ne II] 12.81 μm ratio for a given age and density as the metallicity decreases from super-solar (2 $Z_{\odot}$) to solar. Thus, metallicity-related effects are unlikely to be the dominant cause of the relative increase of [Ne III] 15.56 μm strength outside the central regions of these galaxies. They may in fact to be overcome by some stronger mechanism.

The trend with stellar population age is strong. The expected [Ne III] 15.56 μm/[Ne II] 12.81 μm ratio of an instantaneous burst of star formation falls below 10^{-3} for ages >6 Myr (Rigby & Rieke 2004). Thornley et al. (2000) showed that the range of the [Ne III] 15.56 μm/[Ne II] 12.81 μm ratio in starburst galaxies is compatible with models for bursts of star formation. However, from their models and those of Rigby &

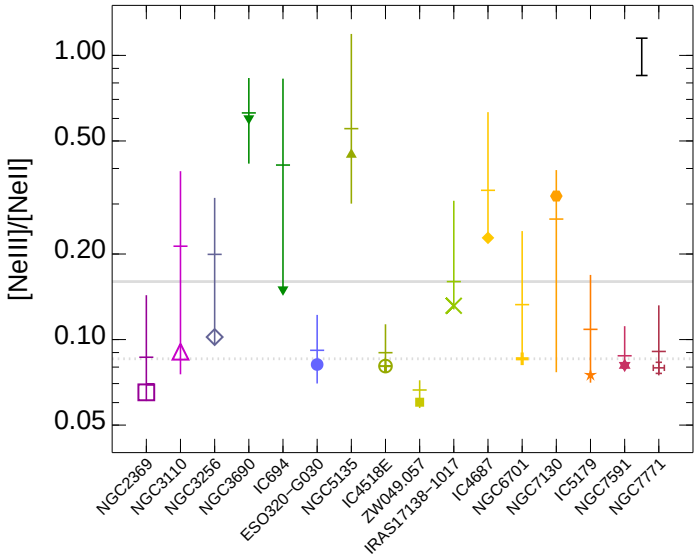

Figure 4.7: Range of the observed [Ne III] 15.56 μm/[Ne II] 12.81 μm ratio from the spectral maps. The galaxy symbol (as in Figure 4.5) indicates the value of the ratio in the nucleus. The horizontal mark is the median of the ratio of each galaxy. The solid gray line is the median of the medians and the dotted line is the median of the nuclear ratios. The black line indicates the typical uncertainty of the ratios.

Rieke (2004), the nuclear values for LIRGs are below the range that would be expected from such star-forming episodes. The observed nuclear ratios could only be explained in terms of the stellar population if: (1) the IMF is truncated at $\sim$30 $M_{\odot}$ in the LIRG nuclei (Thornley et al. 2000, Figure 6); or (2) the star formation rate in *all* the LIRG nuclei has decreased rapidly over the past 10–20 Myr (which seems contrived).

Another explanation is that due to the high densities in the nuclear regions the [Ne III] 15.56 μm/[Ne II] 12.81 μm ratio is suppressed, including the possibility that a fraction of the most massive stars are hidden in ultra-compact H II regions (Rigby & Rieke 2004). The [Ne III] 15.56 μm/[Ne II] 12.81 μm ratio decreases by approximately a factor of 2 if the density increases from 10^3 to 10^5 cm^{-3} (Snijders et al. 2007). We explore the density effects on the neon line ratio in the following section.

Before doing so, we point out that a few galaxies (NGC 3690, NGC 5135 and NGC 7130) have an opposite trend in that the [Ne III] 15.56 μm/[Ne II] 12.81 μm ratio becomes larger in their nuclei. We attribute this behavior to the presence of active nuclei. These three galaxies are the only ones classified as Seyfert type and it is likely that the extra hard-ionizing radiation from the AGN is responsible for the high, three times larger than the median, [Ne III] 15.56 μm/[Ne II] 12.81 μm nuclear ratio.

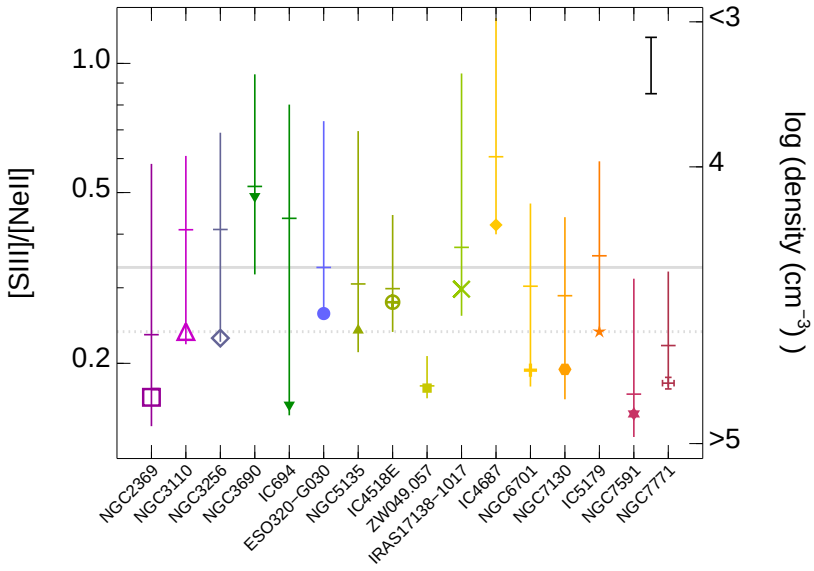

Figure 4.8: Range of the observed [S III] 18.71 μm/[Ne II] 12.81 μm ratio from the spectral maps. The symbols are as in Figure 4.7. The density label corresponds to the [S III] 18.71 μm/[Ne II] 12.81 μm ratio predicted by the Snijders et al. (2007) models for solar metallicity, $q = 1.6 \times 10^8$ and age = 5 Myr. The [Ne III] 15.56 μm/[Ne II] 12.81 μm ratio predicted using these parameters is ∼0.1–0.2 which is in agreement with the observed ratio.

4.5.2.2 The [S III] 18.71 μm/[Ne II] 12.81 μm Line Ratios

The ionization potentials of Ne II and S III are 21.6 eV and 23.3 eV, respectively. Therefore, the [S III] 18.71 μm/[Ne II] 12.81 μm ratio is almost insensitive to the hardness of the radiation field. On the other hand, this ratio is a good tracer of density in the range 10^4–10^6 cm^{-3}, with lower [S III] 18.71 μm/[Ne II] 12.81 μm ratios indicating larger electron densities (Snijders et al. 2007).

Our spatially resolved measurements show that this ratio ranges from ∼0.1 to ∼1.25 (Figure 4.8). Assuming a 5 Myr old stellar population, an intermediate ionization parameter ($q = 1.6 \times 10^8$) and solar metallicity (see caption of Figure 4.8), these ratios correspond to electron densities between 10^3 and 10^5 cm^{-3} (Snijders et al. 2007). Like the [Ne III] 15.56 μm/[Ne II] 12.81 μm ratio, for a given galaxy the lowest values of the [S III] 18.71 μm/[Ne II] 12.81 μm ratio occur in the nuclei (in most cases the nuclear value is between ∼0.13 and 0.25), while higher ratios are found around them (Figure 4.21). This indicates, as expected, that the nuclei are denser than the extranuclear H II regions. According to this spatial distribution the integrated ratios (∼0.2–0.5) are ∼30% larger than the nuclear ratios.

The left panel of Figure 4.9 shows the [S III] 18.71 μm/[Ne II] 12.81 μm ratio versus the [Ne III] 15.56 μm/[Ne II] 12.81 μm ratio from our spatially resolved measurements.

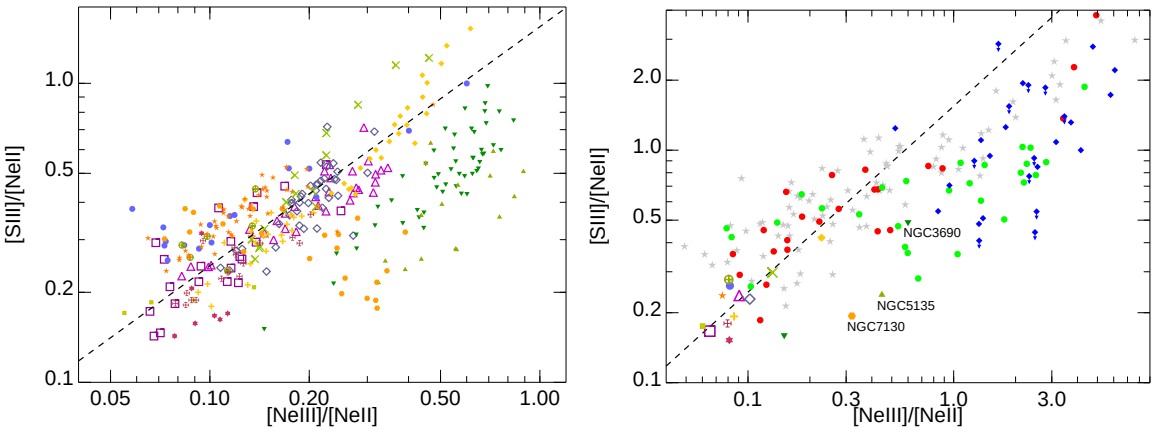

Figure 4.9: Top panel: [S III] 18.71 μm/[Ne II] 12.81 μm ratio vs. [Ne III] 15.56 μm/[Ne II] 12.81 μm ratio from the spatially resolved maps (Each point corresponds to a resolution element including the nuclei). Bottom panel: nuclear ratios of our sample of LIRGs. We can compare them with: H II regions (gray stars) and star-forming galaxies (red circles) of Dale et al. (2009) , Seyfert galaxies of Tommasin et al. (2008) (green circles) and quasars of Veilleux et al. (2009) (blue diamonds). The LIRG symbols are as in Figure 4.7. The black dashed line is the best fit to the spatially resolved data of the LIRGs excluding those galaxies containing an active nucleus which lie below the correlation. We did not apply an extinction correction.

As can be seen from this figure, there is a tight correlation between the two line ratios if we exclude those galaxies hosting an active nucleus (NGC 3690, NGC 5135, and NGC 7130). The best linear fit to the data (excluding the AGNs) is:

$$log(y) = 0.19 \pm 0.02 + (0.81 \pm 0.03) \times log(x) \tag{4.2}$$

where y is the [S III] 18.71 μm/[Ne II] 12.81 μm ratio and x the [Ne III] 15.56 μm/[Ne II] 12.81 μm ratio. In the right panel of Figure 4.9 we plot the nuclear ratios of our LIRGs together with those of extranuclear H II regions and nuclei of nearby galaxies (Dale et al. 2009), Seyfert galaxies (Tommasin et al. 2008) and quasars (Veilleux et al. 2009). Both diagrams show that, in general, for a given density (as traced by the [S III] 18.71 μm/[Ne II] 12.81 μm ratio) the AGNs show larger [Ne III] 15.56 μm/[Ne II] 12.81 μm ratios than starburst galaxies and H II regions. The most straightforward explanation is that the ionizing photons from the active nucleus increase the radiation hardness (the [Ne III] 15.56 μm/[Ne II] 12.81 μm ratio). However some of the Seyfert galaxies and quasars are in the diagram close to H II regions. These may be galaxies harboring an AGN as well as star formation. Moreover, the position of the AGNs and starbursts in Figure 4.9 is consistent with models (Groves et al. 2004b; Dopita et al. 2006).

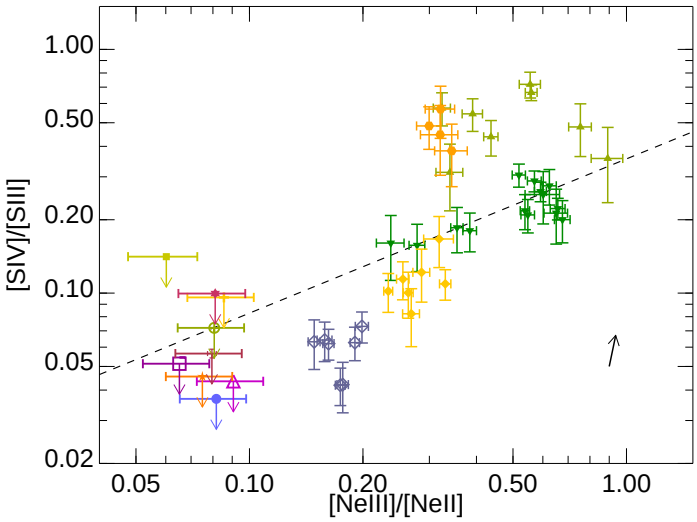

Figure 4.10: [S IV] 10.51 μm/[S III] 18.71 μm ratio vs. [Ne III] 15.56 μm/[Ne II] 12.81 μm ratio from the spatially resolved maps. We did not apply an extinction correction. The galaxy symbols are as in Figure 4.7. When [S IV] 10.51 μm is not detected we represent the upper limit of the nuclear [S IV] 10.51 μm/[S III] 18.71 μm ratio. The dashed line is the correlation found by Gordon et al. (2008) for M101 H II regions and starburst galaxies. The black arrow indicates the extinction correction of A_V=10 mag, assuming a screen geometry. The orange and light green points above the correlation corresponds to galaxies harboring an AGN (see Section 4.5.2.3).

4.5.2.3 The [S IV] 10.51 μm to [Ne III] 15.56 μm and to [S III] 18.71 μm Line Ratios

The [S IV] 10.51 μm and [Ne III] 15.56 μm lines arise from ions with a similar excitation potential, 35 eV and 41 eV, respectively. While the [Ne III] 15.56 μm line is detected in all galaxies, the [S IV] 10.51 μm line is detected in just six galaxies (40 % of the sample). If the [S IV] 10.51 μm emission arises from silicate dust embedded regions, it can be heavily affected by extinction as it is inside the broad 9.7 μm silicate feature. This seems to be the case in ULIRGs (Farrah et al. 2007). However, the depth of the silicate features in our sample of LIRGs are moderate, and generally much lower than in ULIRGs probably indicating lower extinction (see Section 4.4).

Using the photoionization models of Snijders et al. (2007), we can infer the expected range of [S IV] 10.51 μm/[Ne III] 15.56 μm ratios. The values for the range of densities, ionization parameters and stellar population ages covered by the models, excluding the most extreme cases, are compatible with the upper limits we measure. Moreover, we do not find any correlation between the [S IV] 10.51 μm/[Ne III] 15.56 μm ratio and the observed silicate strength (S_{Si}). Thus it is likely that the non-detection of the [S IV]

10.51 μm line is because its flux is under the detection limit.

The [S IV] 10.51 μm/[S III] 18.71 μm and the [Ne III] 15.56 μm/[Ne II] 12.81 μm ratios are well correlated and can be used to estimate the hardness of the radiation field (Verma et al. 2003; Dale et al. 2006; Gordon et al. 2008). Figure 4.10 shows that there is a good correlation between the [S IV] 10.51 μm/[S III] 18.71 μm and [Ne III] 15.56 μm/[Ne II] 12.81 μm ratios of the spatially resolved measurements for our star-forming LIRGs, and indeed, they approximately follow the correlation found by Gordon et al. (2008) for M101 H II regions and starburst galaxies. The upper limits to the [S IV] 10.51 μm/[S III] 18.71 μm ratio are also consistent with this trend.

Two of the galaxies classified as active, NGC 5135 and NGC 7130, lie above the Gordon et al. (2008) correlation. A similar trend was found by Dale et al. (2006) for AGN in the [S IV] 10.51 μm/[S III] 33.48 μm versus the [Ne III] 15.56 μm/[Ne II] 12.81 μm diagram. A possible explanation is that extra [S IV] 10.51 μm emission is produced by the active nucleus. High spatial resolution ground-based observations of these two LIRGs indicate that most of the [S IV] 10.51 μm emission comes from the nucleus, whereas this line is not detected in the surrounding star-forming regions of these galaxies (Díaz-Santos et al. 2010). For the other two galaxies NGC 3690 (classified as Seyfert), and NGC 7591 (classified as composite, intermediate between H II and LINER) the [S IV] 10.51 μm line is more likely to be affected by extinction, as both have nuclear $S_{\rm Si} \sim -0.8$, and thus the observed [S IV] 10.51 μm/[S III] 18.71 μm ratios are lower limits.

4.6 PAH Features

Models predict that the relative strength of the PAH bands depends on the ionization state (Draine & Li 2001; Galliano 2006). The 6.2 μm PAH and 7.7 μm PAH bands dominate the emission of ionized PAH, whereas the 11.3 μm PAH is more intense for neutral PAHs. More complete models of PAH feature behavior have been published recently by Galliano et al. (2008b), who explore the effects of the radiation field hardness and intensity as well as the size distribution of the PAH carriers.

4.6.1 Morphology

Figure 4.18 shows flux maps of three brightest PAH features present in the SL module at 6.2 μm, 7.7 μm, and 11.3 μm, together with the 5.5 μm continuum maps. Table 4.6 shows the ratio between the flux arising from the central 2 kpc and the total emission. The 11.3 μm PAH is clearly more extended than the 5.5 μm continuum in 60%

of the galaxies, arising also from more diffuse regions (see also Díaz-Santos et al. 2010). However, the nuclear contribution to the integrated 6.2 μm PAH emission is comparable to that at the 5.5 μm continuum, and only in two cases (NGC 7130 and NGC 7591) the 6.2 μm PAH emission is more extended than the continuum. When comparing both PAHs, the 11.3 μm PAH emission is more extended than the 6.2 μm PAH emission in about 40 % of the galaxies, while the opposite is never the case.

A direct comparison of the PAH ratios with fine structure line ratios is not possible because the low spectral resolution ($R \sim 60$–120) is not sufficient to separate the emission lines from the PAHs. Alternatively we used high-resolution ($R \sim 600$) data to measure the fine structure lines and the 11.3 μm PAH (Figure 4.21).

In general, the 11.3 μm PAH emission appears to be more extended than the [Ne II] 12.81 μm line. The PAH emission is also more extended than the [Ne II] 12.81 μm+[Ne III] 15.56 μm emission which, as discussed in Section 4.5, traces recent star formation. PAHs have also been used to measure the star formation, since they are a proxy, although not perfect, for the total infrared luminosity (Peeters et al. 2004b; Smith et al. 2007b). From this comparison, it is clear that the 11.3 μm PAH emission does not trace the same stars as the [Ne II] 12.81 μm emission line. In fact, Peeters et al. (2004b) found that the 6.2 μm PAH is not a good tracer of massive star formation (O stars) as seems to be the case of the 11.3 μm PAH.

4.6.2 Extinction Effects on the PAH Ratios

As discussed above, models (Draine & Li 2001; Galliano 2006) predict that neutral PAHs show larger 11.3 μm PAH to 6.2 μm PAH and 11.3 μm PAH to 7.7 μm PAH ratios than ionized PAHs. Figures 4.19 and 4.20 show the SL spectral maps of the 11.3 μm PAH/6.2 μm PAH and 11.3 μm PAH/7.7 μm PAH ratios, respectively. The 11.3 μm PAH/6.2 μm PAH ratio spans a factor of 2, from $\sim$0.45 to $\sim$1.15 and the 11.3 μm PAH/7.7 μm PAH ratio range is $\sim$0.3–0.9. These ranges are similar to those found in starburst galaxies (Brandl et al. 2006).

The 11.3 μm PAH is affected by the broad 9.7 μm silicate feature, thus in highly obscured regions the the 11.3 μm PAH/6.2 μm PAH and the 11.3 μm PAH/7.7 μm PAH ratios can be underestimated. An example of this is the southern nucleus of NGC 3256, one of the most obscured regions ($S_{\rm Si} = -1.4$) in the sample. Its 11.3 μm PAH/ 6.2 μm PAH ratio is lower than that in the surrounding regions.

To explore the effects of the 9.7 μm silicate feature on the PAH ratios, we compare the 11.3 μm PAH/6.2 μm PAH ratio and $S_{\rm Si}$ for the spatially resolved measurements of our LIRGs in Figure 4.11 (left panel). A similar figure was presented by Brandl et al.

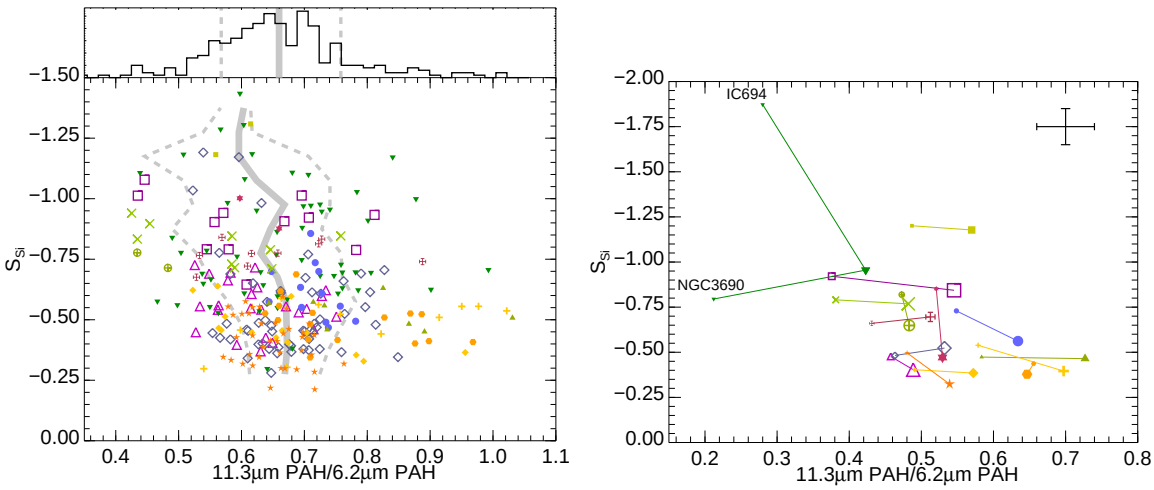

Figure 4.11: 11.3 μm PAH/6.2 μm PAH ratio vs. silicate strength (S_{Si}). Top: Spatially resolved measurements using a 2×2 pixel box. The symbols are as in Figure 4.7. The solid gray line is the median and the dashed gray lines encircle the region containing 68 % of the data points. These are calculated in intervals of 0.25 of the S_{Si}. The top histogram is the distribution of the the 11.3 μm PAH/6.2 μm PAH ratio for the whole sample of LIRGs, in gray are marked the median and the 1σ. Bottom: same as the left panel, but comparing the nuclear (small symbols) and integrated (large symbols) values. For each galaxy the values are connected by a line to guide the eye.

(2006) for the nuclear regions of starburst galaxies. They found that the extinction can change the relative strength of the PAHs by up to a factor of 2. We find, however, that the median value of the 11.3 μm PAH/6.2 μm PAH ratio is approximately constant for silicate strengths weaker than ~ -1.0, and only deeper silicate absorptions seem to affect the 11.3 μm PAH/6.2 μm PAH ratio. Some caution is needed here because there are very few regions in our sample with silicate strengths stronger than -1.0.

As an alternative approach, we corrected these PAH ratios for extinction using the spatially resolved measurements of the S_{Si}. We assumed a foreground screen dust geometry and the extinction law of Smith et al. (2007b). For a typical value of the silicate strength in our sample of $S_{Si} = -0.5$, this extinction reduces the 11.3 μm PAH to 6.2 μm PAH and to 7.7 μm PAH ratios by ∼15 %. If we increase the silicate strength up to -1.0 the reduction is ∼30 %. These are much less than the factor of ∼2 variations in the 11.3 μm PAH/6.2 μm PAH ratio observed in some galaxies (e.g., NGC 3256, NGC 3110, NGC 6701), at an almost constant value of S_{Si}. Thus, we conclude that the observed variations in the PAH ratios are real, and do not significantly depend on the extinction, at least for regions in our sample of LIRGs with relatively shallow silicate absorptions ($S_{Si} > -1$).

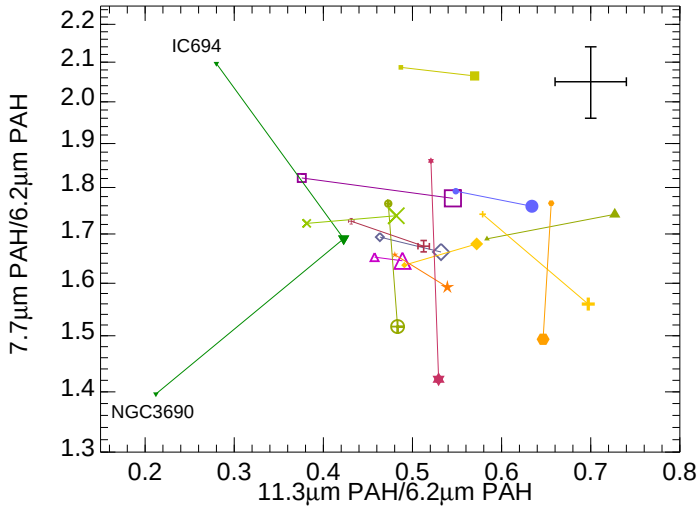

Figure 4.12: 11.3 μm PAH/6.2 μm PAH ratio vs. 7.7 μm PAH/6.2 μm PAH ratio for nuclear and integrated values. Symbols are as in the right panel of Figure 4.11.

4.6.3 Nuclear versus Integrated PAH Ratios

The right panel of Figure 4.11 compares the 11.3 μm PAH/6.2 μm PAH ratio versus $S_{\rm Si}$ values of the nuclear spectra and the integrated spectra. The general trend is that the integrated spectra have shallower silicate absorptions ($\sim$15 % lower $S_{\rm Si}$, on average) and slightly larger ($\sim$20 %, on average) 11.3 μm PAH/6.2 μm PAH ratios.

In Figure 4.12 we represent the 11.3 μm PAH/6.2 μm PAH ratio versus 7.7 μm PAH/6.2 μm PAH ratio, comparing the nuclear and the integrated values of each galaxy. The distribution of the values of the ratio is approximately uniform. However it is interesting to note two clearly different behaviors. The majority of the galaxies show a small variation of the 7.7 μm PAH/6.2 μm PAH ratio and a somewhat larger 11.3 μm PAH/6.2 μm PAH ratio in the integrated spectrum. This behavior is expected, since the 7.7 μm PAH and 6.2 μm PAH are related to ionized PAHs and the 11.3 μm PAH to neutral PAHs. The ionized PAHs emission is concentrated in the nuclear regions, but there is a substantial amount of the 11.3 μm PAH emission arising from diffuse regions throughout the galaxies (see Section 4.6.1). This explains the larger integrated 11.3 μm PAH/6.2 μm PAH ratios of all the LIRGs (see Table 4.3).

Some galaxies, however, show a completely different behavior, with an almost constant 11.3 μm PAH/6.2 μm PAH ratio but a lower 7.7 μm PAH/6.2 μm PAH ratio in the integrated spectrum. The most extreme cases of this behavior are NGC 7130 and NGC 7591. Galliano et al. (2008b) showed that the 7.7 μm PAH/6.2 μm PAH ratio is very sensitive to the size distribution of the PAHs, with smaller PAH molecules producing lower 7.7 μm PAH/6.2 μm PAH ratios. One possibility is that smaller PAH

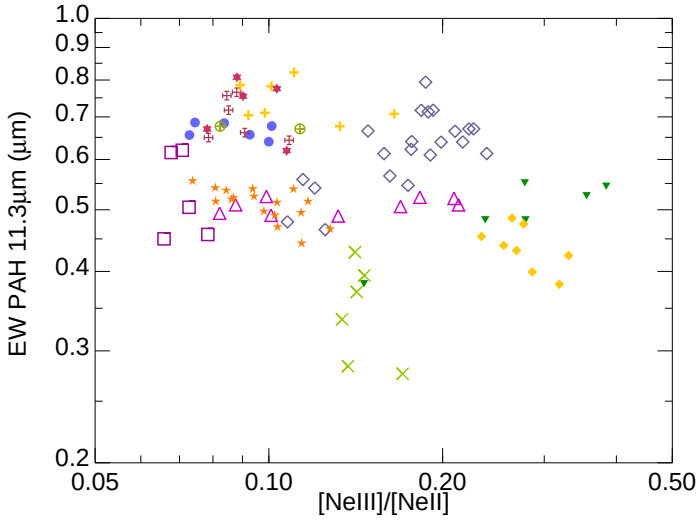

Figure 4.13: Spatially resolved measurements of the EW of the 11.3 μm PAH vs. the [Ne III] 15.56 μm/[Ne II] 12.81 μm ratio for those galaxies not classified as active. Galaxy symbols as in Figure 4.7.

molecules are destroyed in harsher environments, such as those of Seyfert and LINER nuclei. The destruction of small PAHs might suppress the nuclear 6.2 μm PAH emission. This may lead to the different behavior observed in the AGN/LINER nuclei in Figure 4.12. Moreover, the absolute value of the ratio seems to give little information about the nature, starburst or AGN, of the nuclei and we can only distinguish them by the relative variation between nuclear and integrated ratios.

4.6.4 The Effects of the Radiation Field

Since the [Ne III] 15.56 μm/[Ne II] 12.81 μm ratio is a proxy for the hardness of the radiation field, we can compare the spatial variations of this ratio with those of the 11.3 μm PAH/6.2 μm PAH to ascertain if the radiation field has an effect on the PAH ratios. A comparison between Figures 4.19 and 4.21 indicates that the 11.3 μm PAH/6.2 μm PAH ratio does not decrease necessarily in regions of enhanced [Ne III] 15.56 μm/[Ne II] 12.81 μm ratios.

On the other hand, the morphology of the 11.3 μm PAH/7.7 μm PAH ratio (Figure 4.20) resembles that of the [Ne III] 15.56 μm/[Ne II] 12.81 μm ratio. However this resemblance is the opposite of what one would expect. Both ratios present their minima in the nuclear regions for most of the galaxies. Thus while the observed nuclear [Ne III] 15.56 μm/[Ne II] 12.81 μm ratio would indicate lower radiation hardness in the nuclei, the PAH ratio would suggest a larger ionization state. Again, it is likely that

the typical radiation field hardness observed in our sample of LIRGs is not sufficiently large as to affect the PAH emission, as is the case of the low-metallicity galaxies of Wu et al. (2006). Another possible interpretation is that the PAHs and the neon emission are related to different physical processes that due to our limited spatial resolution we cannot separate. As a result, the bulk of the 7.7 μm PAH emission may be produced in star-forming regions, while the 11.3 μm PAH emission also comes from diffuse regions. Thus, low values of the 11.3 μm PAH/7.7 μm PAH ratio trace H II regions, and larger values indicate less recent star formation. The latter interpretation is similar to that of Galliano et al. (2008b). They find that the lowest values of the 11.3 μm PAH/ 7.7 μm PAH ratio are associated with the brightest PAH emission. However, in their galaxies, the 11.3 μm PAH/6.2 μm PAH ratio follows the same trend, whereas this is not the case for the LIRGs studied here. Alternatively, as discussed in the previous section, the size of the grains may affect this ratio. If the smaller grains are favored in and around the nucleus, the 7.7 μm PAH emission would be increased with respect to the 11.3 μm PAH emission. As a consequence, the 11.3 μm PAH/7.7 μm PAH ratio would be lower in the nucleus.

Brandl et al. (2006) studied the dependency of the EW of the PAHs with the radiation hardness for a sample of high-metallicity starburst galaxies. Wu et al. (2006) carried out a similar study, but for low- metallicity galaxies. Whereas Brandl et al. (2006) found that this dependency does not exist, Wu et al. (2006) found the opposite, that is, the harsher radiation of low-metallicity galaxies field lowers the PAH EW. Eventually Gordon et al. (2008) showed that the reason for the discrepancy is the different range of the radiation field hardness in high- and low-metallicity galaxies. In particular, Gordon et al. (2008) found that for ionizations above a certain threshold there is a correlation between the radiation hardness and the PAH EW, but for lower ionizations this dependency disappears. We show in Figure 4.13 the EW of the 11.3 μm PAH and the [Ne III] 15.56 μm/[Ne II] 12.81 μm ratio of those galaxies not classified as AGN. The ionization and metallicity of our LIRGs are similar to those galaxies studied by Brandl et al. (2006) and, similarly to their findings, there is no correlation between these parameters in our sample of LIRGs.

4.6.5 Dependency on the Age of the Stellar Population

Since the [Ne II] 12.81 μm emission traces young stellar populations (<10 Myr), and since the 11.3 μm PAH feature can also be excited by older populations (see Peeters et al. 2004b and Section 4.6.1), the [Ne II] 12.81 μm/11.3 μm PAH ratio can give us an indication of age variations throughout the galaxies (Díaz-Santos et al. 2010). As can

be seen from Figure 4.21, the [Ne II] 12.81 μm/11.3 μm PAH ratio ranges from ∼0.1 to ∼0.6 for our sample of LIRGs. In some LIRGs (e.g., NGC 6701, NGC 7130, NGC 7771, IC 4687) the [Ne II] 12.81 μm/11.3 μm PAH ratio appears enhanced in the high surface brightness H II regions (see the *HST*/NICMOS Paα images in Figure 4.21) with respect to regions of more diffuse emission. In other galaxies the interpretation might not be as straightforward. In some cases the IRS angular resolution is not sufficiently high to isolate the circumnuclear H II regions (e.g., NGC 5135), and the age differences may be smoothed out.

4.7 Molecular Hydrogen

We constructed maps of the molecular hydrogen emission using the pure rotational lines H_2 S(1) at 17.0 μm and the H_2 S(2) at 12.3 μm (Figure 4.21). These lines trace warm (300 K $< T <$ 1000 K) molecular gas in the interstellar medium. The H_2 S(1) morphology appears, generally, different from that of the fine structure lines, which are associated with the ionized gas medium. There are also differences in the velocity fields that will be discussed in Section 4.8. Using the same procedure as described in Section 4.5.1 we find that the H_2 S(1) emission is more extended than the 15 μm continuum in ∼60 % of the sample. In most of these galaxies the size of the H_2 S(1) emitting region is larger than that of the fine structure lines (see Table 4.6).

4.7.1 Temperatures, Column Densities and Masses

We extracted the nuclear spectra of all galaxies using a $13\farcs4 \times 13\farcs4$ aperture. This aperture corresponds to physical scales between 3 and 5 kpc depending on the galaxy. This aperture size is different from that used in the other sections because now we are limited by the lowest spatial resolution of the LH module, where the H_2 S(0) line at 28.2 μm lies. The fluxes of the H_2 lines measured from these spectra are listed in Table 4.7.

The temperature of the warm molecular hydrogen was calculated as described by Roussel et al. (2007). We assumed an ortho-to-para ratio = 3 (Rigopoulou et al. 2002; Roussel et al. 2007), and thus this assumption may introduce some uncertainty as it is used in the temperature calculations. The column densities and masses are highly dependent on the H_2 lines used in these calculations. It is preferable to use the lines H_2 S(0) and H_2 S(1) because they come from the lowest rotational levels of the hydrogen molecule, and therefore they trace the molecular hydrogen gas at the lowest temperatures which dominates determination of the masses (Roussel et al. 2007).

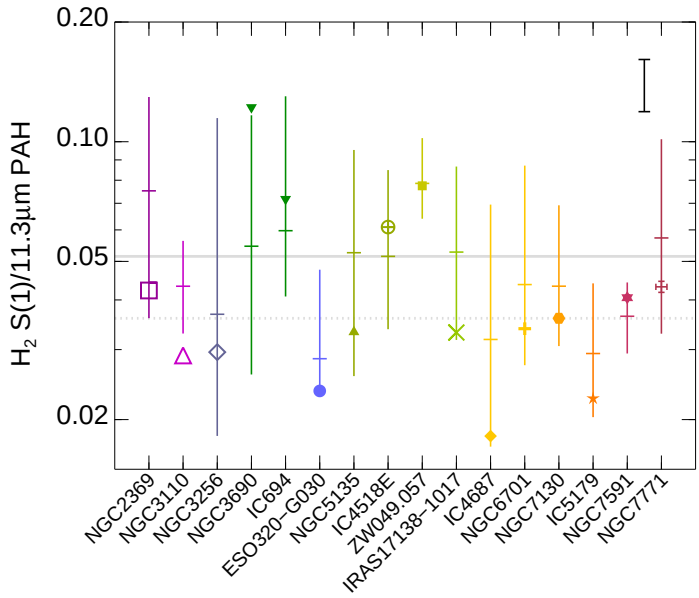

Figure 4.14: Range of the observed H_2 S(1)/11.3 μm PAH ratio for each galaxy. Symbols are as in Figure 4.7.

However the H_2 S(0) line is not detected in all galaxies, and to allow meaningful comparisons we estimated the column densities and masses with the H_2 S(1) and H_2 S(2) lines. The results are presented in Table 4.8. The masses estimated from the H_2 S(1) and H_2 S(0) lines are in the range 0.4 to 3 $\times 10^8\, M_\odot$. These values are comparable to those found in ULIRGs (Higdon et al. 2006), local starbursts and Seyfert galaxies (Rigopoulou et al. 2002; Tommasin et al. 2008). It should be noted that these masses correspond to a beam size of 13.″4×13.″4 which does not include all the molecular hydrogen emission. Then the mass values listed in Table 4.8 should be considered as lower limits to the total H_2 mass of the galaxy. For instance the integrated fluxes of the H_2 S(1) line (Table 4.5) are a factor of between 2 and 3 larger than those used in the mass calculations (Table 4.7). Thus assuming that the physical conditions of the H_2 in the outer parts of the galaxy are similar to those in the inner ∼3–5 kpc, the total mass would be at least a factor of ∼2–3 larger than the values listed in Table 4.8.

4.7.2 Excitation Mechanism and Relation to the PAH Emission

Studies of the molecular hydrogen emission of galactic PDRs indicate that the formation of H_2 occurs in the surfaces of PAHs (see e.g., Habart et al. 2003; Velusamy & Langer 2008) as both the PAH carriers and molecular hydrogen can be excited by UV radiation. Thus the H_2 and the PAH emission morphologies are correlated in these

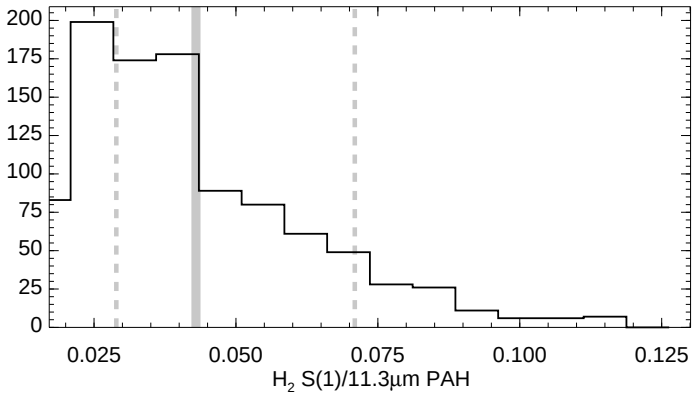

Figure 4.15: Distribution of the observed H_2 S(1)/11.3 μm PAH ratio for all the galaxies from spatially resolved measurements. The lines are as in Figure 4.4

regions. A similar correlation is seen in external galaxies (Rigopoulou et al. 2002; Roussel et al. 2007). However, H_2 can be excited by other mechanisms, such as X-rays (e.g., Lepp & McCray 1983) and shock fronts (e.g., Hollenbach & McKee 1989).

To explore the morphological differences we constructed maps of the H_2 S(1)/ 11.3 μm PAH ratio. The range of this ratio for each galaxy is shown in Figure 4.14. This ratio varies by a factor of 10 in our sample of LIRGs, although, as can be seen in the Figure 4.15, 68% of the values are in a narrower range, from 0.028 to 0.073. Figure 4.16 shows the ratio maps of those galaxies with the most noticeable morphological characteristics.

The 11.3 μm PAH feature falls close to the the 9.7 μm silicate absorption and, although the H_2 S(1) is also close to the silicate absorption at 18 μm, extinction variations could increase artificially the H_2 S(1)/11.3 μm PAH ratio. We used the extinction curve adopted by Smith et al. (2007b) to quantify this effect. If we assume a mixed model for the dust distribution, the ratio can be increased by up to a factor of $\sim$1.4, for the typical silicate absorption observed in our sample of LIRGs. Which is much lower than the observed variation. Choosing a screen geometry, to increase the ratio by a factor of 2 we would need an optical extinction of $A_V \sim$100 mag, which is much larger than our estimates (Section 4.4). Therefore, the effect of the extinction is small compared to the observed variations of the H_2 S(1)/11.3 μm PAH ratio.

We can try to distinguish among the different excitation mechanisms by comparing the 11.3 μm PAH morphology with that of the H_2 emission (Figure 4.21). It is clear that the morphologies are different. The H_2 S(1) emission is more extended than the PAH emission, although the maxima of both emissions are located in the nucleus for most of the galaxies. The only exception is NGC 3256 where the H_2 S(1) peaks at the

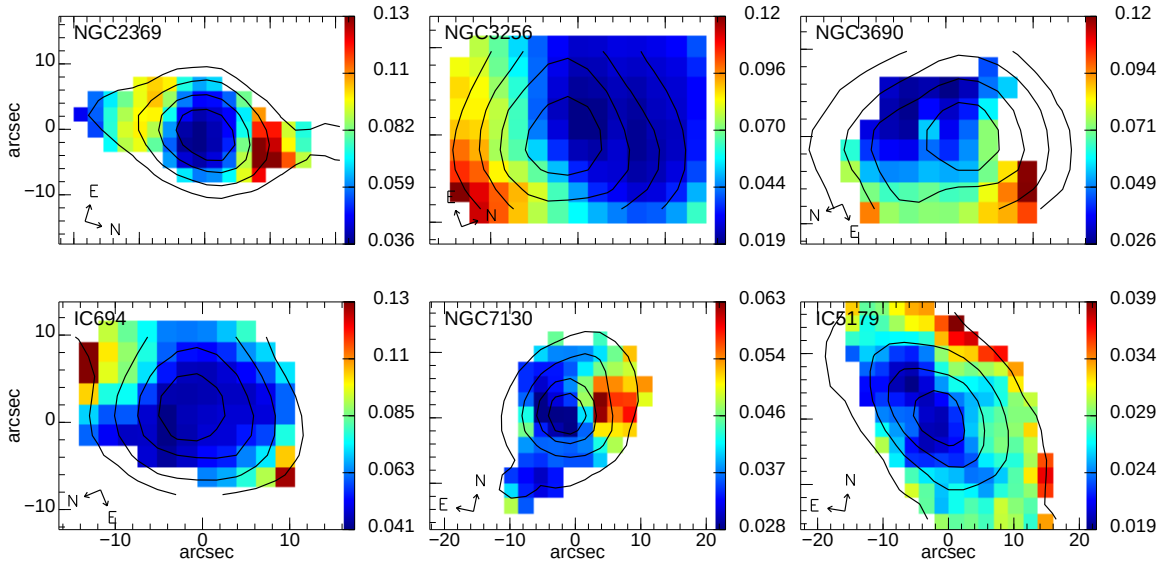

Figure 4.16: Maps of the observed H_2 S(1)/11.3 μm PAH ratio for selected galaxies. For reference we represent the 15 μm continuum contours.

southern nucleus while the PAH maximum is located at northern nucleus. We note, however, that the southern nucleus of this galaxy is very obscured (see Figure 4.22 and Díaz-Santos et al. 2010), and the 11.3 μm PAH map is not corrected for extinction. This suggests that the warm H_2 in LIRGs is produced not only in PDRs, but that the other mechanisms also play a role.

We attribute the increased values of the H_2 S(1)/11.3 μm PAH ratio, not to a deficiency of PAH emission, but rather to an excess emission by H_2, excited by X-ray or shocks. For instance, in the merger system NGC 3256, the largest value of the ratio occurs where the components of the merger are colliding. The H_2 line ratios are inconsistent with X-ray excitation (Shaw et al. 2005). Thus, it is likely that there is some contribution from shocks to the H_2, as appears also to be the case for some regions in NGC 3690 and IC 694 (Alonso-Herrero et al. 2009b). In many cases, the hypothesis of shock excitation is supported by large velocity dispersions (see García-Marín et al. 2006 for NGC 3690/IC 694 and the following section for additional examples).

The galaxy IC 5179 is interesting because its velocity field (see the next section) is highly ordered, so strong shocks are unlikely, and its X-ray luminosity is low. Thus the H_2 emission in this galaxy is likely to be produced in PDRs. The small variations (a factor of 2) of the H_2 S(1)/11.3 μm PAH ratio are probably due to differences in the extinction or differences in the 11.3 μm PAH relative strength with respect to the total PAH luminosity from region to region. For the rest of the galaxies, the morphology of H_2 S(1)/11.3 μm PAH ratio does not allow us to determine whether the H_2 is produced

in PDRs or is excited by shock fronts or X-ray.

4.8 Velocity Fields

Figure 4.23 shows the velocity fields of the [Ne II] 12.81 μm and H_2 S(1) emission lines in the SH module. They cover ∼30"×30", which corresponds to physical scales of ∼6-11 kpc, depending on the galaxy. Most of the [Ne II] 12.81 μm velocity fields are consistent with a rotating disk, although some of them show more complex morphologies (NGC 3110, NGC 3256, IC 694, NGC 6701 and NGC 7130). Only two of the galaxies (NGC 3256 and IC 694) with perturbed velocity fields are part of merger systems. NGC 3110 and NGC 7130 are paired with other galaxies. However not all the galaxies in groups present disturbed velocity fields (e.g., NGC 7771, IC 4518E), at least on the physical scales (∼kpc) probed by the IRS spectral maps.

Figure 4.17 shows the velocity field of the interacting system Arp 299 (IC 694 and NGC 3690) rotated to the usual north up east to the left orientation for easy comparison with other works. The [Ne II] 12.81 μm velocity field, which traces the ionized gas, agrees well with that measured from Hα (see García-Marín et al. 2006). The peak-to-peak variation of the velocity field ∼250 km s^{-1} is also comparable to that measured from Hα. The warm molecular gas (300 K $< T <$ 1000 K) velocity field, traced by the H_2 S(1) line, is similar to the [Ne II] 12.81 μm field (Figure 4.17), as both rotate in the same sense, although there are differences. The molecular hydrogen velocity field does not present the irregular structure of the ionized gas and the neutral gas (see García-Marín et al. 2006). However, the H_2 S(1) velocity field resembles that produced by two disks rotating in opposite sense. This suggests that before the interaction both galaxies were spirals (Augarde & Lequeux 1985). Moreover the H_2 S(1) velocity field shows evident similarities with the CO velocity field (see Aalto et al. 1997; Casoli et al. 1999).

Hα velocity fields are available for NGC 3256 (Lípari et al. 2000), NGC 6701 and NGC 7771 (Alonso-Herrero et al. 2009a) and NGC 7591 (Amram et al. 1994). The [Ne II] 12.81 μm velocity field of NGC 3256 appears perturbed due to the merger nature of this galaxy. It is consistent with the Hα velocity field in shape and amplitude. The Hα velocity maps of NGC 7771 and NGC 6701 are slightly smaller than those presented here. NGC 7771 has and ordered velocity field compatible with a rotating disk whereas NGC 6701 presents a complex morphology both in Hα and mid-IR emission lines. The structure and the peak-to-peak velocity amplitude (∼300 km s^{-1} for NGC 7771 and ∼150 km s^{-1} for NGC 6701) of the [Ne II] 12.81 μm velocity field are in good agreement with those of the Hα velocity field. As in the previous cases, the Hα velocity field of

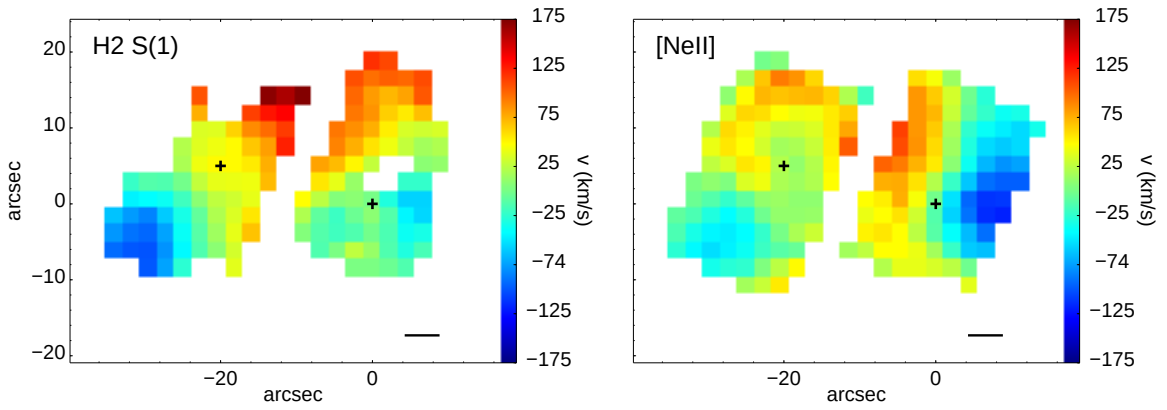

Figure 4.17: Arp 299 (NGC 3690 and IC 694) velocity fields of the molecular gas traced by the H_2 S(1) line (left) and the ionized gas traced by the [Ne II] 12.81 μm line (right). The velocities are referred to the the nucleus B1 of Arp 299. The black crosses mark the nuclei A and B1 of Arp 299. The scale represents 1 kpc. North is up and east to the left.

NGC 7591 is also similar to that of the [Ne II] 12.81 μm.

4.9 Conclusions

We presented the analysis of *Spitzer*/IRS mapping observations of 15 local LIRGs with extended Paα emission. We studied the spatial distribution of the mid-IR spectral features and compared the nuclear and integrated spectra. We calculated fine structure line and PAH ratios which trace the physical conditions in the star-forming regions. The main results are the following:

1. We used the 9.7 μm silicate feature strength versus 6.2 μm PAH EW diagram to classify the activity of the LIRGs. There is a good agreement with the optical classification and this diagram. Most of the LIRGs populate the pure starburst class and only the nuclei classified as Seyfert from optical spectroscopy appear in the diagram in the AGN/SB class. The integrated values show, in general, larger 6.2 μm PAH EW and shallower silicate absorption than the nuclear spectra. That is, the extended star formation partially masks the nuclear activity, resulting in a starburst-like integrated spectra. The silicate feature strength, nuclear and integrated, of our sample of local LIRGs ($S_{\rm Si} \sim -0.4$ to -0.9) is small compared to that found in ULIRGs ($S_{\rm Si}$ up to -4).

2. We constructed maps of the spatial distribution of the [Ne III] 15.56 μm/[Ne II] 12.81 μm, which traces the radiation field hardness, and the [S III] 18.71 μm/

[Ne II] 12.81 μm that varies with the electron density. In general, the minimum of both ratios is located at the nucleus. The nuclear [Ne III] 15.56 μm/[Ne II] 12.81 μm ratio is below the expected range derived by star-formation models. A possible explanation is that due to the high densities in the nuclear regions this ratio is suppressed, including the possibilities that the most massive stars are either missing or buried in ultracompact H II regions. Alternatively, the star formation rate may have decreased rapidly in all nuclei over the last 10–20 Myr.

3. We found a positive correlation between the [Ne III] 15.56 μm/[Ne II] 12.81 μm and [S III] 18.71 μm/[Ne II] 12.81 μm ratios for star-forming regions in our sample of LIRGs and other starburst galaxies. On the other hand, AGNs, for a given [S III] 18.71 μm/[Ne II] 12.81 μm ratio, show a systematically larger [Ne III] 15.56 μm/[Ne II] 12.81 μm ratio. The few starburst galaxies where we detect the [S IV] 10.51 μm emission line follow the correlation between the [S IV] 10.51 μm/[S III] 18.71 μm and [Ne III] 15.56 μm/[Ne II] 12.81 μm observed in H II regions in other galaxies. We observe larger [S IV] 10.51 μm/[S III] 18.71 μm ratios for those galaxies harboring an AGN.

4. We found that the 11.3 μm PAH emission is more extended than that of the 5.5 μm continuum. However, the ratio of the nuclear (2 kpc) 6.2 μm PAH emission with respect to the integrated emission is comparable to that of the 5.5 μm continuum in most cases. We find no correlation between the [Ne III] 15.56 μm/[Ne II] 12.81 μm ratio and the 11.3 μm PAH EW, thus the effect of the radiation field hardness in the PAH emission, for the [Ne III] 15.56 μm/[Ne II] 12.81 μm ratio range in our sample of LIRGs, may not be important. We propose that the 11.3 μm PAH/7.7 μm PAH ratio depends on the age of the stellar population. While the 7.7 μm PAH comes from young star-forming regions, the 11.3 μm PAH arises also from diffuse medium, thus the 11.3 μm PAH/7.7 μm PAH is lower in young H II regions. We also found that large [Ne II] 12.81 μm/11.3 μm PAH ratios may indicate recent star formation.

5. We explored the variation of the PAH ratios across the galaxies. In most cases these variations are real, that is, they are not due to extinction. In general the integrated 11.3 μm PAH/6.2 μm PAH ratios are larger than the nuclear values, probably indicating that the integrated emission includes more neutral conditions. The nuclear and integrated 7.7 μm PAH/6.2 μm PAH ratios are almost constant, except in the nuclei of galaxies classified as AGN where this ratio is higher. Since the 6.2 μm PAH emission is more associated with small molecules,

the increased 7.7 μm PAH/6.2 μm PAH ratio in AGN could be explained if the small PAH molecules are more easily destroyed in the harsh environments of active nuclei.

6. Using the H_2 S(0) at 28.2 μm and the H_2 S(1) at 17.0 μm lines integrated over 13"×13" (3–5 kpc) we estimated the mass of the warm ($T \sim 300$ K) molecular hydrogen. It ranges from 0.4 to $2.6\times10^8\,M_\odot$, and they are similar to those of ULIRGs, local starbursts and Seyfert galaxies. However these masses are lower limits since it is only included the H_2 emission from the central few kpc of the galaxies and the total mass of warm molecular hydrogen is likely to be, at least, a factor of 2 larger.

7. The similarity between the PAHs and molecular hydrogen morphologies suggests that the main excitation mechanism of the latter is the UV radiation too. However there are some regions with an excess of H_2 emission with respect to the PAH emission, thus the other mechanisms should contribute noticeably to the H_2 emission. Some of these regions are associated with interacting systems, where large-scale shocks may also play a role in exciting the molecular hydrogen.

8. Despite the modest spectral resolution of the SH module, we showed that useful velocity information can be obtained from the SH spectra. For most of the galaxies and on the physical scales probed by the IRS spectra (∼kpc) the velocity fields are comparable with that produced by a rotating disk. For the galaxies with available Hα velocity fields, the [Ne II] 12.81 μm velocity fields are in good agreement with those of the Hα, both in shape and peak-to-peak velocities.

4.A Tables

Table 4.2: Low-resolution (SL) Nuclear Spectra

Galaxy	Size	$S_{\rm Si}$	PAH EW (μm)			
	(kpc)		6.2 μm	11.3 μm	$\frac{7.7\,\mu\text{m PAH}}{6.2\,\mu\text{m PAH}}$	$\frac{11.3\,\mu\text{m PAH}}{6.2\,\mu\text{m PAH}}$
NGC2369	1.2	-0.92	0.43 ± 0.04	0.33 ± 0.02	1.8 ± 0.1	0.38 ± 0.01
NGC3110	2.0	-0.48	0.58 ± 0.11	0.48 ± 0.05	1.7 ± 0.1	0.46 ± 0.01
NGC3256	1.1	-0.48	0.53 ± 0.02	0.33 ± 0.01	1.7 ± 0.1	0.46 ± 0.01
NGC369	1.2	-0.80	0.11 ± 0.01	0.045 ± 0.001	1.4 ± 0.1	0.21 ± 0.01
IC694	1.2	-1.9	0.34 ± 0.01	0.23 ± 0.01	2.1 ± 0.1	0.28 ± 0.02
ESO320-G030	1.2	-0.73	0.49 ± 0.06	0.50 ± 0.03	1.8 ± 0.1	0.55 ± 0.01
NGC5135	1.6	-0.47	0.30 ± 0.02	0.31 ± 0.02	1.7 ± 0.1	0.58 ± 0.01
IC4518E	1.8	-0.82	0.39 ± 0.28	0.44 ± 0.17	1.8 ± 0.2	0.47 ± 0.05
ZW049.057	1.5	-1.2	0.39 ± 0.15	0.48 ± 0.16	2.1 ± 0.1	0.49 ± 0.03
IRAS17138-1017	2.0	-0.79	0.56 ± 0.06	0.40 ± 0.03	1.7 ± 0.1	0.38 ± 0.01
IC4687	2.0	-0.40	0.66 ± 0.08	0.55 ± 0.03	1.6 ± 0.1	0.49 ± 0.01
NGC6701	1.5	-0.54	0.46 ± 0.07	0.45 ± 0.05	1.7 ± 0.1	0.58 ± 0.01
NGC7130	1.9	-0.44	0.25 ± 0.04	0.23 ± 0.04	1.8 ± 0.1	0.66 ± 0.02
IC5179	1.3	-0.50	0.57 ± 0.08	0.46 ± 0.03	1.7 ± 0.1	0.48 ± 0.01
NGC7591	1.9	-0.85	0.39 ± 0.12	0.35 ± 0.06	1.9 ± 0.1	0.52 ± 0.02
NGC7771	1.7	-0.66	0.46 ± 0.06	0.38 ± 0.04	1.7 ± 0.1	0.43 ± 0.01

Table 4.3: Low-resolution (SL) Integrated Spectra

Galaxy	Size	$S_{\rm Si}$	PAH EW (μm)			
	(kpc)		6.2 μm	11.3 μm	$\frac{7.7\,\mu\text{m PAH}}{6.2\,\mu\text{m PAH}}$	$\frac{11.3\,\mu\text{m PAH}}{6.2\,\mu\text{m PAH}}$
NGC2369	8.8×6.2	-0.84	0.43 ± 0.08	0.40 ± 0.03	1.8 ± 0.1	0.55 ± 0.01
NGC3110	15.4×9.8	-0.40	0.73 ± 1.02	0.53 ± 0.05	1.6 ± 0.3	0.49 ± 0.06
NGC3256	7.6×3.8	-0.52	0.59 ± 0.02	0.43 ± 0.01	1.7 ± 0.1	0.53 ± 0.01
NGC3690	8.3×5.7	-0.96	0.29 ± 0.01	0.21 ± 0.01	1.7 ± 0.1	0.42 ± 0.03
IC694	8.3×5.7	-0.96	0.29 ± 0.01	0.21 ± 0.01	1.7 ± 0.1	0.42 ± 0.03
ESO320-G030	5.9×4.6	-0.56	0.53 ± 0.10	0.53 ± 0.04	1.8 ± 0.1	0.63 ± 0.01
NGC5135	10×5.9	-0.46	0.33 ± 0.05	0.35 ± 0.03	1.7 ± 0.1	0.73 ± 0.02
IC4518E	6.4×6.4	-0.65	0.62 ± 0.39	0.53 ± 0.16	1.5 ± 0.1	0.48 ± 0.03
ZW049.057	4.9×3.8	-1.2	0.42 ± 0.30	0.47 ± 0.19	2.1 ± 0.2	0.57 ± 0.06
IRAS17138-1017	10×4.3	-0.77	0.58 ± 0.10	0.43 ± 0.04	1.7 ± 0.1	0.48 ± 0.01
IC4687	13×5.8	-0.38	0.64 ± 0.11	0.54 ± 0.04	1.7 ± 0.1	0.57 ± 0.01
NGC6701	13×6.5	-0.40	0.53 ± 0.12	0.52 ± 0.05	1.6 ± 0.1	0.70 ± 0.02
NGC7130	12×8.2	-0.38	0.47 ± 0.10	0.37 ± 0.05	1.5 ± 0.1	0.65 ± 0.02
IC5179	10×5.5	-0.32	0.62 ± 0.08	0.51 ± 0.03	1.6 ± 0.1	0.54 ± 0.01
NGC7591	16×8.8	-0.47	0.63 ± 0.31	0.43 ± 0.08	1.4 ± 0.1	0.53 ± 0.03
NGC7771	11×7.8	-0.70	0.49 ± 0.07	0.41 ± 0.03	1.7 ± 0.1	0.51 ± 0.01

Table 4.4: High-resolution (SH) Nuclear Spectra

Name	Size[a]	[S IV]	[Ne II]	[Ne III]	[S III]	H_2 S(2)	H_2 S(1)	
	(kpc)	10.51μm	12.81μm	15.55μm	18.71μm	12.28μm	17.04μm	11.3 μm PAH
NGC2369	1.2	<0.44	52. ± 3.	3.4 ± 0.2	8.6 ± 0.2	3.1 ± 0.2	5.5 ± 0.2	138. ± 3.
NGC3110	1.9	<0.27	26. ± 1.	2.4 ± 0.1	6.2 ± 0.2	1.3 ± 0.3	2.8 ± 0.1	99. ± 2.
NGC3256	1.1	1.8 ± 0.3	260. ± 14.	27. ± 1.	60. ± 1.	8.0 ± 0.8	14. ± 1.	489. ± 5.
ESO320-G030	1.2	<0.39	41. ± 2.	3.3 ± 0.1	11. ± 0.1	2.8 ± 0.3	4.0 ± 0.1	172. ± 3.
NGC5135	1.6	8.0 ± 0.2	51. ± 3.	23. ± 1.	12. ± 0.1	3.2 ± 0.3	4.9 ± 0.2	166. ± 3.
IC4518E	1.8	<0.082	1.1 ± 0.1	0.13 ± 0.02	0.24 ± 0.08	0.13 ± 0.05	0.34 ± 0.05	5.4 ± 0.5
ZW049.057	1.5	<0.26	10. ± 1.	0.63 ± 0.07	1.8 ± 0.2	1.4 ± 0.3	2.2 ± 0.1	32. ± 3.
IRAS17138-1017	2.0	1.0 ± 0.2	64. ± 3.	8.5 ± 0.2	19. ± 1.	2.1 ± 0.6	4.0 ± 0.4	135. ± 3.
IC4687	2.0	2.3 ± 0.2	55. ± 2.	12. ± 0.1	23. ± 0.1	2.0 ± 0.3	3.2 ± 0.2	189. ± 3.
NGC6701	1.5	<0.49	27. ± 2.	2.3 ± 0.1	5.1 ± 0.2	1.9 ± 0.2	3.4 ± 0.2	103. ± 2.
NGC7130	1.9	3.6 ± 0.4	38. ± 3.	12. ± 1.	7.4 ± 0.6	1.7 ± 0.8	2.9 ± 0.3	93. ± 3.
IC5179	1.3	<0.39	36. ± 2.	2.7 ± 0.1	8.5 ± 0.3	1.4 ± 0.1	2.6 ± 0.1	120. ± 3.
NGC7591	1.9	<0.24	16. ± 1.	1.3 ± 0.1	2.4 ± 0.2	1.1 ± 0.2	1.8 ± 0.2	48. ± 2.
NGC7771	1.7	<0.38	37. ± 2.	3.0 ± 0.1	6.7 ± 0.4	3.0 ± 0.5	4.8 ± 0.2	115. ± 4.

Notes. Fluxes are expressed in units of $10^{-17}\,\mathrm{W\,m^{-2}}$. The fluxes of Arp 299 (NGC 3690 and IC 694) are given in Alonso-Herrero et al. (2009b).
[a] Projected square size of the aperture in kpc. The aperture size is 5.″5×5.″5 for all the galaxies.

Table 4.5: High-resolution (SH) Integrated Spectra

Name	Size[a]	[S IV]	[Ne II]	[Ne III]	[S III]	H_2 S(2)	H_2 S(1)	
	(kpc)	10.51μm	12.81μm	15.55μm	18.71μm	12.28μm	17.04μm	11.3 μm PAH
NGC2369	9.7×6.2	<5.5	194. ± 11.	15. ± 3.	44. ± 4.	19. ± 6.	51. ± 2.	798. ± 34.
NGC3110	15×8.4	<6.9	164. ± 14.	30. ± 3.	59. ± 5.	<5.1	33. ± 3.	877. ± 29.
NGC3256	6.0×3.8	15. ± 3.	1229. ± 48.	189. ± 5.	395. ± 8.	65. ± 6.	124. ± 3.	2998. ± 30.
ESO320-G030	6.3×4.2	<4.8	152. ± 7.	12. ± 2.	47. ± 5.	13. ± 4.	21. ± 2.	677. ± 29.
NGC5135	9.0×5.0	19. ± 2.	141. ± 12.	66. ± 3.	39. ± 3.	14. ± 4.	32. ± 2.	593. ± 24.
IC4518E	8.0×6.4	<1.6	11. ± 1.	0.90 ± 0.32	3.7 ± 1.0	<1.0	2.1 ± 0.5	34. ± 3.
ZW049.057	4.8×4.3	<4.3	23. ± 3.	<2.2	<1.4	<6.1	7.9 ± 1.0	89. ± 24.
IRAS17138-1017	11.5×5.8	<3.9	159. ± 9.	25. ± 1.	54. ± 3.	8.3 ± 3.7	24. ± 2.	505. ± 22.
IC4687	11×7.2	10. ± 2.	198. ± 10.	57. ± 2.	103. ± 3.	8.9 ± 5.5	22. ± 1.	750. ± 23.
NGC6701	8.1×5.4	<14.	117. ± 9.	16. ± 3.	32. ± 7.	<8.8	26. ± 3.	600. ± 14.
NGC7130	16×10	<9.6	158. ± 14.	36. ± 4.	39. ± 7.	<7.0	29. ± 5.	643. ± 29.
IC5179	10×6.9	<9.2	290. ± 17.	28. ± 3.	91. ± 5.	19. ± 5.	35. ± 6.	1334. ± 29.
NGC7591	8.8×6.8	<5.8	54. ± 5.	4.4 ± 2.5	10. ± 3.	<3.6	10. ± 4.	266. ± 13.
NGC7771	14×6	<12.	148. ± 11.	<9.2	41. ± 9.	20. ± 10.	41. ± 4.	675. ± 23.

Notes. Fluxes are expressed in units of $10^{-17}\,\mathrm{W\,m^{-2}}$. The fluxes of Arp 299 (NGC 3690/IC 694) are given in Alonso-Herrero et al. (2009b).
[a] Approximated projected square size of the aperture in kpc. See Section 4.3.3 for details.

Table 4.6: Nuclear/Integrated Flux Ratio

Name	Central 2.0 kpc/ Integrated Flux			Central 2.0 kpc/ Integrated Flux			
	5.5 μm Continuum	6.2 μm PAH	11.3 μm PAH	15 μm Continuum	[Ne II] 12.81 μm	[Ne III] 15.56 μm	H_2 S(1)
NGC2369	0.41 ± 0.02	0.41 ± 0.01	0.32 ± 0.01	0.39 ± 0.02	0.36 ± 0.02	0.36 ± 0.02	0.20 ± 0.02
NGC3110	0.13 ± 0.05	0.12 ± 0.02	0.10 ± 0.01	0.13 ± 0.01	0.07 ± 0.03	0.12 ± 0.02	0.08 ± 0.03
NGC3256	0.38 ± 0.01	0.36 ± 0.01	0.34 ± 0.01	0.39 ± 0.01	0.31 ± 0.01	0.41 ± 0.01	0.20 ± 0.03
ESO320-G030	0.57 ± 0.02	0.54 ± 0.01	0.49 ± 0.01	0.48 ± 0.01	0.49 ± 0.02	0.40 ± 0.01	0.38 ± 0.02
NGC5135	0.45 ± 0.01	0.42 ± 0.01	0.35 ± 0.01	0.39 ± 0.01	0.36 ± 0.01	0.28 ± 0.01	0.19 ± 0.03
IC4518E	0.21 ± 0.10	0.18 ± 0.10	0.15 ± 0.03	0.14 ± 0.02	···	0.15 ± 0.01	0.19 ± 0.06
ZW049.057	0.53 ± 0.08	···	0.50 ± 0.02	0.52 ± 0.02	···	0.47 ± 0.02	···
IRAS17138-1017	0.31 ± 0.03	0.31 ± 0.02	0.25 ± 0.01	0.31 ± 0.01	0.27 ± 0.01	0.19 ± 0.01	0.15 ± 0.05
IC4687	0.24 ± 0.03	0.25 ± 0.01	0.23 ± 0.01	0.19 ± 0.01	0.17 ± 0.01	0.15 ± 0.01	0.13 ± 0.05
NGC6701	0.25 ± 0.03	0.23 ± 0.02	0.20 ± 0.02	0.22 ± 0.01	0.16 ± 0.02	0.24 ± 0.01	0.15 ± 0.03
NGC7130	0.28 ± 0.02	0.13 ± 0.03	0.14 ± 0.02	0.14 ± 0.01	0.21 ± 0.03	0.10 ± 0.01	0.09 ± 0.05
IC5179	0.23 ± 0.03	0.20 ± 0.01	0.18 ± 0.01	0.19 ± 0.01	0.16 ± 0.02	0.11 ± 0.01	0.13 ± 0.03
NGC7591	0.22 ± 0.05	0.14 ± 0.05	0.13 ± 0.02	0.22 ± 0.01	0.23 ± 0.03	0.23 ± 0.01	0.17 ± 0.04
NGC7771	0.24 ± 0.02	0.28 ± 0.02	0.23 ± 0.01	0.24 ± 0.01	0.20 ± 0.03	0.23 ± 0.01	0.12 ± 0.04

Notes. Fluxes are expressed in units of $10^{-17}\,\mathrm{W\,m^{-2}}$. The fluxes of Arp 299 (NGC 3690/IC 694) are given in Alonso-Herrero et al. (2009b).
[(a)] Projected square size of the aperture in kpc. The aperture size is $5\farcs5\times5\farcs5$ for all the galaxies.

Table 4.7: Molecular Hydrogen Emission Line Fluxes

Name	Size[a] (kpc)	H_2 S(2) 12.27 μm	H_2 S(1) 17.03 μm	H_2 S(0) 28.22 μm
NGC2369	2.9	10. ± 1.	19. ± 2.	3.5 ± 0.5
NGC3110	4.6	4. ± 1.	10. ± 0.9	1.6 ± 0.2
NGC3256	2.7	34. ± 3.	61. ± 5.	9. ± 3.
NGC3690	2.9	11. ± 4.	22. ± 1.	3.8 ± 0.6
IC694	2.9	20. ± 3.	29. ± 1.	5.7 ± 0.9
ESO320-G030	2.9	8.1 ± 1.2	13. ± 1.	1.7 ± 0.7
NGC5135	3.9	9.3 ± 1.4	17. ± 1.	1.3 ± 0.5
IC4518E	4.4	0.3 ± 0.1	1.1 ± 0.2	1.0 ± 0.1
ZW049.057	3.7	3.3 ± 0.8	5.8 ± 0.4	< 0.6
IRAS17138-1017	4.9	6.3 ± 1.3	14. ± 1.	1.9 ± 0.5
IC4687	4.9	6.5 ± 1.1	12. ± 1.	1.8 ± 0.4
NGC6701	3.7	4.6 ± 0.8	10. ± 1.	1.9 ± 0.9
NGC7130	4.6	4.2 ± 1.7	9.9 ± 0.7	1.4 ± 0.3
IC5179	3.2	6.3 ± 0.8	11.2 ± 0.8	1.4 ± 0.2
NGC7591	4.6	3.0 ± 1.0	5.5 ± 0.6	1.0 ± 0.3
NGC7771	4.1	8.7 ± 1.2	16. ± 1.	3.5 ± 1.8

Notes. Fluxes are expressed in units of $10^{-17}\,\mathrm{W\,m^{-2}}$.
[a] Projected square size of the aperture in kpc. The aperture size is $13\farcs4\times13\farcs4$ for all the galaxies.

Table 4.8: Derived Warm Molecular Hydrogen Temperatures, Column Densities and Masses

Name	T(S(0)-S(1)) (K)	N_0 ($\times10^{20}$ cm^{-2})	M_0 ($\times10^8\,M_\odot$)	T(S(1)-S(2)) (K)	N_1 ($\times10^{20}$ cm^{-2})	M_1 ($\times10^8\,M_\odot$)
NGC2369	168	8.8	1.3	348	5.1	0.73
NGC3110	178	3.7	1.3	305	2.4	0.86
NGC3256	181	19.	2.1	369	12.	1.3
NGC3690	172	8.9	1.2	351	5.3	0.72
IC694	163	15.	2.0	415	7.8	1.1
ESO320-G030	189	3.4	0.43	390	2.2	0.28
NGC5135	236	1.9	0.44	361	1.5	0.36
IC4518E	108	9.2	2.7	252	3.0	0.87
ZW049.057	>205	<1.0	<0.22	373	0.74	0.16
IRAS17138-1017	185	4.1	1.5	324	2.7	1.0
IC4687	178	4.1	1.5	361	2.5	0.92
NGC6701	168	4.7	1.0	323	2.8	0.61
NGC7130	183	3.0	0.97	320	2.0	0.65
IC5179	194	2.6	0.40	369	1.7	0.27
NGC7591	167	2.5	0.85	362	1.4	0.48
NGC7771	157	10.0	2.6	363	5.2	1.3

Notes. N_0 and M_0 are the column density and mass derived from the H_2 lines S(0) and S(1). N_1 and M_1 correspond to the column density and mass derived from the S(1) and S(2) lines.

4.B Spectral Maps

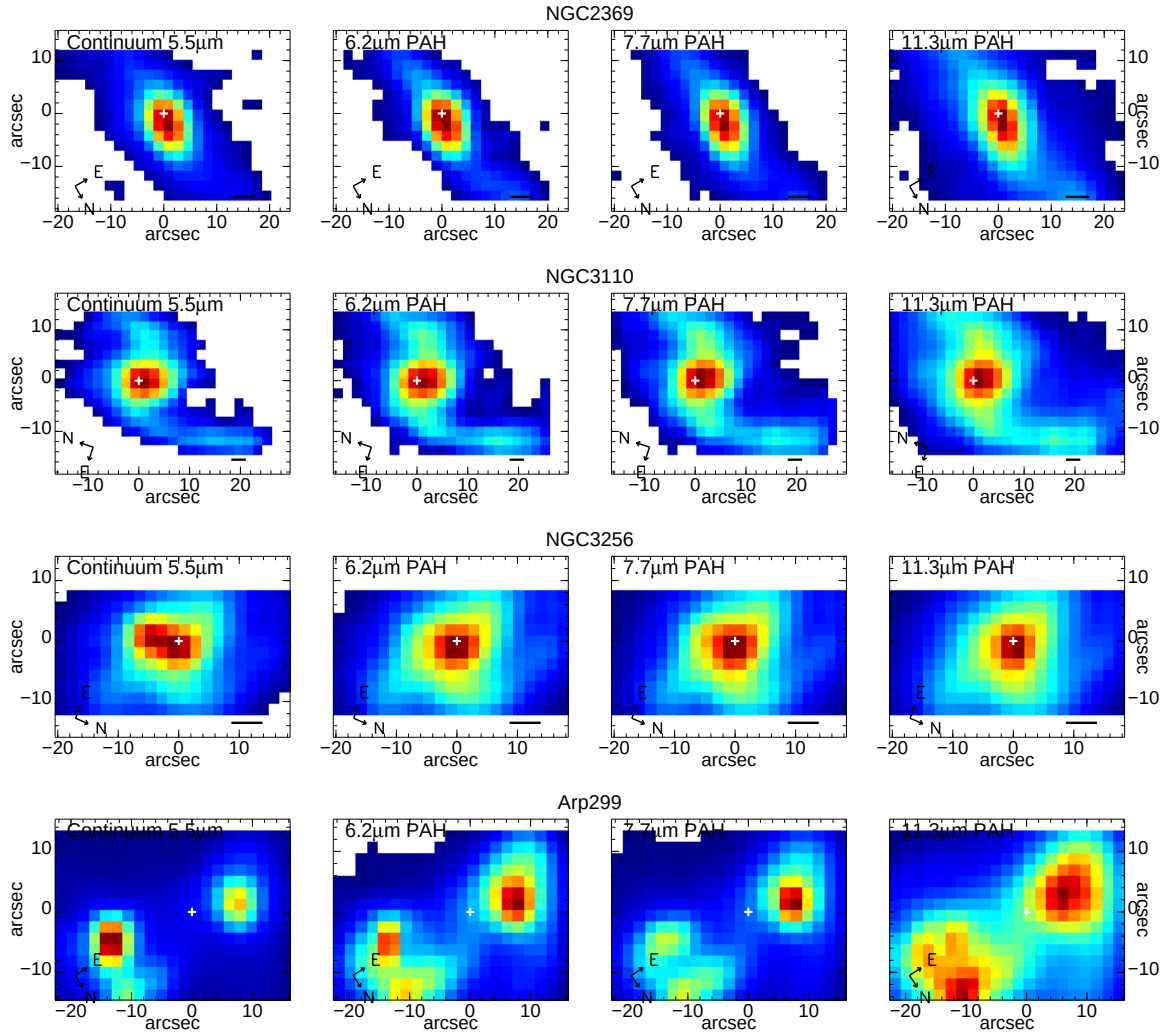

Figure 4.18: *Spitzer*/IRS SL spectral maps of the 5.5 μm continuum, the 6.2 μm PAH, the 7.7 μm PAH and the 11.3 μm PAH. The white cross marks the coordinates of the nucleus. The image orientation is indicated on the maps for each galaxy. The scale represents 1 kpc. The maps are shown in a square root scale.

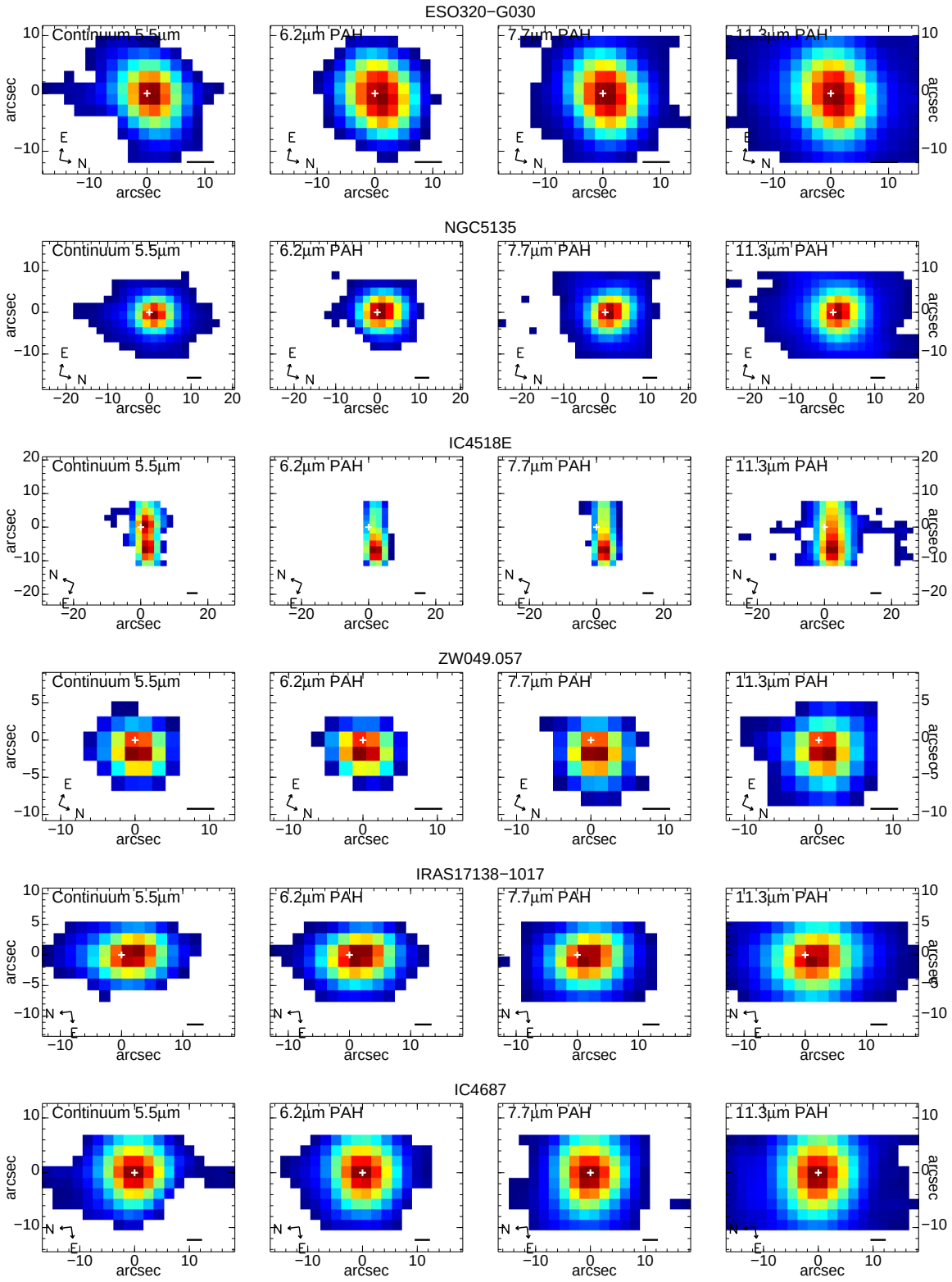

Figure 4.18: *Continued.*

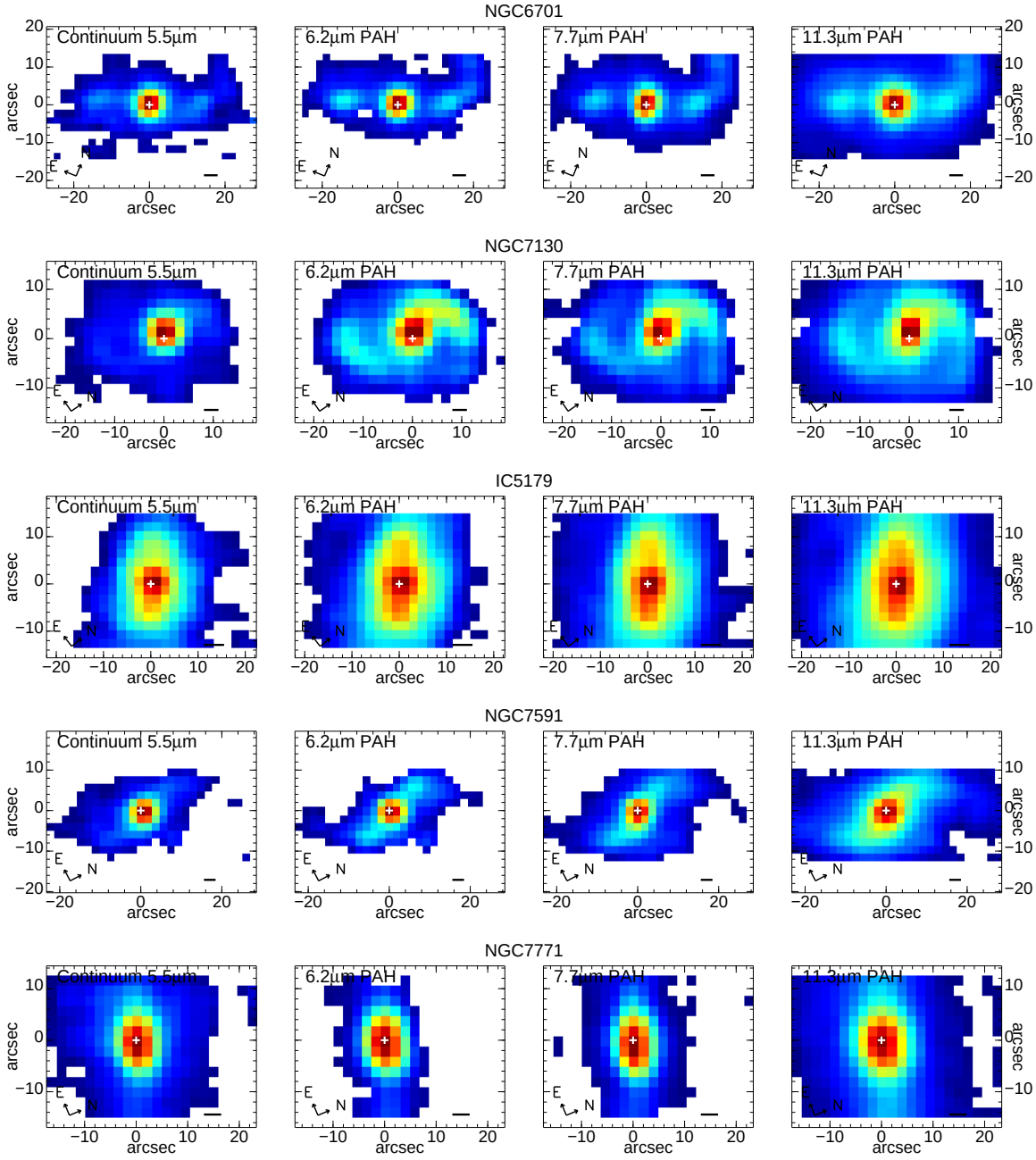

Figure 4.18: *Continued.*

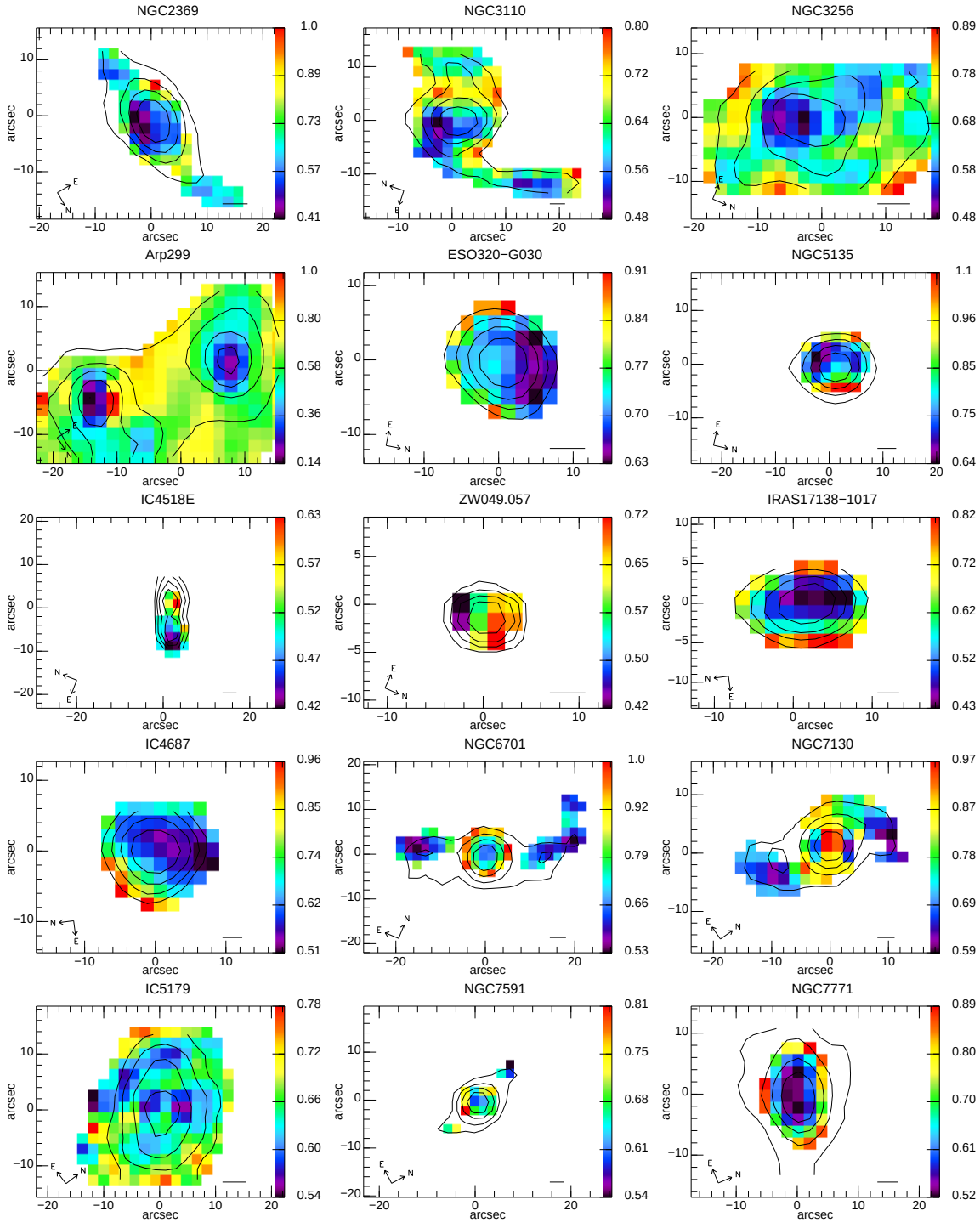

Figure 4.19: *Spitzer*/IRS SL spectral maps of the 11.3 μm PAH/6.2 μm PAH ratio. The 5.5 μm continuum contours, in a logarithm scale, are displayed to guide the eye. The image orientation is indicated on the maps for each galaxy. The scale represents 1 kpc. The ratio maps are shown in a linear scale.

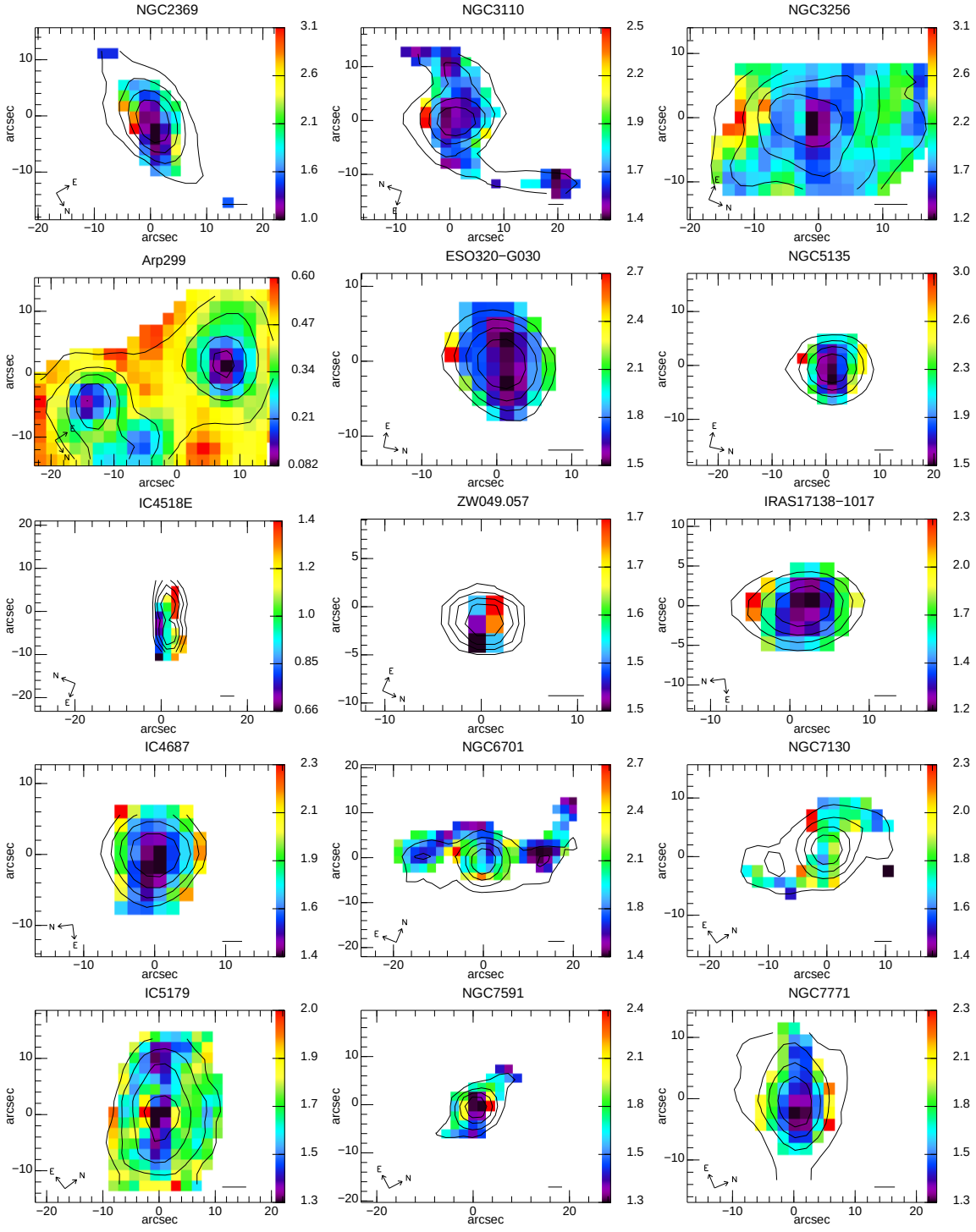

Figure 4.20: *Spitzer*/IRS SL spectral maps of the 11.3 μm PAH/7.7 μm PAH ratio. The 5.5 μm continuum contours, in a logarithm scale, are displayed to guide the eye. The image orientation is indicated on the maps for each galaxy. The scale represents 1 kpc. The ratio maps are shown in a linear scale.

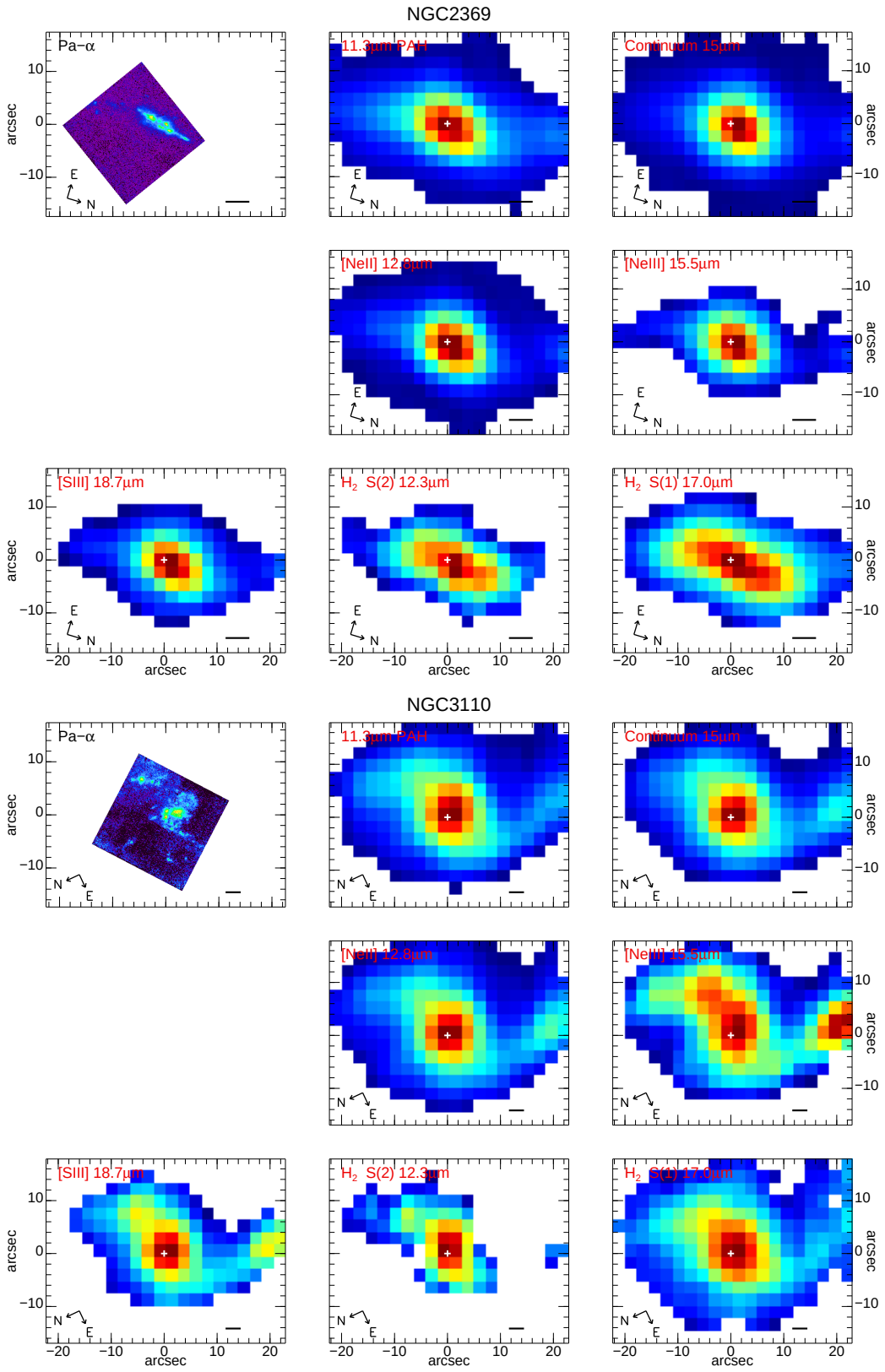

Figure 4.21: *Spitzer*/IRS SH spectral maps of the 11.3 μm PAH feature, the 15 μm continuum, the fine structure line emission of [S IV] 10.51 μm, [Ne II] 12.81 μm, [Ne III] 15.56 μm, [S III] 18.71 μm and the molecular hydrogen lines H_2 S(2) at 12.3 μm and H_2 S(1) at 17.0 μm. The white cross marks the coordinates of the nucleus. The image orientation is indicated on the maps for each galaxy. The scale represents 1 kpc. The maps are shown in a square root scale.

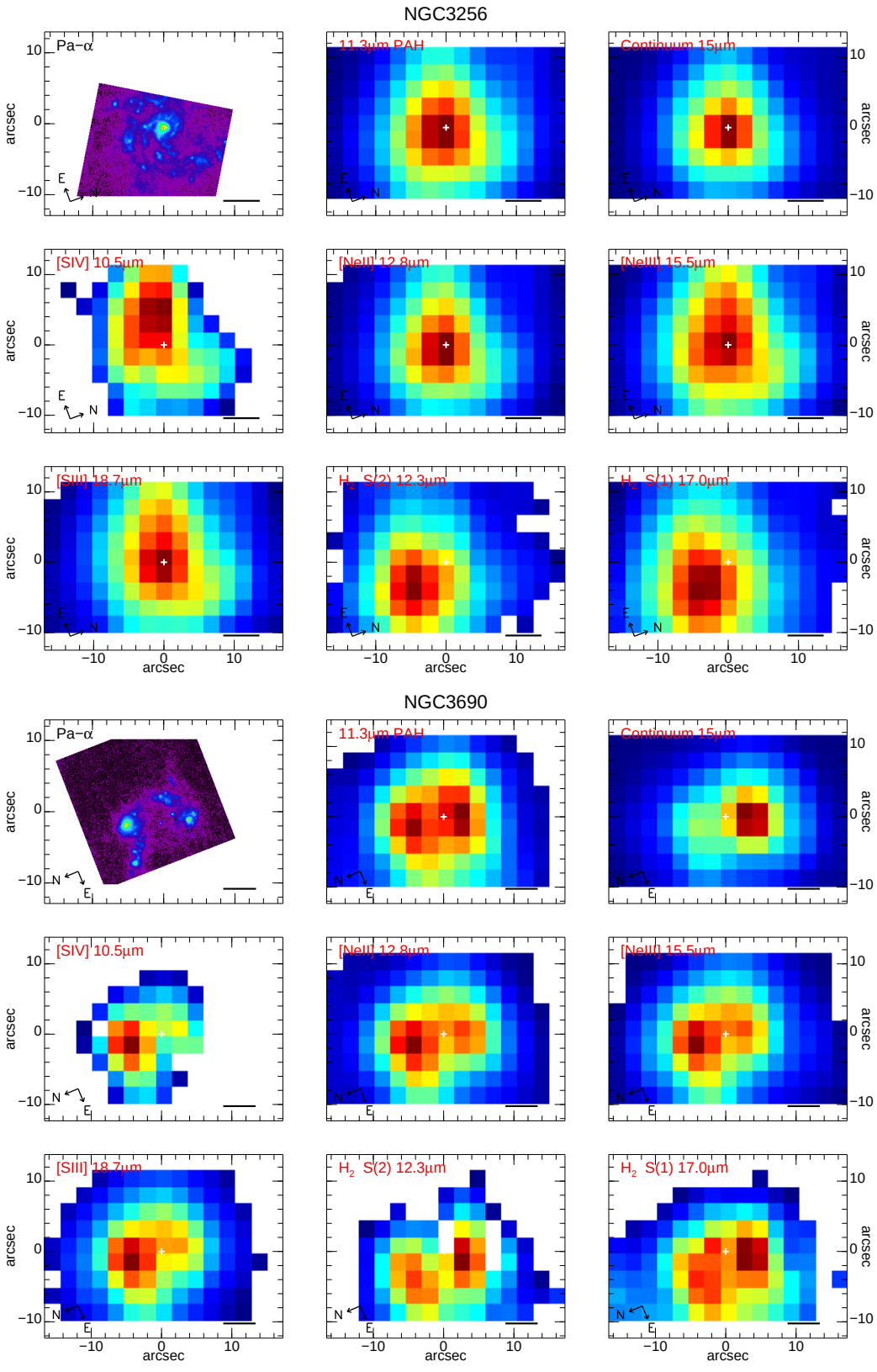

Figure 4.21: *Continued.*

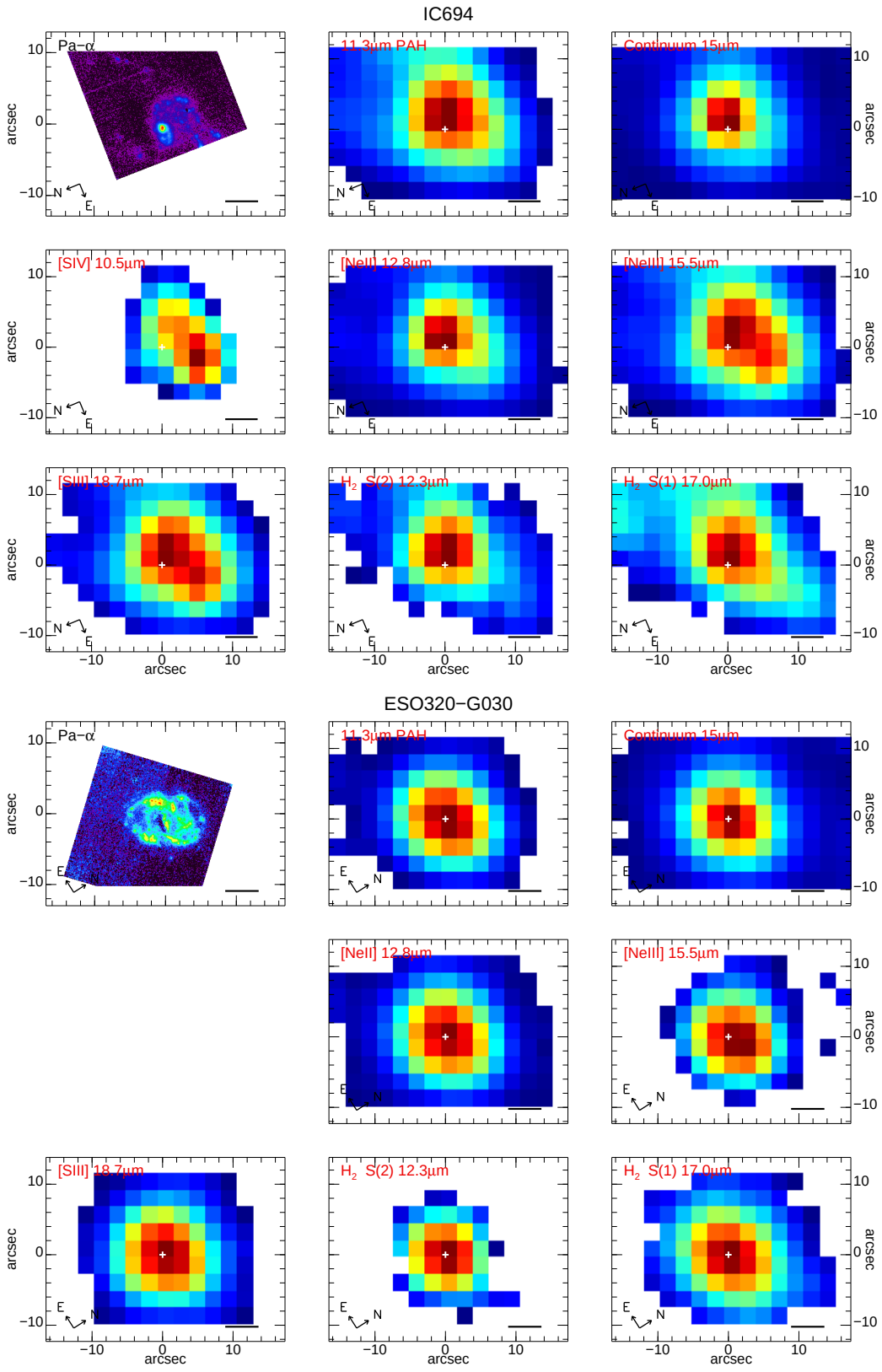

Figure 4.21: *Continued.*

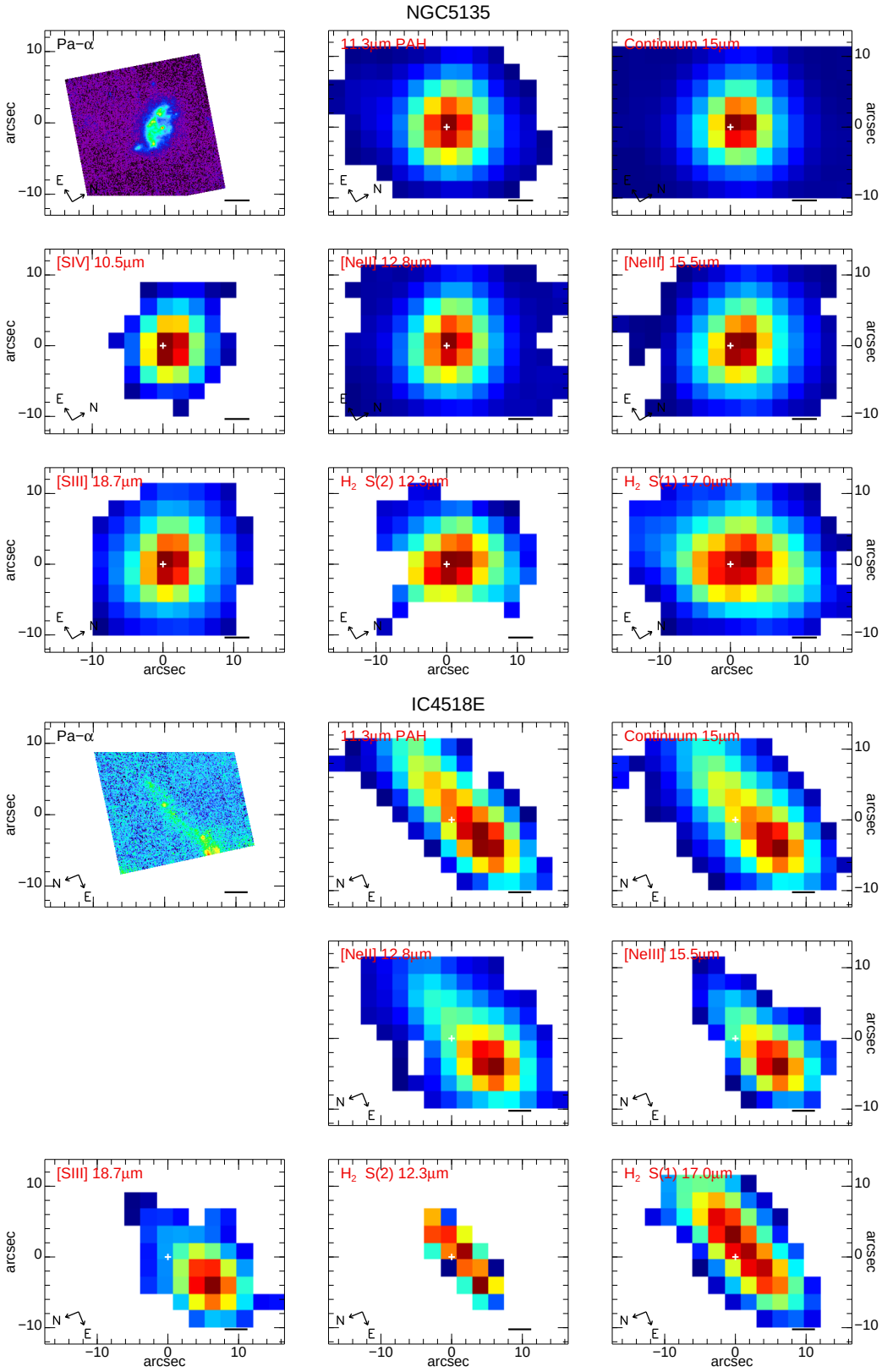
NGC5135
Pa−α
11.3μm PAH
Continuum 15μm
[SIV] 10.5μm
[NeII] 12.8μm
[NeIII] 15.5μm
[SIII] 18.7μm
H2 S(2) 12.3μm
H2 S(1) 17.0μm
IC4518E
Pa−α
11.3μm PAH
Continuum 15μm
[NeII] 12.8μm
[NeIII] 15.5μm
[SIII] 18.7μm
H2 S(2) 12.3μm
H2 S(1) 17.0μm
arcsec
E
N

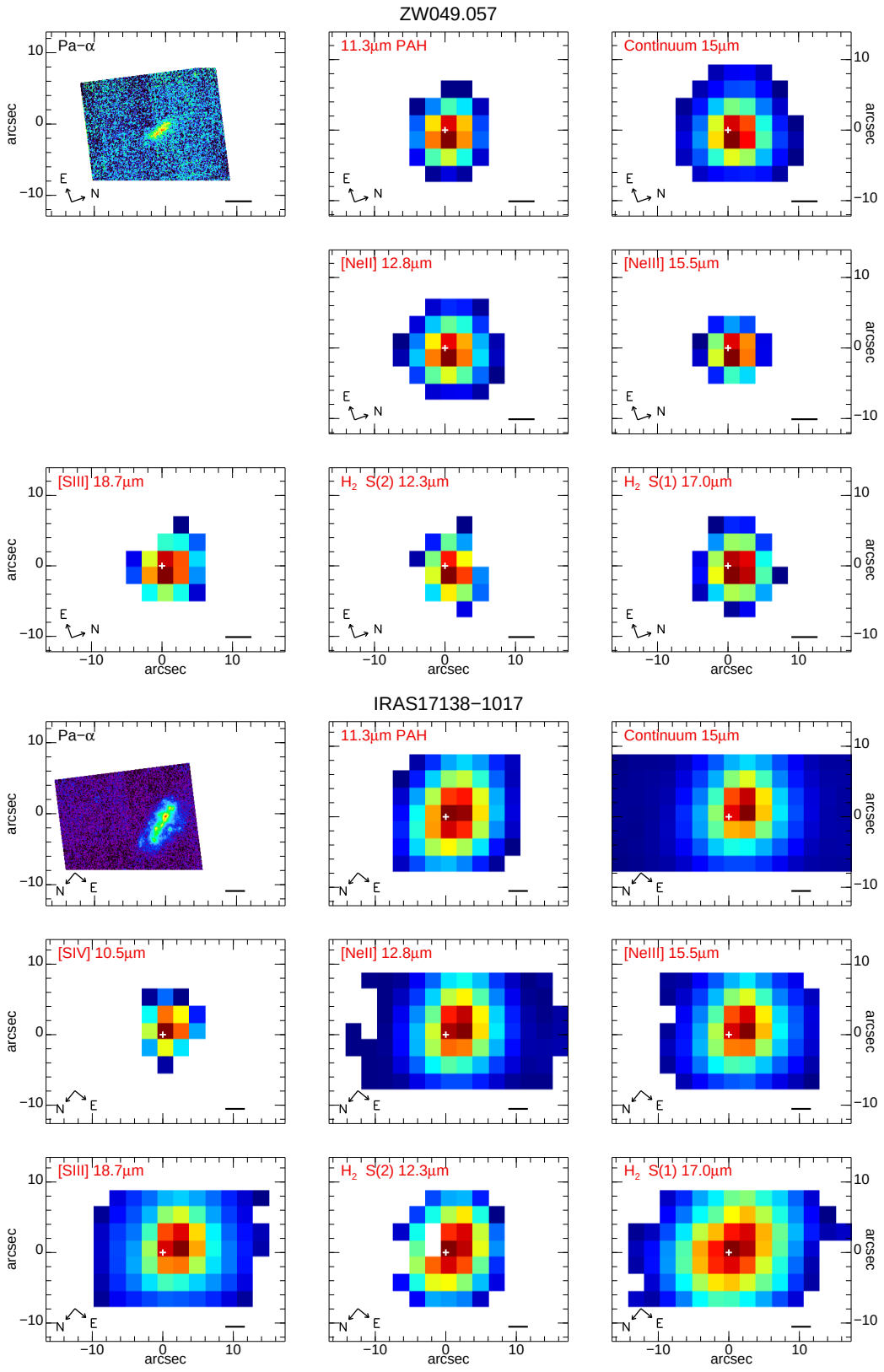

Figure 4.20: *Continued.*

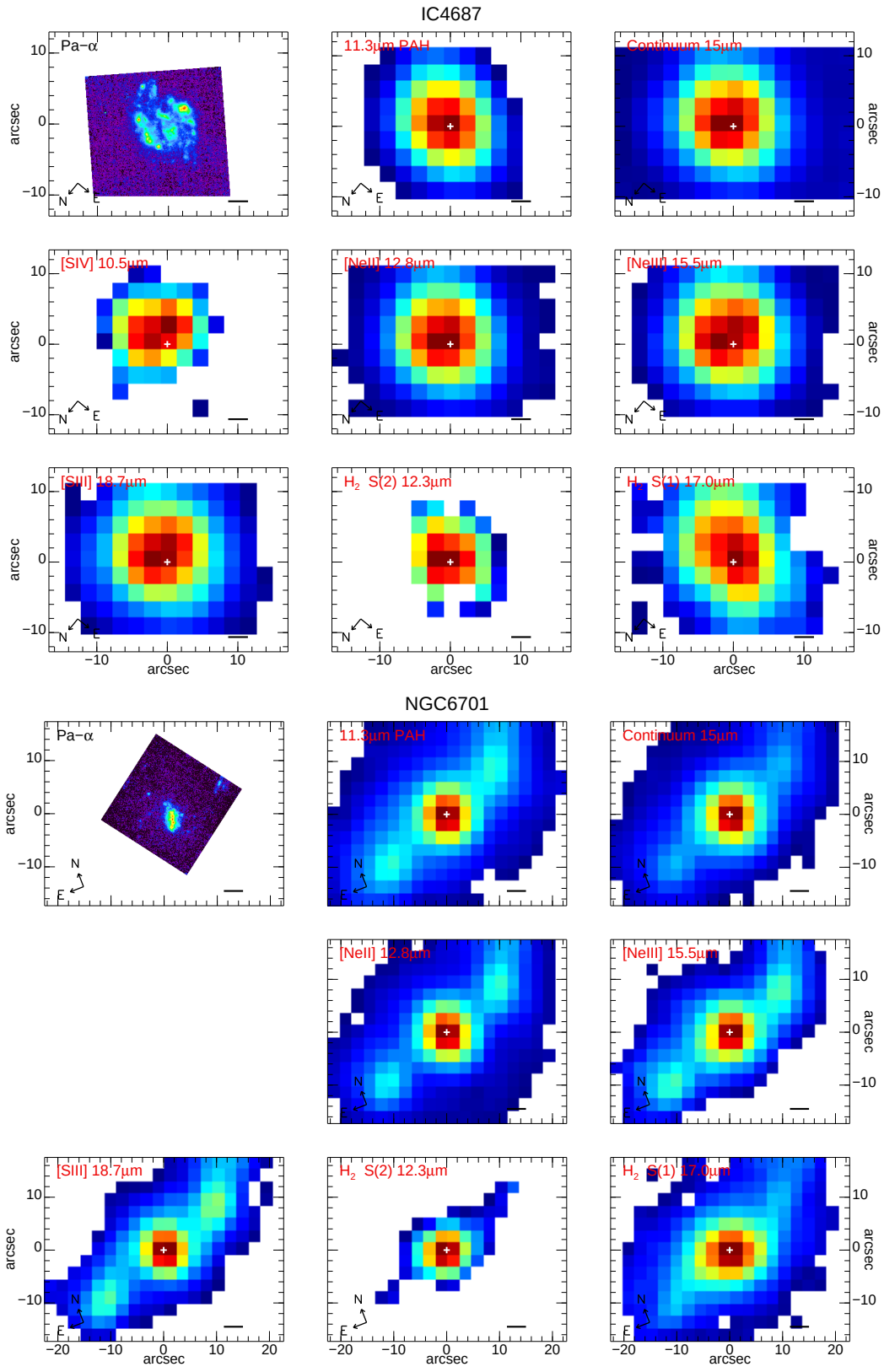

Figure 4.20: *Continued.*

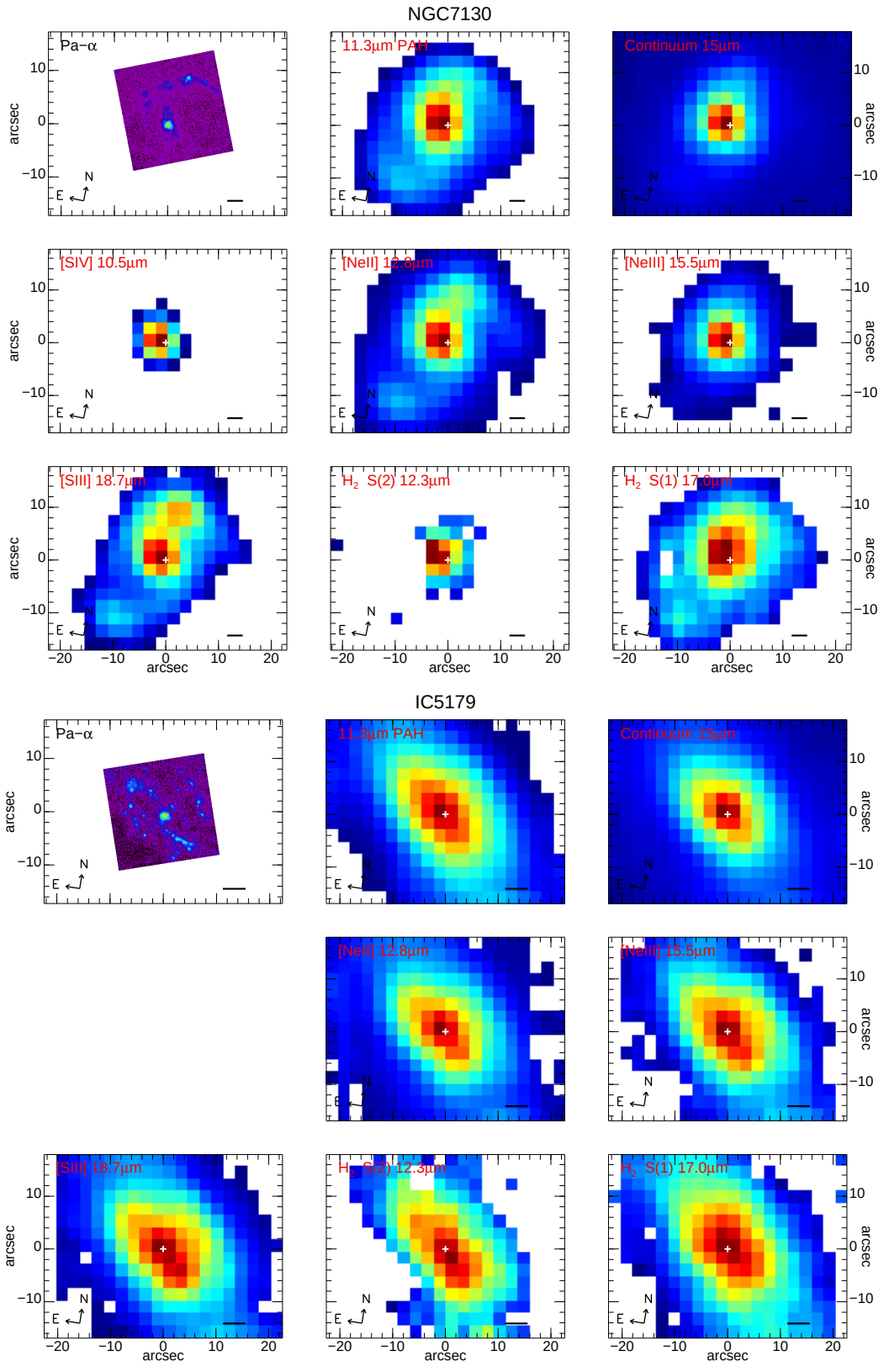

Figure 4.20: *Continued.*

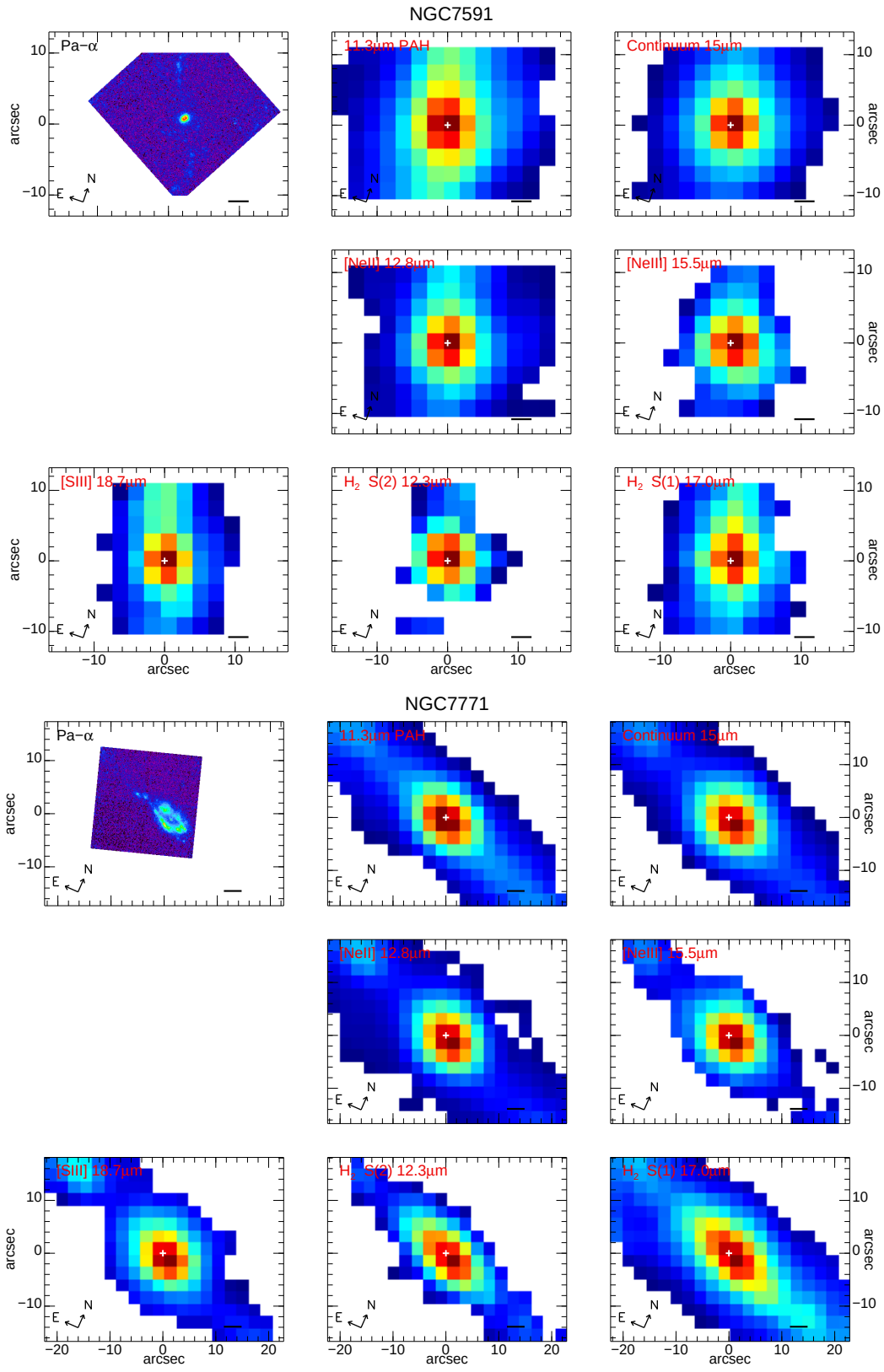

Figure 4.20: *Continued.*

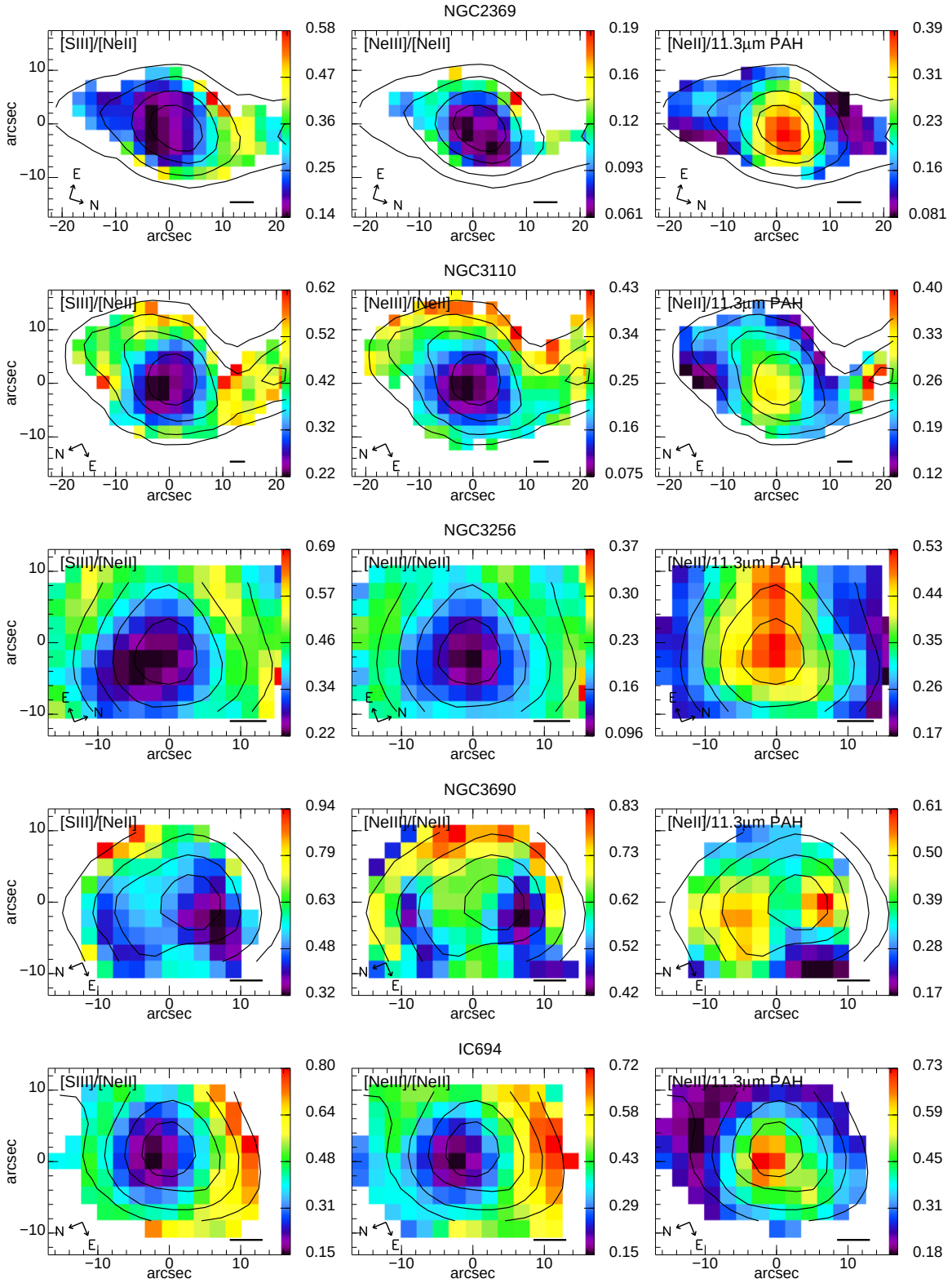

Figure 4.21: *Spitzer*/IRS SH spectral maps of the [S III] 18.71 μm/[Ne II] 12.81 μm ratio, the [Ne III] 15.56 μm/[Ne II] 12.81 μm ratio and the [Ne II] 12.81 μm/11.3 μm PAH. The 15.0 μm continuum contours are displayed to guide the eye. The image orientation is indicated on the maps for each galaxy. The scale represents 1 kpc. The ratio maps are shown in a linear scale.

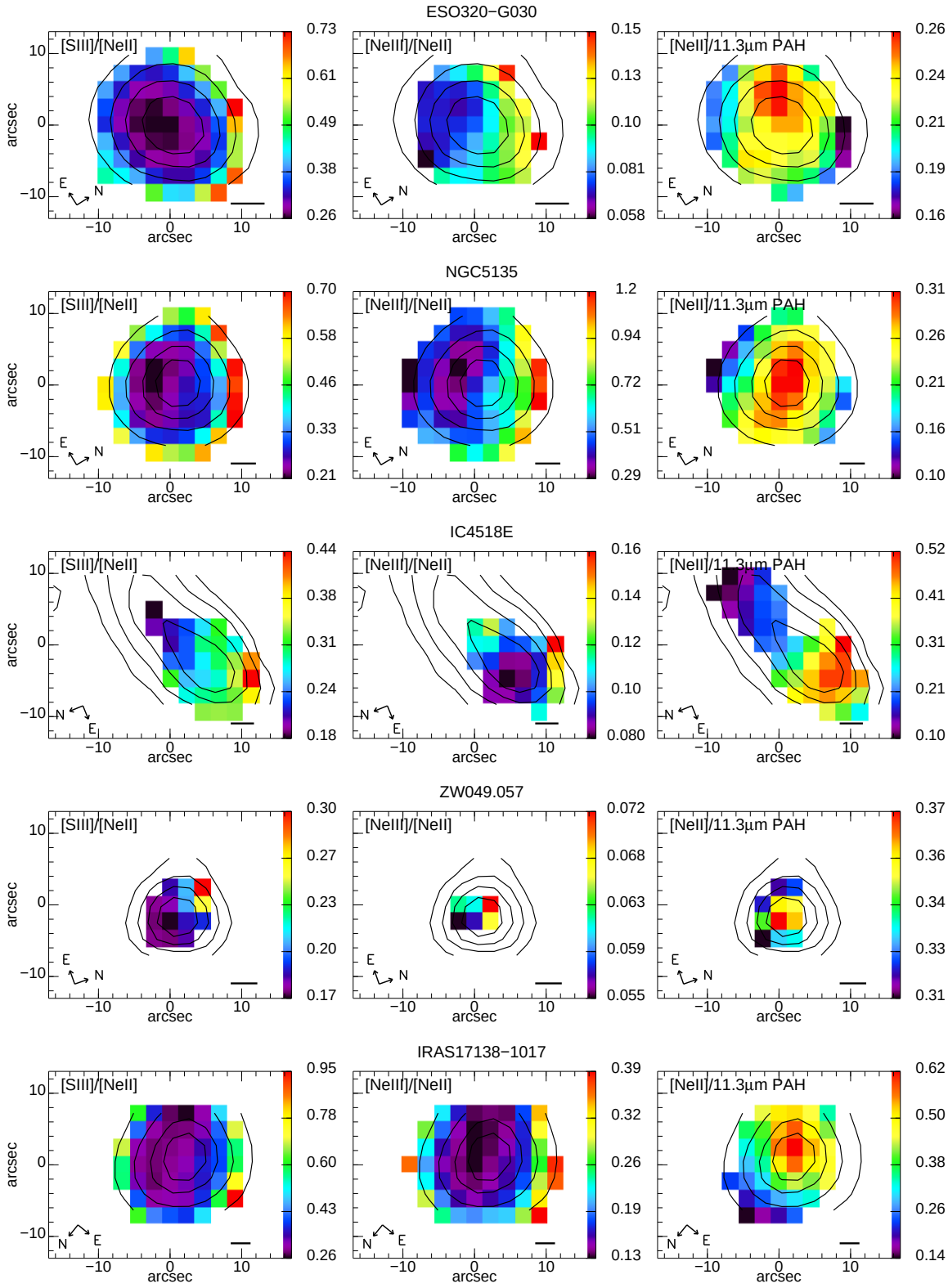

Figure 4.21: *Continued.*

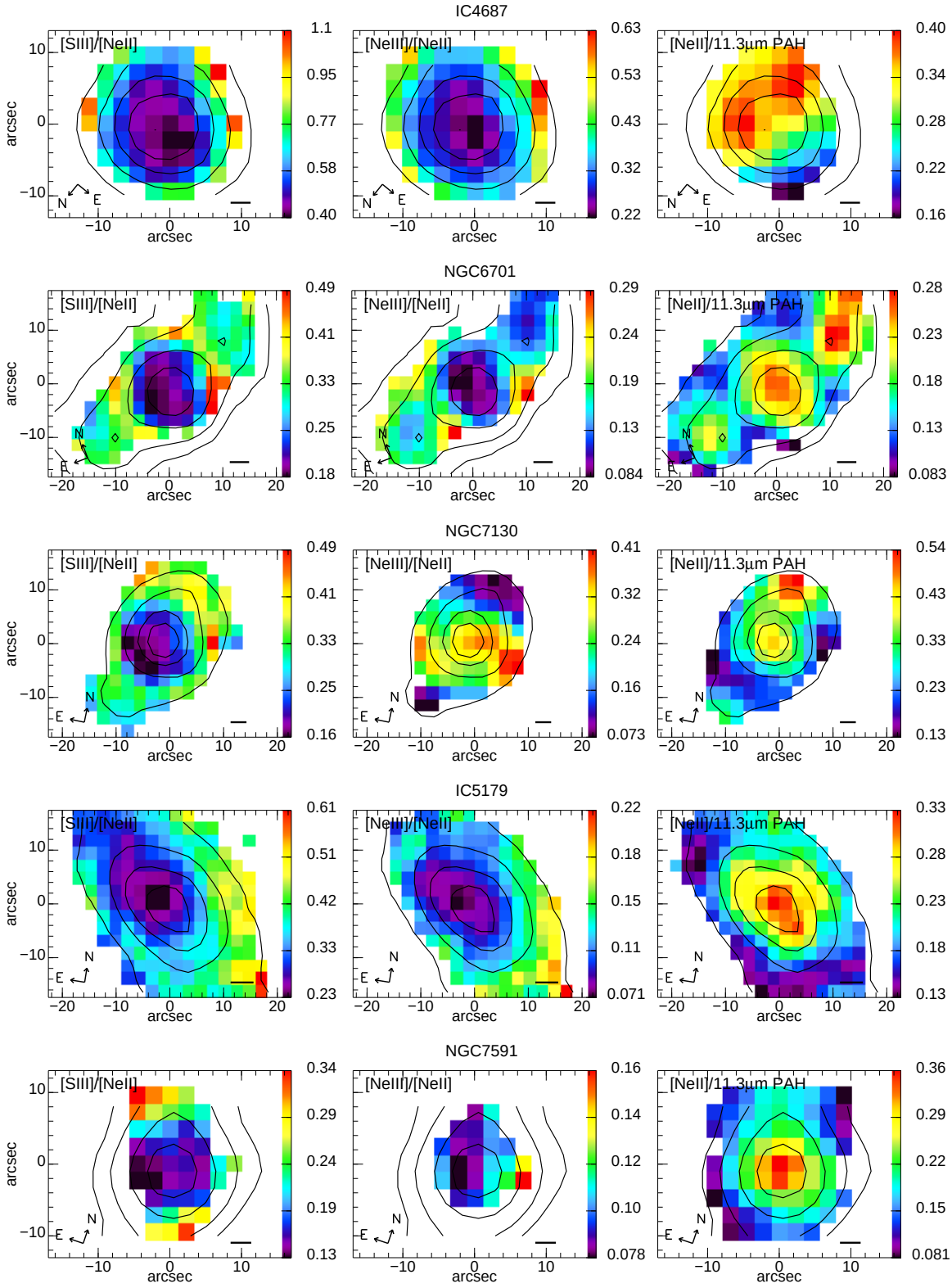

Figure 4.21: *Continued.*

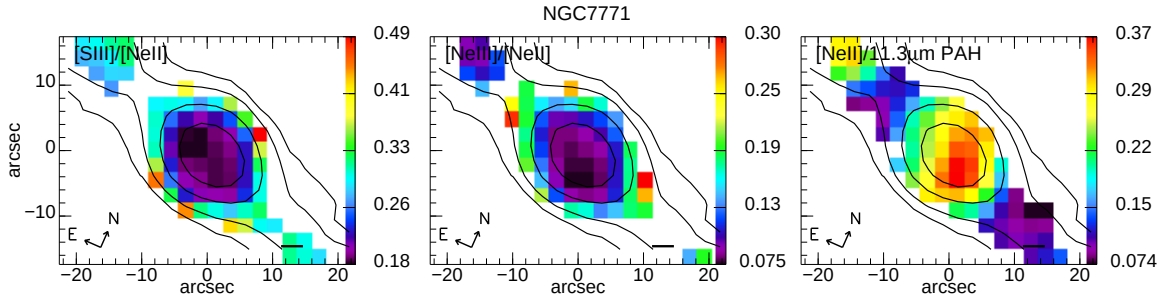

Figure 4.21: *Continued.*

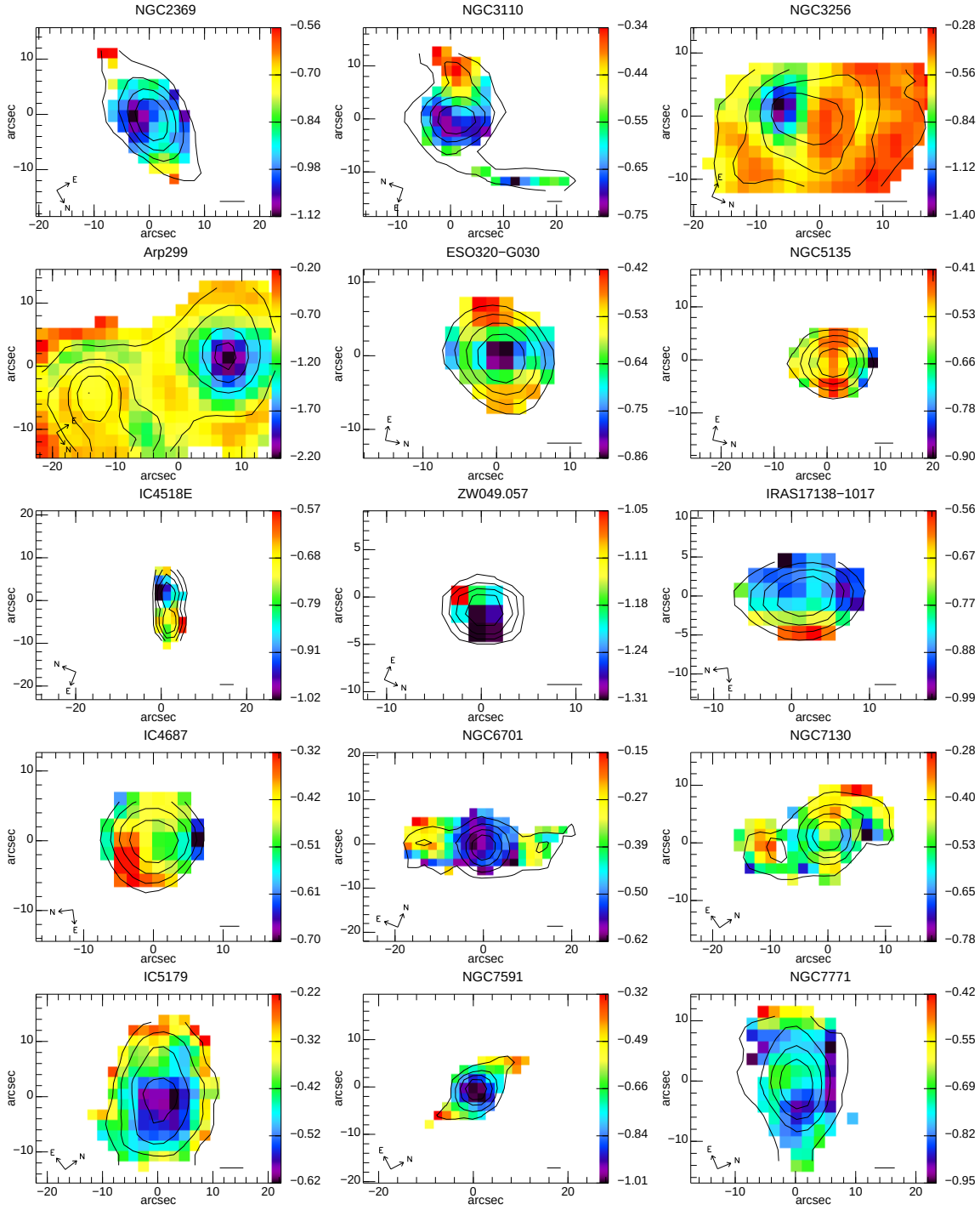

Figure 4.22: Maps of the 9.7 μm silicate feature strength as defined in Section 4.3.4. The 5.5 μm continuum contours are displayed to guide the eye. The image orientation is indicated on the maps for each galaxy. The scale represents 1 kpc. The maps are shown in a linear scale.

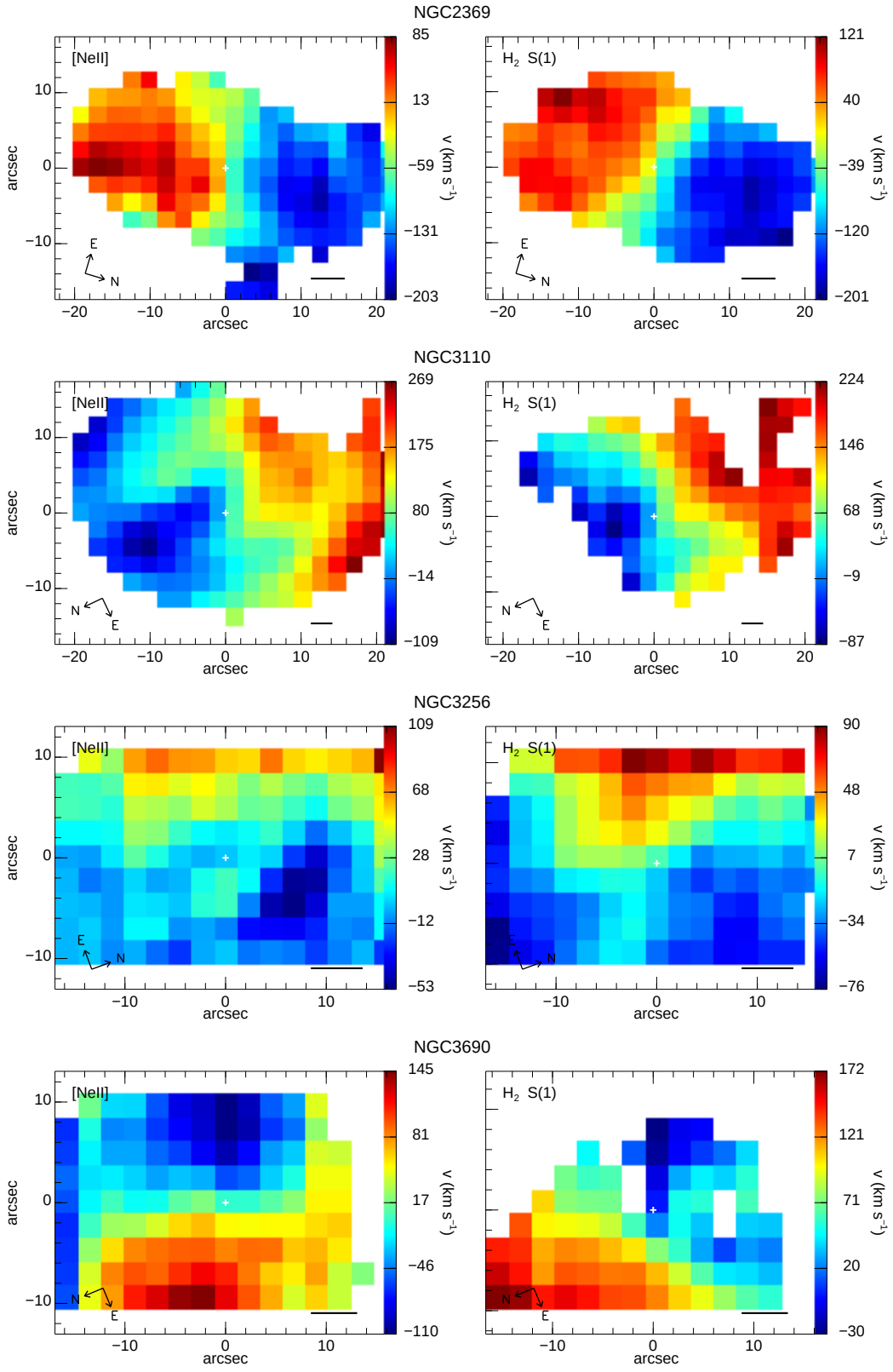

Figure 4.23: Maps of the observed velocity field of [Ne II] 12.81 μmand H_2 S(1) at 17.0 μm. The white cross marks the coordinates of the nucleus. The image orientation is indicated on the maps for each galaxy. The scale represents 1 kpc.

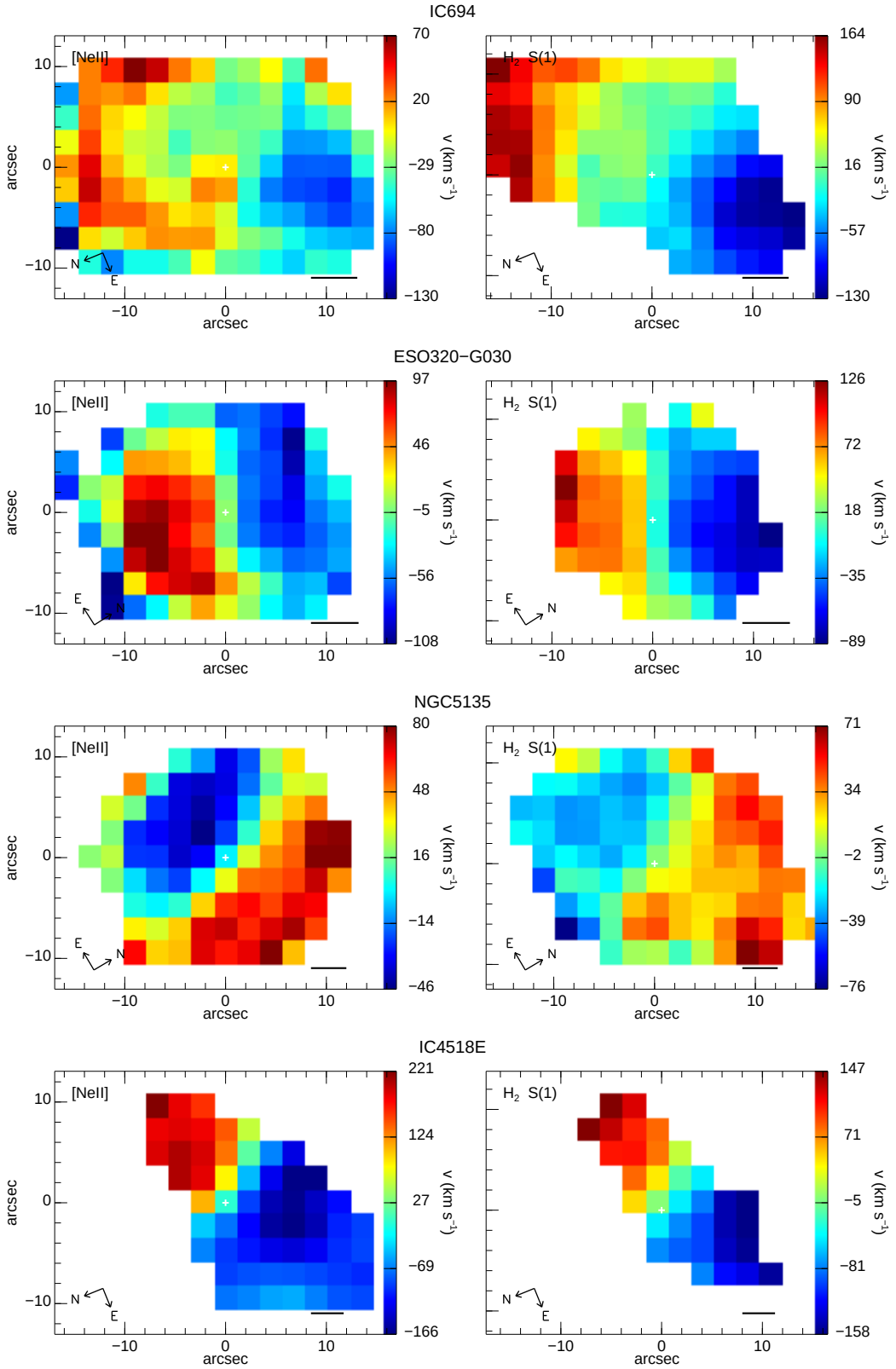

Figure 4.23: *Continued.*

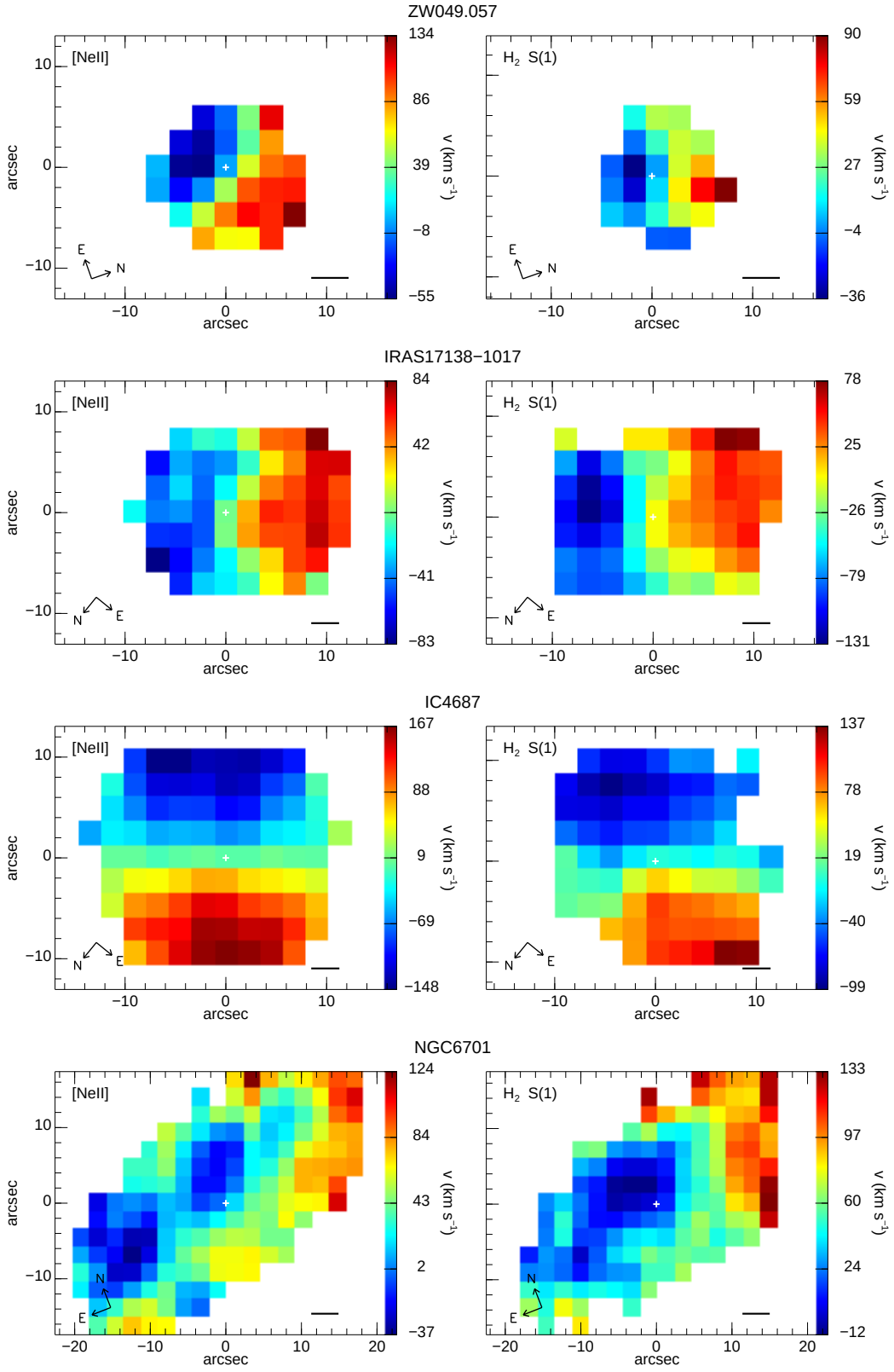

Figure 4.23: *Continued.*

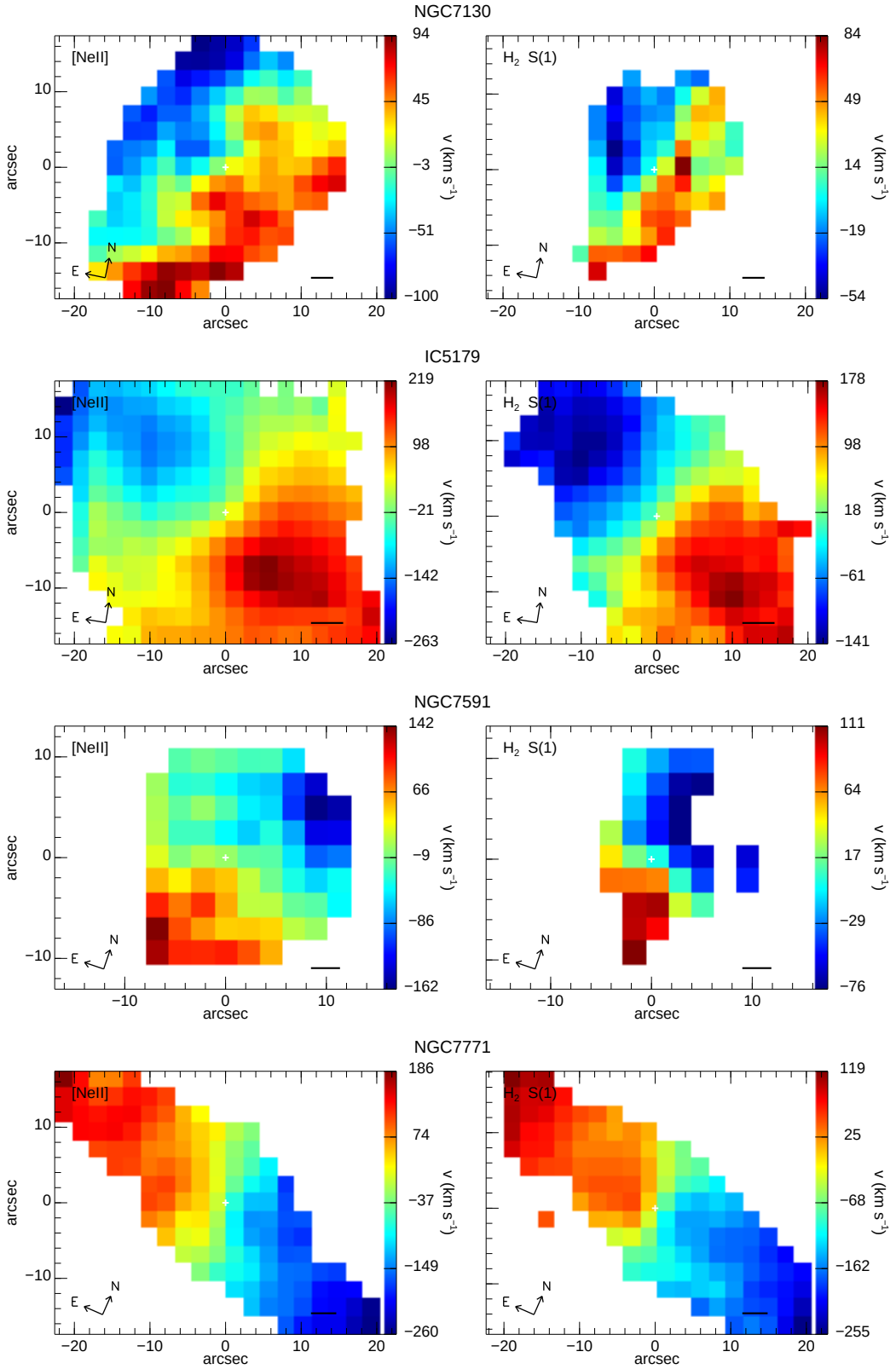

Figure 4.23: *Continued.*

4.C Description of Individual Objects

4.C.1 NGC 2369

The mid-IR emission of NGC 2369 is dominated by the resolved nucleus. The molecular hydrogen (H_2 S(1) and H_2 S(2)) emission appears more extended along the galaxy disk than the 11.3 μm PAH emission. This causes a relatively large H_2 S(1)/ 11.3 μm PAH ratio in the regions around the nucleus. The [Ne II] 12.81 μm/11.3 μm PAH ratio map reveals an H II region $\sim$17 arcsec ($\sim$3.4 kpc projected) away from the nucleus to the south. The nuclear silicate strength, $S_{\rm Si} \sim$–0.9, is slightly larger than the average silicate strength of our LIRGs sample, probably because this galaxy is seen almost edge-on.

4.C.2 NGC 3110

It is a face-on galaxy with numerous H II regions along the spiral arms(Hattori et al. 2004). The [Ne III] 15.56 μm emission of this galaxy is especially bright and it resembles that of the Hα emission. The [Ne III] 15.56 μm/[Ne II] 12.81 μm ratio of the extranuclear H II regions is $\sim$5 times larger than the nuclear ratio. The deepest silicate absorption is located at the nucleus.

4.C.3 NGC 3256

It is galaxy merger with two nuclei. The southern nucleus, located 5 arcsec away from the north nucleus, is highly obscured, although it is visible in the 5.5 μm continuum map. It has one of the deepest silicate absorption feature in our sample, $S_{\rm Si} \sim -1.4$. The silicate feature of the rest of the galaxy is similar to that found in the rest of the galaxies of our sample. The PAH, continuum and atomic emission (except [S IV] 10.51 μm) peak at the north nucleus. The maximum of the [S IV] 10.51 μm emission is located $\sim$5 arcsec to the east of the north nucleus, and it is probably related to a star-forming region. This is the only extranuclear region ($d >\sim 1$ kpc), apart from region C in Arp 299 (Alonso-Herrero et al. 2009b), where we detect the [S IV] 10.51 μm line. The H_2 emission arises mainly from the southern nucleus and the surrounding regions.

4.C.4 ESO 320-G030

Due to the low spatial resolution of the IRS maps, we cannot distinguish any morphological detail in the emission maps this galaxy, although it is clearly spatially

resolved. The maximum of the silicate feature absorption is located at the nucleus.

4.C.5 NGC 5135

This galaxy hosts a Sy2 nucleus surrounded by intense star formation (Bedregal et al. 2009 and references therein), that we cannot separate due the limited spatial resolution of the IRS spectral maps. However the line ratios (e.g [Ne III] 15.56 μm/[Ne II] 12.81 μm ratio) show some asymmetries that may be associated with the truncated ring-like structure of this galaxy. At our scale ($\sim$0.5 kpc), we do not see any noticeable variations in the PAH emission due to the AGN activity. The silicate absorption feature is relatively shallow, –0.47, and the maximum value is not located at the nucleus.

4.C.6 IC 4518E

This galaxy is part of an interacting pair (IC 4518E/IC 4518W). Most of the mid infrared emission (PAH, fine structure line and 15 μm continuum) emission is dominated by an H II region located $\sim$7 arcsec to the south-east from the nucleus. The nuclear bright is similar to that of the southwestern H II region emission only for the molecular hydrogen [H_2 S(1)] and the 5.5 μm continuum. The deepest silicate absorption is found at the nucleus.

4.C.7 Zw 049.057

Due to the low signal-to-noise ratio of the observations of Zw 049.057, the maps of this galaxy contain very few pixels. The nuclear silicate absorption is, $S_{\rm Si}$=–1.2, which is large when compared to that of the other LIRGs.

4.C.8 IRAS 17138−1017

The limited spatial resolution of the emission maps does not allow us to identify any morphological details in this galaxy. The maximum of the silicate absorption may not be located at the nucleus. Note however that the near-infrared (Alonso-Herrero et al. 2006) and the mid-infrared (Díaz-Santos et al. 2008) morphologies do not allow us to determine the position of the nucleus.

4.C.9 IC 4687

IC 4687 is part of an interacting system (IC 4686/IC 4687). Only IC 4687 was observed in the spectral mapping mode. In the emission line map it is not possible to

isolate any region of interest, however the emission is spatially resolved. We detect the [S IV] 10.51 μm line, that seems to be associated to the nuclear H II regions seen in the Paα image. Two of these regions have slightly larger [Ne II] 12.81 μm/11.3 μm PAH ratio than the rest of the galaxy. The nuclear [Ne III] 15.56 μm/[Ne II] 12.81 μm ratio of this galaxy is somewhat larger than those of the other H II galaxies in our sample. The maximum of the silicate feature is not located at the nucleus.

4.C.10 NGC 6701

This LIRG is classified as composite from optical spectroscopy (Alonso-Herrero et al. 2009a). We can identify two extranuclear H II regions symmetrically located ∼10 arcsec away from the nucleus, one at each spiral arm. As is the case with the other extranuclear H II regions, the molecular hydrogen of these two regions is relatively low when compared with the H_2 nuclear emission. The silicate absorption is deeper in the nucleus than in the rest of the galaxy.

4.C.11 NGC 7130

This is a face-on galaxy whose nuclear activity is classified as Sy2. We detect 2 extranuclear H II regions located in the spiral arms. The brightest is located to the north, ∼10 arcsec from the nucleus. The other one is ∼14 arcsec to the south-east from the nucleus. The continuum and [Ne III] 15.56 μm emissions are concentrated at the nucleus. The PAH features and fine structure lines are bright in the spiral arms too. The minimum of the [Ne III] 15.56 μm/[Ne II] 12.81 μm ratio is not located at the nucleus, as for the majority of the LIRGs in our sample. We detect nuclear [S IV] 10.51 μm emission. Also, this is one of the few galaxies in the sample whose 11.3 μm PAH/6.2 μm PAH ratio minimum is not located at the nucleus. These facts may be related to the active nature of the nucleus of this galaxy.

4.C.12 IC 5179

This is a face-on spiral galaxy classified as H II-like from optical spectroscopy, and it shows numerous H II regions distributed in the spiral arms (Alonso-Herrero et al. 2006). These H II regions are not resolved in the *Spitzer* maps. They appear as a relatively uniform extended emission (PAH features and atomic lines) over ∼8 kpc. The continuum emission is slightly more concentrated toward the nucleus. The patterns in the ratio maps are possibly related to the intricate distribution of the H II regions. The nucleus is the most obscured region of this galaxy.

4.C.13 NGC 7591

The nuclear activity of NGC 7591 is classified as composite (Alonso-Herrero et al. 2009a). Only in the low spectral resolution maps we can clearly distinguish the spiral arms of this face-on galaxy. The continuum emission is concentrated at the nucleus, while we can see bright PAH and fine structure lines emission in the galaxy arms. The nucleus is the region with the deepest silicate absorption feature.

4.C.14 NGC 7771

The nucleus of this LIRG is classified as H II-like from optical spectroscopy. It has a nuclear ring of star formation clearly seen in the Paα images (Figure 4.21, see also Alonso-Herrero et al. 2006 and Alonso-Herrero et al. 2009a), but it is not resolved by the IRS observations. This galaxy is seen almost edge-on and we can clearly observe the spiral arms in the line emission maps. We detect an H II region in the eastern arm, $\sim$20 arcsec (6 kpc) away from the nucleus. The continuum is dominated by the nucleus. The H_2 emission extends $\sim$5 kpc in the west galaxy arm with apparently no bright fine structure/PAH emission associated with it. The silicate feature spatial distribution is somewhat irregular and we do not see any morphological detail.

Chapter 5

The X-ray Emission of Local Luminous Infrared Galaxies

We study the X-ray emission of a representative sample of 27 local LIRGs. The median IR luminosity of our sample is $\log(L_{\rm IR}/L_{\odot}) = 11.2$*, therefore the low-luminosity end of the LIRG class is well represented, as well as the spectral class. We used new XMM-Newton data as well as Chandra and XMM-Newton archive data. The soft X-ray (0.5-2 keV) emission of most of the galaxies (>80 %), including LIRGs hosting a Seyfert 2 nucleus, is dominated by star-formation-related processes. These LIRGs follow the SFR versus soft X-ray luminosity correlation observed in local starbursts. We find that ∼15 % of the non-Seyfert LIRGs have an excessively hard X-ray emission relative to that expected from star-formation, which might indicate the presence of an obscured AGN. The rest of the non-Seyfert LIRGs follow the SFR versus hard X-ray (2-10 keV) luminosity correlation of local starbursts. The non-detection of the 6.4 keV Fe K*α *emission line in the non-Seyfert LIRGs allows us to put an upper limit on the bolometric luminosity of an obscured AGN,* $L_{\rm bol} < 10^{43}\,erg\,s^{-1}$*. That is, if these galaxies were hosting a low-luminosity AGN, its contribution to the total luminosity would be less than 10 %. Finally we estimate that the AGN contribution to the total luminosity for our sample of local LIRGs is between 7 % and 10 %.*

5.1 Introduction

The star-formation in local LIRGs is distributed over few kpc scales (Alonso-Herrero et al. 2006; Hattori et al. 2004; Rodríguez-Zaurín et al. 2011). This is similar to local starbursts and $z \sim 2$ infrared bright galaxies (Daddi et al. 2007; Rigby et al. 2008; Farrah et al. 2008; Rujopakarn et al. 2010), but at odds with local ULIRGs where most of the activity is taking place in very compact regions (the central kpc). Similarly,

the fraction of AGN-dominated local ULIRGs increases with increasing IR luminosity. About 40 % of the ULIRGs are classified as Seyfert (Veilleux et al. 1995; Kim et al. 1998). This motivates the study of local LIRGs because they might be scaled-down versions of more distant IR-bright galaxies.

The X-ray emission of starburst galaxies is mainly produced by HMXB, SNR, O stars and hot gas heated by the energy that originated in supernova explosions (Persic & Rephaeli 2002; Fabbiano 2006). The hard X-ray (2–10 keV) emission is dominated by HMXBs, although the contribution of hot gas ($kT > 3$ keV) heated by supernovae may dominate the hard X-ray emission for the most intense starbursts (Strickland & Heckman 2009; Iwasawa et al. 2011; Colina et al. 2012, submitted). On the other hand, the soft part of the X-ray emission (0.5–2 keV) emission is mostly produced by gas at $kT \sim 0.3$–0.7 keV.

It has been shown that there is a good correlation between the hard X-ray luminosity and the SFR for local starbursts (e.g., Ranalli et al. 2003; Grimm et al. 2003; Persic et al. 2004). However, the contribution to the hard X-ray luminosity from low-mass X-ray binaries (LMXB), which is not related to the current SFR, is not always negligible. For instance Colbert et al. (2004) and Lehmer et al. (2010) estimated that the LMXB contribution is significant for galaxies with low SFR/$M_\star$. It should be noted that the X-ray emission of a star-formation burst is delayed with respect to other SFR tracers. Consequently, an evolution with time is expected in the X-ray emission of the star-forming galaxies (Mas-Hesse et al. 2008; Rosa González et al. 2009). This evolution might explain part of the scatter in the X-ray luminosity vs. SFR correlations.

According to their IR luminosity, the SFR of LIRGs ranges from ∼20 to 200 $M_\odot\,\mathrm{yr}^{-1}$ (Kennicutt 1998). Therefore strong X-ray emission ($\sim 10^{41}\,\mathrm{erg\,s}^{-1}$) associated to star-formation is expected from these galaxies. The AGN contribution to the X-ray emission of LIRGs is expected to be low. Pure Seyfert AGN emission is detected in ∼15 % of the LIRGs using optical spectroscopy (Kim et al. 1998), however a dust-embedded AGN could be present in some of the them. Thanks to X-ray observations of LIRGs we are able to determine whether an obscured AGN is present, or, in the case of non-detection, set an upper limit to the AGN contribution.

Previous studies of the X-ray emission produced by star-formation have been focused on nearby starbursts (e.g., Ptak et al. 1999; Jiménez-Bailón et al. 2003; Ranalli et al. 2003; Grimm et al. 2003; Persic et al. 2004; Colbert et al. 2004) or ULIRGs (e.g., Rieke 1988; Perez-Olea & Colina 1996; Ptak et al. 2003; Franceschini et al. 2003; Teng et al. 2005; Teng & Veilleux 2010).

Although there is a number of papers on individual LIRGs (e.g., Lira et al. 2002; Blustin et al. 2003; Jenkins et al. 2004, 2005; Levenson et al. 2004, 2005; Miniutti et al.

2007), there are few studies of the X-ray properties of LIRGs as a class (e.g., Risaliti et al. 2000; Lehmer et al. 2010; Iwasawa et al. 2011). Risaliti et al. (2000) studied a sample of 78 objects, biased toward Seyfert LIRGs (90 %). They concluded that many of the sources might be completely Compton-thick ($N_{\rm H} > 10^{25}$). Using an unbiased subsample of LIRGs, they found that ∼60 % of the LIRGs host AGN although they are weak or heavily obscured. More recently, Iwasawa et al. (2011) carried out a study of the most luminous local IR galaxies ($11.7 < \log(L_{\rm IR}/L_{\odot}) < 12.5$). About 50 % of them are likely to contain an AGN, increasing the fraction of AGN sources with increasing $L_{\rm IR}$. The authors found that their non-AGN galaxies have lower hard X-ray luminosities than expected from the local starbursts hard X-ray vs. SFR correlation. They suggested that the hard X-ray emission of these (U)LIRGs is dominated by hot gas and not by HMXBs as in local starbursts.

In this chapter we discuss the properties of the X-ray emission produced by star-formation and AGN related processes in a sample of 27 local LIRGs observed with *XMM-Newton* and *Chandra*.

5.2 The Sample of LIRGs

5.2.1 Definition of the Sample

Our sample of LIRGs contains 27 galaxies with *XMM-Newton* or *Chandra* data drawn from the volume-limited sample of local LIRGs of (Alonso-Herrero et al. 2006; see Chapter 2).

In Figure 5.1 we compare the $L_{\rm IR}$ distribution of our sample with that of the parent sample. The Kolmogorov-Smirnov two-sample test shows that it is not possible to reject ($p > 0.49$) that both samples come from the same distribution. According to their nuclear activity classification, 47±10 % and 46±13 % are H II-type in the parent sample and in our sample respectively. On the other hand, Seyfert galaxies represent 22±7 % of the parent sample and 27±10 % of our sample. That is, our X-ray sample is not biased toward active galaxies. Therefore these 27 galaxies constitute a representative sample of the local LIRGs in terms of both IR luminosity and nuclear activity. The median $\log(L_{\rm IR}/L_{\odot})$ of the sample is 11.2, similar to that of the entire sample (see Chapter 2).The selected galaxies are listed in Table 5.1.

5.2.2 Star-formation Rate and Stellar Mass

The IR luminosity in bright-IR galaxies is produced by dust heated by massive young stars. The dust absorbs a large part (>90 % for LIRGs, Buat et al. 2007) of

Table 5.1: Sample of local LIRGs

Galaxy Name	$D_{\rm L}$ (Mpc)	Nuclear Spect. class[a]	log $L_{\rm IR}$[b] ($L_\odot$)	X-ray data
NGC23	64.7	composite	11.1	Lehmer et al. (2010)
NGC1614	69.1	composite	11.7	*XMM-Newton* (archive)
NGC2369	46.0	composite	11.1	*XMM-Newton* (our data)
NGC3110	72.6	H II	11.3	”
NGC3256	40.1	H II	11.7	*XMM-Newton* (archive)
NGC3690*	44.0	Sy2	11.4	”
IC694*	44.6	LINER	11.6	”
ESO320-G030	43.7	H II	11.2	*XMM-Newton* (our data)
IC860	55.7	···	11.1	Lehmer et al. (2010)
MCG−03-34-064	72.5	Sy2	11.1	*XMM-Newton* (archive)
NGC5135	58.8	Sy2	11.3	Levenson et al. (2004)
NGC5653	50.7	H II	11.0	Lehmer et al. (2010)
NGC5734	57.7	composite	11.0	*XMM-Newton* (our data)
NGC5743	59.5	H II	10.9	”
IC4518W*	68.2	Sy2	11.2	*XMM-Newton* (archive)
Zw049.057	55.7	composite	11.2	Lehmer et al. (2010)
IC4686*	71.6	H II	11.0	*XMM-Newton* (our data)
IC4687*	73.9	H II	11.3	”
IC4734	66.8	H II	11.3	”
MCG+04-48-002	60.6	H II	11.0	*XMM-Newton* (archive)
NGC7130	70.0	Sy2	11.4	Levenson et al. (2005)
IC5179	48.5	H II	11.2	*XMM-Newton* (our data)
NGC7469	70.0	Sy1	11.6	*XMM-Newton* (archive)
NGC7679	74.7	Sy1	11.1	”
NGC7769	60.0	composite	10.9	”
NGC7770*	59.6	H II	10.8	”
NGC7771*	62.1	H II	11.3	”

Notes. [(a)] Classification of the nuclear activity from optical spectroscopy. Galaxies classified as composite are likely to be a combination of AGN activity and star-formation (see Chapter 2). [(b)] Logarithm of the IR luminosity, $L(8\text{–}1000\,\mu\text{m})$, calculated as defined in Sanders & Mirabel (1996). [(*)] The logarithm of the integrated $L_{\rm IR}$ in solar units of these systems are: NGC 3690 + IC 694, 11.8; IC 4518W + IC 4518E, 11.2; IC 4686 + IC 4687, 11.5; and NGC 7770 + NGC7771, 11.4.

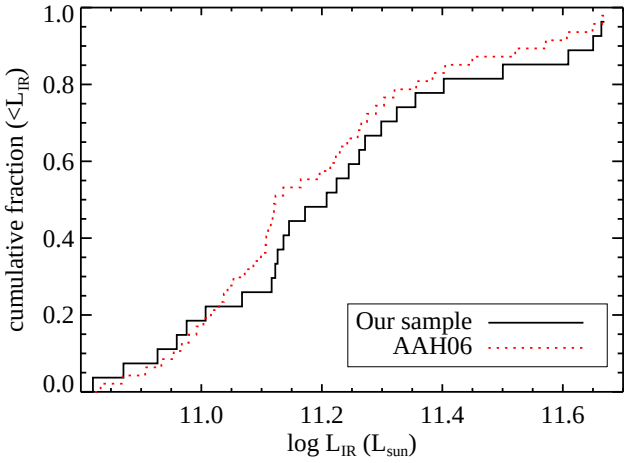

Figure 5.1: Comparison of the cumulative galaxy distributions as a function of the $L_{\rm IR}$ of our sample of LIRGs and the parent sample (AAH06).

the UV light from these stars that is re-emitted as thermal radiation in the mid- and far-IR. The IR luminosity accordingly is a good tracer of the SFR for these galaxies (see Kennicutt 1998 for review). We note, however, that the far-IR luminosity may also include the emission of a cooler dust component that is heated by the interstellar radiation field and is not related with the current SFR. To minimize the contribution of the cooler dust, we used the *Spitzer*/MIPS 24 μm luminosity instead of the $L_{\rm IR}$, which includes longer wavelengths, to estimate the SFR. Moreover, the better spatial resolution of the *Spitzer*/MIPS 24 μm data, compared with *IRAS*, allowed us to separate the individual galaxy emission of interacting systems. We used the SFR calibration of Rieke et al. (2009):

$$\begin{aligned} {\rm SFR_{IR}}\,(M_\odot\ {\rm yr}^{-1}) = 7.8\times10^{-10} L_{24\,\mu{\rm m}}\,(L_\odot) \\ \times\{7.76\times10^{-11} L_{24\,\mu{\rm m}}\,(L_\odot)\}^{0.048}\,. \end{aligned} \tag{5.1}$$

For this calibration Rieke et al. (2009) assumed a Kroupa (2001) IMF over the stellar mass range from 0.08 to 100 $M_\odot$. A correction to account for the leaked UV light from young stars is included in the calibration. Alonso-Herrero et al. (2011) estimated the AGN contribution at 24 μm in these LIRGs. The authors decomposed their *Spitzer*/IRS mid-IR spectra into AGN and starburst components using clumpy torus models and star-forming galaxy templates. We used these estimates to subtract the AGN luminosity at 24 μm before calculating the obscured SFR. The AGN fractions and the calculated $\rm SFR_{IR}$ are listed in Table 5.2.

Some galaxies were observed with the *XMM-Newton* OM in the UVW2 band

(2120 Å). We corrected the observed UV flux from Galactic extinction using the Fitzpatrick (1999) extinction curve and the Galactic color excess, $E(B–V)$, from NED. For these galaxies we compared the SFR derived from the UV continuum with that from the IR luminosity. Assuming a flat continuum in L_ν in the UV range (1500–2800 Å) and scaling to a Kroupa IMF, the $\mathrm{SFR_{UV}}$ can be expressed as

$$\mathrm{SFR_{UV}}\,(M_\odot\ \mathrm{yr}^{-1}) = 9.2 \times 10^{-29} L_\nu\,(\mathrm{erg\ s^{-1}\ Hz^{-1}})\,, \tag{5.2}$$

where L_ν is the UV continuum luminosity (Kennicutt 1998).

The $\mathrm{SFR_{IR}}/\mathrm{SFR_{UV}}$ ratio ranges from ∼2–115 for our LIRGs. This corresponds to an UV leakage from 1 to 30 % of the total luminosity if the IR and the UV emissions trace the same stellar populations. This agrees well with the ratio expected for LIRGs (Buat et al. 2007).

To estimate the stellar mass of the galaxies, we used the integrated J-, H-, and K-band near-IR magnitudes from the Two Micron All Sky Survey (2MASS) large galaxy atlas (Jarrett et al. 2003) and the 2MASS extended source catalog (Jarrett et al. 2000). The near-IR emission is well-suited to calculate the stellar mass because the contribution from young stars is usually negligible and the scatter in the mass-to-light ratio is relatively small (∼0.4 dex). Following Bell & de Jong (2001), we used the K-band luminosity together with the $J - H$ color to obtain the stellar mass. We adjusted the normalization for the Kroupa IMF:

$$\log \frac{M_\star}{M_\odot} = \log \frac{L_\mathrm{K}}{L_{\odot,\mathrm{K}}} + 1.44(J - H) - 1.17\,. \tag{5.3}$$

The SFRs, IR/UV ratios and stellar masses for our sample are listed in Table 5.2.

Table 5.2: Galaxy Properties

Galaxy Name	$E(B–V)^a$ (mag)	$F_{\rm UV}{}^b$ (mJy)	$F_{\rm UV}^{\rm corr\ c}$ (mJy)	$J-H^d$ (mag)	$F_{\rm K}{}^e$ (mJy)	$F_{24\mu{\rm m}}{}^f$ (Jy)	$\log M_\star{}^g$ ($M_\odot$)	$C_{24\mu{\rm m}}^{\rm AGN\,h}$	$\rm SFR_{IR}{}^i$ ($M_\odot\,{\rm yr}^{-1}$)	$\frac{\rm SFR_{IR}}{\rm SFR_{UV}}{}^j$
NGC23	0.04	···	···	0.70	175	0.89	11.2	0.05	11	···
NGC1614	0.15	0.93	3.5	0.77	101	5.64	11.1	···	92	49
NGC2369	0.11	0.15	0.4	0.78	253	1.83	11.2	0.08	12	115
NGC3110	0.04	2.58	3.5	0.73	96	0.98	11.1	<0.04	15	8
NGC3256	0.12	5.12	14.8	0.74	360	12.86	11.1	<0.04	69	26
NGC3690	0.02	···	···	0.76	116	8.19	10.8	0.28	38	···
IC694	0.02	···	···	0.79	96	8.85	10.7	<0.02	59	···
ESO320-G030	0.13	0.33	1.0	0.78	129	1.72	10.9	<0.04	10	46
IC860	0.01	···	···	0.75	36	0.85	10.4	<0.05	8	···
MCG−03-34-064	0.08	···	···	0.73	77	2.45	11.0	0.85	7	···
NGC5135	0.06	···	···	0.76	177	2.02	11.2	0.14	19	···
NGC5653	0.01	···	···	0.70	132	1.11	10.9	0.04	9	···
NGC5734	0.10	0.41	0.9	0.78	140	0.59	11.1	<0.04	6	17
NGC5743	0.10	1.79	4.1	0.73	75	0.43	10.8	0.15	4	2
IC4518W	0.16	···	···	0.78	44	1.00	10.8	0.67	5	···
Zw049.057	0.04	···	···	0.80	22	0.52	10.3	<0.05	5	···
IC4686	0.10	0.76	1.8	0.70	15	0.86	10.2	···	13	13
IC4687	0.10	0.65	1.6	0.75	61	1.66	10.9	0.05	29	30
IC4734	0.09	0.39	0.9	0.78	77	1.03	11.0	<0.05	15	33
MCG+04-48-002	0.45	···	···	0.92	71	0.69	11.1	0.41	5	···
NGC7130	0.03	···	···	0.69	125	1.88	11.1	0.15	25	···
IC5179	0.02	5.12	6.1	0.71	222	1.90	11.1	<0.03	14	9
NGC7469	0.07	···	···	0.81	166	4.80	11.4	0.40	48	···

Table 5.2: *Continued*

Galaxy Name	$E(B–V)^a$ (mag)	$F_{\rm UV}{}^b$ (mJy)	$F_{\rm UV}^{\rm corr}{}^c$ (mJy)	$J-H^d$ (mag)	$F_{\rm K}{}^e$ (mJy)	$F_{24\mu{\rm m}}{}^f$ (Jy)	$\log M_\star{}^g$ ($M_\odot$)	$C_{24\mu{\rm m}}^{\rm AGN}{}^h$	${\rm SFR_{IR}}{}^i$ ($M_\odot\,{\rm yr}^{-1}$)	$\frac{\rm SFR_{IR}}{\rm SFR_{UV}}{}^j$
NGC7679	0.07	···	···	0.63	60	0.85	10.8	0.23	11	···
NGC7769	0.07	···	···	0.70	162	0.50	11.1	0.10	5	···
NGC7770	0.07	···	···	0.71	28	0.40	10.3	0.27	3	···
NGC7771	0.07	···	···	0.76	287	1.29	11.5	0.04	15	···

Notes. [(a)] Galactic color excess $E(B–V)$ from NED. [(b)] Observed *XMM-Newton*/OM UVW2 (2120 Å) flux. [(c)] *XMM-Newton*/OM UVW2 (2120 Å) flux corrected for Galactic extinction using the Fitzpatrick (1999) extinction curve. [(d)] $J-H$ color calculated from the 2MASS magnitudes. [(e)] Integrated K-band flux from 2MASS. [(f)] *Spitzer*/MIPS 24 μm flux. [(g)] Logarithm of the stellar mass obtained from the K-band luminosity and the $J-H$ color. [(h)] AGN fractional contribution to the total 24 μm emission from Alonso-Herrero et al. (2011). [(i)] Star-formation rate based on the 24 μm luminosity. The AGN contribution to the 24 μm luminosity is subtracted. [(j)] Ratio of the star-formation rates estimated from the IR and UV luminosities.

5.3 Spatial Analysis of the *XMM-Newton* Data

5.3.1 Morphologies

We obtained X-ray images of these LIRGs as described in Section 2.3.1. Figure 5.2 shows the soft (0.5–2 keV) and hard (2–7 keV) X-ray images for the LIRGs together with the *XMM-Newton*/OM UV (2120 Å) and near-IR *Spitzer*/IRAC (3.6 μm) images for comparison.

In our sample of LIRGs we find different X-ray emission morphologies. Most of them are dominated by the nuclear emission and appear as point-like (or slightly resolved) sources at the *XMM-Newton* angular resolution, 4–6 arcsec. At the distances of these LIRGs this corresponds to 0.9–2 kpc. Six galaxies (NGC 3110, NGC 3256, NGC 5734, NGC 5743, IC 5179, and NGC 7769), $\sim$20 % of the sample, show extended soft X-ray emission. This indicates that at least some of the sources responsible for the origin of the X-ray emission (X-ray binaries, SNR, diffuse hot plasma, etc.) are extended over several kpc (>1 kpc). Higher angular resolution images with *Chandra* of LIRGs confirm that the X-ray emission comes from multiple point sources as well as from diffuse emission distributed over the galaxies (Zezas et al. 2003; Levenson et al. 2004, 2005; Lehmer et al. 2010).

The S/N ratio in the hard *XMM-Newton* X-ray band (2–10 keV) of the H II galaxies is too low to measure the size of the X-ray emitting region accurately. The only exception is NGC 3256, which appears approximately as extended as its soft X-ray emission. The higher spatial resolution *Chandra* X-ray images of NGC 3256 reveal that both the soft and hard X-ray emissions are resolved into multiple point sources, besides the two nuclei, and diffuse emission (Lira et al. 2002).

The hard X-ray emission of the Seyfert galaxies is dominated by the AGN, consequently they appear as point sources in this energy range.

5.3.2 Extranuclear Sources

In two LIRGs observed with *XMM-Newton* (NGC 2369 and NGC 7771) we find bright extranuclear X-ray sources that might be ultraluminous X-ray sources (ULXs). Note that we can only isolate such X-ray sources if they are located more than 0.9–2 kpc away from the nucleus owing to the spatial resolution of the images. That is, ULXs may exist in the rest of the sample within the central 0.9–2 kpc.

The two sources located at either side of the nucleus of NGC 7771 (NGC 7771 X-1 and NGC 7771 X-2) were studied by Jenkins et al. (2005). The spectra of both sources are well-fitted with an absorbed power-law (Γ = 1.6 and 1.7) plus a soft component

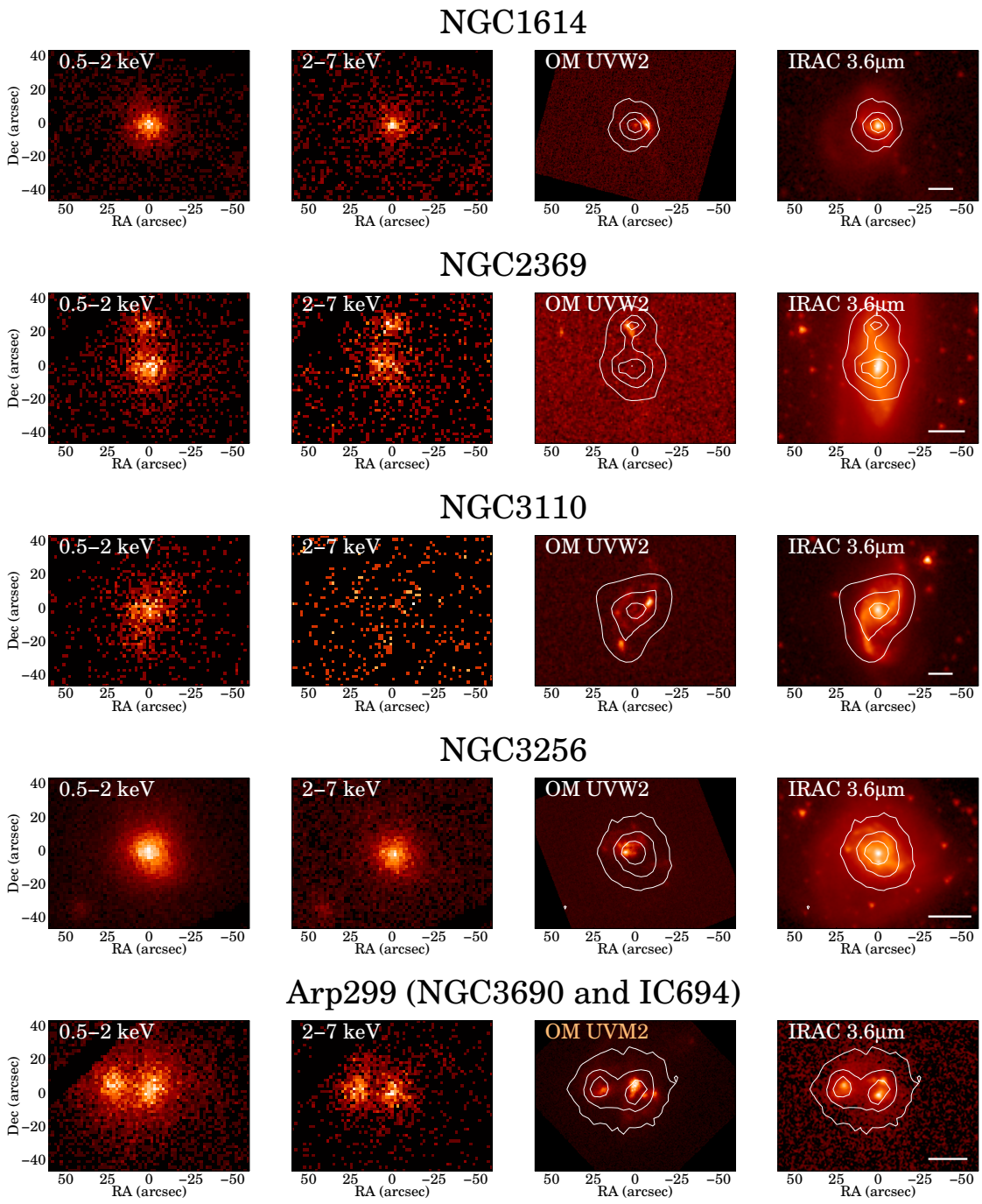

Figure 5.2: *XMM-Newton*/EPIC pn 0.5-2 keV and 2-7 keV images (first and second panels from the left), *XMM-Newton*/OM UVW2 (2120 Å) images for the galaxies observed with this filter (third panel from the left). The third panel of Arp299 and MCG+04-48-002 corresponds to the *XMM-Newton*/OM UVM2 (2310 Å) filter. *Spitzer*/IRAC 3.6 μm images (fourth panel from the left). For reference we represent in the third and forth panels the smoothed 0.5-7 keV contours. The white line in the right panels represents 5 kpc at the distance of the galaxy. All images are shown in a square root scale. North is up and east is to the left.

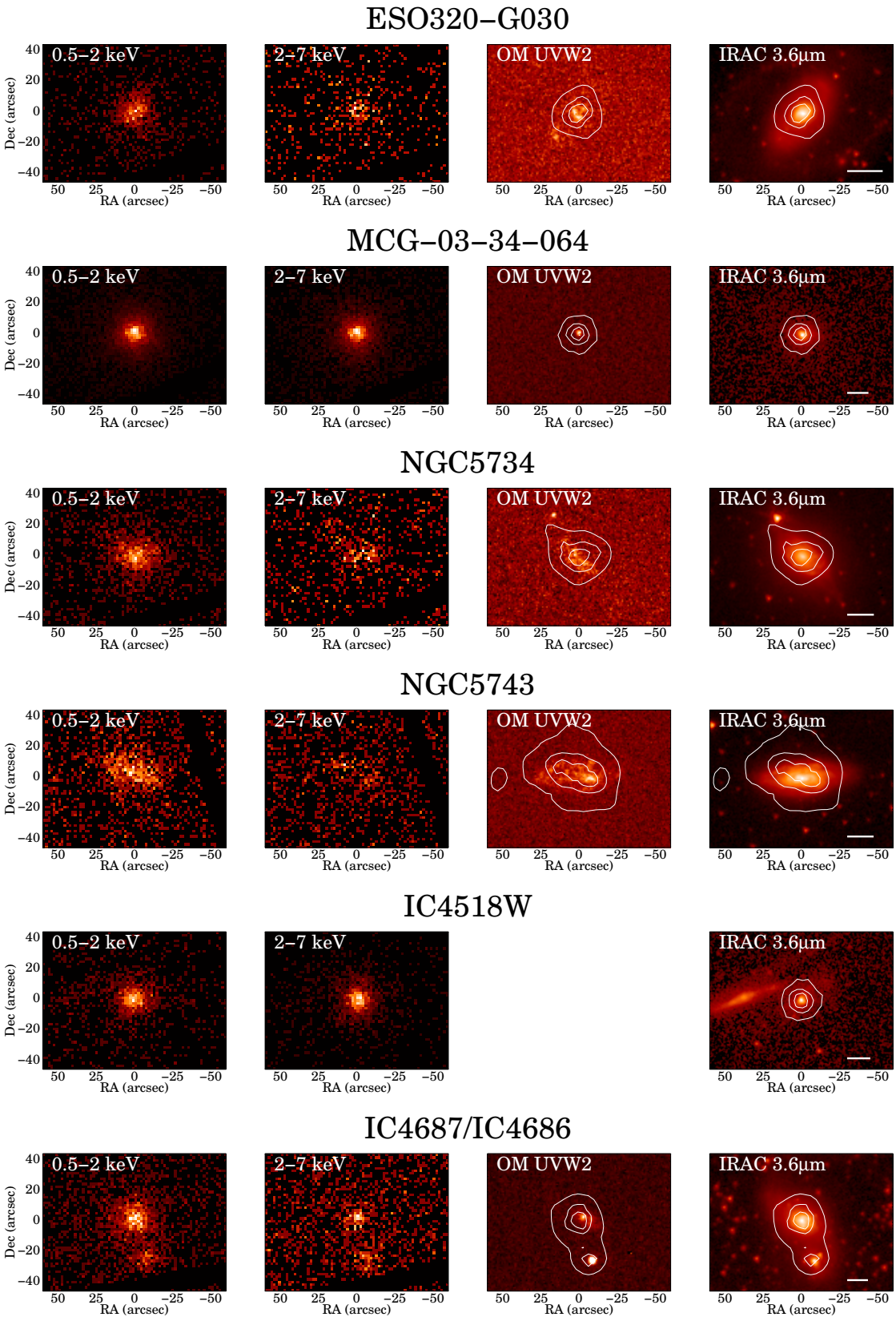

Figure 5.2: *Continued.*

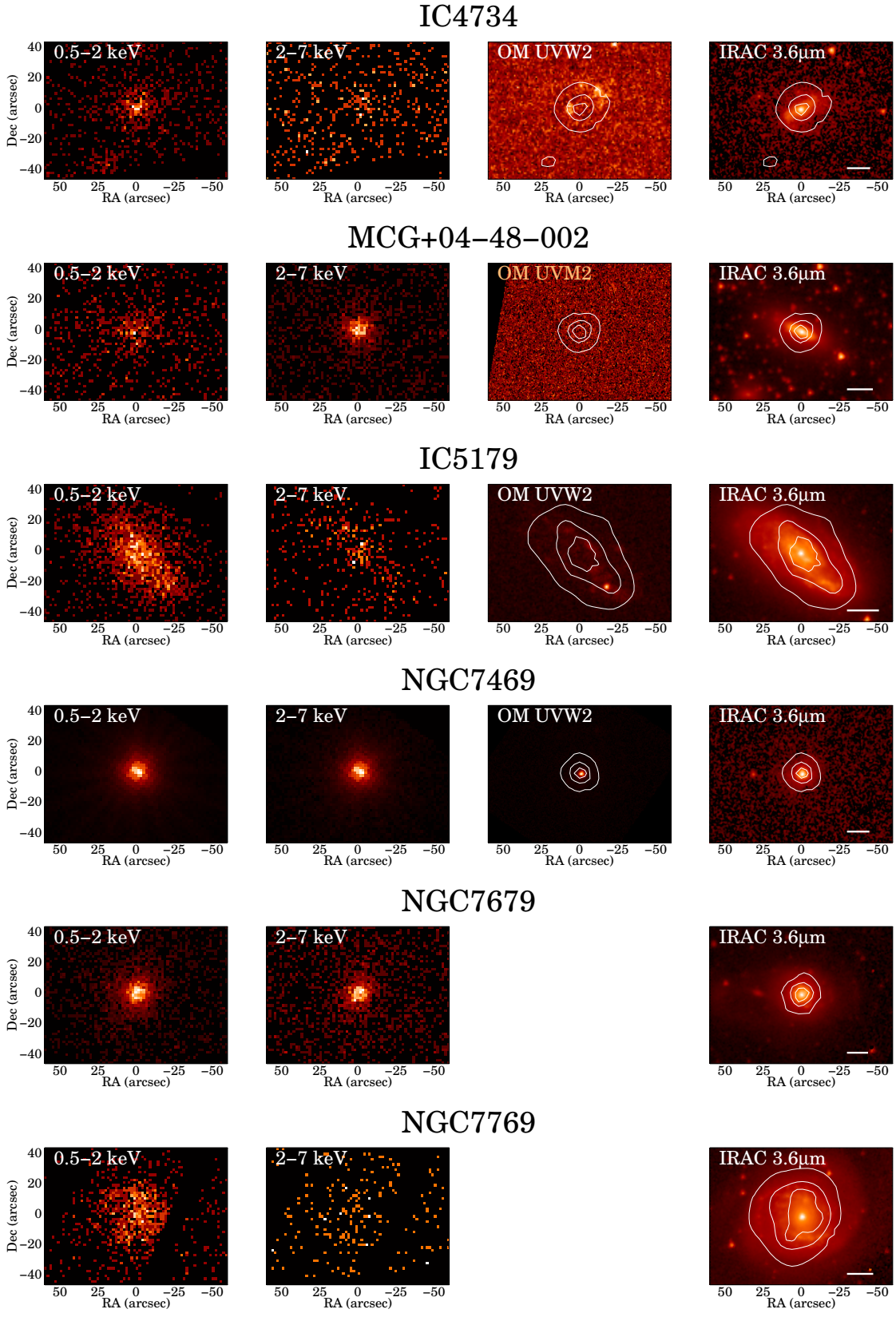

Figure 5.2: *Continued.*

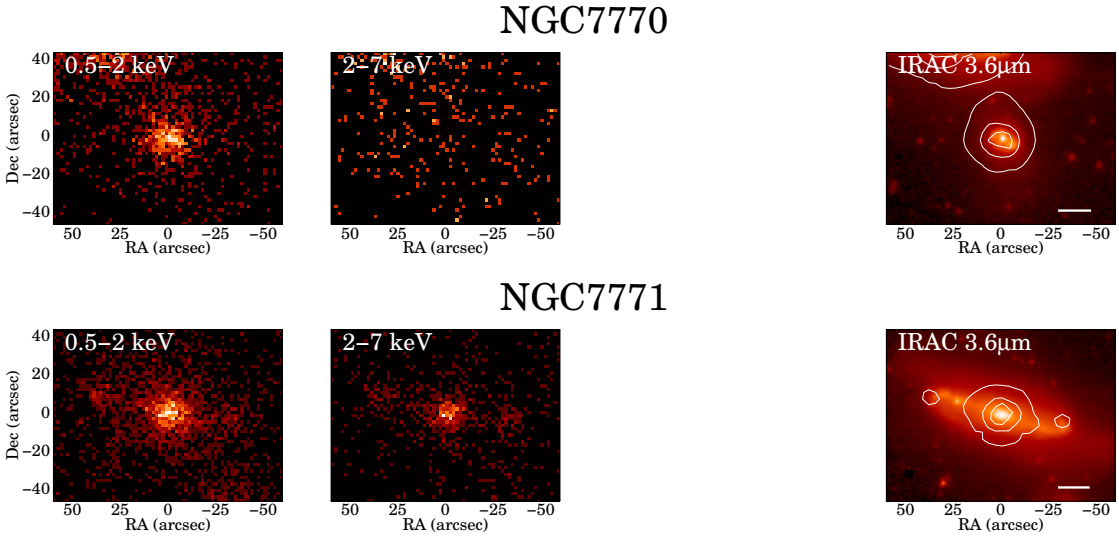

Figure 5.2: *Continued.*

(thermal plasma at 0.3 keV and a blackbody disk at 0.2 keV). The unabsorbed luminosities ($L^{int}_{0.5-8\,\mathrm{keV}}$) of these sources are $1.7 \pm 1.0 \times 10^{40}$ erg s^{-1} and $1.4 \pm 0.8 \times 10^{40}$ erg s^{-1}.

The ULX candidate in NGC 2369 is located 25 arcsec (∼5 kpc) to the north of the nucleus (NGC 2369 X-1 at R.A. (J2000) = 7:16:38.5 Decl. (J2000) = –62:20:16). An absorbed power-law model reproduces the observed spectrum of this source well (χ^2/dof = 31/42, Figure 5.3) and implies an intrinsic X-ray luminosity $L^{int}_{0.5-8\,\mathrm{keV}} = 3.2 \pm 0.6 \times 10^{40}$ erg s^{-1}. This is one order of magnitude higher than the ULX luminosity threshold ($L^{int}_{0.5-8\,\mathrm{keV}} > 10^{39}$ erg s^{-1}) and comparable to the luminosities measured for other ULXs. The parameters of the model ($\Gamma = 1.6 \pm 0.2$ and $N_{\mathrm{H}} = 1.3 \pm 0.5 \times 10^{21}$ cm^{-2}) are also similar to those obtained for other ULXs (Swartz et al. 2004). The angular resolution of the *XMM-Newton* data does not allow us to determine if this emission comes from a single source (i.e., ULX or a background AGN) or, conversely, if it is the integrated emission from multiple sources. NGC 2369 X-1 is coincident with an extended UV emitting region that seems to be located in the spiral arms of NGC 2369 (Figure 5.2). Therefore the background AGN possibility is unlikely. The SFR of this region derived from their UV and IR luminosities[1] is 0.9 $M_{\odot}$ yr^{-1} (see Section 5.2.2). Accordingly the expected hard X-ray luminosity from star-formation (∼2.3×10^{39} erg s^{-1}, see Section 5.5) is ∼10 times lower than the observed luminosity. Moreover, no excess soft X-ray emission from hot (∼0.7 keV) gas, which is common in star-forming

[1]The UV (2120 Å) and IR fluxes of the NGC 2369 X-1 region are $F^{\mathrm{corr}}_{\mathrm{UV}} = 0.4$ mJy and $F_{24\mu\mathrm{m}} = 0.14$ Jy.

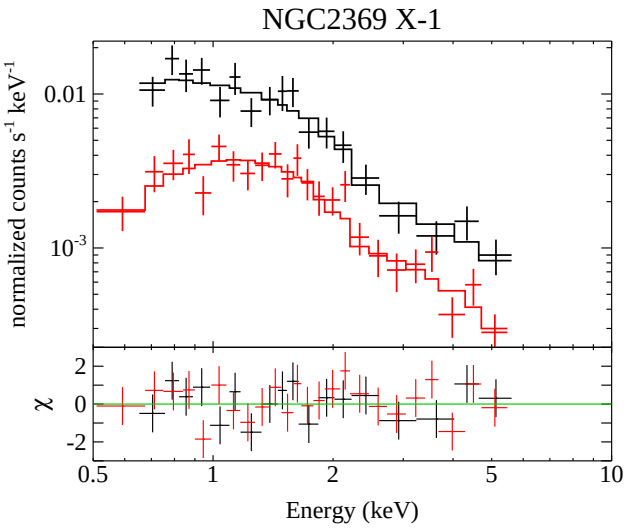

Figure 5.3: EPIC pn (black) and combined EPIC MOS (red) 0.5–10 keV spectrum of NGC 2369 X-1 together with the spectral model consisting of an absorbed power-law (see Section 5.3.2).

regions, is detected in its spectra (Figure 5.3). All these pieces of evidence suggest that the X-ray emission of NGC 2369 X-1 is dominated by a single bright source.

5.4 Spectral Analysis of the *XMM-Newton* Data

At 60 Mpc (typical distance of these LIRGs) the *XMM-Newton* spatial resolution (6″) corresponds to 1.7 kpc. This means that we are not able to resolve individual emitting sources. Instead, the *XMM-Newton* spectra of these LIRGs probably include the emission from X-ray binaries (low- and high-mass), SNRs and diffuse hot plasma. An AGN may be present as well. Therefore, we would ideally include one component for each in the X-ray model. However, this is not possible because (1) it is complicated to determine the characteristic spectrum of these objects and even more complicated to determine the characteristic integrated spectrum of these objects in a galaxy; and (2) the S/N ratio of our data is not sufficiently high to obtain statistically meaningful results with a very complex model. We used the `XSPEC` package (version 12.5) to fit the EPIC MOS and pn spectra simultaneously. The RGS data of the three galaxies with sufficient counts (see Section 2.3.1) are compatible with the fit obtained using just the EPIC data. Adding the RGS data does not improve the constraints on the model parameters significantly. Consequently, the RGS data are not used in the spectral analysis. The fits of some individual sources are discussed in Appendix 5.A.

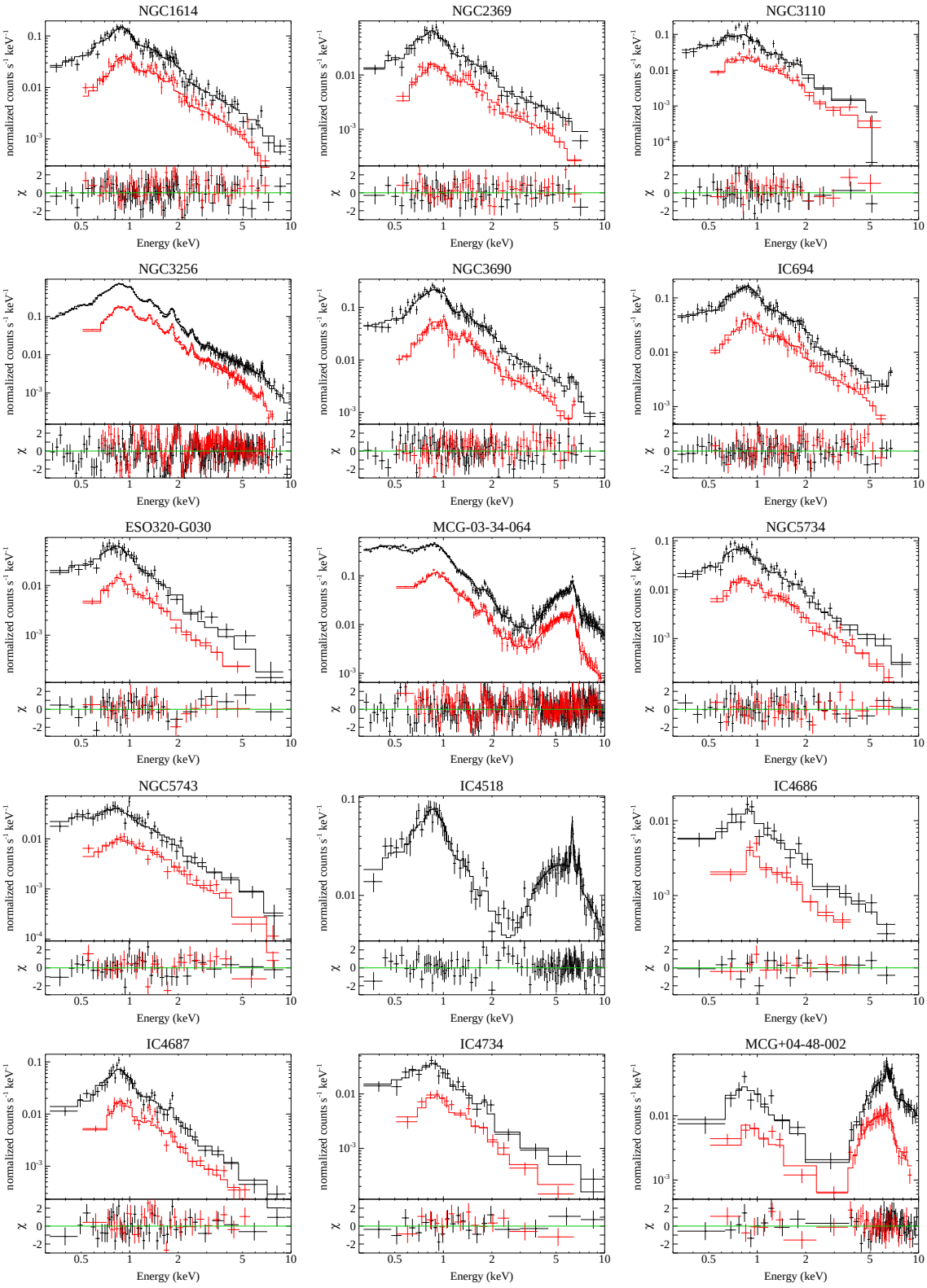

Figure 5.4: Observed EPIC pn (black) and combined EPIC MOS (red) 0.3-10 keV spectra, best-fitting model and residuals of the LIRGs observed by *XMM-Newton*.

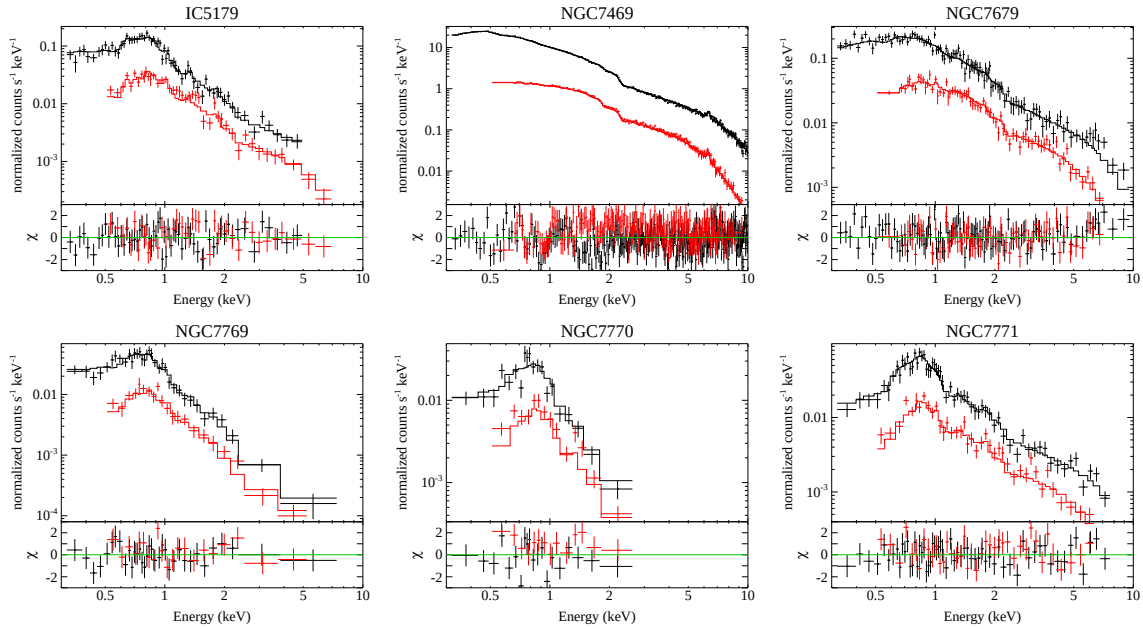

Figure 5.4: *Continued.*

5.4.1 The X-ray Spectra of Star-forming Galaxies

We fitted the spectra of the star-forming galaxies using a simple model consisting of a soft thermal plasma (*mekal*) plus an absorbed power-law. The absorption of the thermal plasma component is not well constrained and it is compatible with no absorption for most of the galaxies. It was only necessary in the fit of the NGC 3256 and NGC 3690 spectra. The thermal plasma represents the soft X-ray emitting gas heated by SN shocks, whereas the power-law reproduces the observed hard X-ray continuum produced by X-ray binaries and/or AGN. We also added the absorption caused by the Galactic hydrogen column density to the model (Kalberla et al. 2005). The absolute value of the plasma metallicity is not well constrained for our relatively low S/N ratio spectra. However, the [Fe/O] ratio can be determined because the most prominent spectral features in the soft X-ray range are produced by these elements (the Fe L-shell and the O K-shell). Consequently, the plasma abundances were fixed to the solar values except for the Fe abundance. The latter was left as a free parameter to calculate the [Fe/O] ratio. This model provides a reasonable fit to the data ($\chi^2_{\rm red} < 1.2$) for most of the galaxies. We included a Gaussian line when a Fe Kα emission line was present in the spectrum (NGC 3256, NGC 3690, and IC 694). For those galaxies with undetected 6.4 keV emission line we calculated the upper limits for a narrow emission line. Figure 5.4 shows the X-ray spectra together with the model for all galaxies with *XMM-Newton* data.

Table 5.3: Fe K Line

Galaxy Name	E^a (keV)	EW (keV)	$F_{\rm Fe\,K}$ (10^{-15} erg cm^{-2} s^{-1})
NGC23	...	...	...
NGC1614	6.4	<0.62	<16
NGC2369	6.4	<0.34	<5.7
NGC3110	6.4	<0.76	<3.0
NGC3256	6.4	<0.07	<3.5
	$6.60^{+0.10}_{-0.04}$	0.2	8.2
NGC3690	$6.6^{+0.2}_{-0.3}$	0.93	67
IC694	6.4	<0.2	<9.4
	$6.67^{+0.10}_{-0.11}$	0.85	60
ESO320-G030	6.4	<1.8	<6.5
IC860	...	...	...
MCG−03-34-064	$6.39^{+0.02}_{-0.02}$	0.11	92
NGC5135[b]	$6.39^{+0.03}_{-0.04}$	2.4	∼50
NGC5653	...	...	...
NGC5734	6.4	<0.8	<6.6
NGC5743	6.4	<1.4	<13
IC4518W	$6.39^{+0.03}_{-0.03}$	0.46	120
	$7.1^{+0.1}_{-0.2}$	0.21	52
Zw049.057	...	...	...
IC4686	6.4	<0.8	<5.1
IC4687	6.4	<1.4	<8.7
IC4734	6.4	<3.5	<11
MCG+04-48-002	$6.47^{+0.05}_{-0.06}$	0.12	66
NGC7130[c]	$6.40^{+0.05}_{-0.05}$	1.8	∼35
IC5179	6.4	<0.41	<6.3
NGC7469	$6.42^{+0.03}_{-0.03}$	0.070	203
NGC7679	6.4	<0.42	<30
NGC7769	6.4	<1.8	<3.5
NGC7770	6.4	<8.5	<9.6
NGC7771	6.4	<0.47	<10

Notes. Observed fluxes and EW of the Fe K emission lines. Upper limits are calculated assuming an unresolved Gaussian emission line at 6.4 keV. [(a)] Rest frame energy of the emission line. When no uncertainties are quoted the value was fixed. [(b,c)] Data from Levenson et al. (2004) and Levenson et al. (2005) respectively.

The parameters of the fits are listed in Table 5.4. The typical values of the model parameters are $\Gamma \sim 1.3$–2.2, $N_{\rm H} \sim 1{\times}10^{21}$–$5{\times}10^{21}$ cm^{-2}, $kT \sim 0.5$–0.7 keV and [Fe/O] ~ -0.5–-0.1. The measured $N_{\rm H}$ corresponds to $A_{\rm V} \sim 0.5$–2.3 mag using the Güver & Özel (2009) conversion factor. In general, the X-ray derived absorption is lower than that obtained from the near-IR colors (∼3 mag) and the Paα/Hα ratio (∼2–5 mag) for these galaxies (Alonso-Herrero et al. 2006). The temperature of the plasma and its contribution to the hard X-ray emission of these LIRGs are comparable with those of local starbursts (0.8 keV and 3 %, Persic & Rephaeli 2003). However, the power-law component is slightly steeper than in local starbursts, $\Gamma = 1.2$ (Persic & Rephaeli 2003) versus $\Gamma = 1.8$ in these LIRGs. The upper limits and fluxes of the Fe Kα emission line are listed Table 5.3.

Table 5.4: X-ray Model Fits. Starburst Model.

Galaxy Name	$N_{\rm H,Gal}{}^{a}$ (10^{22} cm^{-2})	$N_{\rm H,1}$ (10^{22} cm^{-2})	kT (keV)	Fe/O^{b}	$N_{\rm H,2}$ (10^{22} cm^{-2})	Γ	χ^2/dof	$F_{0.5-2}{}^{c}$ (10^{-14} erg cm^{-2} s^{-1})	$F_{2-10}{}^{c}$	$L_{0.5-2}{}^{d}$ (10^{40} erg s^{-1})	$L_{2-10}{}^{d}$	$L_{\rm plasma}{}^{e}$ (%)
NGC1614	0.06	<0.26	$0.73^{+0.05}_{-0.06}$	$0.44^{+0.17}_{-0.09}$	$0.38^{+0.20}_{-0.14}$	$1.97^{+0.18}_{-0.13}$	199/152	$17.7^{+1.7}_{-2.4}$	$27.6^{+1.7}_{-4.2}$	19.4	16.4	2.1
NGC2369	0.10	<0.13	$0.60^{+0.05}_{-0.06}$	$0.51^{+0.25}_{-0.17}$	$0.13^{+0.28}_{-0.07}$	$1.49^{+0.11}_{-0.12}$	87/96	$7.5^{+1.0}_{-1.4}$	$16.4^{+1.6}_{-1.8}$	3.0	4.4	0.9
NGC2369*	...	...	...	...	...	...	...	...	...	4.5	6.4	...
NGC3110	0.03	<0.35	$0.53^{+0.08}_{-0.09}$	$0.29^{+0.17}_{-0.09}$	$0.27^{+0.48}_{-0.13}$	$2.53^{+0.48}_{-0.36}$	92/75	$9.7^{+1.3}_{-1.6}$	$5.3^{+0.4}_{-2.3}$	9.6	3.3	3.0
NGC3256	0.09	$0.18^{+0.01}_{-0.02}$	$0.62^{+0.01}_{-0.01}$	$0.37^{+0.03}_{-0.03}$	$0.14^{+0.03}_{-0.03}$	$2.02^{+0.07}_{-0.12}$	561/335	$71.1^{+1.7}_{-2.9}$	$49.2^{+2.4}_{-2.9}$	29.5	9.7	12.3
NGC3690	0.01	$0.11^{+0.16}_{-0.08}$	$0.63^{+0.06}_{-0.05}$	$0.48^{+0.33}_{-0.14}$	$0.29^{+0.22}_{-0.12}$	$1.76^{+0.17}_{-0.18}$	168/142	$30.0^{+2.6}_{-5.9}$	$45.8^{+3.9}_{-7.7}$	11.2	10.8	1.9
IC694	0.01	<0.18	$0.66^{+0.03}_{-0.03}$	$0.46^{+0.21}_{-0.08}$	$0.37^{+0.22}_{-0.19}$	$1.86^{+0.18}_{-0.14}$	131/128	$25.4^{+2.6}_{-4.0}$	$42.5^{+3.6}_{-7.3}$	10.0	10.5	1.3
ESO320-G030	0.09	<0.21	$0.61^{+0.06}_{-0.06}$	$0.70^{+0.53}_{-0.32}$	$0.07^{+0.07}_{-0.06}$	$2.13^{+0.44}_{-0.28}$	62/67	$5.8^{+0.5}_{-1.6}$	$4.7^{+0.6}_{-0.6}$	2.0	1.1	2.0
NGC5734	0.07	<0.28	$0.49^{+0.07}_{-0.06}$	$0.56^{+0.20}_{-0.18}$	$0.13^{+0.17}_{-0.06}$	$1.92^{+0.18}_{-0.17}$	78/88	$7.3^{+0.6}_{-1.3}$	$9.0^{+0.6}_{-1.1}$	4.7	3.8	0.7
NGC5743	0.07	...	$0.61^{+0.10}_{-0.14}$	$0.63^{+0.37}_{-0.37}$	...	$1.68^{+0.15}_{-0.17}$	61/71	$5.4^{+0.2}_{-0.7}$	$9.6^{+1.1}_{-1.1}$	2.9	4.1	0.5
IC4686	0.07	...	$0.72^{+0.15}_{-0.10}$	...	...	$1.27^{+0.12}_{-0.16}$	18/25	$2.4^{+0.3}_{-0.2}$	$7.1^{+0.9}_{-1.1}$	1.7	4.2	0.4
IC4687	0.07	<0.19	$0.67^{+0.04}_{-0.04}$	$0.54^{+0.16}_{-0.13}$	$0.48^{+0.36}_{-0.23}$	$2.22^{+0.32}_{-0.28}$	100/78	$7.7^{+0.9}_{-2.1}$	$7.7^{+1.0}_{-2.8}$	10.7	5.6	3.0
IC4734	0.07	...	$0.69^{+0.09}_{-0.08}$	$0.31^{+0.29}_{-0.13}$	...	$1.46^{+0.29}_{-0.20}$	35/42	$4.0^{+0.3}_{-0.6}$	$5.4^{+0.9}_{-2.8}$	2.7	3.0	3.0
IC5179	0.01	<0.06	$0.55^{+0.04}_{-0.04}$	$0.35^{+0.11}_{-0.08}$	<0.10	$1.44^{+0.12}_{-0.12}$	91/100	$12.7^{+0.6}_{-0.8}$	$15.2^{+1.2}_{-2.0}$	3.9	4.4	1.4
NGC7679	0.05	<0.10	$0.48^{+0.09}_{-0.10}$	$0.29^{+0.20}_{-0.14}$	<0.01	$1.64^{+0.07}_{-0.07}$	172/172	$35.6^{+0.7}_{-3.3}$	$66.3^{+3.7}_{-3.7}$	27.7	44.5	0.2
NGC7769	0.04	...	$0.49^{+0.04}_{-0.07}$	$0.52^{+0.21}_{-0.18}$	...	$2.17^{+0.18}_{-0.18}$	42/53	$5.4^{+0.3}_{-0.6}$	$2.7^{+0.3}_{-0.5}$	2.7	1.2	2.0
NGC7770	0.04	...	$0.58^{+0.06}_{-0.06}$	$0.35^{+0.28}_{-0.13}$	...	$1.84^{+0.45}_{-0.63}$	50/29	$3.0^{+0.2}_{-0.5}$	$1.3^{+0.3}_{-0.9}$	1.5	0.5	6.9
NGC7771	0.04	<0.11	$0.60^{+0.04}_{-0.04}$	$0.44^{+0.10}_{-0.08}$	$0.51^{+0.31}_{-0.29}$	$1.46^{+0.20}_{-0.18}$	101/95	$7.9^{+0.6}_{-1.3}$	$18.6^{+1.8}_{-3.4}$	6.1	8.9	1.0
NGC7771*	...	...	...	...	...	...	...	...	...	7.5	11.3	...

Notes. The model used for the fits was Abs($N_{\rm H,Gal}$){Abs($N_{\rm H,1}$)(v)mekal(kT, Fe/O) + Abs($N_{\rm H,2}$)[power-law(Γ)]}, where Abs is a photo-electric absorption model and (v)mekal is a thermal plasma (with variable metal abundances). $^{(a)}$ Galactic absorbing hydrogen column density from Kalberla et al. (2005). $^{(b)}$ Fe/O abundances ratio with respect to the solar values of Anders & Grevesse (1989). $^{(c)}$ 0.5–2 keV and 2–10 keV X-ray observed flux. $^{(d)}$ 0.5–2 keV and 2–10 keV X-ray luminosity corrected for Galactic extinction ($N_{\rm H,Gal}$) and intrinsic absorption ($N_{\rm H}$). $^{(e)}$ Fraction of the 2–10 keV luminosity from the thermal plasma component. $^{(\star)}$ Integrated luminosity including extranuclear ULX sources.

Table 5.5: X-ray Model Fits. AGN Model.

Galaxy Name	$N_{\rm H,Gal}{}^{a}$ ($10^{22}\,{\rm cm}^{-2}$)	kT (keV)	Fe/O^{b}	$N_{\rm H,SB}$ ($10^{22}\,{\rm cm}^{-2}$)	Γ_{SB}	$N_{\rm H,AGN}$ ($10^{22}\,{\rm cm}^{-2}$)	Γ_{AGN}	χ^2/dof	$F_{0.5-2}{}^{c}$ ($10^{-14}\,{\rm erg\,cm^{-2}\,s^{-1}}$)	$F_{2-10}{}^{c}$	$L_{0.5-2}{}^{d}$ ($10^{40}\,{\rm erg\,s^{-1}}$)	$L_{2-10}{}^{e}$
IC4518W	0.09	$0.66^{+0.05}_{-0.06}$	$0.49^{+0.41}_{-0.23}$	<0.10	1.85	$24.28^{+2.24}_{-2.05}$	$1.59^{+0.17}_{-0.29}$	106/105	$9.4^{+0.8}_{-1.8}$	$169.8^{+30.9}_{-27.7}$	7.0	220.2
MCG+04-48-002	0.21	$0.53^{+0.12}_{-0.14}$	···	<1.30	1.85	$63.19^{+10.34}_{-6.51}$	$1.75^{+0.55}_{-0.30}$	89/109	$3.2^{+0.7}_{-1.8}$	$275.3^{+9.2}_{-116.3}$	2.8	688.0

Notes. The model used for the fits was Abs($N_{\rm H,Gal}$){(v)mekal(kT, Fe/O) + Abs($N_{\rm H,SB}$)[power-law(Γ_{SB})] + Abs($N_{\rm H,AGN}$)[power-law(Γ_{AGN})]}, where Abs is a photo-electric absorption model and mekal is a thermal plasma. A Gaussian emission line was added ∼6.4 keV to account for the Fe Kα emission line. An extra Gaussian emission line at 7.1 keV is needed for IC4518W (see Table 5.3). $^{(a)}$ Galactic absorbing hydrogen column density from Kalberla et al. (2005). $^{(b)}$ Fe/O abundances ratio with respect to the solar values of Anders & Grevesse (1989). $^{(c)}$ 0.5–2 keV and 2–10 keV X-ray observed flux. $^{(d)}$ 0.5–2 keV X-ray luminosity corrected for Galactic extinction ($N_{\rm H,Gal}$). $^{(e)}$ 2–10 keV X-ray luminosity corrected for Galactic extinction ($N_{\rm H,Gal}$) and intrinsic absorption ($N_{\rm H,AGN}$).

5.4.2 AGN X-ray Spectra

The X-ray spectra of two galaxies, IC 4518W, MCG+04-48-002, are poorly fitted by the star-formation model described above. The hard X-ray emission of these galaxies is dominated by the AGN (Figure 5.4). We added an absorbed power-law and a Gaussian emission line at 6.4 keV to the star-formation model to account for the AGN emission. For IC 4518W we added another Gaussian emission line at 7.1 keV. For these galaxies the power-law index of the star-formation component is poorly constrained because of the AGN contribution to the hard X-ray emission. Hence we fixed it to the median value obtained for the other LIRGs ($\Gamma = 1.85$). This model provides a good fit to the data, $\chi^2_{\rm red} \leq 1$, for the two galaxies. For this reason, we did not include an AGN reflection component (*pexrav*). By doing this we may underestimate the absorbing column density toward the AGN. This model fits the soft X-ray emission of these galaxies well. However, this does not imply a star-formation origin of the soft X-ray emission because the thermal plasma and the power-law continuum can be produced by an AGN. The origin of the soft X-ray emission is discussed in Section 5.5. The model parameters for these two galaxies are given in Table 5.5.

5.4.3 Literature X-ray Data

The X-ray luminosities taken from the literature are listed in Table 5.6. This table includes the six galaxies observed with *Chandra* plus two galaxies observed with *XMM-Newton*. For these two objects, MCG−03-34-064 and NGC 7469, we repeated the fits of the *XMM-Newton* data using the models given by Miniutti et al. (2007) and Blustin et al. (2003), respectively, to take advantage of the latest calibration.

5.5 X-ray Emission from Star-formation Activity

5.5.1 Soft X-ray Emission versus SFR

At soft energies (0.5–2-0 keV), the X-ray emission is produced by diffuse hot gas heated by supernova explosions as well as X-ray binaries. Therefore the soft X-ray emission is expected to be correlated with the SFR (Ranalli et al. 2003; Rosa González et al. 2009).

The correlation found by Ranalli et al. (2003) between the soft X-ray and the far-infrared (FIR, 40–500 μm) luminosities is not linear. The galaxies in their study cover a large range in far-IR luminosities and it is possible that for those galaxies with the lowest SFR, the total SFR is not dominated by the obscured SFR traced by the FIR

Table 5.6: Galaxies Taken from the Literature.

Galaxy Name	$L_{0.5-2\,\mathrm{keV}}$	$L_{2-10\,\mathrm{keV}}$	Ref.
	$(10^{40}\,\mathrm{erg\,s^{-1}})$		
NGC23	6.7	4.2	1
IC860	0.3	1.1	1
MCG−03-34-064*	26.6	111	2
NGC5135	17.9	18.9	3
NGC5653	2.8	1.5	1
Zw049.057	0.2	1.5	1
NGC7130	15.4	15.4	4
NGC7469*	1630	1690	5

Notes. 0.5–2 keV and 2–10 keV absorption corrected luminosities of the galaxies taken from the literature adapted to the cosmology used throughout this thesis. $^{(\star)}$ For the galaxies with *XMM-Newton* observations we fitted the data using the best-fit model given in the corresponding reference.

References. (1) Lehmer et al. 2010; (2) Miniutti et al. 2007; (3) Levenson et al. 2004; (4) Levenson et al. 2005; (5) Blustin et al. 2003.

luminosity (see Pérez-González et al. 2006; Kennicutt et al. 2009). To account for the unobscured star-formation, we used the near-UV (2267 Å) fluxes from Gil de Paz et al. (2007), which we translated into SFR (see Section 5.2.2). We found near-UV fluxes for 65 % of the Ranalli et al. (2003) sample. To calculate the obscured SFR, we used the *IRAS* fluxes to obtain the total IR luminosity (8–1000 μm). Then we used the calibration of Kennicutt (1998), correcting for our adopted Kroupa IMF. We added IR and UV SFR to obtain the total SFR. The SFR traced by the UV light contributes to the total SFR between 5 % and 60 % with a median contribution of 20% for the galaxies of the Ranalli et al. (2003) sample. For the LIRGs we neglected the unobscured star-formation because it contributes less than 10 % for most of the galaxies (see Table 5.2 and Howell et al. 2010; Rodríguez-Zaurín et al. 2011). In the left panel of Figure 5.5 we compare the $\mathrm{SFR_{IR+UV}}$ with the soft X-ray luminosity for our sample of LIRGs together with the nearby galaxies of Ranalli et al. (2003). The best-fit[2] slope in log-log space is 1.1 ± 0.1, which is compatible with a linear relation. Assuming a constant $\mathrm{SFR_{IR+UV}}/L_{0.5-2\,\mathrm{keV}}$ ratio, we found

$$\mathrm{SFR_{IR+UV}}\,(M_{\odot}\,\mathrm{yr^{-1}}) = 3.4 \times 10^{-40} L_{0.5-2\,\mathrm{keV}}\,(\mathrm{erg\,s^{-1}}) \tag{5.4}$$

[2]We only used the galaxies classified as H II and the galaxies of Ranalli et al. (2003) for the fit.

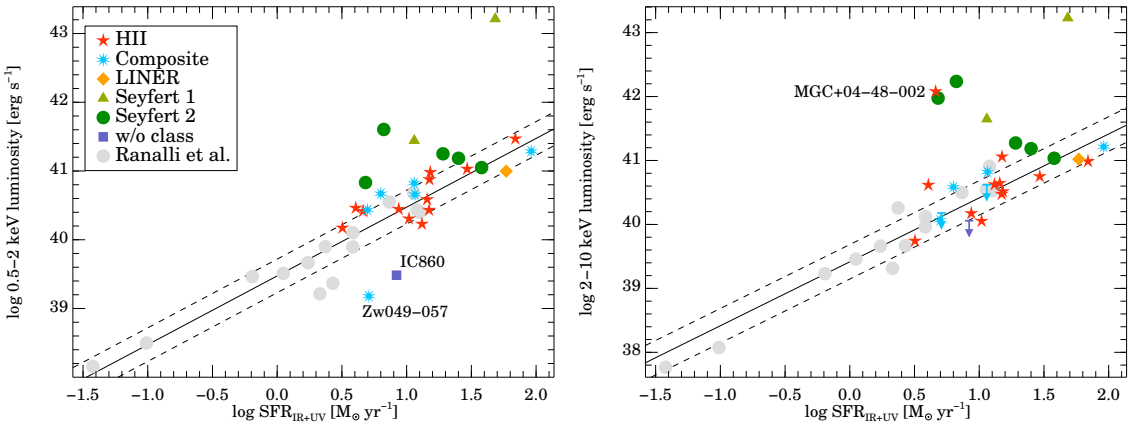

Figure 5.5: Soft (0.5–2 keV; left) and hard (2–10 keV; right) X-ray luminosity corrected for absorption vs. SFR calculated combining the UV and IR luminosities (Section 5.2.2). Red stars are H II galaxies. Light green triangles and dark green circles are Type 1 and 2 Seyfert galaxies, respectively. Blue stars are composite galaxies, orange diamonds are LINERs and blue squares are galaxies without classification from optical spectroscopy. Galaxies from Ranalli et al. (2003) are plotted as gray circles. The solid line is our best linear fit to those LIRGs classified as H II and the Ranalli et al. (2003) galaxies. The dashed lines indicate the $\pm 1\sigma$ dispersion in this relation.

with a 0.24 dex scatter. Mas-Hesse et al. (2008) modeled the soft X-ray luminosity expected from a starburst. They assumed that the mechanical energy from the starburst (SN and stellar winds) heats the interstellar diffuse gas with an efficiency of 1–5 %. After correcting for the different IMF normalization, their calibration for a young extended burst is consistent with Equation 5.4 within the scatter.

The Seyfert 2 galaxies in our sample of LIRGs lie on the correlation (NGC 3690 and IC 4518W), or have a low (less than a factor of 3) soft X-ray emission excess (MCG−03-34-064, NGC 5135, and NGC 7130). In Type 2 Seyferts the absorbing hydrogen column density toward the AGN is high and consequently most of the soft X-ray emission coming from the AGN is absorbed. Therefore we conclude that when a sufficiently powerful starburst is present it may contribute significantly to the observed soft X-ray emission. The two Seyfert 1s (NGC 7469 and NGC 7679) in our sample have a soft X-ray emission excess relative to their SFR caused by the AGN emission. Two objects (IC 860 and Zw 049.057) lie below the correlation. The low number of counts of these galaxies does not allow us to correct the soft X-ray fluxes properly for their internal absorption. In addition, the high 9.7 μm silicate absorption of these galaxies (Alonso-Herrero et al. 2011) suggests that they are highly obscured, therefore this correction is likely to be large (Shi et al. 2006).

5.5.2 Hard X-ray Emission versus SFR

The HMXBs dominate the hard X-ray (2–10 keV) emission of a starburst galaxy when there is no AGN. Consequently the hard X-ray emission is also a tracer of the SFR (Ranalli et al. 2003; Grimm et al. 2003; Persic et al. 2004; Lehmer et al. 2010).

The right panel of Figure 5.5 shows that there is a good correlation between the hard X-ray emission and the SFR when there is no AGN. The best-fit slope is 1.1±0.1 (in log-log space). Assuming a directly proportional relation between the $\mathrm{SFR_{IR+UV}}$ and the $L_{2-10\,\mathrm{keV}}$, we obtained

$$\mathrm{SFR_{IR+UV}}\,(M_\odot\ \mathrm{yr}^{-1}) = 3.9\times10^{-40} L_{2-10\,\mathrm{keV}}\,(\mathrm{erg\ s}^{-1}) \tag{5.5}$$

with a 0.27 dex scatter. In the fit we used all H II galaxies (excluding MGC+04-48-002 whose X-ray spectra resembles that of a Seyfert 2 galaxy, see Appendix 5.A) and the galaxies of the Ranalli et al. (2003) sample. This calibration agrees within the uncertainties with that of Ranalli et al. (2003). However, Lehmer et al. (2010) found a highly non-linear relation (slope = 0.76) between the SFR and the $L_{2-10\,\mathrm{keV}}$. In their fit they included high-luminosity LIRGs and ULIRGs. These galaxies are underluminous in the 2–10 keV range (see Iwasawa et al. 2009; Lehmer et al. 2010), which may affect the relation slope.

Owing to the low number of galaxies with SFR of less than $\sim4\,M_\odot\,\mathrm{yr}^{-1}$ in our sample, it is uncertain whether the correlation is still valid in the low SFR range or not. Indeed, a change in the slope of the $L_{2-10\,\mathrm{keV}}$ versus SFR relation is expected for this range (Grimm et al. 2003). For these galaxies with low SFR a bright HMXB can dominate the galaxy-integrated hard X-ray luminosity.

As can be seen in the right panel of Figure 5.5, the hard X-ray emission of three Seyfert galaxies (NGC 3690, NGC 5135, and NGC 7130) is compatible (within 2σ) with that expected from star-formation. These galaxies are known to host powerful starbursts that might dominate their energy output (González Delgado et al. 1998; Alonso-Herrero et al. 2009b; Bedregal et al. 2009; Alonso-Herrero et al. 2011). For these three galaxies high angular resolution *Chandra* images were used to isolate and quantify the AGN emission, which was found to be approximately 70 % of the total hard X-ray emission (Zezas et al. 2003; Levenson et al. 2004, 2005).

In the previous fit we neglected the contribution of the LMXBs to the hard X-ray luminosity. The emission of the LMXBs is proportional to the stellar mass of the galaxy (Gilfanov 2004), and LMXBs may be important for galaxies with the lowest SFR/M⋆ ratios. Assuming that there is a linear correlation between the 2–10 keV galaxy-integrated emission of LMXBs and HMXBs with the stellar mass and the SFR,

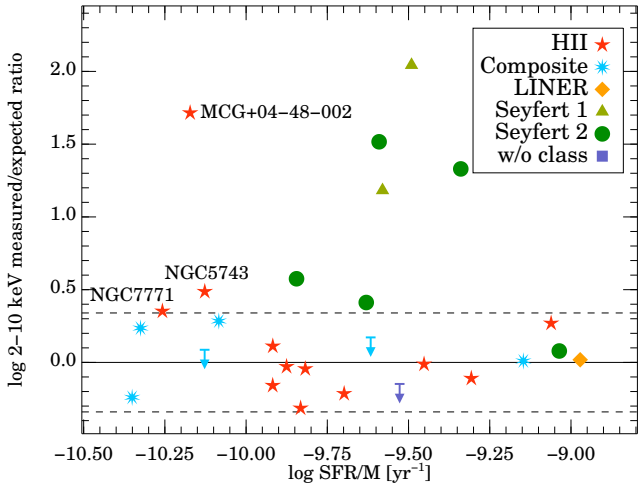

Figure 5.6: Observed/expected hard X-ray (2–10 keV) luminosity ratio vs. SFR/$M_\star$ ratio. The expected X-ray luminosity only includes the X-ray emission from LMXB and HMXB and it is based on the relation $L_{\rm X} = \alpha M_\star + \beta{\rm SFR}$ from Lehmer et al. (2010). The dashed lines indicate the scatter in this relation. Galaxy symbols are as in Figure 5.5.

respectively, Lehmer et al. (2010) constrained the relation

$$L_{2-10\,{\rm keV}} = \alpha M_\star + \beta{\rm SFR} \tag{5.6}$$

for a sample of nearby normal galaxies, LIRGs, and ULIRGs. They found $\alpha = (9.05 \pm 0.37) \times 10^{28}$ erg s^{-1} $M_\odot^{-1}$ and $\beta = (1.62 \pm 0.22) \times 10^{39}$ erg s^{-1} $(M_\odot\,{\rm yr}^{-1})^{-1}$. From this equation we estimate that the contribution of LMXBs to the integrated hard X-ray luminosity is less than 15 % for our sample of LIRGs. This is much lower than the scatter of the SFR versus hard X-ray luminosity correlation, and therefore it would not be the main cause of the observed scatter.

Figure 5.6 shows that the predicted X-ray luminosity using Equation 5.6 agrees with that observed for most of the H II galaxies in our sample of LIRGs. Likewise, most of the Seyfert galaxies have hard X-ray luminosities 10 times higher than that expected from star-formation. The three Seyferts (NGC 3690, NGC 5135, and NGC 7130) that lie within 2σ of the expected relation for star-formation are those with powerful starbursts.

5.5.3 Fe Kα Line from Star-formation

Although the Fe Kα emission line is detected mainly in active galaxies, it has been found in starbursts (e.g., M 82 and NGC 253, Cappi et al. 1999). In the latter its origin is associated with X-ray binaries and SNRs. The 6.4 keV Fe Kα line is observed in

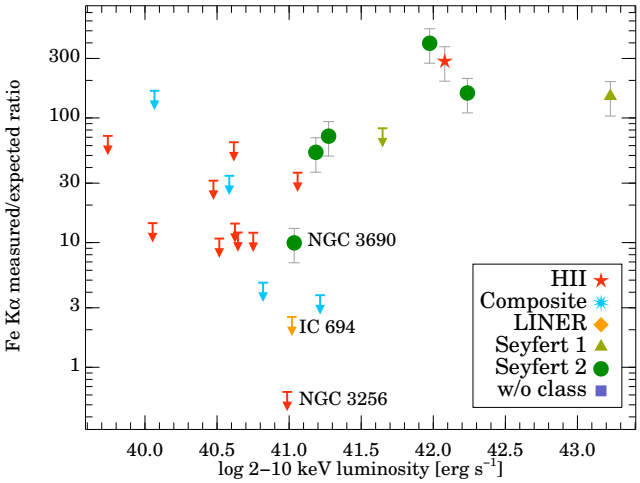

Figure 5.7: Observed/expected 6.4 keV Fe Kα luminosity from star-formation (see Section 5.5.3) vs. 2–10 keV luminosity. Galaxy symbols are as in Figure 5.5.

Galactic X-ray binaries (White et al. 1983; Torrejón et al. 2010). Using high-resolution X-ray spectroscopy, Torrejón et al. (2010) studied a sample of 41 X-ray binaries. They detected the Fe Kα line in all the HMXBs (10), but only in 10 % of the LMXB. For this reason and because the X-ray binary population in starbursts is dominated by HMXBs we only consider HMXBs in the following.

We estimated the median EW of the Fe Kα line produced in X-ray binaries using the data of Torrejón et al. (2010), EW $= 0.07 \pm 0.04$ keV. Assuming that the spectra of the HMXBs in the 2–10 keV energy range can be represented as a power-law with photon index $\Gamma = 1.2$ (Persic & Rephaeli 2002), we obtain $\log L_{\mathrm{FeK}\alpha}/L_{2-10\,\mathrm{keV}} = -2.1 \pm 0.6$. The variation of this ratio with Γ is small, less than 0.1 dex for Γ between 1 and 2.

The integrated hard X-ray luminosity, $L_{2-10\,\mathrm{keV}}$, from HMXBs is directly related to the SFR (see Lehmer et al. 2010 and Equation 5.6). Combining these relations, we obtain

$$L_{\mathrm{FeK}\alpha}^{\mathrm{HMXB}}\ (\mathrm{erg\,s^{-1}}) = (1.3 \pm 0.4) \times 10^{37}\,\mathrm{SFR}\ (M_{\odot}\,\mathrm{yr}^{-1})\,. \tag{5.7}$$

With this equation we estimated the expected flux of the 6.4 keV Fe Kα line from HMXBs. In Figure 5.7 we show the expected/observed Fe Kα emission line ratio. For all galaxies without line detection the upper limits are compatible with our flux estimation for star-formation. Because this line is correlated with the luminosity of the AGN when present, these upper limits also put an upper limit on the AGN contribution to the total energy output of the galaxy (see Section 5.6.1).

The detection of the ionized iron line at 6.7 keV in IC 694 and NCG 3256 (Table

5.3) indicates the presence of hot gas ($kT > 3\,\mathrm{keV}$) in these galaxies. Therefore their hard X-ray emission may be dominated by hot gas, as is the case in high-luminosity LIRGs and ULIRGs (Iwasawa et al. 2009, 2011; Colina et al. 2012, submitted). This is in contrast with local starbursts, where the hard X-ray emission is mostly caused by HMXBs. Figure 5.7 shows that the upper limit for the 6.4 keV line in NGC 3256 is lower than the expected value for HMXBs. This provides additional support for a noticeable contribution from hot gas to the hard X-ray emission, at least in some LIRGs.

For Seyfert galaxies the observed-to-expected Fe Kα emission ratio is higher than $\sim$50, reaching $\sim$300 in some cases. Clearly, the Fe Kα emission is dominated by the AGN in these galaxies.

5.5.4 Metal Abundances of the Thermal Plasma

The soft X-ray spectrum of starburst galaxies is dominated by the emission of a diffuse thermal plasma with temperatures in the range 0.1 to 1 keV. It is believed that it is heated by shock-fronts generated by SN explosions and stellar winds (Persic et al. 2004). Table 5.4 shows the Fe/O ratio with respect to the solar values[3] of our sample. Owing to the limited S/N ratio of the spectra we were not able to obtain the absolute abundances. The average Fe/O ratio with respect to the solar abundance is 0.5 ± 0.2. The underabundance of Fe relative to α elements has been observed in nearby starbursts (Strickland et al. 2004; Grimes et al. 2005) and local (U)LIRGs (Iwasawa et al. 2011).

Various processes have been proposed to explain these results. In the dwarf starburst galaxy NGC 1559 the α elements abundance with respect to Fe is consistent with the enhanced production of α elements in Type II SNe (Martin et al. 2002). Indeed the Fe/O ratio measured in these LIRGs is consistent with the IMF-averaged Fe relative to α elements ratio expected from Type II SNe (Gibson et al. 1997). Alternatively, Strickland et al. (2000) suggested that the X-ray emission is produced in the boundary layer between the cold interstellar medium and the SN winds, therefore the underabundance of Fe could be caused by the Fe depletion into dust grains. To distinguish between Fe depletion and enhanced α elements production in Type II SNe it is necessary to determine the abundances relatives to hydrogen and compare them with the galaxy metallicity (Strickland et al. 2004).

[3]We used the solar abundances of Anders & Grevesse (1989).

5.6 AGN Activity of LIRGs from X-ray Emission

5.6.1 Low Luminosity AGN

The Fe Kα emission line is one of the most prominent signatures of obscured AGN in the hard X-ray energy range. In Compton-thick AGN ($N_{\rm H} > 10^{24}$ cm^{-2}) the Fe Kα line at 6.4 keV has a high EW (> 1 keV; Levenson et al. 2006, see also Section 1.3.2). Fe Kα emission lines with high EW have been detected in ULIRGs, indicating that some ULIRGs (∼20–30 %) contain buried AGNs, although their X-ray emission is dominated by star formation (Ptak et al. 2003; Franceschini et al. 2003).

Table 5.3 shows the Fe Kα EW measured for our sample of LIRGs. The Fe Kα EW upper limits for 40 % of the galaxies are compatible with EW higher than 1 keV. These galaxies could host a Compton-thick AGN. However, if they do, it would not be a bright AGN. Their bolometric luminosity would be lower than 10^{43} erg s^{-1} (estimated from the upper limits of the Fe Kα emission line flux, see Section 5.6.2). That is, the AGN contribution in these galaxies would be less than 10 % of the total luminosity (IR luminosity). By comparison, for the Seyfert galaxies in the sample the AGN contribution ranges from less than 1 % to 35 % (see Section 5.6.3).

Apart from the Fe Kα emission line, the AGN continuum, absorbed or reflected (depending on the absorbing column density), might be detected in the hard X-ray (2–10 keV) range. Three of the non-Seyfert galaxies (NGC 5743, MCG+04-48-002, and NGC 7771) have hard X-ray luminosities between 5 and 100 times higher than those expected from star formation (Figure 5.6). NGC 5743 is classified as H II from optical spectroscopy, although the detection of the [Ne V] lines at 14.3 and 24.3 μm (Chapter 3) indicates that an AGN is present in this galaxy. These [Ne V] lines are also detected in the mid-infrared spectrum of MCG+04-48-002 (Pereira-Santaella et al. 2010b). The presence of an AGN in this object is also confirmed by its 20–100 keV emission (Bassani et al. 2006). In the case of NGC 7771 the nuclear activity type is H II (Alonso-Herrero et al. 2009a). The only evidence of an AGN in this galaxy is the detection of the Fe Kα line[4] and the excessively hard X-ray emission (Jenkins et al. 2005).

5.6.2 Obscured AGN

Five of the LIRGs in our sample (NGC 3690, MCG−03-34-064, NGC 5135, IC 4518W, and NGC 7130) are Seyfert 2 galaxies. In addition, the mid-IR and X-ray properties of MCG+04-48-002 suggest the presence of a bright AGN, although it is not detected

[4]In our spectral analysis of NGC 7771 we do not detect the Fe Kα line, although our upper limit is compatible with the line flux measured by Jenkins et al. (2005).

in the optical spectrum (Masetti et al. 2006). These galaxies are likely to host an obscured AGN.

We can constrain the hydrogen column density toward the AGN from their X-ray spectra for three galaxies: MCG−03-34-064, IC 4518W, and MCG+04-48-002. It is $< 10^{24}\,\mathrm{cm}^{-2}$ for all of them. Therefore, they are not Compton-thick AGN. After correcting the observed luminosity for this absorption, we obtain the intrinsic AGN X-ray luminosity (Table 5.7). These three galaxies are also detected in the *Swift*/BAT 14–195 keV all-sky survey (Tueller et al. 2010). The 14–195 keV emission is less affected by absorption than the 2–10 keV emission. Therefore it is a direct indicator of the intrinsic AGN luminosity except for the most obscured Compton-thick AGN[5] ($N_{\mathrm{H}} > 10^{26}\,\mathrm{cm}^{-2}$; e.g., Matt et al. 1997).

Using the Marconi et al. (2004) AGN template, Rigby et al. (2009) calculated that the $L_{2-10\,\mathrm{keV}}/L_{14-195\,\mathrm{keV}}$ ratio is 0.37. This ratio is between 0.77 and 0.12 for these three LIRGs and is comparable to that observed in a sample of local *Swift*/BAT selected AGNs (Figure 6 of Winter et al. 2009). MCG−03-34-064 has the highest ratio and also the steepest continuum ($\Gamma \sim 2.7$). Likewise, IC 4518W has the lowest ratio and the lowest photon index ($\Gamma \sim 1.6$). Thus the continuum slope might affect the $L_{2-10\,\mathrm{keV}}/L_{14-195\,\mathrm{keV}}$ ratio. However, the *Swift*/BAT flux contamination by nearby sources, the uncertainty in the contribution of the AGN reflected continuum to the 14–195 keV luminosity (which represents about 40 % of the total AGN emission at 30 keV, Ueda et al. 2003), and the AGN variability may be important factors that affect the observed $L_{2-10\,\mathrm{keV}}/L_{14-195\,\mathrm{keV}}$ ratio.

The other three Seyfert 2s in our LIRGs sample (NGC 3690, NGC 5135, and NGC 7130) might be Compton-thick AGN. In fact, NGC 5135 and NGC 7130 have been classified as Compton-thick based on their high Fe Kα EW (see Levenson et al. 2004, 2005). The Fe Kα EW of NGC 3690 is 0.93 keV (see Table 5.3). It is slightly less than the typical values of Compton-thick AGN (>1 keV). However, the star-formation contribution to the hard X-ray continuum is ∼30 % in NGC 3690 (see Section 5.5.2) and therefore decreases the observed EW of the Fe Kα emission line. To estimate the AGN X-ray luminosity of these objects, we used the flux of the Fe Kα emission line because it seems to be a good indicator of the intrinsic AGN luminosity (Ptak et al. 2003; Levenson et al. 2006; LaMassa et al. 2009). We assumed $L_{\mathrm{FeK}\alpha}/L^{int}_{2-10\,\mathrm{keV}} = 2 \times 10^{-3}$ (Levenson et al. 2006). However, we note that this ratio depends on both the geometry of the AGN-obscuring material and the column density in our line of sight (Liu & Wang

[5]However, owing to the angular resolution of the *Swift*-BAT survey (19.5 arcmin), the 14–195 keV fluxes can be contaminated by other nearby Seyfert galaxies (MCG−03-34-064 and MCG−03-34-063, MCG+04-48-002 and NGC 6921).

2010; Yaqoob et al. 2010; Murphy & Yaqoob 2009). Consequently a large uncertainty, a factor of ∼5, is expected in the intrinsic AGN luminosities of these galaxies.

None of these three Compton-thick candidates are detected in the *Swift*-BAT 14–195 keV survey. The 14–195 keV luminosity upper limits are slightly lower than the expected luminosity for their 2–10 keV emission. The large scatter (a factor of 6) in the $L_{14-195\,\mathrm{keV}}/L_{2-10\,\mathrm{keV}}$ ratio for the detections and the uncertainties discussed above might explain this.

The 2–10 keV and 14–195 keV luminosities are listed in Table 5.7. For completeness, the two Seyfert 1 galaxies in our sample are also included in the table.

5.6.3 AGN Contribution to the LIRGs Luminosity

We calculated the fraction of the bolometric luminosity produced by AGN in our sample of LIRGs. We used the $L_{\mathrm{IR}}(8\text{–}1000\,\mu\mathrm{m})$ as the total luminosity of the LIRGs. The AGN luminosity was estimated from the X-ray data.

There are eight active galaxies in our sample. This represents 30 % of the sample, although the AGN do not dominate the luminosity of any of them. For these galaxies we estimated the AGN luminosity from their X-ray spectral model or from their Fe Kα line luminosity (Section 5.6.2). To obtain the AGN bolometric luminosity, we applied the bolometric correction of Marconi et al. (2004). Comparing the bolometric AGN luminosity with the IR luminosity (Table 5.7), we find that the median AGN contribution is 25 % and ranges from less than 1 % to 35 % for the Seyfert LIRGs. For the rest of the sample we used the upper limit of the Fe Kα line luminosity to obtain the upper limit for the AGN luminosity (Section 5.6.1).

The AGN luminosity of the active LIRGs contributes 7 % of the total luminosity of the sample. If we also consider the upper limits of the AGN luminosity of the star-forming galaxies, the AGN contribution is < 10 %. That is, AGN contribute between 7 % and 10 % to the total energy output of our sample of local LIRGs. This is agrees with the value obtained for local LIRGs, 7–12 %, by Petric et al. (2011) and Alonso-Herrero et al. (2011) using mid-IR diagnostics.

5.7 Conclusions

We have analyzed the X-ray properties of a representative sample of 27 local LIRGs. The median $\log(L_{\mathrm{IR}}/L_{\odot})$ is 11.2, therefore the low-luminosity end of the LIRG class is well represented. The main results are as follows:

1. For most of the galaxies the soft X-ray emission (0.5–2 keV) can be associated

Table 5.7: AGN luminosity

Galaxy Name	Type	$L^{int}_{2-10\,\mathrm{keV}}$	$L_{14-195\,\mathrm{keV}}{}^{a}$	$L^{\mathrm{AGN}}_{\mathrm{bol}}$	$L_{\mathrm{IR}}/L^{\mathrm{AGN}}_{\mathrm{bol}}$
			(10^{42} erg s^{-1})		
NGC3690	Sy2	3.9^{b}	<10	55	19
MCG−03-34-064	Sy2	15	20	290	1.7
NGC5135	Sy2	10^{b}	<16	180	3.9
IC4518W	Sy2	2.2	18	26	21
MCG+04-48-002	···	6.9	38	120	3.0
NGC7130	Sy2	10^{b}	<23	180	5.1
NGC7469	Sy1	17	39	340	5.0
NGC7679	Sy1	0.4	15^{c}	4.1	120

Notes. Intrinsic AGN 2–10 keV, 14–195 keV and bolometric luminosities. We used the bolometric corrections of Marconi et al. (2004). $^{(a)}$ Observed *Swift*/BAT 14–195 keV luminosity from Tueller et al. (2010). For non-detections we assumed a flux $<3.9\times10^{-11}$ erg cm^{-2} s^{-1}, which is the 4.8 σ sensitivity achieved for 95 % of the sky in this survey. $^{(b)}$ Estimated from the 6.4 keV Fe Kα emission line luminosity using the relation $L_{\mathrm{FeK}\alpha}/L_{2-10\,\mathrm{keV}} = 2\times10^{-3}$ from Levenson et al. (2006). $^{(c)}$ The $L_{14-195\,\mathrm{keV}}$ of NGC 7679 is likely to be contaminated by the nearby Seyfert 2 NGC 7682.

to the star-formation activity. This is true even for some Seyfert 2s that host powerful starbursts and highly obscured AGN. We found a proportional correlation between the SFR (unobscured plus obscured) and the $L_{0.5-2\,\mathrm{keV}}$ (Equation 5.4). This relation is compatible with that obtained from synthesis models (Mas-Hesse et al. 2008). Only LIRGs hosting Seyfert 1 deviate significantly from this correlation.

2. We found that the hard X-ray (2–10 keV) emission of those LIRGs classified as H II like is also proportional to the SFR (Equation 5.5). This correlation is compatible with that found for nearby starbursts (Ranalli et al. 2003; Persic et al. 2004). In this relationship LIRGs hosting Seyfert nuclei (type 1 and type 2) show in general an excess of 2–10 keV emission that is clearly attributed to the AGN. However, some LIRGs hosting a Seyfert 2 nucleus and with powerful starbursts relative to their obscured AGN also lie on the correlation.

3. The soft X-ray emission can be modeled with a thermal plasma. The plasma abundance has subsolar Fe/O ratios. This can be explained by the α elements enrichment caused by Type II SNe or by the Fe depletion into dust grains. The data analyzed here do not allow us to reject any of these possibilities.

4. We did not detect the Fe Kα emission line at 6.4 keV in most (>90 %) of the H II LIRGs. Only in one H II LIRG (MCG+04-48-002) is the presence of an obscured AGN evident from the X-ray data. Therefore, we can rule out the presence of luminous obscured (or Compton-thick) AGN in these H II LIRGs. If present, the AGN contribution to the bolometric luminosity would be less than 10 %.

5. Three Seyfert LIRGs (10 %) in our sample are Compton-thick AGN candidates based on their high Fe Kα EW. The rest are Seyfert 2s (2, 7 %) with $N_{\rm H} < 10^{24}\,{\rm cm}^{-2}$ or Seyfert 1s (2, 7 %). The median AGN contribution to the bolometric luminosity of those LIRGs hosting a Seyfert nucleus is 25 %, ranging from 1 % to 35 %.

6. The AGN emission represents about 7 % of the total energy output of our sample. Taking into account the upper limits for the AGN contribution in the H II LIRGs, the total AGN contribution is between 7 % and 10 %. This agrees with the values estimated from mid-IR data (Alonso-Herrero et al. 2011; Petric et al. 2011) for complete samples of LIRGs.

5.A Notes on Individual Sources

In this appendix we discuss the X-ray spectral analysis of some galaxies with *XMM-Newton* data.

NGC 3256 It is the most luminous nearby (z<0.01) merger system. Its energy output is dominated by a powerful starburst. Previous *ASCA*, *Chandra*, and *XMM-Newton* X-ray observations of this galaxy have been analyzed in detail by Moran et al. (1999), Lira et al. (2002) and Jenkins et al. (2004), respectively. We used a simple model (absorbed *vmekal* + power-law) to fit the *XMM-Newton* spectrum. It provides an acceptable fit ($\chi^2_{\rm red} \sim 1.7$) for our analysis. Jenkins et al. (2004) tentatively detected a Fe Kα emission line at ∼6–7 keV. The higher S/N ratio data analyzed here clearly show an emission line at $6.60^{+0.10}_{-0.04}$ keV (Table 5.3). The energy of the line suggests that it is produced by ionized Fe, possibly related to supernovae activity. The upper limit for the EW of a neutral Fe Kα line at 6.4 keV is <70 eV (Table 5.3). This low EW is not compatible with that expected from a luminous Compton-thick AGN.

Arp 299 (NGC 3690 and IC 694) It is a luminous infrared ($L_{\rm IR} = 6 \times 10^{11}$ $L_\odot$) merger system. It hosts one of the most powerful starbursts in local galaxies (Alonso-Herrero et al. 2009b). The X-ray emission below 10 keV is dominated by star formation, however a Compton-thick AGN is found in the system (Della Ceca et al. 2002). The hard X-ray spectrum of the nucleus of NGC 3690 indicates that the obscured AGN is probably located there (Zezas et al. 2003). Ballo et al. (2004) detected the Fe Kα emission feature in both system components NGC 3690 and IC 694. They found that the energy of the emission line in NGC 3690 is consistent with neutral iron, but in our fit the energy of the emission line is only poorly constrained (Table 5.3). The measured 6.4 keV Fe Kα flux is ∼10 times higher than that expected from star formation suggesting the presence of an AGN in NGC 3690. The energy of the emission line in IC 694 is consistent with the Fe Kα from ionized iron that may be produced in highly ionized gas around the AGN or SN explosions (Ballo et al. 2004). For the fit we used a model consisting of an absorbed thermal plasma plus a power-law. We included a Gaussian profile to account for the Fe Kα emission lines.

MCG−03-34-064 This galaxy is classified as Seyfert 1.8. The soft X-ray spectrum is dominated by a thermal component likely produced by star formation and gas photoionized by the AGN. The AGN absorbed component dominates the spectrum in the hard X-ray range. An Fe Kα emission line is detected at 6.4 keV, consistent with neu-

tral iron. A detailed analysis of the *XMM-Newton* data of this galaxy was presented by Miniutti et al. (2007).

IC 4518W It is a Seyfert 2 galaxy. Its *XMM-Newton* and *INTEGRAL* observations are described by de Rosa et al. (2008). This is the only galaxy in the sample in which we detected two prominent emission lines in the hard X-ray spectrum, one at 6.39±0.03 keV and a weaker emission line at $7.1^{+0.1}_{-0.2}$ (Table 5.3). The former is compatible with Fe Kα emission from neutral Fe. The latter may be Fe Kα produced by highly ionized iron, Fe Kβ or these lines blended. Comastri et al. (2010) found the Fe Kβ line in some obscured AGN. However, the Fe Kβ/Fe Kα ratio from neutral iron is 0.12–0.17 (Palmeri et al. 2003) and the ratio between the 6.39 and the 7.1 keV emission lines in IC 4518W is larger (0.4). Accordingly there might be a contribution from the Fe XXVI Kα emission line.

MCG+04-48-002 This galaxy is classified as H II from optical spectroscopy, but its radio, hard X-ray emission, and mid-IR spectrum suggest the presence of an obscured AGN (Masetti et al. 2006, Chapter 3). *Suzaku* observations of this galaxy were analyzed by Winter et al. (2009). We detected an emission line at $6.47^{+0.05}_{-0.06}$ that is compatible with neutral Fe Kα. The high hydrogen column density ($N_{\rm H} = 63.2^{+10.0}_{-5.5} \times 10^{22}\,{\rm cm}^{-2}$) toward the AGN and the powerful star-formation might explain why no AGN signatures are found in its optical spectrum.

NGC 7679 is a composite Seyfert 1/starburst galaxy. It is sometimes misclassified as Seyfert 2 (see Shi et al. 2010). The hard X-ray spectrum is well reproduced by a power-law model, but we had to add a soft thermal plasma component to account for the soft X-ray excess. Della Ceca et al. (2001) reported X-ray fluxes ∼7 times higher in the soft and hard bands from the analysis of contemporaneous (1998) *ASCA* and *BeppoSax* observations of this galaxy. Previous X-ray observations of NGC 7679 are available with *Einstein* (1981) and *ROSAT* (1990). The fluxes in the 0.2–4 keV (*Einstein*) and 0.1–2.4 keV (*ROSAT*) bands are a factor of ∼2 higher than those measured in the *XMM-Newton* data (Della Ceca et al. 2001). These flux variations reflect the long-term variability of the X-ray emission of this galaxy.

Chapter 6

Conclusions and Future Work

Luminous infrared galaxies (LIRGs) and ultraluminous infrared galaxies (ULIRGs) are galaxies that emit most of their light in the infrared (IR) wavelength range. LIRGs have IR luminosities ($L_{\rm IR}$) in the range between 10^{11} and $10^{12}\,L_{\odot}$, whereas ULIRGs have $L_{\rm IR}$ larger than $10^{12}\,L_{\odot}$. They are powered by strong star-formation and/or an active galactic nucleus (AGN). Although in the local universe (U)LIRGs are not common, at high-redshift, $z \sim 1$–2, this class of galaxies dominates the star-formation rate (SFR) density of the Universe. The star formation in approximately half of the local LIRGs is distributed over few kpc scales. This is similar to high-redshift LIRGs and ULIRGs, but at odds with local ULIRGs where most of the activity is taking place in very compact regions (<1 kpc). Therefore, local LIRGs seem to be the local counterparts of high-redshift (U)LIRGs galaxies.

In this thesis we have studied the properties of a complete volume-limited sample of local LIRGs ($0.009 < z < 0.017$) using mid-IR and X-ray observations. The sample was drawn from the *IRAS* Revised Bright Galaxy Sample (RBGS; Sanders et al. 2003) and it contains 53 individual galaxies (45 *IRAS* systems). The nuclear activity classification based on optical spectroscopy shows that most of them are H II (47 %) or composite[1] systems (31 %). The rest, 22 %, of the galaxies are classified as Seyfert, 3 as Type 1 and 7 as Type 2. These fractions are similar to those of other local LIRGs samples.

As part of this thesis work, mid-IR *Spitzer* imaging and spectroscopic data, as well as X-ray data from *XMM-Newton* and *Chandra* of these local LIRGs were analyzed. Our study included the analysis of *Spitzer*/IRS spectral mapping observations from two GTO programs. In addition, X-ray data for LIRGs without bright AGNs were obtained through two *XMM-Newton* guest observer programs. We complemented our dataset with *Spitzer*, *XMM-Newton*, and *Chandra* archival data.

[1]Composite galaxies are likely to be a combination of AGN activity and star-formation.

In Chapter 3 we performed a statistical study of the mid-IR high-ionization emission lines produced by AGN and star-formation of a large sample of local galaxies, including LIRGs, observed with *Spitzer*. In Chapter 4 mid-IR spectral mapping data were used to study the resolved properties of a sample of 15 local LIRGs. In Chapter 5, we studied the star-formation and AGN X-ray emission of a representative sample of 27 local LIRGs. The main results of this thesis are summarized as follows:

Mid-IR High-ionization Emission Lines of Local Galaxies

- We confirm the tight linear correlation between the fluxes and luminosities of the high-ionization emission lines [O IV] 25.89 μm and [Ne V] 24.32 μm, which are believed to be good tracers of the AGN luminosity. This correlation spans 5 orders of magnitude ($38 < \log L_{[\mathrm{Ne\,V}]24\mu\mathrm{m}}\,(\mathrm{erg\,s^{-1}}) < 43$), ranging from LINERs, low-luminosity Seyfert galaxies, types 1 and 2, to QSOs. The typical [O IV] 25.89 μm/[Ne V] 24.32 μm ratio for AGNs is 3.5, with an rms scatter of 0.8. The correlation also holds between the [O IV] 25.89 μm and the [Ne V] 14.32 μm lines, although the scatter is larger. There is also a good linear correlation between the [Ne III] 15.56 μm and the [Ne V] 14.32 μm fluxes and luminosities for Seyfert galaxies and QSO.

- We calculate the [O IV] 25.89 μm emission due to star formation [$\log L_{[\mathrm{O\,IV}]}\ (\mathrm{erg\,s^{-1}}) < \log L_{\mathrm{IR}}\,(\mathrm{erg\,s^{-1}}) - 4.7 \pm 0.6$] and estimate that it may dominate the total [O IV] 25.89 μm emission when the intrinsic AGN luminosity is a factor of 20 smaller than the star-forming luminosity. In general, we find that the [O IV] 25.89 μm emission is dominated by the AGN in Seyfert galaxies, whereas star-formation can explain the [O IV] 25.89 μm emission of optically classified H II galaxies.

- We find that a significant number of Seyfert galaxies from the 12 μm sample (30 %) and the RSA sample (40 %) show evidence for excess [Ne III] 15.56 μm emission relative to their [O IV] 25.89 μm emission associated with star formation. The larger fraction in the RSA sample is explained because the RSA sample contains a larger fraction of low-luminosity AGNs ($L_{[\mathrm{O\,IV}]} < 10^{41}\,\mathrm{erg\,s^{-1}}$) in which these star-formation excesses are easier to detect.

- Our modeling shows that the nebular conditions in the NLRs are remarkably similar among all the AGNs in our sample. This similarity allows us to compare conditions critically in the NLRs of the type 1 and 2 galaxies. There appear to be no significant overall differences, consistent with the unified AGN model. We constrained the ionization parameter in the range $-2.8 < \log U < -2.5$ and the hydrogen column density $20 < \log n_{\mathrm{H}}\,(\mathrm{cm^{-2}}) < 21$.

The Mid-IR Emission of Local LIRGs

- We find that the PAH emission and depth of the 9.7 μm silicate feature are similar to those found in local starbursts. Indeed, these local LIRGs populate the pure starburst region in the 6.2 μm PAH EW versus strength of the 9.7 μm silicate feature diagram of Spoon et al. (2007). The silicate feature strengths, nuclear and integrated, of our sample of LIRGs are small compared to those found in ULIRGs.

- The nuclear [Ne III] 15.56 μm/[Ne II] 12.81 μm ratio is below the expected range derived by star-formation models. A possible explanation is that due to the high densities in the nuclear regions this ratio is suppressed, including the possibilities that the most massive stars are either missing or buried in ultracompact H II regions. Alternatively, the star formation rate may have decreased rapidly in all nuclei over the last 10–20 Myr (which seems contrived).

- Using the H_2 S(0) at 28.2 μm and the S(1) at 17.0 μm emission lines we estimate the mass of the warm ($T \sim 300$ K) molecular hydrogen. It ranges from 0.4 to $2.6\times10^8\,M_\odot$. This range is similar to those of ULIRGs, local starbursts, and Seyfert galaxies. In addition the similarity between the PAH and molecular hydrogen morphologies and the small variation of the PAH to H_2 emission ratio in the sample suggests that the main excitation mechanism of the latter is the UV radiation too.

The X-ray Emission of Local LIRGs

- For most of the LIRGs in our sample the soft X-ray emission (0.5–2 keV) can be associated to the star-formation activity. This is true even for some Seyfert 2s that host powerful starbursts and highly obscured AGN. We find a proportional correlation between the SFR (unobscured plus obscured) and the $L_{0.5-2\,\mathrm{keV}}$. This relation is compatible with that obtained from synthesis models (Mas-Hesse et al. 2008). Only LIRGs hosting Seyfert 1 deviate significantly from this correlation.

- We find that the hard X-ray (2–10 keV) emission of those LIRGs classified as H II like is also proportional to the SFR. This correlation is compatible with that found for nearby starbursts (Ranalli et al. 2003; Persic et al. 2004). In this relationship LIRGs hosting Seyfert nuclei (Type 1 and Type 2) show in general an excess of 2–10 keV emission clearly attributed to the AGN. However, some LIRGs hosting a Seyfert 2 nucleus and with powerful starbursts, relative to their obscured AGN, also lie on the SFR correlation.

- We do not detect the Fe Kα emission line at 6.4 keV in most (>90 %) of the H II LIRGs. Therefore, we can rule out the presence of luminous obscured (or Compton-thick) AGN in these H II LIRGs. If present, the AGN contribution to the bolometric luminosity would be less than 10 %. On the other hand, three Seyfert LIRGs in our sample (10 %) are Compton-thick ($N_{\rm H} > 10^{24}\,{\rm cm}^{-2}$) AGN candidates based on their large Fe Kα EW. The rest are Seyfert 2s (2, 7 %) with $N_{\rm H} < 10^{24}\,{\rm cm}^{-2}$ or Seyfert 1s (2, 7 %). The median AGN contribution to the bolometric luminosity of those LIRGs hosting a Seyfert nucleus is 25 %, ranging from 1 % to 35 %.

- The AGN emission represents about 7 % of the total energy output of the sample. Taking into account the upper limits for the AGN contribution in the H II LIRGs, the total AGN contribution in our sample is between 7 % and 10 %. This is in agreement with the values estimated from mid-IR data (Alonso-Herrero et al. 2011; Petric et al. 2011).

Future Work

In this thesis work we have investigated the mid-IR and X-ray emissions of local LIRGs. Although the general properties and trends of these emissions are explained, some specific and important topics require further research.

In the first place, a large part of the star-formation taking place in local LIRGs occurs in highly obscured regions, mainly in their nuclei. However, the ratio between the obscured and unobscured SFRs is not well known and the combined study of optical and infrared SFR indicators is needed.

Moreover, the precise physical conditions in the nuclear star-forming regions of LIRGs are unknown. An IMF truncated at $\sim$30 $M_{\odot}$ and/or a fraction of the most massive stars hidden in ultra-compact H II regions have been suggested as possible explanations to the observations. The study of key mid-IR spectral features such as the [Ne II] 12.81 μm emission line or the PAH bands using high angular resolution observations from ground telescopes (e.g., CanariCan mounted on the Gran Telescopio Canarias), as well as sensitive space observations with future facilities (e.g., *JWST*, *SPICA*) will help to understand how stars are formed in these relatively embedded regions.

We showed that the hard X-ray emission in our sample of local LIRGs is correlated with the SFR. Nevertheless, the exact origin of this emission is not clear. In local starbursts the hard X-ray emission is believed to be dominated by HMXBs, however

stacked X-ray observations of (U)LIRGs suggest the presence of extremely hot gas ($T > 10^7$ K) heated by SN explosions that might contribute importantly to the hard X-ray emission. Detailed analysis of deep and high angular resolution X-ray observations and comparison with multi-wavelength data of (U)LIRGs are required to determine the relative contribution of each component.

Chapter 7

Conclusiones

Las galaxias luminosas y ultraluminosas infrarrojas (LIRGS y ULIRGs) emiten la mayor parte de su luz en el infrarrojo (IR). Las LIRGs tienen luminosidades IR ($L_{\rm IR}$) entre 10^{11} y $10^{12}\,L_{\odot}$, mientras que las ULIRGs tienen $L_{\rm IR}{>}10^{12}\,L_{\odot}$. La emisión de estas galaxias procede de intensos brotes de formación estelar y/o un núcleo galáctico activo (AGN). En el universo local no son una clase común de galaxias, sin embargo, a alto desplazamiento al rojo, $z \sim 1$–2, la densidad de tasa de formación estelar del Universo está dominada por (U)LIRGs. La formación estelar en aproximadamente la mitad de las LIRGs locales está distribuida en escalas de varios kpc. Esto es similar a lo que se observa en las (U)LIRGs a alto z, pero contrario a lo que ocurre en las ULIRGs locales en las que toda la actividad tiene lugar en regiones muy compactas ($<1\,$kpc). Por lo tanto, las LIRGs locales parecen ser las homólogas locales de las (U)LIRGs a alto z.

En esta tesis hemos estudiado las propiedades de una muestra completa limitada en volumen de LIRGs locales ($0.009 < z < 0.017$) usando datos en el infrarrojo medio y rayos X. La muestra fue seleccionada a partir del catálogo "*IRAS Revised Galaxy Sample*" (Sanders et al. 2003) y contiene 53 galaxias individuales (45 sistemas *IRAS*). La clasificación de la actividad nuclear obtenida con espectroscopia óptica muestra que la mayor parte de ellas son de tipo H II (47 %) o sistemas compuestos[1] (31 %). El resto, el 22 %, se clasifican como Seyfert, 3 de Tipo 1 y 7 de Tipo 2. Estas fracciones son similares a las de otras muestras de LIRGs locales.

Como parte de este trabajo hemos analizado datos en el infrarrojo medio obtenidos con el telescopio espacial *Spitzer* y datos de rayos X obtenidos con los telescopios espaciales *XMM-Newton* y *Chandra*. En este estudio están incluidos datos de *Spitzer* procedentes de dos programas de tiempo garantizado, además de datos de *XMM-Newton* obtenidos a través de dos programas de observador invitado. Por último, com-

[1] La actividad nuclear compuesta indica, muy probablemente, una combinación de AGN y formación estelar.

plementamos nuestros datos con observaciones disponibles en los archivos de *Spitzer*, *XMM-Newton*, y *Chandra*.

En el Capítulo 3 presentamos un estudio estadístico de la emisión de las líneas de alta ionización en el infrarrojo medio producidas por formación estelar y AGNs en galaxias locales. En el Capítulo 4 usamos los mapeados espectrales obtenidos con *Spitzer* para estudiar las propiedades de la emisión infrarroja media resuelta espacialmente de una muestra de 15 LIRGs. Por último en el Capítulo 5 estudiamos la emisión de rayos X de la formación estelar y los AGNs en una muestra representativa de 27 LIRGs locales. Los resultados principales de esta tesis están resumidos a continuación:

Líneas de alta ionización en el infrarrojo medio producidas por formación estelar y AGNs

- Confirmamos la buena correlación lineal entre los flujos y luminosidades de las líneas de alta ionización [O IV] 25.89 μm y [Ne V] 24.32 μm, que se cree que trazan de forma precisa la luminosidad de los AGN. Esta correlación se extiende 5 órdenes de magnitud [$38 < \log L_{[\mathrm{Ne\,V}]24\mu\mathrm{m}}\,(\mathrm{erg\,s^{-1}}) < 43$], por lo que incluye desde LINERs y galaxias Seyfert de baja luminosidad, de tipos 1 y 2, hasta cuásares. El cociente típico de [O IV] 25.89 μm/[Ne V] 24.32 μm para los AGNs es 3.5, con una dispersión de 0.8. Igualmente existe una correlación entre las líneas de [O IV] 25.89 μm y [Ne V] 14.32 μm, aunque la dispersión es mayor. También hay una buena correlación lineal entre la emisión de [Ne III] 15.56 μm y [Ne V] 14.32 μm para las galaxias de tipo Seyfert y cuásares.

- Calculamos que la emisión de [O IV] 25.89 μm producida por formación estelar es $\log L_{[\mathrm{O\,IV}]}\ (\mathrm{erg\,s^{-1}}) < \log L_{\mathrm{IR}}\,(\mathrm{erg\,s^{-1}}) - 4.7 \pm 0.6$, y estimamos que ésta puede dominar la emisión total de [O IV] 25.89 μm cuando la luminosidad intrínseca del AGN es 20 veces menor que la luminosidad total producida por la formación estelar. En general, encontramos que la emisión de [O IV] 25.89 μm está dominada por el AGN en galaxias de tipo Seyfert, mientras que la formación estelar puede explicar la emisión de [O IV] 25.89 μm en las galaxias clasificadas como H II.

- Encontramos que un numero significativo de galaxias de tipo Seyfert de las muestras de 12 μm (30 %) y RSA (40 %) tienen un exceso de emisión de [Ne III] 15.56 μm respecto a la que se espera de acuerdo a su emisión de [O IV] 25.89 μm. Este exceso estaría asociado a formación estelar. La mayor fracción de galaxias con este exceso en la muestra RSA es debida a que esta muestra contiene un mayor número de AGNs de baja luminosidad ($L_{[\mathrm{O\,IV}]} < 10^{41}\,\mathrm{erg\,s^{-1}}$) en los que este exceso de emisión es más fácil de detectar.

- Nuestro modelado de las condiciones del gas en la región de líneas estrechas muestra que estas condiciones son sorprendentemente similares entre todos los AGNs de nuestra muestra. Esta semejanza nos permite comparar las condiciones en los AGNs de tipo 1 y 2, que no muestran diferencias significativas, como se espera según el modelo unificado de AGN. Los parámetros obtenidos en el modelado son: parámetro de ionización $-2.8 < \log U < -2.5$ y densidad de columna de hidrógeno $20 < \log n_{\rm H}\,({\rm cm}^{-2}) < 21$.

La emisión infrarroja media de las LIRGs locales

- Encontramos que la emisión de los PAH y la profundidad de los silicatos a 9.7 μm en nuestra muestra de LIRGs es similar a lo que se observa en galaxias locales con brotes de formación estelar. De hecho, estas LIRGs ocupan la región de galaxias con formación estelar pura en el diagrama de Spoon et al. (2007) de la anchura equivalente del PAH a 6.2 μm frente a la profundidad de los silicatos. La profundidad de los silicatos medida en los espectros nucleares e integrados en nuestra muestra de LIRGs es pequeña comparada con las que se miden en ULIRGs locales.

- El cociente entre la emisión nuclear de [Ne III] 15.56 μm y [Ne II] 12.81 μm es menor que el predicho por los modelos de formación estelar. Una posible explicación es que las altas densidades en los núcleos de las LIRGs disminuyen este cociente. Esto incluye la posibilidad de que falten las estrellas más masivas o bien estén ocultas en regiones H II ultracompactas. Otra posibilidad es que la formación estelar haya decrecido rápidamente en todos los núcleos en los últimos 10–20 Myr, lo cual parece artificioso.

- Hemos usando las líneas de H_2 S(0) a 28.2 μm y S(1) a 17.0 μm para estimar la masa de gas molecular templado ($T \sim 300$ K). Obtenemos que esta masa está entre 0.4 y $2.6{\times}10^8\,M_\odot$ en nuestra muestra de LIRGs. Este rango de masas es similar al que se observa en ULIRGs locales y galaxias locales con brotes de formación estelar. El parecido entre las morfologías de la emisión de H_2 y la de los PAH, además de la pequeña variación en el cociente entre la emisión de los PAH y el H_2 sugiere que el principal mecanismo de excitación del H_2 templado en nuestra muestra de LIRGs locales es también la radiación UV.

La emisión de rayos X de las LIRGs locales

- En la mayoría de las LIRGs de nuestra muestra la emisión de rayos X blandos (0.5–2 keV) se puede asociar a la formación estelar. Esto también ocurre en algunas galaxias de tipo Seyfert 2 que contienen intensos brotes de formación

estelar y AGNs muy oscurecidos. Encontramos que existe una relación de proporcionalidad entre la tasa de formación estelar (oscurecida más no oscurecida) y la $L_{0.5-2\,\mathrm{keV}}$. Esta relación es compatible con lo que se obtiene con modelos de síntesis (Mas-Hesse et al. 2008). Solamente las LIRGs que contienen un AGN de tipo 1 se desvían de forma considerable de la correlación.

- De la misma manera encontramos que la emisión de rayos X duros (2–10 keV) de las LIRGs de tipo H II es proporcional a la tasa de formación estelar. Esta correlación es compatible con la que se encuentra en galaxias locales con brotes de formación estelar (Ranalli et al. 2003; Persic et al. 2004). En esta relación las LIRGs que contienen AGNs de tipo 1 y 2 tienen, en general, un exceso de emisión de rayos X duros claramente producidos por el AGN. Sin embargo, algunas LIRGs con AGNs de tipo 2 e intensos brotes de formación estelar, no se desvían de la correlación.

- No detectamos la línea de Fe Kα a 6.4 keV en la gran mayoría (>90 %) de las LIRGs de tipo H II. Por lo tanto, podemos descartar la presencia de un AGN luminoso muy oscurecido en estas galaxias. Si estuviera presente, su contribución a la luminosidad bolométrica de la galaxia sería menor del 10 %. Por otra parte, podemos decir que 3 LIRGs de tipo Seyfert 2 de nuestra muestra (10 %) son candidatos a tener $N_{\mathrm{H}} > 10^{24}\,\mathrm{cm}^{-2}$ (*Compton-thick*) basándonos en la gran anchura equivalente de la línea Fe Kα. El resto son Seyfert de tipo 2 (2, 7 %) con $N_{\mathrm{H}} < 10^{24}\,\mathrm{cm}^{-2}$ o de tipo 1 (2, 7 %). La contribución mediana del AGN a la luminosidad bolométrica de las LIRGs de tipo Seyfert es un 25 %, aunque varía entre un 1 % y un 35 %.

- La emisión de los AGNs representa alrededor de un 7 % de la energía total emitida por las galaxias de nuestra muestra. Teniendo en cuenta los límites superiores para las LIRGs de tipo H II, tenemos que la contribución a la luminosidad total de nuestra muestra de LIRGs locales debida a los AGNs está entre un 7 % y un 10 %. Este valor está de acuerdo con las estimaciones obtenidas a partir de observaciones en el infrarrojo medio (Alonso-Herrero et al. 2011; Petric et al. 2011).

Publications

Referred Publications

1. *Local Luminous Infrared Galaxies. II. AGN Activity from Spitzer/IRS Spectra*
   Alonso-Herrero, A., **Pereira-Santaella, M.**, Rieke, G. H., & Rigopoulou, D. 2011, ApJ, in press, arXiv:1109.1372

2. *The X-ray Emission of Local Luminous Infrared Galaxies*
   Pereira-Santaella, M., Alonso-Herrero, A., Santos-Lleo, M., Colina, L., Jiménez-Bailón, E., Longinotti, A. L., Rieke, G. H., Ward, M., & Esquej, P. 2011, A&A, in press, arXiv:1109.0921

3. *The starburst-AGN connection of Mrk 938: an infrared and X-ray view*
   Esquej, P., Alonso-Herrero, A., Pérez-García, A. M., **Pereira-Santaella, M.**, et al. 2011, MNRAS, submitted

4. *Star formation laws in Luminous Infrared Galaxies: New observational constraints on models*
   García-Burillo, S., Usero, A., Alonso-Herrero, A., Graciá-Carpio, J., **Pereira-Santaella, M.**, Colina, L., Planesas, P., & Arribas, S. 2011, A&A, submitted

5. *Spatially Resolved [Fe II] Emission in NGC 5135. Clues for Understanding the Origin of the Hard X-rays in Luminous Infrared Galaxies*
   Colina, L., **Pereira-Santaella, M.**, Alonso-Herrero, A., Bedregal, A., & Arribas, S. 2011, ApJ, submitted

6. *The Mid-infrared High-ionization Lines from Active Galactic Nuclei and Star-forming Galaxies*
   Pereira-Santaella, M., Diamond-Stanic, A. M., Alonso-Herrero, A., & Rieke, G. H. 2010, ApJ, 725, 2270

7. *Local Luminous Infrared Galaxies. I. Spatially Resolved Observations with the Spitzer Infrared Spectrograph*
   Pereira-Santaella, M., Alonso-Herrero, A., Rieke, G. H., Colina, L., Díaz-Santos, T., Smith, J.-D. T., Pérez-González, P. G., & Engelbracht, C. W. 2010, ApJS, 188, 447

8. *A High Spatial Resolution Mid-Infrared Spectroscopic Study of the Nuclei and Star-Forming Regions in Luminous Infrared Galaxies*
   Díaz-Santos, T., Alonso-Herrero, A., Colina, L., Packham, C., Levenson, N. A., **Pereira-Santaella, M.**, Roche, P. F., & Telesco, C. M. 2010, ApJ, 711, 328

9. *Local luminous infrared galaxies: Spatially resolved mid-infrared observations with Spitzer/IRS*
   Alonso-Herrero, A., **Pereira-Santaella, M.**, Rieke, G. H., Colina, L., Engelbracht, C. W., Pérez-González, P. G., Díaz-Santos, T., & Smith, J.-D. T. 2010, Advances in Space Research, 45, 99

10. *The Extreme Star Formation Activity of Arp 299 Revealed by Spitzer IRS Spectral Mapping*
    Alonso-Herrero, A., Rieke, G. H., Colina, L., **Pereira-Santaella, M.**, García-Marín, M., Smith, J.-D. T., Brandl, B., Charmandaris, V., & Armus, L. 2009, ApJ, 697, 660

References

Aalto, S., Radford, S. J. E., Scoville, N. Z., & Sargent, A. I. 1997, ApJ, 475, L107+

Allamandola, L. J., Tielens, A. G. G. M., & Barker, J. R. 1989, ApJS, 71, 733

Allen, M. G., Groves, B. A., Dopita, M. A., Sutherland, R. S., & Kewley, L. J. 2008, ApJS, 178, 20

Alonso-Herrero, A., García-Marín, M., Monreal-Ibero, A., et al. 2009a, A&A, 506, 1541

Alonso-Herrero, A., Pereira-Santaella, M., Rieke, G. H., & Rigopoulou, D. 2011, ApJ, arXiv:1109.1372

Alonso-Herrero, A., Quillen, A. C., Rieke, G. H., Ivanov, V. D., & Efstathiou, A. 2003, AJ, 126, 81

Alonso-Herrero, A., Rieke, G. H., Colina, L., et al. 2009b, ApJ, 697, 660

Alonso-Herrero, A., Rieke, G. H., Rieke, M. J., et al. 2006, ApJ, 650, 835

Alonso-Herrero, A., Rieke, G. H., Rieke, M. J., & Scoville, N. Z. 2000, ApJ, 532, 845

Amram, P., Marcelin, M., Balkowski, C., et al. 1994, A&AS, 103, 5

Anders, E. & Grevesse, N. 1989, Geochim. Cosmochim. Acta, 53, 197

Antonucci, R. 1993, ARA&A, 31, 473

Appleton, P. N., Xu, K. C., Reach, W., et al. 2006, ApJ, 639, L51

Armus, L., Bernard-Salas, J., Spoon, H. W. W., et al. 2006, ApJ, 640, 204

Armus, L., Charmandaris, V., Bernard-Salas, J., et al. 2007, ApJ, 656, 148

Armus, L., Charmandaris, V., Spoon, H. W. W., et al. 2004, ApJS, 154, 178

Armus, L., Mazzarella, J. M., Evans, A. S., et al. 2009, PASP, 121, 559

Augarde, R. & Lequeux, J. 1985, A&A, 147, 273

Baan, W. A., Salzer, J. J., & Lewinter, R. D. 1998, ApJ, 509, 633

Baldwin, J. A., Phillips, M. M., & Terlevich, R. 1981, PASP, 93, 5

Ballo, L., Braito, V., Della Ceca, R., et al. 2004, ApJ, 600, 634

Barnes, J. E. & Hernquist, L. 1996, ApJ, 471, 115

Baskin, A. & Laor, A. 2005, MNRAS, 358, 1043

Bassani, L., Molina, M., Malizia, A., et al. 2006, ApJ, 636, L65

Baum, S. A., Gallimore, J. F., O'Dea, C. P., et al. 2010, ApJ, 710, 289

Bedregal, A. G., Colina, L., Alonso-Herrero, A., & Arribas, S. 2009, ApJ, 698, 1852

Beirão, P., Brandl, B. R., Appleton, P. N., et al. 2008, ApJ, 676, 304

Beirão, P., Brandl, B. R., Devost, D., et al. 2006, ApJ, 643, L1

Bell, E. F. & de Jong, R. S. 2001, ApJ, 550, 212

Bernard-Salas, J., Spoon, H. W. W., Charmandaris, V., et al. 2009, ApJS, 184, 230

Black, J. H. & van Dishoeck, E. F. 1987, ApJ, 322, 412

Blustin, A. J., Branduardi-Raymont, G., Behar, E., et al. 2003, A&A, 403, 481

Brandl, B. R., Bernard-Salas, J., Spoon, H. W. W., et al. 2006, ApJ, 653, 1129

Buat, V., Takeuchi, T. T., Iglesias-Páramo, J., et al. 2007, ApJS, 173, 404

Buchanan, C. L., Gallimore, J. F., O'Dea, C. P., et al. 2006, AJ, 132, 401

Burton, M. G., Hollenbach, D. J., & Tielens, A. G. G. 1992, ApJ, 399, 563

Calzetti, D., Kennicutt, R. C., Engelbracht, C. W., et al. 2007, ApJ, 666, 870

Cappi, M., Persic, M., Bassani, L., et al. 1999, A&A, 350, 777

Caputi, K. I., Lagache, G., Yan, L., et al. 2007, ApJ, 660, 97

Casoli, F., Willaime, M., Viallefond, F., & Gerin, M. 1999, A&A, 346, 663

Chapman, N. L., Mundy, L. G., Lai, S., & Evans, N. J. 2009, ApJ, 690, 496

Charmandaris, V., Stacey, G. J., & Gull, G. 2002, ApJ, 571, 282

Chiar, J. E. & Tielens, A. G. G. M. 2006, ApJ, 637, 774

Clements, D. L., Sutherland, W. J., McMahon, R. G., & Saunders, W. 1996, MNRAS, 279, 477

Colbert, E. J. M., Heckman, T. M., Ptak, A. F., Strickland, D. K., & Weaver, K. A. 2004, ApJ, 602, 231

Colina, L., Pereira-Santaella, M., Alonso-Herrero, A., Bedregal, A. G., & Arribas, S. 2012, submitted, ApJ

Comastri, A. 2004, in Astrophysics and Space Science Library, Vol. 308, Supermassive Black Holes in the Distant Universe, ed. A. J. Barger, 245–+

Comastri, A., Iwasawa, K., Gilli, R., et al. 2010, ApJ, 717, 787

Corbett, E. A., Kewley, L., Appleton, P. N., et al. 2003, ApJ, 583, 670

Crenshaw, D. M., Kraemer, S. B., & George, I. M. 2003, ARA&A, 41, 117

Crowther, P. A., Beck, S. C., Willis, A. J., et al. 1999, MNRAS, 304, 654

Daddi, E., Dickinson, M., Morrison, G., et al. 2007, ApJ, 670, 156

Dale, D. A., Smith, J. D. T., Armus, L., et al. 2006, ApJ, 646, 161

Dale, D. A., Smith, J. D. T., Schlawin, E. A., et al. 2009, ApJ, 693, 1821

de Rosa, A., Bassani, L., Ubertini, P., et al. 2008, A&A, 483, 749

Della Ceca, R., Ballo, L., Tavecchio, F., et al. 2002, ApJ, 581, L9

Della Ceca, R., Pellegrini, S., Bassani, L., et al. 2001, A&A, 375, 781

Deo, R. P., Crenshaw, D. M., Kraemer, S. B., et al. 2007, ApJ, 671, 124

Devost, D., Brandl, B. R., Armus, L., et al. 2004, ApJS, 154, 242

Diamond-Stanic, A. M. & Rieke, G. H. 2010, ApJ, 724, 140

Diamond-Stanic, A. M., Rieke, G. H., & Rigby, J. R. 2009, ApJ, 698, 623

Díaz-Santos, T., Alonso-Herrero, A., Colina, L., et al. 2010, ApJ, 711, 328

Díaz-Santos, T., Alonso-Herrero, A., Colina, L., et al. 2008, ApJ, 685, 211

Dopita, M. A., Fischera, J., Sutherland, R. S., et al. 2006, ApJS, 167, 177

Dopita, M. A., Pereira, M., Kewley, L. J., & Capaccioli, M. 2002, ApJS, 143, 47

Draine, B. T. 2003, ARA&A, 41, 241

Draine, B. T. & Li, A. 2001, ApJ, 551, 807

Dudik, R. P., Satyapal, S., & Marcu, D. 2009, ApJ, 691, 1501

Dudik, R. P., Weingartner, J. C., Satyapal, S., et al. 2007, ApJ, 664, 71

Engelbracht, C. W., Rieke, G. H., Gordon, K. D., et al. 2008, ApJ, 678, 804

Fabbiano, G. 2006, ARA&A, 44, 323

Farrah, D., Bernard-Salas, J., Spoon, H. W. W., et al. 2007, ApJ, 667, 149

Farrah, D., Lonsdale, C. J., Weedman, D. W., et al. 2008, ApJ, 677, 957

Fazio, G. G., Hora, J. L., Allen, L. E., et al. 2004, ApJS, 154, 10

Ferrière, K. M. 2001, Reviews of Modern Physics, 73, 1031

Fitzpatrick, E. L. 1999, PASP, 111, 63

Flaherty, K. M., Pipher, J. L., Megeath, S. T., et al. 2007, ApJ, 663, 1069

Franceschini, A., Aussel, H., Cesarsky, C. J., Elbaz, D., & Fadda, D. 2001, A&A, 378, 1

Franceschini, A., Braito, V., Persic, M., et al. 2003, MNRAS, 343, 1181

Galliano, F. 2006, arXiv:astro-ph/0610852

Galliano, F., Dwek, E., & Chanial, P. 2008a, ApJ, 672, 214

Galliano, F., Madden, S. C., Tielens, A. G. G. M., Peeters, E., & Jones, A. P. 2008b, ApJ, 679, 310

García-Marín, M., Colina, L., Arribas, S., Alonso-Herrero, A., & Mediavilla, E. 2006, ApJ, 650, 850

Genzel, R., Lutz, D., Sturm, E., et al. 1998, ApJ, 498, 579

Gibson, B. K., Loewenstein, M., & Mushotzky, R. F. 1997, MNRAS, 290, 623

Gil de Paz, A., Boissier, S., Madore, B. F., et al. 2007, ApJS, 173, 185

Gilfanov, M. 2004, MNRAS, 349, 146

Giveon, U., Sternberg, A., Lutz, D., Feuchtgruber, H., & Pauldrach, A. W. A. 2002, ApJ, 566, 880

González Delgado, R. M., Heckman, T., Leitherer, C., et al. 1998, ApJ, 505, 174

Gordon, K. D., Engelbracht, C. W., Rieke, G. H., et al. 2008, ApJ, 682, 336

Gorjian, V., Cleary, K., Werner, M. W., & Lawrence, C. R. 2007, ApJ, 655, L73

Goto, T., Arnouts, S., Malkan, M., et al. 2011, MNRAS, 811

Goulding, A. D. & Alexander, D. M. 2009, MNRAS, 398, 1165

Grimes, J. P., Heckman, T., Strickland, D., & Ptak, A. 2005, ApJ, 628, 187

Grimm, H., Gilfanov, M., & Sunyaev, R. 2003, MNRAS, 339, 793

Groves, B., Dopita, M., & Sutherland, R. 2006, A&A, 458, 405

Groves, B. A., Dopita, M. A., & Sutherland, R. S. 2004a, ApJS, 153, 9

Groves, B. A., Dopita, M. A., & Sutherland, R. S. 2004b, ApJS, 153, 75

Güver, T. & Özel, F. 2009, MNRAS, 400, 2050

Habart, E., Boulanger, F., Verstraete, L., et al. 2003, A&A, 397, 623

Hao, L., Weedman, D. W., Spoon, H. W. W., et al. 2007, ApJ, 655, L77

Harper, Jr., D. A. & Low, F. J. 1973, ApJ, 182, L89+

Hattori, T., Yoshida, M., Ohtani, H., et al. 2004, AJ, 127, 736

Helou, G., Lu, N. Y., Werner, M. W., Malhotra, S., & Silbermann, N. 2000, ApJ, 532, L21

Helou, G. & Walker, D. W., eds. 1988, Infrared astronomical satellite (IRAS) catalogs and atlases. Volume 7: The small scale structure catalog, Vol. 7

Higdon, S. J. U., Armus, L., Higdon, J. L., Soifer, B. T., & Spoon, H. W. W. 2006, ApJ, 648, 323

Ho, L. C., Filippenko, A. V., & Sargent, W. L. W. 1997, ApJS, 112, 315

Ho, L. C. & Keto, E. 2007, ApJ, 658, 314

Hollenbach, D. & McKee, C. F. 1989, ApJ, 342, 306

Houck, J. R., Roellig, T. L., van Cleve, J., et al. 2004, ApJS, 154, 18

Houck, J. R., Schneider, D. P., Danielson, G. E., et al. 1985, ApJ, 290, L5

Houck, J. R., Weedman, D. W., Le Floc'h, E., & Hao, L. 2007, ApJ, 671, 323

Howell, J. H., Armus, L., Mazzarella, J. M., et al. 2010, ApJ, 715, 572

Imanishi, M., Dudley, C. C., Maiolino, R., et al. 2007, ApJS, 171, 72

Imanishi, M. & Wada, K. 2004, ApJ, 617, 214

Iwasawa, K., Sanders, D. B., Evans, A. S., et al. 2009, ApJ, 695, L103

Iwasawa, K., Sanders, D. B., Teng, S. H., et al. 2011, A&A, 529, A106+

Jarrett, T. H., Chester, T., Cutri, R., et al. 2000, AJ, 119, 2498

Jarrett, T. H., Chester, T., Cutri, R., Schneider, S. E., & Huchra, J. P. 2003, AJ, 125, 525

Jenkins, L. P., Roberts, T. P., Ward, M. J., & Zezas, A. 2004, MNRAS, 352, 1335

Jenkins, L. P., Roberts, T. P., Ward, M. J., & Zezas, A. 2005, MNRAS, 357, 109

Jiang, B. W., Gao, J., Omont, A., Schuller, F., & Simon, G. 2006, A&A, 446, 551

Jiménez-Bailón, E., Piconcelli, E., Guainazzi, M., et al. 2005, A&A, 435, 449

Jiménez-Bailón, E., Santos-Lleó, M., Mas-Hesse, J. M., et al. 2003, ApJ, 593, 127

Jones, D. H., Read, M. A., Saunders, W., et al. 2009, MNRAS, 399, 683

Jones, D. H., Saunders, W., Colless, M., et al. 2004, MNRAS, 355, 747

Kalberla, P. M. W., Burton, W. B., Hartmann, D., et al. 2005, A&A, 440, 775

Kauffmann, G., Heckman, T. M., Tremonti, C., et al. 2003, MNRAS, 346, 1055

Kennicutt, R. C., Hao, C., Calzetti, D., et al. 2009, ApJ, 703, 1672

Kennicutt, Jr., R. C. 1998, ARA&A, 36, 189

Kessler, M. F., Steinz, J. A., Anderegg, M. E., et al. 1996, A&A, 315, L27

Kewley, L. J., Groves, B., Kauffmann, G., & Heckman, T. 2006, MNRAS, 372, 961

Kewley, L. J., Heisler, C. A., Dopita, M. A., & Lumsden, S. 2001, ApJS, 132, 37

Kim, D., Sanders, D. B., Veilleux, S., Mazzarella, J. M., & Soifer, B. T. 1995, ApJS, 98, 129

Kim, D., Veilleux, S., & Sanders, D. B. 1998, ApJ, 508, 627

Kim, D.-C. & Sanders, D. B. 1998, ApJS, 119, 41

Kleinmann, D. E. & Low, F. J. 1970, ApJ, 159, L165+

Kollatschny, W., Kotulla, R., Pietsch, W., Bischoff, K., & Zetzl, M. 2008, A&A, 484, 897

Kóspál, Á., Ábrahám, P., Apai, D., et al. 2008, MNRAS, 383, 1015

Kraemer, S. B., Turner, T. J., Crenshaw, D. M., & George, I. M. 1999, ApJ, 519, 69

Krist, J. 2002, *Tiny Tim/SIRTF User's Guide* (Pasadena, SSC)

Kroupa, P. 2001, MNRAS, 322, 231

Lagache, G., Puget, J.-L., & Dole, H. 2005, ARA&A, 43, 727

Lahuis, F., Spoon, H. W. W., Tielens, A. G. G. M., et al. 2007, ApJ, 659, 296

LaMassa, S. M., Heckman, T. M., Ptak, A., et al. 2009, ApJ, 705, 568

Larson, R. B. & Tinsley, B. M. 1978, ApJ, 219, 46

Le Floc'h, E., Papovich, C., Dole, H., et al. 2005, ApJ, 632, 169

Lee, J. C., Hwang, H. S., Lee, M. G., Kim, M., & Kim, S. C. 2011, MNRAS, 414, 702

Lehmer, B. D., Alexander, D. M., Bauer, F. E., et al. 2010, ApJ, 724, 559

Lepp, S. & McCray, R. 1983, ApJ, 269, 560

Levenson, N. A., Heckman, T. M., Krolik, J. H., Weaver, K. A., & Życki, P. T. 2006, ApJ, 648, 111

Levenson, N. A., Sirocky, M. M., Hao, L., et al. 2007, ApJ, 654, L45

Levenson, N. A., Weaver, K. A., Heckman, T. M., Awaki, H., & Terashima, Y. 2004, ApJ, 602, 135

Levenson, N. A., Weaver, K. A., Heckman, T. M., Awaki, H., & Terashima, Y. 2005, ApJ, 618, 167

Liedahl, D. A. & Paerels, F. 1996, ApJ, 468, L33+

Lípari, S., Díaz, R., Taniguchi, Y., et al. 2000, AJ, 120, 645

Lira, P., Ward, M., Zezas, A., Alonso-Herrero, A., & Ueno, S. 2002, MNRAS, 330, 259

Liu, T. & Wang, J.-X. 2010, ApJ, 725, 2381

Lu, N., Helou, G., Werner, M. W., et al. 2003, ApJ, 588, 199

Lutz, D., Kunze, D., Spoon, H. W. W., & Thornley, M. D. 1998a, A&A, 333, L75

Lutz, D., Spoon, H. W. W., Rigopoulou, D., Moorwood, A. F. M., & Genzel, R. 1998b, ApJ, 505, L103

Maiolino, R. & Rieke, G. H. 1995, ApJ, 454, 95

Maiolino, R., Ruiz, M., Rieke, G. H., & Keller, L. D. 1995, ApJ, 446, 561

Maloney, P. R., Hollenbach, D. J., & Tielens, A. G. G. M. 1996, ApJ, 466, 561

Marconi, A., Risaliti, G., Gilli, R., et al. 2004, MNRAS, 351, 169

Markwardt, C. B. 2009, in Astronomical Society of the Pacific Conference Series, Vol. 411, Astronomical Society of the Pacific Conference Series, ed. D. A. Bohlender, D. Durand, & P. Dowler, 251–+

Martin, C. L., Kobulnicky, H. A., & Heckman, T. M. 2002, ApJ, 574, 663

Mas-Hesse, J. M., Otí-Floranes, H., & Cerviño, M. 2008, A&A, 483, 71

Masetti, N., Bassani, L., Bazzano, A., et al. 2006, A&A, 455, 11

Matt, G., Guainazzi, M., Frontera, F., et al. 1997, A&A, 325, L13

McClure, M. 2009, ApJ, 693, L81

Meléndez, M., Kraemer, S. B., Armentrout, B. K., et al. 2008a, ApJ, 682, 94

Meléndez, M., Kraemer, S. B., Schmitt, H. R., et al. 2008b, ApJ, 689, 95

Melnick, J. & Mirabel, I. F. 1990, A&A, 231, L19

Menéndez-Delmestre, K., Blain, A. W., Smail, I., et al. 2009, ApJ, 699, 667

Miniutti, G., Ponti, G., Dadina, M., Cappi, M., & Malaguti, G. 2007, MNRAS, 375, 227

Moran, E. C., Lehnert, M. D., & Helfand, D. J. 1999, ApJ, 526, 649

Murphy, K. D. & Yaqoob, T. 2009, MNRAS, 397, 1549

Murphy, Jr., T. W., Armus, L., Matthews, K., et al. 1996, AJ, 111, 1025

Naab, T. & Burkert, A. 2003, ApJ, 597, 893

Nagao, T., Murayama, T., & Taniguchi, Y. 2001, ApJ, 546, 744

Nardini, E. & Risaliti, G. 2011, MNRAS, 415, 619

Nardini, E., Risaliti, G., Salvati, M., et al. 2008, MNRAS, 385, L130

Nardini, E., Risaliti, G., Watabe, Y., Salvati, M., & Sani, E. 2010, MNRAS, 405, 2505

Nenkova, M., Sirocky, M. M., Nikutta, R., Ivezić, Ž., & Elitzur, M. 2008, ApJ, 685, 160

Neugebauer, G., Becklin, E. E., Oke, J. B., & Searle, L. 1976, ApJ, 205, 29

Neugebauer, G., Habing, H. J., van Duinen, R., et al. 1984, ApJ, 278, L1

Nordgren, T. E., Chengalur, J. N., Salpeter, E. E., & Terzian, Y. 1997, AJ, 114, 77

Ogle, P., Whysong, D., & Antonucci, R. 2006, ApJ, 647, 161

Oliva, E., Moorwood, A. F. M., Drapatz, S., Lutz, D., & Sturm, E. 1999, A&A, 343, 943

Oliver, S. J., Rowan-Robinson, M., Broadhurst, T. J., et al. 1996, MNRAS, 280, 673

Osterbrock, D. E. & Ferland, G. J. 2006, Astrophysics of gaseous nebulae and active galactic nuclei, ed. D. E. Osterbrock & G. J. Ferland

Palmeri, P., Mendoza, C., Kallman, T. R., Bautista, M. A., & Meléndez, M. 2003, A&A, 410, 359

Parra, R., Conway, J. E., Aalto, S., et al. 2010, ApJ, 720, 555

Peeters, E., Allamandola, L. J., Hudgins, D. M., Hony, S., & Tielens, A. G. G. M. 2004a, in Astronomical Society of the Pacific Conference Series, Vol. 309, Astrophysics of Dust, ed. A. N. Witt, G. C. Clayton, & B. T. Draine, 141–+

Peeters, E., Spoon, H. W. W., & Tielens, A. G. G. M. 2004b, ApJ, 613, 986

Pereira-Santaella, M., Alonso-Herrero, A., Rieke, G. H., et al. 2010a, ApJS, 188, 447

Pereira-Santaella, M., Alonso-Herrero, A., Santos-Lleo, M., et al. 2011, A&A, arXiv:1109.0921

Pereira-Santaella, M., Diamond-Stanic, A. M., Alonso-Herrero, A., & Rieke, G. H. 2010b, ApJ, 725, 2270

Pérez-González, P. G., Kennicutt, Jr., R. C., Gordon, K. D., et al. 2006, ApJ, 648, 987

Pérez-González, P. G., Rieke, G. H., Egami, E., et al. 2005, ApJ, 630, 82

Perez-Olea, D. E. & Colina, L. 1996, ApJ, 468, 191

Persic, M. & Rephaeli, Y. 2002, A&A, 382, 843

Persic, M. & Rephaeli, Y. 2003, A&A, 399, 9

Persic, M., Rephaeli, Y., Braito, V., et al. 2004, A&A, 419, 849

Petric, A. O., Armus, L., Howell, J., et al. 2011, ApJ, 730, 28

Piconcelli, E., Jimenez-Bailón, E., Guainazzi, M., et al. 2004, MNRAS, 351, 161

Pilbratt, G. L., Riedinger, J. R., Passvogel, T., et al. 2010, A&A, 518, L1+

Pope, A., Chary, R.-R., Dickinson, M., & Scott, D. 2007, in Astronomical Society of the Pacific Conference Series, Vol. 380, Deepest Astronomical Surveys, ed. J. Afonso, H. C. Ferguson, B. Mobasher, & R. Norris, 387–+

Pottasch, S. R., Surendiranath, R., Bernard-Salas, J., & Roellig, T. L. 2009, A&A, 502, 189

Ptak, A., Heckman, T., Levenson, N. A., Weaver, K., & Strickland, D. 2003, ApJ, 592, 782

Ptak, A., Serlemitsos, P., Yaqoob, T., & Mushotzky, R. 1999, ApJS, 120, 179

Ptak, A., Serlemitsos, P., Yaqoob, T., Mushotzky, R., & Tsuru, T. 1997, AJ, 113, 1286

Ramos Almeida, C., Levenson, N. A., Rodríguez Espinosa, J. M., et al. 2009, ApJ, 702, 1127

Ranalli, P., Comastri, A., & Setti, G. 2003, A&A, 399, 39

Rieke, G. H. 1988, ApJ, 331, L5

Rieke, G. H., Alonso-Herrero, A., Weiner, B. J., et al. 2009, ApJ, 692, 556

Rieke, G. H., Cutri, R. M., Black, J. H., et al. 1985, ApJ, 290, 116

Rieke, G. H. & Lebofsky, M. J. 1979, ARA&A, 17, 477

Rieke, G. H. & Lebofsky, M. J. 1985, ApJ, 288, 618

Rieke, G. H. & Low, F. J. 1972, ApJ, 176, L95+

Rieke, G. H. & Low, F. J. 1975, ApJ, 199, L13

Rieke, G. H., Young, E. T., Engelbracht, C. W., et al. 2004, ApJS, 154, 25

Rigby, J. R., Diamond-Stanic, A. M., & Aniano, G. 2009, ApJ, 700, 1878

Rigby, J. R., Marcillac, D., Egami, E., et al. 2008, ApJ, 675, 262

Rigby, J. R. & Rieke, G. H. 2004, ApJ, 606, 237

Rigopoulou, D., Kunze, D., Lutz, D., Genzel, R., & Moorwood, A. F. M. 2002, A&A, 389, 374

Rigopoulou, D., Spoon, H. W. W., Genzel, R., et al. 1999, AJ, 118, 2625

Risaliti, G., Gilli, R., Maiolino, R., & Salvati, M. 2000, A&A, 357, 13

Risaliti, G., Maiolino, R., Marconi, A., et al. 2006, MNRAS, 365, 303

Risaliti, G., Maiolino, R., & Salvati, M. 1999, ApJ, 522, 157

Roche, P. F., Aitken, D. K., Smith, C. H., & Ward, M. J. 1991, MNRAS, 248, 606

Rodríguez-Zaurín, J., Arribas, S., Monreal-Ibero, A., et al. 2011, A&A, 527, A60+

Rosa González, D., Terlevich, E., Jiménez Bailón, E., et al. 2009, MNRAS, 399, 487

Rosenthal, D., Bertoldi, F., & Drapatz, S. 2000, A&A, 356, 705

Roussel, H., Helou, G., Hollenbach, D. J., et al. 2007, ApJ, 669, 959

Rujopakarn, W., Eisenstein, D. J., Rieke, G. H., et al. 2010, ApJ, 718, 1171

Rupke, D. S. N., Veilleux, S., & Baker, A. J. 2008, ApJ, 674, 172

Rush, B., Malkan, M. A., & Spinoglio, L. 1993, ApJS, 89, 1

Sanders, D. B., Mazzarella, J. M., Kim, D.-C., Surace, J. A., & Soifer, B. T. 2003, AJ, 126, 1607

Sanders, D. B. & Mirabel, I. F. 1996, ARA&A, 34, 749

Sanders, D. B., Soifer, B. T., Elias, J. H., et al. 1988, ApJ, 325, 74

Satyapal, S., Sambruna, R. M., & Dudik, R. P. 2004, A&A, 414, 825

Satyapal, S., Vega, D., Dudik, R. P., Abel, N. P., & Heckman, T. 2008, ApJ, 677, 926

Schaerer, D. & Stasińska, G. 1999, A&A, 345, L17

Shaw, G., Ferland, G. J., Abel, N. P., Stancil, P. C., & van Hoof, P. A. M. 2005, ApJ, 624, 794

Shi, Y., Rieke, G. H., Hines, D. C., et al. 2006, ApJ, 653, 127

Shi, Y., Rieke, G. H., Ogle, P., Jiang, L., & Diamond-Stanic, A. M. 2009, ApJ, 703, 1107

Shi, Y., Rieke, G. H., Smith, P., et al. 2010, ApJ, 714, 115

Sirocky, M. M., Levenson, N. A., Elitzur, M., Spoon, H. W. W., & Armus, L. 2008, ApJ, 678, 729

Smith, J. D. T., Armus, L., Dale, D. A., et al. 2007a, PASP, 119, 1133

Smith, J. D. T., Draine, B. T., Dale, D. A., et al. 2007b, ApJ, 656, 770

Smith, J. D. T., Rudnick, L., Delaney, T., et al. 2009, ApJ, 693, 713

Smith, R. K., Brickhouse, N. S., Liedahl, D. A., & Raymond, J. C. 2001, ApJ, 556, L91

Snijders, L., Kewley, L. J., & van der Werf, P. P. 2007, ApJ, 669, 269

Soifer, B. T. & Neugebauer, G. 1991, AJ, 101, 354

Soifer, B. T., Neugebauer, G., & Houck, J. R. 1987a, ARA&A, 25, 187

Soifer, B. T., Neugebauer, G., Matthews, K., et al. 2000, AJ, 119, 509

Soifer, B. T., Sanders, D. B., Madore, B. F., et al. 1987b, ApJ, 320, 238

Spoon, H. W. W., Keane, J. V., Tielens, A. G. G. M., et al. 2002, A&A, 385, 1022

Spoon, H. W. W., Marshall, J. A., Houck, J. R., et al. 2007, ApJ, 654, L49

Strickland, D. K. & Heckman, T. M. 2009, ApJ, 697, 2030

Strickland, D. K., Heckman, T. M., Colbert, E. J. M., Hoopes, C. G., & Weaver, K. A. 2004, ApJS, 151, 193

Strickland, D. K., Heckman, T. M., Weaver, K. A., & Dahlem, M. 2000, AJ, 120, 2965

Strickland, D. K., Heckman, T. M., Weaver, K. A., Hoopes, C. G., & Dahlem, M. 2002, ApJ, 568, 689

Sturm, E., Lutz, D., Verma, A., et al. 2002, A&A, 393, 821

Sturm, E., Rupke, D., Contursi, A., et al. 2006, ApJ, 653, L13

Sturm, E., Schweitzer, M., Lutz, D., et al. 2005, ApJ, 629, L21

Surace, J. A., Sanders, D. B., & Mazzarella, J. M. 2004, AJ, 127, 3235

Swartz, D. A., Ghosh, K. K., Tennant, A. F., & Wu, K. 2004, ApJS, 154, 519

Takeuchi, T. T., Yoshikawa, K., & Ishii, T. T. 2003, ApJ, 587, L89

Telesco, C. M. & Harper, D. A. 1980, ApJ, 235, 392

Teng, S. H. & Veilleux, S. 2010, ApJ, 725, 1848

Teng, S. H., Wilson, A. S., Veilleux, S., et al. 2005, ApJ, 633, 664

Thornley, M. D., Schreiber, N. M. F., Lutz, D., et al. 2000, ApJ, 539, 641

Tine, S., Lepp, S., Gredel, R., & Dalgarno, A. 1997, ApJ, 481, 282

Tommasin, S., Spinoglio, L., Malkan, M. A., & Fazio, G. 2010, ApJ, 709, 1257

Tommasin, S., Spinoglio, L., Malkan, M. A., et al. 2008, ApJ, 676, 836

Toomre, A. 1977, in Evolution of Galaxies and Stellar Populations, ed. B. M. Tinsley & R. B. Larson, 401–+

Toomre, A. & Toomre, J. 1972, ApJ, 178, 623

Torrejón, J. M., Schulz, N. S., Nowak, M. A., & Kallman, T. R. 2010, ApJ, 715, 947

Tran, Q. D., Lutz, D., Genzel, R., et al. 2001, ApJ, 552, 527

Tueller, J., Baumgartner, W. H., Markwardt, C. B., et al. 2010, ApJS, 186, 378

Ueda, Y., Akiyama, M., Ohta, K., & Miyaji, T. 2003, ApJ, 598, 886

Urry, C. M. & Padovani, P. 1995, PASP, 107, 803

Valiante, E., Lutz, D., Sturm, E., Genzel, R., & Chapin, E. L. 2009, ApJ, 701, 1814

Veilleux, S., Kim, D., & Sanders, D. B. 2002, ApJS, 143, 315

Veilleux, S., Kim, D.-C., & Sanders, D. B. 1999, ApJ, 522, 113

Veilleux, S., Kim, D.-C., Sanders, D. B., Mazzarella, J. M., & Soifer, B. T. 1995, ApJS, 98, 171

Veilleux, S., Rupke, D. S. N., Kim, D.-C., et al. 2009, ApJS, 182, 628

Velusamy, T. & Langer, W. D. 2008, AJ, 136, 602

Verma, A., Lutz, D., Sturm, E., et al. 2003, A&A, 403, 829

Weaver, K. A., Meléndez, M., Mushotzky, R. F., et al. 2010, ApJ, 716, 1151

Weedman, D. W., Hao, L., Higdon, S. J. U., et al. 2005, ApJ, 633, 706

Werner, M. W., Roellig, T. L., Low, F. J., et al. 2004, ApJS, 154, 1

White, N. E., Swank, J. H., & Holt, S. S. 1983, ApJ, 270, 711

Wilms, J., Allen, A., & McCray, R. 2000, ApJ, 542, 914

Winter, L. M., Mushotzky, R. F., Terashima, Y., & Ueda, Y. 2009, ApJ, 701, 1644

Wu, H., Zou, Z. L., Xia, X. Y., & Deng, Z. G. 1998, A&AS, 132, 181

Wu, Y., Charmandaris, V., Hao, L., et al. 2006, ApJ, 639, 157

Yan, L., Chary, R., Armus, L., et al. 2005, ApJ, 628, 604

Yaqoob, T., Murphy, K. D., Miller, L., & Turner, T. J. 2010, MNRAS, 401, 411

Yuan, T.-T., Kewley, L. J., & Sanders, D. B. 2010, ApJ, 709, 884

Zezas, A., Ward, M. J., & Murray, S. S. 2003, ApJ, 594, L31

List of Figures

List of Tables